


This item was submitted to Loughborough University as an EngD thesis by the author and is made available in the Institutional Repository (<https://dspace.lboro.ac.uk/>) under the following Creative Commons Licence conditions.




creative
commons
C O M M O N S D E E D


Attribution-NonCommercial-NoDerivs 2.5


You are free:

- to copy, distribute, display, and perform the work

Under the following conditions:

 **BY:** **Attribution.** You must attribute the work in the manner specified by the author or licensor.

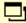
 **Noncommercial.** You may not use this work for commercial purposes.

 **No Derivative Works.** You may not alter, transform, or build upon this work.

- For any reuse or distribution, you must make clear to others the license terms of this work.
- Any of these conditions can be waived if you get permission from the copyright holder.

Your fair use and other rights are in no way affected by the above.

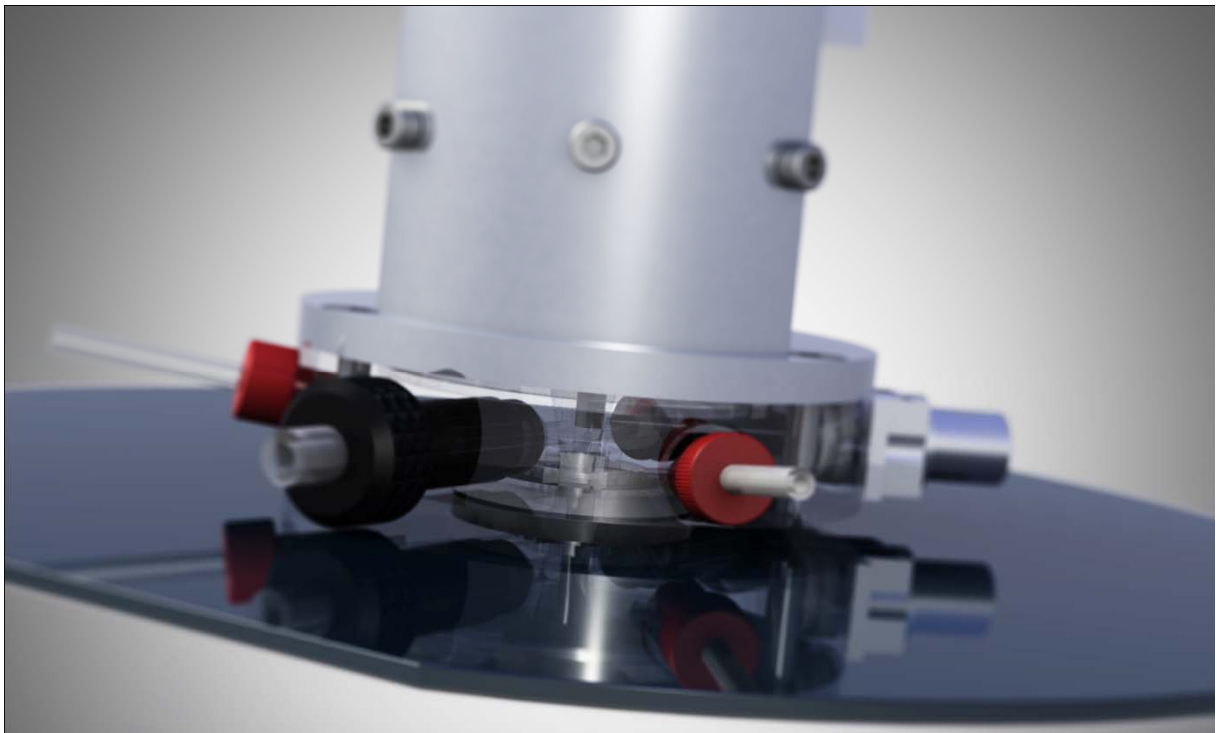
This is a human-readable summary of the [Legal Code \(the full license\)](#).

[Disclaimer](#) 

For the full text of this licence, please go to:
<http://creativecommons.org/licenses/by-nc-nd/2.5/>

A Non-Contact Laser Ablation Cell for Mass Spectrometry

Dhinesh Asogan



Electro Scientific Industries
New Wave Research Division
8 Avro Court
Ermine Business Park
Huntingdon
Cambridge
PE29 6XS

Centre for Innovative and Collaborative
Engineering
Department of Civil & Building Engineering
Loughborough University
Loughborough
Leicestershire
LE11 3TU

Thesis Access Form

Copy No **Location**

Author Dhinesh Asogan

Title A Non-Contact Laser Ablation Cell for Mass Spectrometry

Status of access OPEN / ~~RESTRICTED~~ / ~~CONFIDENTIAL~~

Moratorium period:-..... years, ending-..... / 200.....-.....

Conditions of access proved by (CAPITALS):

Supervisor (Signature)

School of

Author's Declaration: I agree the following conditions:

Open access work shall be made available (in the University and externally) and reproduced as necessary at the discretion of the University Librarian or Dean of School. It may also be digitised by the British Library and made freely available on the Internet to registered users of the EThOS service subject to the EThOS supply agreements.

The statement itself shall apply to ALL copies including electronic copies:

This copy has been supplied on the understanding that it is copyright material and that no quotation from the thesis may be published without proper acknowledgement.

Restricted/confidential work: All access and any photocopying shall be strictly subject to written permission from the University Dean of School and any external sponsor, if any.

Author's signature

Date

Users declaration: for signature during any Moratorium period (Not Open work):

I undertake to uphold the above conditions:

Date	Name (CAPITALS)	Signature	Address

Certificate of Originality

This is to certify that I am responsible for the work submitted in this thesis, that the original work is my own except as specified in acknowledgments or in footnotes, and that neither the thesis nor the original work contained therein has been submitted to this or any other institution for a higher degree.

Author's signature

Date

A NON-CONTACT LASER ABLATION CELL FOR MASS SPECTROMETRY

By

Dhinesh Asogan

A dissertation thesis submitted in partial fulfilment of the requirements for the award of the degree Doctor of Engineering (EngD), at Loughborough University

September 2011

© by Dhinesh Asogan 2011

Electro Scientific Industries
New Wave Research Division
8 Avro Court
Ermine Business Park
Huntingdon
Cambridge
PE29 6XS

Centre for Innovative and Collaborative
Engineering
Department of Civil & Building Engineering
Loughborough University
Loughborough
Leicestershire
LE11 3TU

TABLE OF CONTENTS

Acknowledgements	i
Abstract	iii
Preface	v
Used Acronyms / Abbreviations	vii
List of Figures	ix
List of Tables	xiii
List of Papers	xv
1 Introduction	1-1
1.1 Electro Scientific Industries Inc., New Wave Research Division	1-1
1.2 Mass Spectrometry.....	1-2
1.2.1 Ionisation Sources.....	1-2
1.2.2 Mass Analysers.....	1-8
1.2.3 Detectors.....	1-18
1.3 Lasers in Analytical Chemistry	1-19
1.3.1 Laser Induced Thermal Desorption (LITD).....	1-20
1.3.2 Matrix Assisted Laser Desorption Ionisation	1-20
1.3.3 Mechanisms of Particle Desorption	1-20
1.4 Laser Ablation	1-23
1.4.1 Laser Ablation Plume Regions.....	1-24
1.4.2 Particle Size Distribution in Laser Ablation.....	1-25
1.5 Application of Lasers in Mass Spectrometry.....	1-27
1.5.1 MALDI Mapping	1-28
1.5.2 Atmospheric Pressure MALDI Interfaces	1-28
1.6 Laser Ablation Cell Development	1-32
1.6.1 Large, Enclosed Cell Strategies.....	1-32
1.6.2 Non-Contact Cell Strategies.....	1-35
2 Overarching Aim and Objectives	2-1
2.1 Design Brief.....	2-1
2.2 Performance	2-2
3 Research Methodology	3-1
3.1 Validation Methodological Considerations	3-1
4 The Research Undertaken	4-1
4.1 Design of the Non-Contact Cell	4-2
4.2 Principle of Operation of the Non-Contact Cell	4-9
4.3 Gas Dynamics through the Cell	4-10
4.3.1 Effect of Input Flow Rate on Gas Transmission Efficiency	4-11
4.3.2 Gas Flow Composition Study.....	4-15
4.3.3 Effect of Cell Distance to Sample on Gas Transmission Efficiency.....	4-17
4.4 Performance Testing: Transport Efficiency and Raw Signal Intensity	4-25
4.4.1 NIST CRM-613	4-25
4.4.2 Silicon Wafer	4-32
4.5 Performance Testing: Molecular Ion Formation, Time Resolved Reproducibility and Signal Stability.....	4-36
4.5.1 Sensitivity and Molecular Ion Formation	4-39
4.5.2 Time-resolved Reproducibility	4-42

4.5.3	Time-resolved Stability.....	4-45
4.6	Numerical Simulations: Gas Flow Paths.....	4-47
4.6.1	Governing Equations	4-47
4.6.2	Numerical Solution Setup	4-54
4.6.3	Non-Contact Cell Mesh Generation and Boundary Definitions	4-55
4.6.4	Gas Flow Patterns	4-57
4.6.5	Particle Transport	4-60
5	Parallel Research	5-1
5.1	Aerosol Lens Stacks for Particle Transport.....	5-1
5.1.1	Selected Applications for Aerodynamic Lenses	5-3
5.1.2	Aerodynamic Lenses as Particle Size Selectors	5-4
5.1.3	Design Calculations	5-4
5.1.4	Simulations	5-12
5.1.5	Testing.....	5-14
5.2	Single-Point Calibration Strategy for the Analysis of Silicon Wafers by Laser Ablation-Inductively Coupled Plasma-Mass Spectrometry.....	5-19
5.2.1	Calibration Strategy	5-20
5.2.2	Experimental.....	5-21
5.2.3	Results and Discussions	5-22
5.2.4	Conclusions and Further Work	5-24
5.3	MALDI sampling using the non-contact cell	5-26
5.3.1	Experimental.....	5-27
6	Findings & Implications	6-1
6.1	Implications for New Wave Research and Relevant Industries.....	6-1
6.2	Critical Evaluation and Further Research	6-2
7	References	7-1
Appendix A	Apparatus and Method for Laser Irradiation (Paper 1)	A-1
Appendix B	An open, non-contact cell for laser ablation-inductively coupled plasma-mass spectrometry (Paper 2).....	B-1
Appendix C	Numerical simulations of gas flows through an open, non-contact cell for LA-ICP-MS (Paper 3).....	C-1
Appendix D	Technical Drawings	D-1

ACKNOWLEDGEMENTS

I would like to take this opportunity to express my gratitude to a number of people and institutions for their support and wisdom over the past six years.

Firstly, I would like to thank the EPSRC, the New Wave Research division of Electro Scientific Industries, CICE and the Department of Chemistry at Loughborough University for providing funding, equipment and facilities that allowed this project to proceed.

I would particularly like to thank my academic supervisors, Prof. Barry Sharp and Prof. Roger Smith for their understanding and guidance throughout the project. I would also like to thank my industrial supervisor and colleagues Dr. Ciaran O' Connor, Dr. Damon Green, Dr. Rob Hutchinson, Jay Wilkins and Mantreh Nournia from ESI for their support and commercial guidance.

I would like to express my thanks to Bob Ludlam and his team at the Wolfson School of Mechanical Engineering workshop at Loughborough University for building the first alpha prototype of the cell and also for guiding me in the ways of designing with manufacture in mind. Similarly, I would also like to thank Albrook Engineering of Loughborough for providing engineering services when Bob was unable to.

Thanks to the CICE staff, namely Prof. Dino Bouchlaghem, Prof. Chimay Anumba, Jo Brewin, Sara Cowin, Colette Bujdoso and Nadine Smith, who kept me on the straight and narrow throughout the project, and for throwing fantastic Christmas parties.

My gratitude goes to the technical staff at the chemistry department: Trevor Brown, Andy Kowalski and Stuart Pinkney, thank you for your ideas, support and helping me engineer solutions to new problems. To Dave Wilson, thank you and rest in peace.

To the members of the Centre for Analytical Science at Loughborough, thank you for your support and friendship throughout. I would particularly like to thank Adam Douglas, David Douglas and Claire Camp for helping me keep the lab running as best we could.

I would like to thank all of my friends for their support, kindness and laughter.

To my Mum and Dad, Vasantha and Asogan, and my sister Mrudhula, without your support I would not be the person I am today. Thank you for keeping me going.

THIS PAGE IS INTENTIONALLY BLANK

ABSTRACT

A common analytical problem in applying LA sampling concerns dealing with large planar samples, *e.g.* gel plates, Si wafers, tissue sections or geological samples.

As the current state of the art stands, there are two solutions to this problem: either sub-sample the substrate or build a custom cell. Both have their inherent drawbacks. With sub-sampling, the main issue is to ensure that a representative is sample taken to correctly determine the analytes of interest. Constructing custom cells can be time consuming, even for research groups that are experienced or skilled, as they have to be validated before data can be published.

There are various published designs and ideas that attempt to deal with the issue of large samples, all of which ultimately enclose the sample in a box.

The work presented in this thesis shows a viable alternative to enclosed sampling chambers. The ‘non-contact cell’ is an open cell that uses novel gas dynamics to remove the necessity for an enclosed box and, therefore, enables samples of any arbitrary size to be sampled. The upper size limit of a sample is set by the travel of the XY stages on the laser ablation system, not the dimensions of the ablation cell.

KEY WORDS

Laser Ablation, Mass Spectrometry, Laser Scribing, Semiconductor, Biomolecular Imaging, Elemental Spectroscopy

THIS PAGE IS INTENTIONALLY BLANK

PREFACE

This thesis presents research conducted during the period July 2005 to August 2010 in partial fulfilment of the requirements of the Engineering Doctorate (EngD) programme. The research was conducted in collaboration with the Centre for Innovative and Collaborative Engineering and the Centre for Analytical Science, both at Loughborough University. The research was funded by the Engineering and Physical Sciences Research Council, and sponsored by Electro Scientific Industries Inc., a major player in both the semiconductor and laser industries.

The EngD programme is a four-year post-graduate award, the core of which is to find solutions to industrially relevant problems within an industrial context. It is an alternative to a traditional PhD, providing a more vocationally oriented doctorate programme that is better suited to industry needs.

The EngD programme is examined by a discourse around a body of published papers, and as such should be read alongside those papers. This thesis is supported by one patent application, one paper and a technical note bound as appendices. The discourse laid out in this thesis will link these three publications within the context of laser based chemical analysis and provide a commentary on the industrial significance of the research undertaken.

THIS PAGE IS INTENTIONALLY BLANK

USED ACRONYMS / ABBREVIATIONS

AP	Atmospheric Pressure
AWG	American Wire Gauge
BNC	Bayonet Nut Coupling
CAD	Computer Aided Design
CCD	Charge-coupled Device
cDTPA	cyclic diethylenetriaminepentaacetic anhydride
CFD	Computational Fluid Dynamics
CI	Chemical Ionisation
CHCA	α -cyano-4-hydroxycinnamic acid
cps	Counts-per-second
CRM	Certified Reference Material
DC	Direct Current
DHB	2,5-dihydroxybenzoic acid
DRAM	Dynamic Random Access Memory
DNA	Deoxyribose nucleic acid
EDM	Electro Discharge Machining
EI	Electron Impact Ionisation
Er:YAG	Erbium doped Yttrium-Aluminium-Garnet
ESA	Electrostatic Analyser
ESI	Electrospray Ionisation
ESI Inc.	Electro Scientific Industries Incorporated
FAB	Fast Atom Bombardment
Fab. Plant	Semiconductor Fabrication Facility
FT	Fourier Transform
FV	Finite Volumes
HDPE	High Density Polyethylene
HEAD	High Efficiency Aerosol Dispersion
ICP	Inductively Coupled Plasma
ICR	Ion Cyclotron Resonance
IE	Ionisation Energy
IR	Infrared
ITO	Indium-tin oxide
KED	Kinetic Energy Discrimination
LASER	Light Amplification by Stimulated Emission of Radiation (also “laser”)
LA	Laser Ablation
LCD	Liquid Crystal Display
LDI	Laser Desorption Ionisation
LED	Light Emitting Diode
LIBS	Laser Induced Breakdown Spectroscopy
LITD	Laser Induced Thermal Desorption
MALDI	Matrix Assisted Laser Desorption Ionisation
MS	Mass Spectrometry
<i>m/z</i>	Mass-to-charge ratio

NCC	Non-Contact Cell
Nd:YAG	Neodymium doped Yttrium-Aluminium-Garnet laser medium
NIST	National Institute of Standards and Technology
NWR	New Wave Research
PA	Pneumatically Assisted
PDF	Pulsed Dynamic Focussing
PMMA	Polymethylmethacrylate (Perspex® (UK) or Plexiglas® (USA))
POM	Polyoxymethylene (Delrin®)
ppm	parts-per-million (units)
PSD	Particle Size Distribution
PTFE	Polytetrafluoroethylene (Teflon®)
RF	Radio-Frequency
RNA	Ribose nucleic acid
RSD	Relative Standard Deviation
SA	Sinapinic acid
SEM	Secondary Electron Multiplier
ToF	Time of Flight
TLC	Thin Layer Chromatography
UP	Universal Platform
UV	Ultraviolet
XRF	X-Ray Fluorescence

LIST OF FIGURES

Figure 1.1:	A simple schematic illustrating the stages involved in mass spectrometry. ..	1-2
Figure 1.2:	Action of an electrospray tip.	1-4
Figure 1.3:	The ICP torch setup.....	1-5
Figure 1.4:	A schematic showing the force applied to a charged beam of ions by an electromagnet (adapted from Gross ^[10]).	1-8
Figure 1.5:	Simultaneous detection using a magnetic sector mass analyser.....	1-9
Figure 1.6:	Sequential detection using a magnetic sector mass analyser.....	1-9
Figure 1.7:	Simple schematic of an Electrostatic Analyser.	1-10
Figure 1.8:	Schematic layout of a reverse Nier-Johnson double focussing sector field mass analyser.....	1-11
Figure 1.9:	Schematic of a quadrupole mass analyser.....	1-12
Figure 1.10:	Schematic of a 3D ion trap mass analyser.....	1-13
Figure 1.11:	Schematic of a time of flight mass analyser with reflector region.....	1-16
Figure 1.12:	Cutaway diagram of an Orbitrap mass analyser showing a stabilised ion cloud around the central ion and the split outer electrodes (adapted from Makarov ^[13]).....	1-16
Figure 1.13:	Schematic of a generic secondary electron multiplier.	1-18
Figure 1.14:	Schematic of the plume regions generated by laser ablation	1-24
Figure 1.15:	Schematic of an AP MALDI Interface	1-29
Figure 1.16:	Simple Schematic of the Gas Channel Plate Used by O'Connor <i>et al.</i> ^[30]	1-29
Figure 1.17:	Schematic of an Improved AP-MALDI Interface Adapted for PDF	1-30
Figure 1.18:	Simplified Schematic of the MassTech AP-MALDI PDF Source.....	1-31
Figure 1.19:	Side view of the HEAD cell, developed by Pisonero <i>et al.</i> ^[38]	1-33
Figure 1.20:	Top view of the HEAD cell developed by Pisonero <i>et al.</i> ^[38]	1-33
Figure 1.21:	Schematic of the laser ablation cell developed by Feldmann <i>et al.</i> ^[39]	1-34
Figure 1.22:	Schematic of the continuous ablation cell developed by Barringer. ^[46]	1-35
Figure 1.23:	Front and side views of the 'Vaporization Cell' patented by Barringer. ^[47] ..	1-36
Figure 4.1:	Rendered image of the non contact cell main body (upper surface – Revision G)	4-2
Figure 4.2:	Rendered image of the non-contact cell (lower surface – Revision G).....	4-2
Figure 4.3:	Rendered exploded view of the main body, top plate and optical window assembly	4-4
Figure 4.4:	Rendered exploded view of the objective mount plate assembly	4-5
Figure 4.5:	Main body of the non-contact cell showing installation of mesh components (revision G).....	4-6
Figure 4.6:	Rendered exploded view of the redesigned mesh assembly (revision H)	4-7
Figure 4.7:	Rendered exploded view of the BNC ground plane connector assembly attached to the side of the non-contact cell.....	4-8
Figure 4.8:	Cross section of the non-contact cell showing concentric inlet channels, inner cell volume, output channels and approximate direction of gas flow (Revision H).	4-9
Figure 4.9:	The prototype non-contact cell mounted on a New Wave Research UP-213 laser system floating above a 120 mm silicon wafer sample.	4-10
Figure 4.10:	Output flow rate and transmission efficiency (relative to carrier channel flow rate) <i>vs.</i> carrier channel flow rate for the non-contact cell.....	4-11
Figure 4.11:	Output flow rate and transmission efficiency (relative to curtain channel flow rate) <i>vs.</i> curtain channel flow rate for the non-contact cell.....	4-12
Figure 4.12:	Output flow rate <i>vs.</i> carrier channel flow rate and curtain channel flow rate for the non-contact cell.....	4-13
Figure 4.13:	Transmission efficiency relative to total input flow <i>vs.</i> carrier channel flow rate and curtain channel flow rate for the non-contact cell	4-13
Figure 4.14:	Theoretical and measured transmission through the non-contact cell at six pairs of curtain and carrier channel flow rates	4-14

Figure 4.15:	Nitrogen and oxygen content of the output flow <i>vs.</i> carrier channel flow rate for the non-contact cell.....	4-15
Figure 4.16:	Nitrogen and oxygen content of the output flow <i>vs.</i> curtain channel flow rate for the non-contact cell.....	4-16
Figure 4.17:	Output flow rate <i>vs.</i> carrier channel flow rate and sample-to-cell distance with (a) curtain channel switched off and (b) curtain channel switched on.....	4-17
Figure 4.18:	Transmission efficiency (relative to total flow) <i>vs.</i> carrier channel flow rate and sample-to-cell distance with (a) curtain channel switched off and (b) curtain channel switched on.....	4-18
Figure 4.19.:	Output flow rate <i>vs.</i> nebuliser driving pressure for a Conikal nebuliser with a 1 ml min ⁻¹ liquid uptake capacity.	4-19
Figure 4.20:	Adjusted output flow rate <i>vs.</i> nebuliser driving pressure for a Conikal nebuliser with a 1 ml min ⁻¹ liquid uptake capacity.	4-20
Figure 4.21:	Schematic of a cross flow jet-pump.....	4-20
Figure 4.22:	Jet-pump negative pressure difference <i>vs.</i> argon driving flow pressure and jet-to-throat separation using a 254 μm jet nozzle.....	4-21
Figure 4.23:	Output flow rate <i>vs.</i> jet-pump driving pressure for a jet-pump with a 254 μm nozzle.....	4-22
Figure 4.24:	Adjusted output flow rate <i>vs.</i> jet-pump driving pressure for a jet-pump with a 254 μm nozzle.	4-23
Figure 4.25:	Signal intensity <i>vs.</i> laser power for NIST CRM-613 in the standard New Wave Research sampling cell using a UP-213 laser ablation system.....	4-26
Figure 4.26:	Normalised ²³² Th signals <i>vs.</i> time for a 5 min line scan on NIST CRM-613 showing wash-in and wash-out times for the standard cell and the non-contact cell.....	4-27
Figure 4.27:	NIST CRM-613 post ablation by the non-contact cell showing line scan and spot scan positions.....	4-28
Figure 4.28:	Signal intensity <i>vs.</i> time scans for ²³² Th from 5 min line scans on NIST CRM-613 using the non-contact cell.....	4-28
Figure 4.29:	²³² Th/ ¹⁶ O ratio <i>vs.</i> time from 5 min line scans on NIST CRM-613 using the non-contact cell.....	4-29
Figure 4.30:	²³² Th/ ²³⁸ U ratio <i>vs.</i> time from 5 min line scans on NIST CRM-613 using the non-contact cell.....	4-30
Figure 4.31:	²³² Th, ²³⁸ U, ²⁴⁸ ThO and ²⁵⁴ UO signal intensity <i>vs.</i> time from spot-line scans on NIST CRM-613 using the standard sampling cell	4-31
Figure 4.32:	²³² Th, ²³⁸ U, ²⁴⁸ ThO and ²⁵⁴ UO signal intensity <i>vs.</i> time from spot-line scans on NIST CRM-613 using the non-contact cell	4-32
Figure 4.33:	Si Wafer samples post ablation sampled by (a) the non-contact cell and (b) the standard cell, showing amorphous silicon (brown powder) on the surface of the crystalline wafer.....	4-32
Figure 4.34:	Normalised ³¹ P signal intensity <i>vs.</i> time for a 5 min line scan on a silicon wafer sample showing wash-in and wash-out times for the standard cell and the non-contact cell.....	4-33
Figure 4.35:	³¹ P signal intensity <i>vs.</i> time from spot-line scans on silicon wafer using the standard sampling cell.....	4-34
Figure 4.36:	³¹ P signal intensity <i>vs.</i> time from spot-line scans on silicon wafer using the non-contact cell.....	4-34
Figure 4.37:	Signal intensity <i>vs.</i> height from sample for NIST CRM-613 using the non-contact cell on a UP-193 laser ablation system.....	4-38
Figure 4.38:	Signal variation and molecular ion formation for ⁸⁵ Rb in both the standard sampling cell and the non-contact cell (at various heights).....	4-39
Figure 4.39:	Signal variation, nitride and oxide formation for ²³² Th in both the standard sampling cell and the non-contact cell (at various heights).....	4-40
Figure 4.40:	Signal variation, nitride and oxide formation for ²³⁸ U in both the standard sampling cell and the non-contact cell (at various heights).....	4-41

Figure 4.41:	Signal intensity <i>vs.</i> time for NIST CRM-613 using the standard sampling cell on a UP-193 laser ablation system showing a wash-in time of approximately 10 s and a wash-out time of approximately 15 s.....	4-42
Figure 4.42:	Signal intensity <i>vs.</i> time for NIST CRM-613 using the non-contact cell on a UP-193 laser ablation system showing a wash-in time of 5 s and a wash-out time of 7.5 s.....	4-43
Figure 4.43:	Signal intensity <i>vs.</i> time for NIST CRM-613 using the standard sampling cell on a UP-193 laser ablation system showing signal reproducibility for six sequential laser shots.	4-43
Figure 4.44:	Signal intensity <i>vs.</i> time for NIST CRM-613 using the non-contact cell on a UP-193 laser ablation system showing signal reproducibility for six sequential laser shots.	4-44
Figure 4.45:	Signal intensity <i>vs.</i> time of NIST CRM-613 using the standard sampling cell on a UP-193 laser ablation system for a 2 minute single 100 μm spot drill.	4-45
Figure 4.46:	Signal intensity <i>vs.</i> time of NIST CRM-613 using the non-contact cell on a UP-193 laser ablation system for a 2 min single 100 μm spot drill.	4-46
Figure 4.47:	Signal intensity <i>vs.</i> time of NIST CRM-613 using both the standard sampling cell and the non-contact cell on a UP-193 laser ablation system for a 2 min single 100 μm spot drill.....	4-46
Figure 4.48:	Pressure drop <i>vs.</i> volumetric flow rate for air through the micro-jet array repeat unit	4-52
Figure 4.49:	Mesh used to simulate the gas flows through the non-contact cell, showing fluid (blue) cells and partial (green) cells in (a) top, (b) isometric, (c) front and (d) zoomed front views.	4-55
Figure 4.50:	Position and values for boundary conditions used in numerical simulations for the non-contact cell.	4-56
Figure 4.51:	False colour images showing volume fraction of air across the wafer surface (a) with and (b) without the micro-jet array	4-57
Figure 4.52:	False colour images of (a) helium and (b) nitrogen volume fraction across the sample surface without the micro-jet array	4-57
Figure 4.53:	Flow trajectories from the sweep gas inlet, showing entrainment of the sweep gas into the curtain gas channel.	4-58
Figure 4.54:	False colour images of (a) helium and (b) nitrogen volume fraction across the sample surface with the micro-jet array in place.	4-58
Figure 4.55:	Flow trajectories for the sweep gas channel with the micro-jet array in place, showing flow separation and increased independence from the curtain gas channel.	4-59
Figure 4.56:	Shape of a transient 100 μm laser track.	4-60
Figure 4.57:	Particle flow trajectories for 1 μm glass particles ($\dot{m} = 5 \text{ ng min}^{-1}$) through the non-contact cell both (a) without and (b) with the micro-jet array. Trajectories are coloured with particle velocity.	4-60
Figure 4.58:	Deposition of soft, biological material on the non-contact cell window. In this figure, the material has been burnt into the window coating.....	4-61
Figure 4.59:	Calculated velocity profiles of trajectories for 1 μm spherical particles through the NCC with (blue) and without (red) the micro-jet array in place.	4-61
Figure 5.1:	A single cone vacuum interface illustrating losses in sampling	5-1
Figure 5.2:	Action of a virtual impactor flow concentrator showing increased particle concentration.....	5-2
Figure 5.3:	An aerodynamic lens system showing carrier gas streamline contraction and approximate particle streamlines dependent on Stokes' number	5-2
Figure 5.4:	Typical configuration of a focusing aerodynamic lens system	5-4
Figure 5.5:	Dimension of the single lens setup	5-12
Figure 5.6:	Particle transmission efficiency <i>vs.</i> particle size for four lens sizes	5-13
Figure 5.7:	Contraction factors <i>vs.</i> particle size for four lens sizes	5-13
Figure 5.8:	Schematic layout of the sample introduction system for LA-AL-ICP-MS ...	5-14
Figure 5.9:	Signal intensity <i>vs.</i> volumetric He flow rate for ^{207}Pb	5-15
Figure 5.10:	$^{207}\text{Pb}/^{232}\text{Th}$ ratio <i>vs.</i> volumetric He flow rate.	5-17

Figure 5.11:	Microscope image of an ablated track through a silicon wafer	5-23
Figure 5.12:	Background and drift corrected signal dependence on laser power for iron, cobalt and indium in a matrix blank vanillic acid disc.	5-28
Figure 5.13:	Background and drift corrected signal dependence on laser power for iron, cobalt and indium in an indium spiked vanillic acid disc	5-29
Figure 5.14:	Background and drift corrected signal dependence on laser power for iron, cobalt and indium in a cyanocobalamin doped, indium spiked vanillic acid disc.....	5-29

LIST OF TABLES

Table 4.1:	LA-ICP-MS Settings for the validation of the non-contact cell on the UP-213 laser ablation system.....	4-25
Table 4.2:	Oxide levels from thorium and uranium in NIST-613 for both the standard and non-contact cells.	4-30
Table 4.3:	LA-ICP-MS settings for the validation of the non-contact cell on the UP-193 laser ablation system.....	4-37
Table 4.4:	Optimum jet-pump flow rates for different sample-to-cell heights of the non-contact cell.....	4-38
Table 4.5:	Summary of numerical results obtained by CFD for the non-contact cell...	4-59
Table 5.1:	LA-AL-ICP-MS Settings.....	5-14
Table 5.2:	Adjusted concentrations for elements used in LA-AL-ICP-MS experiment, based on an electron density of $1.6 \times 10^{15} \text{ cm}^{-3}$ and a 6800 K plasma temperature. ^[8]	5-16
Table 5.3:	Theoretical nuclide ratios between lead, thorium and uranium isotopes....	5-16
Table 5.4:	Operating conditions for LA-ICP-MS experiments	5-21
Table 5.5:	Limits of Detection obtained for LA-ICP-MS.....	5-22
Table 5.6:	Dopant densities obtained by LA-ICP-MS compared to 4-point probe resistivity	5-22
Table 5.7:	Composition by weight of four mixtures used to investigate the viability of MALDI using a 213 nm laser ablation system.....	5-27

THIS PAGE IS INTENTIONALLY BLANK

LIST OF PAPERS

The following papers, included in the appendices, have been produced in partial fulfilment of the award requirements of the Engineering Doctorate during the course of the research.

PAPER 1 (SEE APPENDIX A)

“Apparatus and Method for Laser Irradiation”

Dhinesh Asogan, Barry L. Sharp, Ciaran J. P. O' Connor,

US Patent Application No: US 2010/0207038 A1

Filed: Feb. 13, 2009

Published: Aug. 19, 2010

PAPER 2 (SEE APPENDIX B)

“An open, non-contact cell for laser ablation-inductively coupled plasma-mass spectrometry”

Dhinesh Asogan, Barry L. Sharp, Ciaran J. P. O' Connor, Damon A. Green and Robert W. Hutchinson,

Journal of Analytical Atomic Spectrometry, 2009, Vol. **24**, pp. 917 – 923

DOI: 10.1039/B904850B

PAPER 3 (SEE APPENDIX C)

“Numerical simulations of gas flows through an open, non-contact cell for LA-ICP-MS”

Dhinesh Asogan, Barry L. Sharp, Ciaran J. P. O' Connor, Damon A. Green and Jay Wilkins,

Journal of Analytical Atomic Spectrometry, 2011, Vol. **26**, pp. 631 – 634

DOI: 10.1039/CoJA00166J

THIS PAGE IS INTENTIONALLY BLANK

1 Introduction

This chapter provides an introduction to the sponsoring company and the use of lasers in analytical chemistry, with particular attention to the technique of laser ablation (LA) used in conjunction with inductively coupled plasma-mass spectrometry (ICP-MS), with a view to place the research undertaken into context.

1.1 Electro Scientific Industries Inc., New Wave Research Division

Electro Scientific Industries Incorporated (ESI Inc.) is one of the world's leading suppliers of laser systems for micro-engineering applications. ESI Inc. designs and develops a broad range of products for advanced electronic devices in use in the world today.

Founded in 1944 as Brown Engineering, ESI Inc. initially produced high-precision resistance measurement instrumentation and reference standards. In 1980 the company further expanded their product line by introducing an advanced laser system for use by semiconductor manufacturers in the repair of dynamic random access memory (DRAM) chips. Other products include laser drilling systems for advanced semiconductor packaging, lasers for flat panel display repair and failure analysis, and test, termination and inspection systems for passive electronic components.

The New Wave Research (NWR) division was acquired by ESI Inc. in 2007 to provide photonic solutions in adjacent markets such as Light Emitting Diode (LED) production, Liquid Crystal Display (LCD) repair and Laser Ablation for analytical applications. The NWR division is headquartered in Fremont, California, with its European arm being led out of Huntingdon, Cambridge. The NWR division of ESI Inc. currently drives innovation in analytical chemistry within the company, aiming to provide 'next-gen' photonic solutions for today's analysts.

In the past decade, New Wave Research has been committed to improving sample cells used by their laser ablation systems, improving the response, reliability and, ultimately, the quality of the datasets gathered by their customers. Their current line-up of cells includes: the standard cell, a general cell suitable for most analyses; the large format cell, used for analysis of relatively large samples; the paper cell, created for thin samples that can be clamped; and the SuperCell™, for very fast washout for limited/very small samples.

1.2 Mass Spectrometry

This is an established technique that can be used to identify elements and molecular fragments according to their relative molecular masses.^[1] To do this, the analyte must first be ionised in the gaseous phase and the resultant mixture of ions is sent through a mass analyser to separate the ions by mass-to-charge ratio (m/z), and then the ions are detected in the detector. A simple schematic is shown in Figure 1.1 below:



Figure 1.1: A simple schematic illustrating the stages involved in mass spectrometry. ‘Sample Introduction’ and ‘Ionisation’ may not necessarily occur in this order, *e.g.* using electrospray ionisation (see later), ionisation occurs before introduction into the mass spectrometer.

The setup of the mass spectrometer, in terms of sample introduction method, ionisation method etc., depends entirely on the nature of the sample, *e.g.* a liquid sample may be best introduced as a liquid aerosol using a nebuliser, whereas a solid sample may be best introduced as a solid aerosol by laser desorption/ablation.

To prevent the formed analyte ions from either losing their charge to the instrument walls or reacting with gaseous molecules in the atmosphere, from the point of ionisation the mass spectrometer usually operates under high vacuum. The operating pressure is chosen such that the mean free path of the ions is approximately one metre, which occurs at a pressure of around 6.5×10^{-3} Pa.

Mass spectrometers with high voltage ionisation sources use lower pressures to prevent unwanted discharges from the ion source. The pressure used is dependent on the mean free path required, *e.g.* a quadrupole mass analyser needs a low mean free path and therefore can handle higher pressures of up to 10^{-2} Pa, whereas a magnetic/electric sector mass analyser requires a longer mean free path and therefore runs at pressures down to 10^{-5} Pa.

As stated above, the chosen sample introduction technique depends entirely on the samples being analysed. For liquid samples, one of the most common forms of introduction is via a nebuliser^[2] for later ionisation, or by electrospray, whereas with solid samples it is usual to use either laser ablation^[3] or laser desorption.^[4]

1.2.1 Ionisation Sources

The ion source is the component of the mass spectrometer that ionises the sample ready for mass analysis. This component is either concurrent with or proceeds the sample introduction system and is dependent on both the nature of the sample and the mass analyser being used.

One of the first ionisation sources devised was the electron impact (EI) source.^[1] This comprises an electrically heated filament that gives off electrons, which are then accelerated towards the sample *via* an anode. Collisions between these electrons and the sample result in ejection of electrons from the molecule to form positively charged cations. The kinetic energy associated with the electrons fired at the sample can be high enough to interact with

vibrational states in the molecular bonding of the sample, which can cause fragmentation in addition to the ionisation. This is particularly useful for structural analysis of small (up to 1 kilo-Dalton (kDa)) organic molecules.

An extension of the EI source is the chemical ionisation (CI) source, whereby a reagent gas is pumped into the ionisation chamber along with the sample. There are a range of reagent gases available for use in CI sources, the most common being methane, isobutane and ammonia. The reagent gas is pumped in at a significantly higher pressure than the sample; hence, primary ionisation of the reagent gas occurs resulting in both positive reagent gas ions and slow moving, thermal electrons. Because of the higher input pressure, the major fragments in the spectra derive from the reagent gas rather than the sample.

In cases where the sample is more basic than the reagent gas, charge transfer with the reagent gas occurs, *e.g.* through hydride transfer, resulting in positively charged sample ions (positive CI). Where the sample is more acidic than the reagent gas, electron capture (from the reagent gas) or proton transfer (to the reagent gas) occurs resulting in negatively charged sample ions (negative CI).

Chemical ionisation is able to handle slightly larger molecules than electron impact due to the decreased fragmentation. However, as this is still a hard technique this improvement only covers small molecules up to about 1.5 kDa. CI causes high background signals of the reagent gas, so sensitivity can be lower than other techniques; however, provided the analyte mass region is sufficiently separated from the reagent gas region, the mass spectra produced are 'cleaner' with fewer fragment ions, and potentially fewer spectral interferences.

The Fast Atom Bombardment (FAB) source uses inert neutral atoms, usually group 18 elements such as argon or xenon, to physically desorb sample molecules from a probe. The sample is mixed with a non-volatile matrix that is capable of chemically ionising the sample and then subjected to a stream of fast atoms. The preformed ions are ejected from the sample-matrix mixture into the gas phase and transported to the mass analyser. This is a much softer ionisation approach and can achieve ionisation of biomolecules up to 24 kDa in size;^[5] however, since FAB relies on chemical ionisation, the sensitivity of the instrument depends on the ionisation efficiency of the chemical process.

1.2.1.1 Electrospray Ionisation

Electrospray ionisation (ESI) is one of the more popular ionisation techniques for large (bio)molecules.^[1] This is both a soft ionisation source and a sample introduction technique for liquid samples, since the processes leading to ionisation also nebulise the sample. The sample is pumped at low flow rates (typically 1 – 10 $\mu\text{l min}^{-1}$) at atmospheric pressure through a capillary, the tip of which is floated at a potential between +2 to +4 kV. The capillary tip is separated from a counter electrode by up to 2 cm, and the electric field produced causes a charge to accumulate at the sample surface. The sample then breaks down to form droplets.

The sample droplets are desolvated prior to entering the vacuum of the mass spectrometer by a flow of hot nitrogen ($\sim 80^\circ\text{C}$). The rapid desolvation causes the droplets to shrink, bringing the ions in the droplet closer together. The repelling forces between the ions therefore build up to a point where they exceed the cohesive force of the solvated ions and the droplet explodes into smaller droplets (a Coulombic explosion – see Figure 1.2 overleaf).

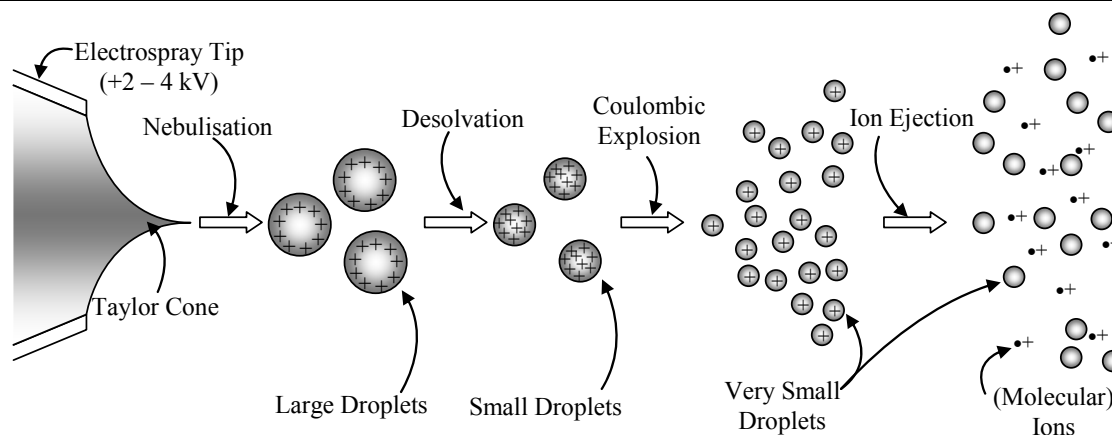


Figure 1.2: Action of an electrospray tip.

The electrospray tip charges the solution by stripping electrons away from the sample just before and during the nebulisation process. After the Coulombic explosion, the formed droplets continue to desolvate and the charge density increases. Charge transfer processes occur to reduce the charge density of the solvent, thus ionising the sample and resulting in multiply charged molecular ions.

Due to losses in thermal energy by evaporation and increasing salt concentration, the vapour pressure of the droplet falls such that there is a limit to how small the droplet can become. At this point, the charge density of the droplet can only be reduced by loss of charge rather than further coulombic explosions, and therefore molecular ions leak out of the droplet into the gas phase.

ESI is capable of ionising molecules at multiple sites, and furthermore, as it is a soft technique, there is little molecular fragmentation. This means the mass spectrometer will be able to handle molecules that would be up to 20 times outside its normal range if the molecules were singly charged. ESI itself can handle samples up to 200,000 kDa in mass.

The main disadvantage is the fact that ESI is intolerant to salt in the sample matrix. The sample matrix must be resistive for the charges to be stripped, and so the samples must be desalted before introduction into the system. This introduces a preparation step into the procedure where the sample may be diluted, degraded or otherwise lost.

1.2.1.2 The Inductively Coupled Plasma

The ICP allows the determination of elements* with high sensitivity and speed.^[1] The plasma comprises a flow of gas (typically argon) that has energy coupled into it by a water-cooled, (copper) radio frequency (RF) load coil, either at 27 or 40 MHz.^[6]

To form the plasma, an outer flow of argon at approximately 13 l min⁻¹ (termed the 'coolant gas') is introduced into the torch tangentially to create a helical flow. A second, inner argon gas flow is introduced at approximately 1 – 1.5 l min⁻¹ (termed the 'auxiliary gas'), again in a helical flow regime. A third flow of argon (the 'carrier gas') is introduced into the central channel of the plasma gases, carrying with it the sample to be analysed as a fine aerosol (see Figure 1.3 across). This aerosol can either be wet or dry.

* The ICP is applied mainly to metallic and metalloid elements as these are much easier to ionise than non-metallic elements; however, non-metallic elements can still be analysed with careful tuning and optimisation.

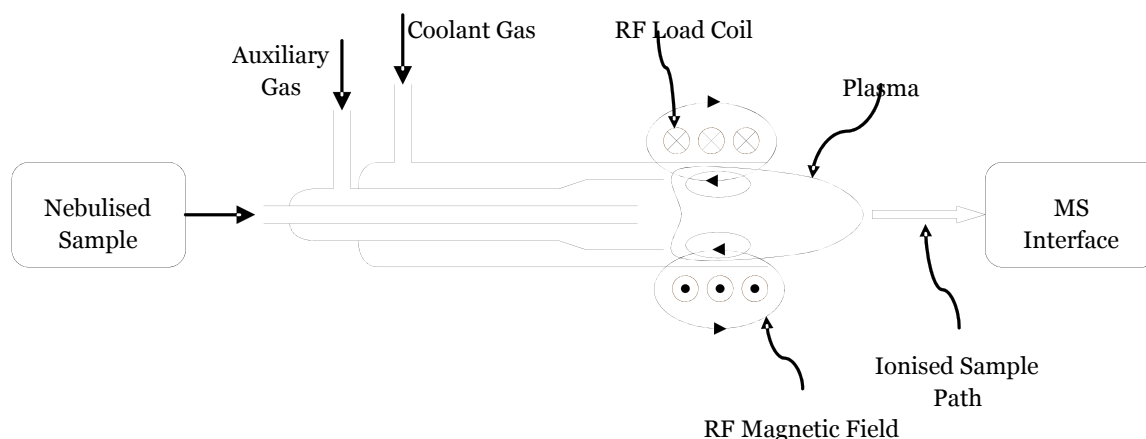


Figure 1.3: The ICP torch setup. The current in the load coil is alternating, and at this time slice the current flow is represented by the \otimes (flow perpendicular to the page, away from the reader) and the \odot (flow perpendicular to the page, towards the reader) within the load coil representation.

The plasma is initially ignited with a Tesla spark (with the carrier gas switched off), which provides the initial ‘seed’ electrons to ionise the plasma gas. This ionised state propagates instantaneously throughout the plasma region, which is confined to an elliptical area within the load coil.

Energy is coupled into the plasma *via* the alternating magnetic field produced by the alternating RF current; the coupled energy from the load coil being sufficient to sustain the plasma. This is usually in the order of 1100 – 1500 W, depending on the sample type and application, although it can be maintained as low as 500 W for some applications.

The coupled energy within the plasma excites the argon flow into a mixture of argon neutral atoms, excited argon atoms, free argon ions and free electrons, all of which can be estimated using the Boltzmann Distribution Function:

$$\frac{N_1}{N_0} = \frac{g_1}{g_0} e^{\frac{-\Delta E}{kT}} \quad (1.1)$$

- Where:
- N_0 : the population density of the low energy state (ground state atom/low order ionisation)
 - N_1 : the population density of the high energy state (excited/ionised/further ionisation)
 - g_0 : degeneracy* of the lower energy state
 - g_1 : degeneracy of the higher energy state
 - ΔE : the energy gap between the two states (electron Volts - eV)
 - k : the Boltzmann Constant (eV K⁻¹)
 - T : the system temperature (K)

*At the atomic level, electrons are arranged in ‘shells’ surrounding the atomic nucleus. These shells are further split into ‘orbitals’, which have a particular shape described by wavefunctions. These essentially describe the probability of finding an electron at a particular point in space. Each orbital has an energy associated with it, and this can be exactly equal to another orbital in the same shell. The number of orbitals with the same energy level for the highest energy electron at that energy state is termed the ‘degeneracy’ of the state.

This distribution is dependent on the activation energy of the transition (ground to excited state or ground to fully ionised state – the ionisation energy) and the temperature of the system; however, the concept of temperature within the plasma is complex.^[6] Whilst the plasma is electrically neutral, it is *not* in thermodynamic equilibrium; hence, it is not possible to assign a single temperature.

There are four separate temperatures used to describe the plasma:

- The Gas Temperature, representing the kinetic energy of the atoms within the plasma
- The Electron Temperature, representing the kinetic energy of the free electrons within the plasma
- The Ionisation Temperature, representing the population density of the ionised state (in this case, the singly charged ions)
- The Excitation Temperature, representing the population density of the atoms in the excited state.

Each of these plasma temperatures can reach between 6000 and 10000 K, which is comparable to the surface temperature of the sun. Once the plasma has been established, the carrier gas is gradually introduced to operating levels, usually 0.7 – 0.9 l min⁻¹. This provides a ‘central channel’ into the plasma region, which is cooler than the surrounding plasma.

The charge in the plasma oscillates at a characteristic frequency (ω_p), which produces its own magnetic field. This field opposes the magnetic field produced by the load coil, which induces a shielding effect meaning the inductive heating provided by the load coil only penetrates to a certain depth, termed the ‘plasma skin depth’ (δ).^[7] This is defined as the length at which energy coupling decays to $1/e$ of its value at the plasma surface, and can be estimated using:

$$\delta = \frac{c}{\omega_p} \quad (1.2)$$

The plasma frequency is calculated using the following:

$$\omega_p = \sqrt{\frac{n_e e^2}{m_e \epsilon_0}} \quad (1.3)$$

Where

n_e :	electron number density (m ⁻³)
e :	electron charge (1.602×10^{-19} C)
m_e :	electron mass (9.1093×10^{-31} kg)
ϵ_0 :	permittivity of free space (8.854×10^{-12} F m ⁻¹)

ICP’s used in analytical spectroscopy typically have an electron number density of 1.6×10^{15} cm⁻³, as determined previously by Houk and Zhai^[8]. This means the plasma oscillation frequency is approximately 2.26 THz; hence, the skin depth is on the order of 0.1 mm. Since the diameter of analytical plasmas is on the order of 12 mm, this means the central channel of an ICP does not experience inductive heating from the load coil; rather, the heating comes from thermal transfer from the outer layers of the plasma. Interestingly, the density of the plasma does not vary across its diameter, as expected with classical mechanics of heat transfer and volume expansion.

The skin depth, induced heating from the load coil and the cooling from the central channel carrier gas results in a toroid-shaped plasma within the confines of the load coil geometry. Due to the flow of the plasma gas, this toroidal plasma is distorted and elongated towards the exit plane. The high velocity plasma gas at the exit plane of the torch entrains the surrounding atmospheric gas forming eddy currents that shape the plasma into the characteristic 'bullet' shape, as depicted in Figure 1.3 previously.

The sample is introduced through the middle of the plasma as a fine aerosol, either wet or dry depending on the sample introduction system chosen. In the central channel the aerosol is desolvated (in the wet case), atomised and ionised within the plasma and then transported to the mass analyser. The atomisation is usually complete, with a very high degree of ionisation for most analytes. For this reason, the ICP is an ideal ionisation source for elemental analysis and isotope ratio measurements.

The degree of ionisation within the plasma depends on the plasma ionisation temperature (T_{Ion}) and the analyte's ionisation energy (ΔE_I , measured in eV). Using both Boltzmann and Einstein statistics, the degree of ionisation can be calculated using a form of the Saha equation:^[9]

$$\frac{n_+}{n_0} = \frac{G_+}{G_0} \cdot \frac{g_e}{n_e} \cdot \frac{1}{\lambda^3} \cdot e^{\left(\frac{-\Delta E_I}{kT_{Ion}}\right)} \quad (1.4)$$

$$\lambda = \sqrt{\left(\frac{h^2}{2\pi m_e kT_{Ion}}\right)}$$

- Where:
- n_0, n_+ : the number densities for the lower and higher energy states respectively (the neutral form and the ionised form respectively in the usual case – cm⁻³).
 - G_0, G_+ : the partition functions for the lower and higher energy states respectively. (This is defined as the sum of the degeneracy of states over all energy levels within the energy state.)
 - g_e : degeneracy of states for the electron. (An electron can exist in two spin states at the same energy level; hence, this number is always 2.)
 - λ : thermal De Broglie wavelength
 - n_e : electron concentration (mol cm⁻³)
 - m_e : electron mass (9.10938×10^{-31} kg).
 - h : the Planck constant (4.136×10^{-15} eV s)
 - k : the Boltzmann Constant (8.617×10^{-5} eV K⁻¹)

Plasma conditions play a major role in analyte ionisation. As mentioned previously, the plasma central channel is only heated from thermal transfer from the outer plasma layers. This means the central channel temperatures are dependent on the thermal conductivity of the central channel, which in turn is dependent on the plasma composition. If the composition varies during an analytical run, the effects on ionisation can alter the results of the analysis. For example, at a plasma ionisation temperature of 7000 K, uranium ($\Delta E = 6.194$ eV, $G_+ = 10$, $G_0 = 13$) and phosphorous ($\Delta E = 10.486$ eV, $G_+ = 1$, $G_0 = 4$) have ionisation efficiencies of 99.95% and 32.50% respectively. At 6500 K, this reduces to 99.87% and 10.16% respectively. Small perturbations in plasma temperature affect higher ionisation energy (IE) analytes more readily than lower IE analytes.

Coupled with the fact that the central channel is entirely dependent on thermal conductivity for heating, it is important to ensure that all samples introduced into the plasma do not alter the plasma composition significantly to alter ionisation. This is usually achieved by diluting liquid samples in the same matrix to buffer out small perturbations.

1.2.2 Mass Analysers

Mass separation in mass spectrometry is carried out by the *mass analyser*, which separates the analytes in the sample according to their m/z values. Each type of mass analyser has advantages and disadvantages according to the method of separation used; hence, different analysers are used for different types of analysis and sample types.

1.2.2.1 Magnetic Sector and Electric Field Analysers

Charged particles experience an accelerating force in a magnetic field, termed the 'Lorentz Force'.^[1, 10] This causes the ion to follow a circular trajectory with a radius (r) dependent on its mass (m) to charge (z) ratio, the accelerating potential at the source (V_s) and the magnitude of the field (B), such that:

$$r = \sqrt{\frac{2V_s m}{zB^2}} \quad (1.5)$$

Hence:
$$\frac{m}{z} = -\frac{r^2 B^2}{2V_s} \quad (1.6)$$

This allows either simultaneous or sequential detection of the analyte ions, depending on the detector used.

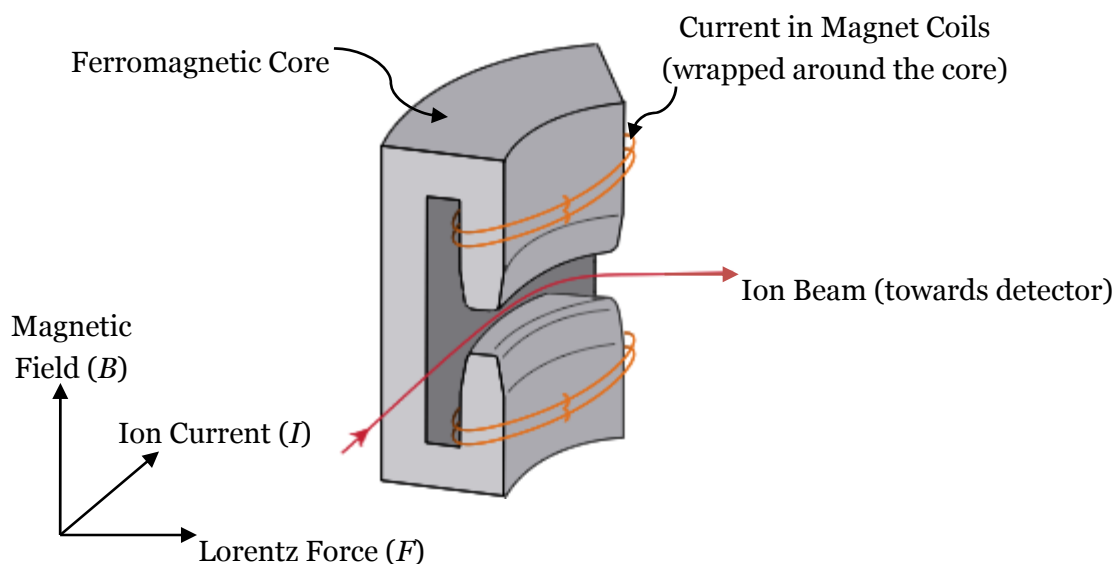


Figure 1.4: A schematic showing the force applied to a charged beam of ions by an electromagnet (adapted from Gross^[10]).

Simultaneous detection can be performed by passing the ions through a constant field and detecting the spatially separated ions on an array detector (see Figure 1.5 below). This type of mass separation is termed ‘dispersive’.

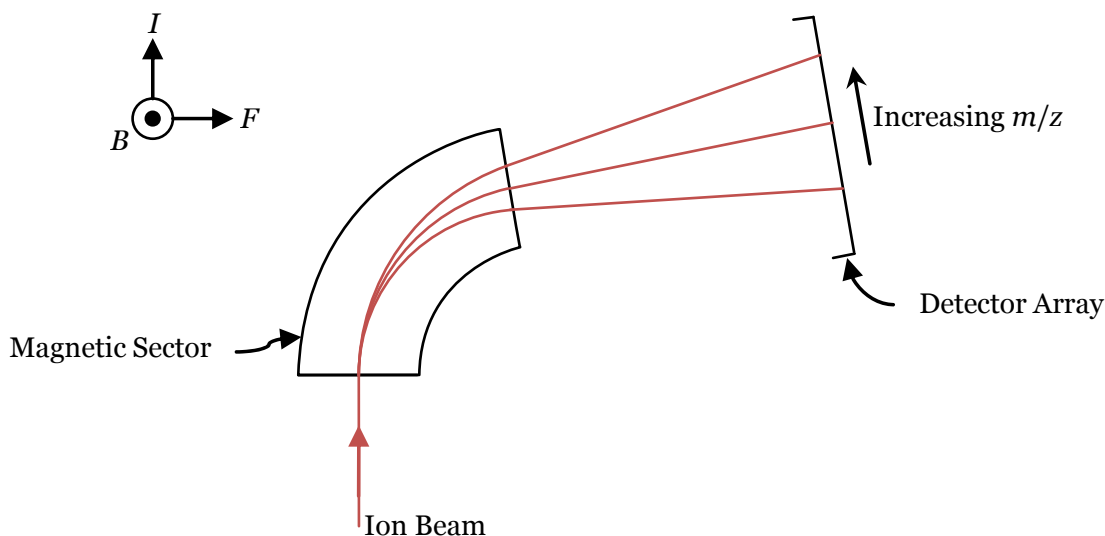


Figure 1.5: Simultaneous detection using a magnetic sector mass analyser

Increasing m/z ratio increases the radius of the path; hence, m/z ratios are spatially resolved on the detector array dependent on Equation (1.5). Generally, a higher m/z ratio corresponds to a higher atomic mass.

For sequential detection, a slit is added to the exit plane of the magnetic sector, effectively fixing the allowed radius. Changing the magnetic field changes the radius of the arc travelled by an ion with a specific m/z value; hence, this setup can work as a tuneable mass filter (see Figure 1.6 below)

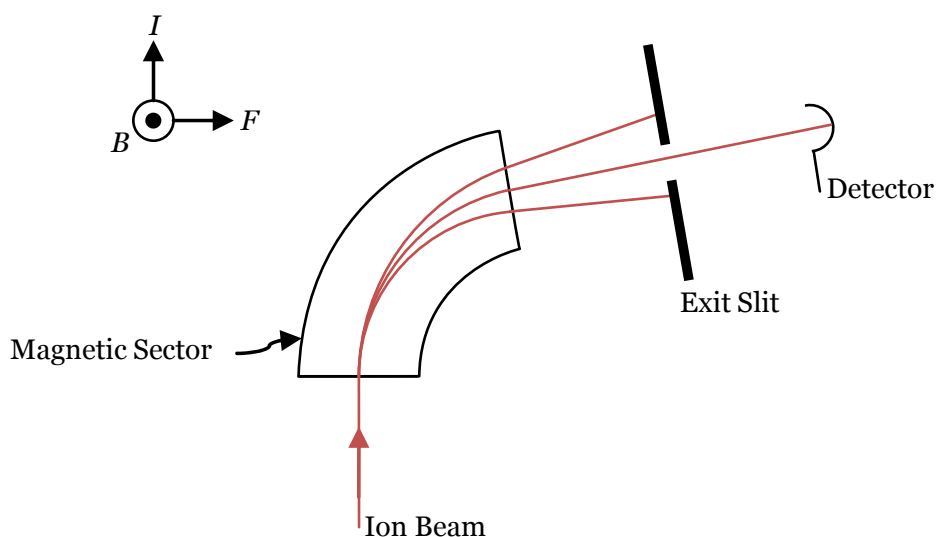


Figure 1.6: Sequential detection using a magnetic sector mass analyser

This principle works theoretically until the kinetic energy is taken into consideration. If the ions are accelerated by a potential difference (V_s), then the kinetic energy (E_k) of the ions is given by:

$$E_k = zV_s$$

Hence:
$$V_s = \frac{E_k}{z} \quad (1.7)$$

Combining Equation (1.5) with Equation (1.7) gives:

$$r = \sqrt{\frac{2E_k m}{z^2 B^2}} = \sqrt{\left(\frac{m}{z}\right) \left(\frac{2E_k}{z B^2}\right)} \quad (1.8)$$

This means the radius is not only dependent on the mass-to-charge ratio, but also on the kinetic energy of the incoming ions. This dispersion due to kinetic energy affects the mass accuracy, as two different masses may have the same path through the magnetic field. Equally, two ions with the same m/z ratio may have a slightly different path, which alters the mass resolution of the analyser. To combat this effect, an electrostatic analyser is employed as a kinetic energy filter.^[1]

An electrostatic analyser (ESA) is constructed out of a cylindrical condenser such that the electric field produced (E) is radial, as shown in Figure 1.7 below. In this case, the force applied to the ion beam is parallel to the electric field, which accelerates the ions toward the inner plate. The top and bottom ‘stabilising’ plates are set at a small, positive potential (on the order of 50 – 100 V) to keep the ion beam in the middle of the analyser. The entry and exit planes of the ESA are usually bounded by slits (not shown), which means the ESA is a sequential energy filter.

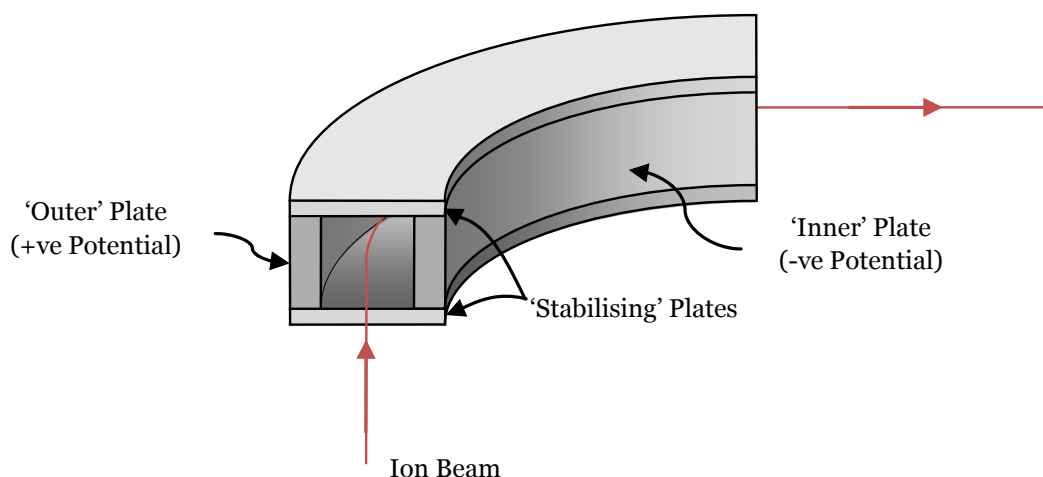


Figure 1.7: Simple schematic of an Electrostatic Analyser.

Since the electric field produced by the ESA is radial, the force applied by the electric field to the ions can be equated to centripetal force, hence:

$$zE = \frac{mv^2}{r} \quad (1.9)$$

Taking into account the kinetic energy ($mv^2 = 2E_k$) gives:

$$zE = \frac{2E_k}{r}$$

Therefore: $r = \frac{2E_k}{zE}$ (1.10)

Equation (1.10) shows that the radius of the ions going through the electrostatic analyser is therefore not dependent on mass, but on the kinetic energy alone. Putting an electric field analyser and a magnetic sector in tandem can therefore separate ions by kinetic energy and mass, and configurations where the ESA compensates for the kinetic energy blurring through the magnetic sector, such as Nier-Johnson and Mattauch-Herzog configurations, are termed 'double-focussing' mass spectrometers.

Configurations employing the electrostatic analyser first are termed 'Nier-Johnson' mass spectrometers. These types of mass spectrometer are typically used with multi-collector or array detectors, as the dispersive element is the final section. The more common mass spectrometer, however, is the 'reverse Nier-Johnson', with the electrostatic analyser second. This allows faster scanning of the mass ranges and is well suited for sequential or single channel mass analysis (elemental mass analysis).

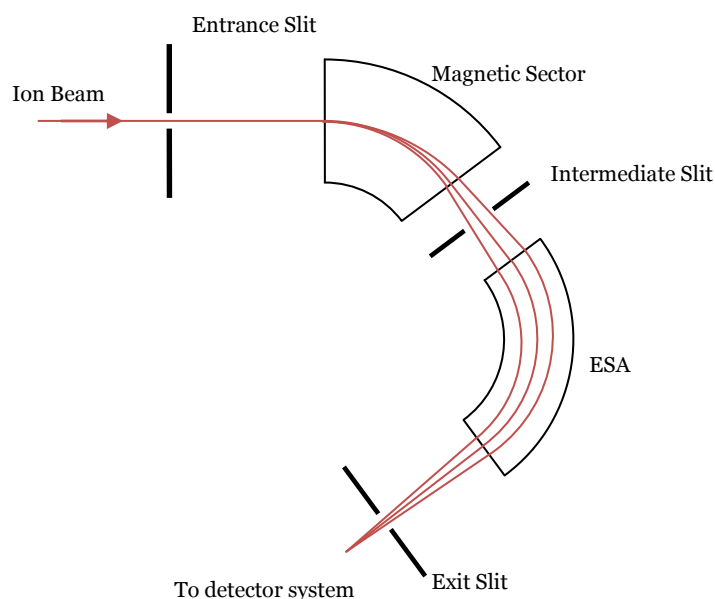


Figure 1.8: Schematic layout of a reverse Nier-Johnson double focussing sector field mass analyser

The double-focussing mass analyser, in theory, can analyse infinite masses, limited only by the strength of the magnetic and electric fields applied. The mass resolution* of tandem magnetic sector-electrostatic mass analysers can reach 10,000.^[11] However, due to the slow scanning of the magnetic sector itself, and the limits on the magnetic strength imposed by size and cost, in practice magnetic sector instruments have an upper mass limit of around 2 kDa.

* The ability for a mass analyser to resolve two separate masses, defined as $R = m/\delta m$, where δm is the smallest mass difference for which two masses m and $(m + \delta m)$ are fully resolved. Two peaks are considered fully resolved if the valley between the two peaks is equal to 10% of the weaker peak intensity.

1.2.2.2 Multipoles

These devices consist of parallel rods, or poles, with a space in the centre.^[1] Application of direct current (DC) and RF electric potentials, U and $V\cos\omega t$ respectively, to these rods in pairs forces ions into an approximately helical trajectory, which is dependent on mass. This device, therefore, acts as a mass filter, the most common form of which is the quadrupole mass analyser. Hexapole and octapole mass filters operate on the same basic principle as the quadrupole, with modifications to accommodate the extra poles; however, they are only practically useful as ion guides. For simplicity, only the quadrupole mass analyser will be explained.

The quadrupole mass analyser is made up of four rods, each pair connected diagonally. Both pairs are subject to a combination of both direct potential and RF potential in the megahertz range, one pair being positive and the other negative (see Figure 1.9 below).

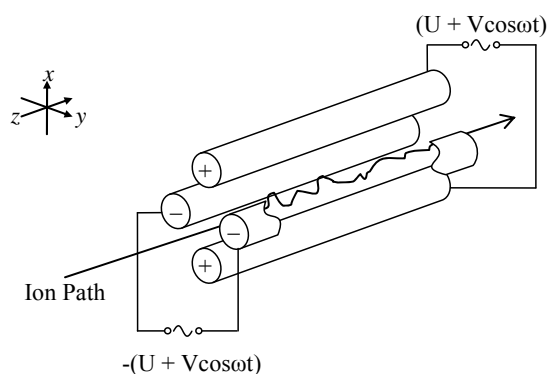


Figure 1.9: Schematic of a quadrupole mass analyser

The ions enter through one side of the quadrupole system and experience accelerating forces independently in the x and y planes, leading to independent x - and y -stability.^[12] The RF peak voltage and DC voltages are altered by the same amount such that the ratio of U/V is constant. This means only ions of specific mass having stability in both planes are allowed to pass through the mass analyser; therefore, only specific masses are allowed through the multipole.

The multipole can also be operated in an 'RF only' mode, which turns it into a multi-mass ion lens focussing an ion beam. If this is then pressurised with a neutral gas (*e.g.* He), it can be turned into a 'collision cell', where collisions between the ion beam and the collision gas result in loss of kinetic energy in the ion beam. This mode can be applied in reducing isobaric interferences from polyatomic ions, which have the same path through a mass analyser as single ions of the same m/z .

Polyatomic ions have larger collisional cross sections than single ions; therefore, they lose more kinetic energy and are slowed down to a larger extent. They can then be filtered from the ion beam by their kinetic energy, so-called Kinetic Energy Discrimination (KED), and reduce their contribution to the signal intensity at that m/z .

A reactive gas can also be used (*e.g.* NH_3). Here, reactions in the multipole can occur and, depending on the reaction kinetics, shift polyatomic ions away from the single ions of the same m/z , thereby reducing interferences.

If the polyatomic ion is large enough, *e.g.* in molecular mass spectrometry, collisions are also likely to result in fragmentation. The linear nature of the multipole means it is suited to tandem mass spectrometry, *i.e.* molecular fragmentation analysis on parent ions, then daughter ions and so on repeated as many times as required. If a collision cell is added between two mass analysers (of any type), fine structure determination is possible through reaction/fragmentation analysis.

Spectra produced from using reaction gas tend to be cleaner than those produced using a neutral collision gas (similar to EI and CI comparisons), and can improve analyte sensitivity provided the reaction gas and the analyte are well resolved by mass.

If the energy spread in the ionised sample is low, the multipole mass analyser is capable of a mass resolution of 10,000, with an upper mass limit of around 4 kDa. In practice, low energy spreads only arise when using electron/chemical ionisation sources, which are typically used for small, molecular samples. For other ionisation techniques, the resolution can be as low as 300, and as such this mass analyser is limited to use in elemental analysis, organic structure determination and analysis of small biomolecules. Larger biomolecules may be analysed by using an ESI source, as this allows up to 20 charges on one molecule, extending the mass limit up to 80 kDa.

1.2.2.3 Ion Trap

Conceptually, the ion trap mass analyser is a modification of the multipole mass analyser.^[1] It comprises a ring electrode and two end-cap electrodes (see Figure 1.10 below). The three-dimensional ion trap can be thought of as a quadrupole mass analyser folded in on itself, the ring electrode being one of the rods curved in on itself with its opposite rod being reduced to a point. The remaining two electrodes are therefore the end-cap electrodes.

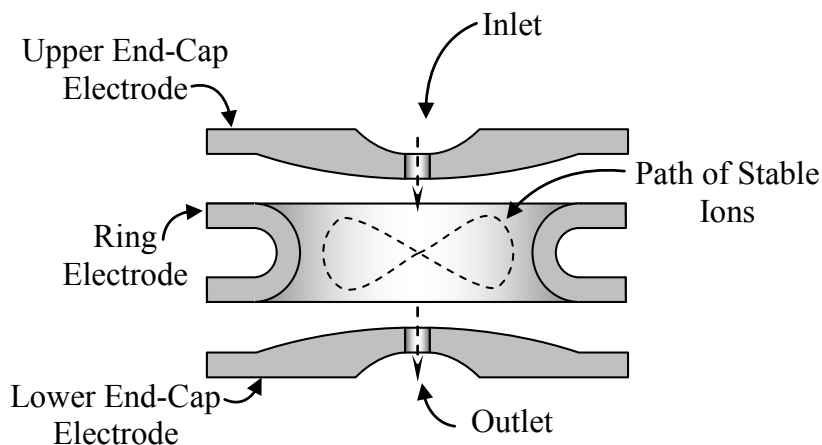


Figure 1.10: Schematic of a 3D ion trap mass analyser

The RF voltage is applied to the end-cap electrodes, whilst the DC voltage is applied to all three electrodes. The overlapping RF and DC potentials over the end-cap electrodes combined with the DC potential of the ring electrode cause the ions to follow a ‘figure of eight’ stability pattern within the ion trap. Varying the size of the RF peak potential causes some ions to become unstable and these ions are ejected through the outlet. The mass spectrum is obtained by selectively ejecting particles of known mass and recording their relative abundances.

The 3D ion trap mass analyser has comparable mass resolution to the multipole mass analyser, *i.e.* 300 for high-energy spread ionisation sources and 10,000 for low energy spread sources. The 3D ion trap improves on the maximum m/z ratio of the multipole to about 6 kDa for most instruments. A high mass ion trap has been reported to have achieved a mass limit of 45 kDa with mass resolution of 25,000, employing a caesium FAB gun as an ionisation source.^[1]

The main drawback of this mass analyser is the fact that the ions are trapped in a confined space. Trapping the ions in this way means there is a localised concentration of positive charge (a space charge) whose mutual repulsion opposes trapping in the energy well. Also, collision reactions can now happen in this space and can result in more fragmentation or adduct formation. This imposes a limit on the amount of sample able to be analysed in any one experiment. This limit is typically around 10^6 ions, which results in a low linear dynamic range for this type of mass analyser.

A linear ion trap is a modification on the quadrupole where the four rods are capped by two end cap electrodes. This works in the same way as the 3D ion trap, but the amount of sample held is increase by two orders of magnitude to 10^8 ions, improving the linear dynamic range.

1.2.2.4 Fourier Transform Ion Cyclotron Resonance

The Ion Cyclotron Resonance (ICR) mass analyser uses the behaviour of ions in a magnetic field to trap ions in a circular path.^[1] At low velocity, the radius of this path is relatively small and the ions are trapped on a trajectory resulting from the centripetal force applied to the ion (F_C), which is equal to the magnetic force provided by the field (F_M):

$$F_M = zvB$$

$$F_C = \frac{mv^2}{r}$$

$$\text{Therefore: } zB = \frac{mv}{r} \quad (1.11)$$

Ions complete a full revolution (length = $2\pi r$) within the cell at a frequency (f) of:

$$f = \frac{v}{2\pi r}$$

$$\text{Hence: } 2\pi f = \frac{v}{r} = \omega = \frac{z}{m} B \quad (1.12)$$

Equation (1.12) shows the angular velocity (ω) is a constant value for any given m/z value in a constant magnetic field, and each m/z value has a characteristic frequency. If the linear velocity is altered, the radius of the trajectory will alter in the same direction to compensate, *i.e.* increasing linear velocity increases the radius of the trajectory.

Applying an RF electric field to ions trapped within a magnetic field couples energy into those ions with a resonant frequency. This increases their kinetic energy and hence their linear velocity, which then increases the radius of the trajectory ejecting ions of a specific mass.

Each ion has a waveform associated with its motion out of the ion cyclotron mass analyser. By quickly scanning through the frequency range, all the ions can be ejected in a period of

about one microsecond. The time resolved waveform will then be the sum of the individual waveforms of the ions within the sample. Using a Fourier Transform (FT) algorithm on this waveform can then extract the mass spectrum.

In principle, the ion cyclotron has no mass limit. However, as the size of the ions increases the stability of the ions within the magnetic field decreases, leading to a practical mass limit of 2000 Da. The advantage, however, is a very high resolution of up to 1,500,000, allowing masses to be measured to within four decimal places with confidence, and two masses differing by less than 0.01 Da to be resolved.

Coupling to an ESI source can again increase the upper mass limit to around 40 kDa. With the ICR, the resolution is so high that molecules yielding $^{12}\text{C}/^{13}\text{C}$ isotopically derived peaks can be resolved at 40 kDa and higher, and the number of peaks within one unit m/z value corresponds to the charge on those peaks. As the ion cyclotron is a type of ion trap, it also has a limit to the amount of sample that can be analysed by the system. It can hold up to 10^6 ions, but above this limit, the repulsive forces scatter the ions out of stable paths.

1.2.2.5 Time of Flight

The time-of-flight (ToF) mass analyser is simply a flight tube of a fixed length (d) under vacuum.^[1] The ions experience an accelerating force from the end of the flight tube by a potential (V_s) and as such that all ions gain the same amount of kinetic energy (E_k):

$$E_k = \frac{mv^2}{2} = zV_s \quad (1.13)$$

The time taken to traverse the flight tube (t) is given by

$$t = \frac{d}{v}$$

Hence
$$v = \frac{d}{t} \quad (1.14)$$

Substituting (1.14) into (1.13) gives:

$$t^2 = \frac{m}{z} \left(\frac{d^2}{2V_s} \right) \quad (1.15)$$

Therefore, the time taken to pass through the flight tube is dependent on the m/z ratio, with those ions with smaller ratios going through quicker. This is particularly suited to mass spectrometric methods that produce ions in a burst, such as pulsed laser desorption mass spectrometry.

The ions entering the flight tube will have a kinetic energy distribution, meaning ions with the same m/z ratio may have different flight times. To correct for this, an electrostatic deflector is used. Ions with higher kinetic energy arrive at the reflector field before ions with lower kinetic energy. These higher energy ions also penetrate further into the ion reflector's field, and therefore spend longer in the reflector region. As the ions exit the reflector region, their kinetic energy is restored to that which they came into the region with, just in the opposite direction. Since the higher energy ions spent longer in the reflector field, they now exit the field after the lower energy ions (see Figure 1.11 overleaf), arriving at the detector at the same time

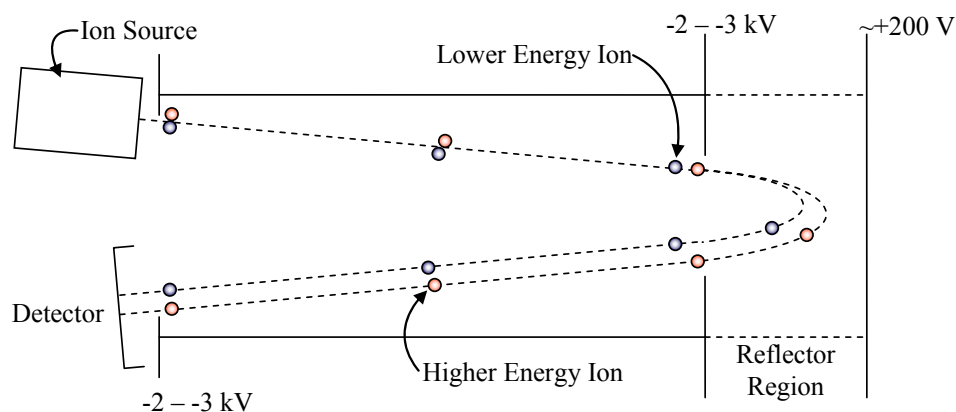


Figure 1.11: Schematic of a time of flight mass analyser with reflector region

The mass range for a ToF mass analyser is truly infinite. For this reason, ToF instruments are the preferred mass analyser for large biomolecules such as proteins and DNA, and are utilised in the field of proteomics. The m/z ratio of a protein is often in the hundreds of kilodaltons, much too high for other mass analysers. The mass resolution of the system can reach 17,000, higher than most multipoles. However, when applied to a 50 kDa protein fragment, this results in a peak width spanning ± 3 Da.

1.2.2.6 The Orbitrap™

The most recent novel technology for mass analysis is the Orbitrap™ mass analyser, a non-RF, orbital electrostatic trap capable of high mass resolution and accuracy (proprietary to Thermo Scientific).^[13] It is another form of a Fourier transform mass analyser like the ICR. All mass analysers suffer from decreasing mass resolution with increasing m/z ; however, whilst the ICR has unmatched mass resolution at the low end, the Orbitrap is capable of outperforming an ICR above ~ 1000 Da.

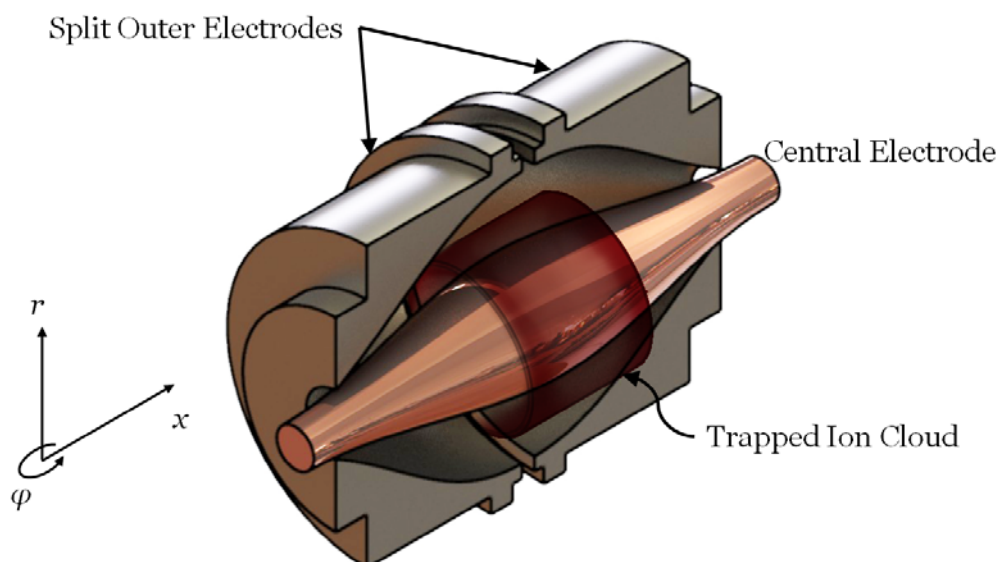


Figure 1.12: Cutaway diagram of an Orbitrap mass analyser showing a stabilised ion cloud around the central ion and the split outer electrodes (adapted from Makarov^[13])

The Orbitrap comprises a barrel shaped split outer electrode and a spindle-shaped central electrode. The shape and voltages applied to the Orbitrap result in a quadro-logarithmic potential distribution forming within the trap.

In cylindrical coordinates, the equation for this potential is:

$$U(r, x) = \frac{k}{2} \left(x^2 - \frac{r^2}{2} \right) + \frac{k}{2} R_m^2 \cdot \ln \left[\frac{r}{R_m} \right] + C \quad (1.16)$$

Where r, x cylindrical coordinates ($x = 0$ at the plane of symmetry for the field)
 k : field curvature
 C : constant
 R_m : characteristic radius for the Orbitrap (when $r > R_m$, the ions are accelerated towards the central electrode, and conversely accelerated away when $r < R_m$)

The ions form stable trajectories in the trap with three frequencies: rotation about the r axis (ω_ϕ), circular motion around the central spindle electrode (ω_r) and axial oscillations along the x axis (ω):

$$\omega_\phi = \omega \sqrt{\frac{\left(\frac{R_m}{r}\right)^2 - 1}{2}} \quad (1.17)$$

$$\omega_r = \omega \sqrt{\left(\frac{R_m}{r}\right)^2 - 2} \quad (1.18)$$

$$\omega = \sqrt{\frac{e}{(m/z)}} \cdot k \quad (1.19)$$

The rotational and radial frequencies depend on the initial radius at the point of injection into the trap, whereas the oscillation along the length of the central spindle electrode is dependent on the mass-to-charge ratio of the ion. Due to the shape of the outer electrodes, the ions discharge on them yielding an ‘image current’, which can be thought of as the profile of the combined ion frequencies. A Fourier transform is applied to this image current to separate out the mass information of the ions trapped in the Orbitrap.

Ions trapped in the Orbitrap usually have kinetic energies in the keV range, and consequently high-energy collisions occur within the trap. Unfortunately, all daughter ions have the same velocity as the parent ion, which means the kinetic energy is dependent on the mass of the daughter fragment. This leads to a kinetic energy spread in the daughter ions that distort the stable trajectories and results in peak broadening.

Additionally, low mass daughter ions fall into the central spindle electrode and are lost, which limits the use of the Orbitrap as a fragmentation analyser. Usually, it is used as an accurate mass detector in conjunction with an RF ion trap, the latter trap being used to provide fragments for the Orbitrap to accurately characterise.

1.2.3 Detectors

The detector is a transducer that converts the ion signal into a useable form that can be recorded and related to the mass. The detector can either directly measure the charge of the analyte, or convert the analyte charge into a secondary particle and measure the signal of this secondary particle.

The earliest detectors were simple photographic plates used with dispersive, magnetic sector instruments. As the charged ions hit the plate, spots would form. The positions of the spots were related to the m/z ratio of the analyte, and the intensities of the spots were related to the amount of analyte present.

Another method of direct charge detection is the Faraday cup. Ions strike the surface of the cup, where they give up their charge. The current produced from this process is then amplified and measured. The sensitivity is limited by the noise of the amplifier attached to the cup; however, as the charge produced in the cup is independent of mass and energy, it is very well suited for isotope ratio measurements with sequential and dispersive mass analysers.

A secondary electron multiplier (SEM) is an example of an indirect detection device. As the charged ion reaches the conversion dynode of the electron multiplier, it causes the emission of a 'secondary electron'. These electrons are then accelerated towards a continuous-dynode electron multiplier. When they strike the surface of the dynode, electrons are dislodged. The surface of the dynode is curved, as these electrons pass through the electron multiplier towards the ground potential, they strike the dynode further times creating more and more electrons thereby amplifying the signal to a measurable level.

These have been largely replaced by discrete dynode electron multipliers, which consists of an array of dynodes set to fire generated electrons towards the next dynode in the sequence.

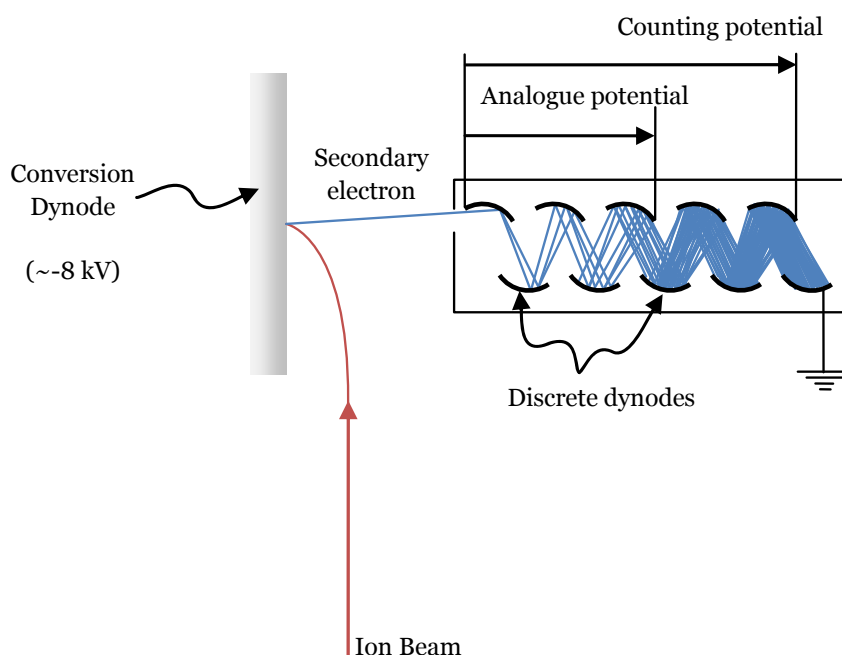


Figure 1.13: Schematic of a generic secondary electron multiplier.

These can be operated in two modes: low-level ‘counting’ mode and a higher-level ‘analogue’ mode.^[14] In the counting mode, the SEM uses the full set of dynodes giving a dynamic range of between $<0.1 - 2 \times 10^6$ counts per second (cps), allowing low levels of ions to be measured. Each dynode has a maximum number of electrons that can be generated (set by the electron multiplier overall voltage), which means this type of detector can be saturated.

When the ion flux is increased to a level that saturates the detector, the signal is ‘tapped off’ using only half the number of dynodes in the SEM array, termed ‘analogue mode’. Saturation of most SEM detectors can occur at high counting rates (approx. 2×10^7 cps), but linearity is lost at 2×10^6 cps; hence, most mass spectrometers switch to analogue mode here.

The analogue mode typically overlaps the counting mode such that the dynamic range is now $5 \times 10^4 - 5 \times 10^9$ cps. By overlapping the ranges, the response curves for each set of multiplier conditions can be calibrated against each other to ensure a wider linear range than conventional continuous dynode multipliers.

A Daly detector (photon multiplier) works in a very similar fashion, where the secondary electrons hit a phosphorescent screen and produce photons. These photons travel through a photo multiplier tube where they strike a conversion dynode to produce electrons. These electrons then carry on through a series of discrete dynodes multiplying at each to amplify the current to a measurable level. SEM’s and Daly detectors suffer from less noise than the Faraday cups as the amplification is internal. However, they are affected by the mass and large analytes produce more secondary particles.

An array detector is a plate with a two- or three-dimensional array of Faraday cups, electron multipliers or photon multipliers arranged into a continuous, planar form-factor. This allows the sensitivity and accuracy of these electronic detectors to be used with dispersive instruments.

1.3 Lasers in Analytical Chemistry

The first type of mass spectrometry to involve lasers was ‘laser desorption ionisation mass spectrometry’, or LDI-MS.^[4] The high photon flux, coherence and narrow wavelength distribution means that lasers can be used to affect transitions selectively within the analyte molecule whilst leaving other components within the sample matrix unaffected.

The laser is used to sequentially release the sample into the gas phase and ionise it, or to perform a concurrent evaporation-ionisation process, thereby acting as both a sample introduction system and an ionisation source. The technique is capable of acting upon samples of any type, provided the wavelength chosen approximately matches a characteristic transition within the sample. Additionally, it can be focussed on the surface of the sample down to the micrometre scale, allowing the surface to be mapped by mass content.

Normally, the analyte is dissolved in an appropriate solvent and dried onto a target, leaving a thin solid film of adsorbed molecules; hence, the target acts as a substrate. The target can be either metallic or insulating, depending on the nature of the sample. In the case of large solid samples such as rock, glasses or ceramics, the bulk sample acts as the substrate and the surface is sampled.

The main drawback of this method of ionisation is that the analyte molecule must have a high absorption coefficient at the employed laser wavelength to transfer energy most efficiently

from the laser to the analyte. Provided this is the case, the method is capable of desorbing and ionising large molecules in the order of 500 kDa, such as proteins and DNA, with little fragmentation.

1.3.1 Laser Induced Thermal Desorption (LITD)

This is an effect seen with small molecules adsorbed onto a solid surface substrate.^[4] If this substrate absorbs the laser radiation, it will heat up on a time scale comparable to the laser pulse length. The sudden temperature rise leads to desorption of these small molecules resulting from an increase in the molecular vibrations in the substrate surface.

Q-switched lasers with pulse lengths in the nanosecond range can lead to sub-thermal velocities for the desorbed molecules, *i.e.* the desorbed molecules have less internal energy than the surface molecules of the substrate they came from. The ability to produce cold molecules from hot surfaces is useful for desorbing large, thermally labile compounds without excessive fragmentation.

The efficiency of LITD depends on the ability of the substrate surface to absorb the laser wavelength and evolve heat. It also depends on the size of the molecules being desorbed (the technique having a limit of around 10 kDa) and the laser irradiance. The threshold for the laser irradiance is around 10^8 W/cm².

1.3.2 Matrix Assisted Laser Desorption Ionisation

Matrix Assisted Laser Desorption Ionisation (MALDI) is a soft desorption/ionisation technique used to produce ions for introduction into a mass spectrometry system.^[4] It is, in essence, a modification of laser desorption ionisation where, instead of choosing a laser close to an absorption maximum in the analyte, a matrix is chosen with an absorption maximum close to the laser wavelength so that the laser energy can be coupled into the matrix and then used to ionise the analyte. The sample is then mixed with the matrix before being acted upon by the laser light.

The matrix-analyte mix is dried onto a metal target and then irradiated with the laser. The irradiance used in MALDI is lower than that used in LITD by at least two orders of magnitude (10^6 W/cm²), and as a result it is much a much softer technique with less fragmentation.

The matrix chosen must have a strong absorption coefficient at the laser wavelength, have a common solvent with the analyte, surround the analyte in solution without forming covalent bonds and have a low volatilisation temperature. The best matrix compounds found for peptide analysis tend to be derivatives of cinnamic acid and benzoic acid, such as 3,5-dimethoxy-4-hydroxycinnamic acid (sinapinic acid – SA) and 2,5-dihydroxybenzoic acid (DHB).

1.3.3 Mechanisms of Particle Desorption

There are many models proposed for the mechanism by which laser desorption induces phase transition within the analyte.^[4] These models address both the mechanism of particle desorption and the low levels of fragmentation of analyte molecules relative to the matrix molecules.

1.3.3.1 Phase Explosion Model

There are two elements to explain this model of laser desorption phase transition: Spinodal Decomposition and the Phonon Avalanche.^[4] In Spinodal Decomposition, the rate of heating of the solid forces sublimation processes to become dominant over melting-evaporation processes, and the area being irradiated is suddenly transformed into the gaseous phase.

The Phonon Avalanche occurs when the phonon modes of the dried analyte-matrix lattice are pumped by the excited vibrational states of the matrix crystals. Phonons produced by both the excitation of the matrix crystal vibrational states and the pumping of the lattice cause instability in the whole system when the rate of energy dissipation is slower than the rate of energy gain within the phonon modes. This then leads on to the phase explosion, ejecting molecules into the gaseous phase.

1.3.3.2 The Cool Plume Model

This model can be used to explain why large molecules are not fragmented using laser desorption given that the energies involved are quite large.^[4] In basic terms, the expansion of the plume is isobaric and adiabatic, therefore it cools rapidly. Due to this cooling, the molecules lose thermal energy to restore thermal equilibrium and are therefore stabilised. Fragmentation will now come from energy transfer from matrix molecules excited in the plume by further pumping by the laser line. The degree of fragmentation will be mainly affected by the choice of matrix molecule.

Another aspect that can be drawn from this model is that thermal ionisation is not possible in MALDI. The ionisation has to come from interactions between the analyte molecules and the matrix molecules.

1.3.3.3 Desorption Induced by Electronic Transition (DIET) Model

The excitation of surface analytes by low energy photons can produce a repulsive anti-bonding electronic state.^[4] This forms a repulsive electric field around the molecule, which causes desorption of the molecule from the surface with a certain amount of kinetic energy.

This mechanism is completely non-thermal, the coherent electronic excitation from the laser leading to coherent motion of the particles. The surface layer is not melted by this process, and the velocities of the particles are mainly perpendicular to the surface of the sample.

A single-photon process will lead to desorption of neutral molecules, but a two-photon process will lead to electron transfer from the sample to the metal target, leading to desorption of ions from the sample surface. Coming from a two-photon process, these ions have more kinetic energy than the neutral molecules, usually an order of magnitude higher. The velocities are still perpendicular to the sample surface.

1.3.3.4 Disintegration via Mechanical Stress and Shock

Thermally induced mechanical stress occurs when the energy of the laser is absorbed by a localised area of the sample surface.^[4] Thermal expansion of the material in this area causes mechanical stress to act, which causes stress fractures to appear in the surface. This eventually leads to mechanical fragmentation of the sample surface, ejecting molecules from the surface. As in the Phase Explosion Model, the rate at which this occurs is such that sublimation processes are dominant over melt-evaporation processes.

To produce intact molecules, the time taken to produce stress fractures must be significantly shorter than the time taken for the sample to reach thermal instability. For this to happen, the sample must have a good light absorption coefficient, a high volume thermal expansion coefficient, high bulk modulus, low critical stress and low thermal lability. Introducing a fine metal powder will increase the efficiency of this particular process.

1.3.3.5 Pressure Pulse Model

This model predicts that as laser photons penetrate the surface of the sample, energy transfer to the sample leads to an increase in kinetic energy of the sample molecules and a pressure gradient is set up.^[4] When a threshold pressure is reached, dependent on the sample, the pressure gradient causes expansion of the surface and hence mechanical desorption.

This model also states that there must be a threshold energy per unit area for the laser light (laser fluence) acting on the sample, dependent on the efficiency of energy transfer between photons and the sample and the cohesive forces within the sample.

1.3.3.6 Energy Redistribution Model

This model is far more applicable to MALDI experiments than to LITD experiments. Whilst the analytes themselves exhibit lower fragmentation than expected, given the amount of energy being supplied, fragmentation of the matrix is apparent.^[4] Primary deposition of energy leads to electronically excited states within the matrix molecules, which then turn into vibrationally excited ground states by internal conversion pathways. It must be noted that the analyte molecules do absorb energy from the photon, but their absorption cross-section is significantly lower than that of the matrix molecules.

From the vibrationally excited state, the energy is transferred from intramolecular bonds to intermolecular bonds between the matrix molecules and analyte molecules, and between the matrix molecules and solid sample as a whole. This serves to heat the sample to the phase transition temperature, which now cools and transfers energy to the analyte molecules. One of these processes will have a low rate coefficient, and as such creates an energy bottleneck. If the bottleneck occurs for the transfer from the sample to the analyte, the time taken for the analyte molecules to reach a temperature where they can reach thermal instability is much longer than the time taken for the solid sample to reach a temperature where phase transition occurs. If, however, the bottleneck occurs for the transfer of energy from the matrix to the sample, then the phase transfer will not be through sublimation processes and the sample will melt and evaporate, still producing intact analyte molecules.

Both MALDI and LITD do not occur *via* one mechanism on its own, but rather *via* a combination of all mechanisms to different degrees. Different combinations of substrates, analytes and matrices will have different contributions from the above mechanisms; however, all mechanisms are influenced by altering by laser fluence in the same manner, *i.e.* increasing fluence increases desorption (and fragmentation) of analytes.

1.4 Laser Ablation

Laser Ablation (LA) is a high irradiance method (in the range of 1 – 20 GW cm⁻²) utilising pulsed lasers that enables the direct analysis of solid samples that are difficult to analyse using wet methods.^[4] For example, if the sample is difficult to digest without using hazardous chemicals, or if digestion leads to losses of the analyte, solid sampling may be advantageous.

Laser ablation uses a high-power-density laser pulse to eject solid material into the gas phase. This can be performed either at atmospheric pressure, typically in a helium or argon gas flow, or under vacuum. In both cases, there is a plasma layer formed just above the surface of the sample from some of the sample. The electrons present in this plasma layer absorb the energy of the laser light incident on the sample and quickly redistributes this energy into thermal and vibrational states within the plume (plasma shielding via inverse Bremsstrahlung*).

Radiative relaxation causes light to be emitted from the plume, which then interacts further with the sample surface. This means after the initial plasma is formed, the wavelength of light getting to the sample surface is not the laser wavelength, but wavelengths characteristic to the plasma and sample. This is the basis for Laser Induced Breakdown Spectroscopy (LIBS),^[15] where the wavelengths emitted by this surface plasma is measured by a charge-coupled device (CCD) camera and is related to the elements in the sample. The plume expands much more rapidly under vacuum conditions than under atmospheric conditions, and hence the plasma shielding effect is less apparent under vacuum.

It must be noted that whilst the power of the laser is sufficient to ionise some of the sample and form the plasma layer, this ionisation is difficult to control and therefore not particularly useful for reproducible quantitative analysis. To combat this drawback, a more efficient ionisation source (usually the ICP) is placed between the LA system and the mass spectrometry system, and LA is used as a sample introduction system rather than a sample ionisation technique.

The mechanisms for plume formation are similar to those found in LITD and MALDI. Thermal mechanisms, however, are less significant as the fluence of the laser is sufficiently high enough for two-photon processes to become more probable. The energy from these two photons is more likely to be greater than the bond energies of many solid lattices used, therefore the laser light can directly break the lattice and eject particles of the sample into the gaseous phase.^[3] Once the plume is formed (see Section 1.4.1 overleaf), the sample can be carried into the mass spectrometer by a gas flow (in the case of LA, a helium or argon flow), or by expansion into a vacuum.

* Bremsstrahlung radiation (“braking radiation”) occurs when high-energy electrons are slowed by impact with other particles, or by a change in the electric field surrounding that electron: the excess energy is then lost as a photon. Inverse Bremsstrahlung is therefore the absorption of photons by electrons.

1.4.1 Laser Ablation Plume Regions

Once in the gaseous phase, the sample molecules are ignited into the plasma phase. The thermal energy produced in this process can heat the plasma up to 50,000 K, creating expansion pressures at the sample surface in the order of 10^8 Pa.^[4] This in turn leads to supersonic expansion of the plume. The ablation plume has four regions involved where different processes can occur (see Figure 1.14 below).

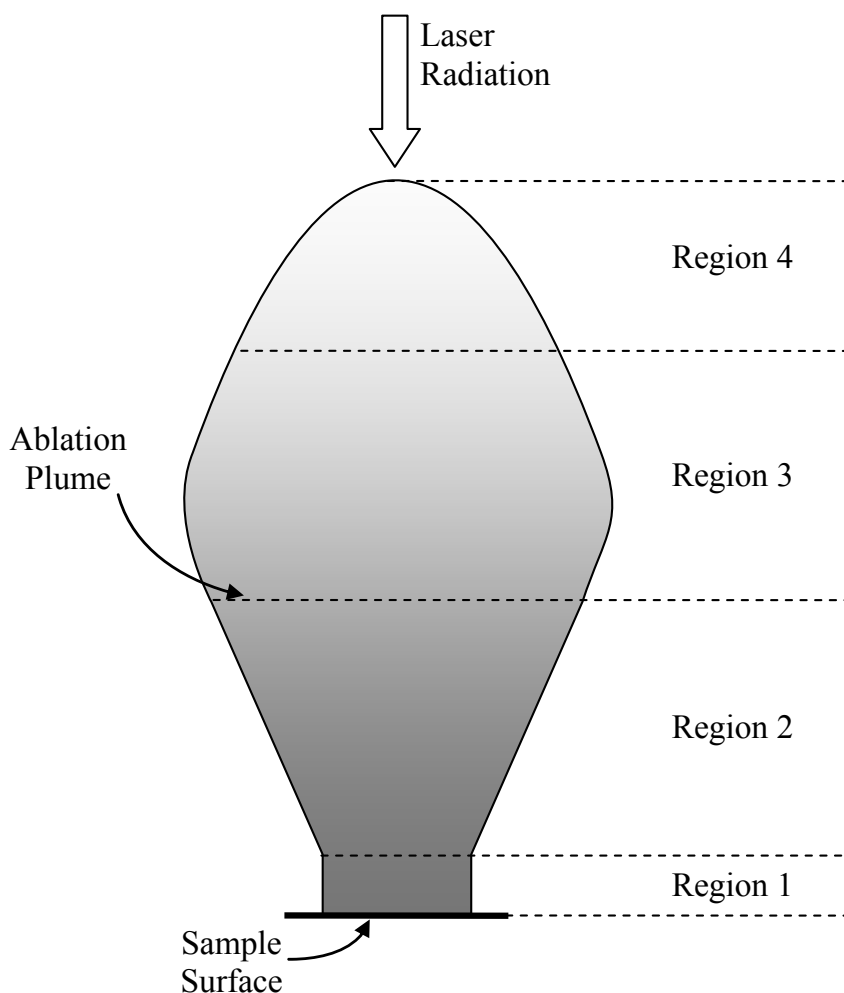


Figure 1.14: Schematic of the plume regions generated by laser ablation

1.4.1.1 Region 1 – The Surface Plasma Region

In this region, the plasma mentioned above is formed from photoignition of ablated particles resulting in the emission of photoelectrons. As the density of electrons in this region increases to a critical value, the refractive index of the plasma falls from 1 to zero, *i.e.* the plasma becomes totally opaque. This is due to absorption of laser light by electrons by inverse Bremsstrahlung absorption and by reflection. This region now absorbs most of the laser light, redistributing it into thermal energy and reradiating it to the surface of the sample.

The expansion of this region is said to be ‘one-dimensional’, as the expansion only occurs in the vertical plane. This is due to the proportion of the particles that are ejected into the gas phase perpendicular to the sample surface. Three-body recombination processes occur here, where electrons recombine with ions to release energy in the form of heat. This mechanism serves to reduce the energy of electrons and heat atoms in the ablation plume.

1.4.1.2 Region 2 – Molecular Beam Expansion

Due to the collisional nature of region 1, what is known as a Knudsen layer forms that has an 'explicit centre-of-mass velocity'.^[4] This produces a beam like adiabatic expansion in both the vertical and horizontal planes.

Three-body recombination processes are important in this region, as they are in region 1, but here this mechanism is no longer the dominant electron energy loss and atom-heating mechanism. This is because at the density involved in region 2, the time taken for a recombination process to occur is similar to the time taken for the region to reach local thermodynamic equilibrium; hence, energy redistribution will not be required.

1.4.1.3 Region 3 – The Coronal Region

In this region collisions do not occur for energetic (hot) electrons and are infrequent at best for thermal electrons as the cooling processes of the adiabatic expansion of region 2 cool the larger particles to a point where they are left behind the electrons. This disrupts the local thermal equilibrium. Three-body recombination mechanisms are not a factor in electron cooling at all, as by this time the laser pulse has ended and there is no incident laser light (unless the pulse length is in the order of milliseconds).

Inverse Bremsstrahlung heating still occurs as some interactions in region 1 can produce light waves through re-radiation. The degree of heating is much smaller than that occurring in region 1, but may oppose adiabatic cooling and serve to force further plume expansion.

1.4.1.4 Region 4 – Charge Separation and Oscillation

In this region, the lack of collisions and the speed of the electrons force a charge separation to appear. This charge separation causes a decelerating force to be applied to the electrons and an accelerating force to be applied to the positive ions. The positive ions, therefore, develop a faster velocity than the electrons and overtake them. The charge separation now swaps: the accelerating force is now applied to the electrons and the decelerating force to the cations. This alternating charge separation causes plasma oscillations to be set up, the frequency of which is dependent on the nature of the plasma. This means the average velocities of both the electrons and the cations are equal, meaning they enter the mass spectrometer together.

1.4.2 Particle Size Distribution in Laser Ablation

The size of the ablated particles has important consequences on the mass spectrum produced.^[16, 17] Large particles are inefficiently transported to and ionised in the ion source (most commonly the ICP), which lowers the sensitivity of the technique. On its own, the decreased sensitivity is not exceptionally difficult to overcome, as larger spot sizes, higher repetition frequency or longer ablation times will cancel out this effect; however, elemental fractionation can occur, altering the relative abundances of elements and isotopes in comparison to those in the sample.

Elemental fractionation itself can occur at many stages and results in the preferential enrichment of elements or isotopes over others within the vapour phase. This can occur during the ablation of the sample, during transport and during the ionisation process. During the ablation step, the volatilisation of samples into the vapour phase depends on the absorption coefficient of the sample. Those molecules with high absorption coefficients at

the laser wavelength absorb more light and are more easily volatilised. This effect is only seen if the ablation step is inefficient, therefore only sampling volatile analytes.

Fractionation in transport and ionisation processes occurs due to particle size. Large particles have a low surface area-to-volume ratio, and hence only analytes with high vapour pressure, *i.e.* volatile analytes, can escape these particles. This means large particles become enriched in low volatility analytes. The largest particles (referred to as immobile) are inefficiently transported to the ion source, whilst the higher volatility elements are transported efficiently in the vapour phase. This leads to a loss in low volatility elements, lowering the measured relative abundance.

Fractionation in the ion source can also be seen due to the unequal volatilisation in large particles. The larger particles that reach the ion source are harder to atomise and ionise than smaller particles or vapour phase analytes, and there are some losses in the lower volatility analytes at this stage also, lowering the measured relative abundance further.

Consequently, to reduce elemental fractionation in samples the ablation process has to be optimised to produce small, mobile particles that are efficiently ionised. This optimisation in the ablation step is controlled by the irradiance of the laser, the laser wavelength, the pulse length, the sampling method and by the carrier gas used.

Higher irradiances lead to increased mechanical stress in the sample surface leading to smaller particles. However, if the pulse length is too long melting can occur, reducing the ablation efficiency and increasing the fractionation.

Shorter laser wavelengths result in more energy per photon, which in turn means more energy being transferred to the lattice vibrational states of the solid sample.^[16, 18, 19] This means the sample is ablated through more intense mechanical pathways and results in smaller particles as the wavelength of the laser is decreased.

The pulse length of the laser affects which mechanisms are excited through the ablation process.^[20] Electron heating and thermalisation pathways last in the order of 100 femtoseconds, cooling and energy transfer to the lattice mechanisms are in the order of a few picoseconds. Thermal diffusion timescales are around ten picoseconds and the onset of thermal melting and subsequent ablation is after about 100 picoseconds.

A laser pulse lasting in the order of nanoseconds would pump energy into all the transient states of the sample and the surface plasma, leading to sample melting. A much shorter pulse, *e.g.* a few femtoseconds, will only interact with the electron heating and thermalisation pathways. All of the incident energy can be transferred into mechanical breakdown and into kinetic energy of the ablated material. This results in smaller ablated particles and reduced fractionation.

The other factor mentioned is the choice of carrier gas used in atmospheric pressure LA. Under atmospheric pressure, the ablated particles can lose thermal energy by agglomerating into larger particles (condensation). The degree of condensation is controlled by the thermal conductivity of the carrier gas.^[21] Carrier gases with relatively high thermal conductivities (*e.g.* helium) can take thermal energy away from the ablation plume at a much quicker rate than those with relatively low thermal conductivities (*e.g.* argon). This results in faster cooling, and thus a shorter condensation period. This ultimately leads to smaller particles in the plume. Under vacuum, condensation does not occur to a noticeable degree, as the rate of

cooling by the rapid expansion is sufficient to end condensation pathways in a very short period of time.

Another factor that affects fractionation is crater morphology. Lasers with Gaussian beam profiles, such as neodymium doped yttrium-aluminium-garnet (Nd:YAG) lasers, can be focussed to small spot sizes, but produce conical craters after time.* These conical craters increase the sampling area and decrease the effective irradiance. Additionally, the increased depth of the crater confines the plume, decreasing the rate of cooling by expansion. This causes melting of the sample by the plume, and condensational growth of sample particles, increasing the fractionation.

1.5 Application of Lasers in Mass Spectrometry

MALDI has generally been used as an ionisation and sample introduction source for analysis in biochemical applications, such as proteomics and biomarker analysis for the detection of diseases^[22-24] and analysis of post mortem samples.^[25] In these cases the sample is homogenised, mixed with matrix, dried and analysed using a ToF mass analyser. For example, Witkowska *et al.*^[22] used MALDI-MS to identify antigens present in *Klebsiella* bacteria. These antigens are expressed as structures called fimbriae, which are proteins that mediate attachment of the bacterium to host cells. Samples of *Klebsiella pneumoniae* (similar antigens to *E. coli*) and *K. oxytoca* were mixed with DHB, dried onto a target plate and desorbed using a 337 nm nitrogen laser. They were able to identify two different types of fimbriae proteins related to different modes of immune response at 15 kDa and 18 kDa using a ToF mass analyser. MALDI is not limited to these 'standard' uses, and this review will focus on the development of MALDI as an analytical tool.

Laser ablation is mainly used in the geological and environmental fields for elemental analysis of solid samples.^[3] For example, Watmough *et al.*^[26] analysed tree ring cores to assess the environmental impact of copper and zinc smelting sites in Canada. Both copper and zinc levels of samples taken near these smelting sites rose and fell in accordance with the opening and closure of the sites. A control sample showed no change, yielding evidence of increased emissions of both elements into the environment by the smelting sites.

Again, use of LA is not limited to these types of analysis, and this review will cover specialised applications. One such application for LA was described by Yang *et al.*^[27] in 2005. In an effort to extend the use of laser ablation, aqueous samples and standards were dried onto marked areas within polystyrene weighing boats using an infrared lamp. The marked areas were then cut out, put into a LA system using an argon flow and irradiated with a 266 nm Nd:YAG laser (at 20 Hz). Two shots of laser energy were used, which allowed complete desorption of the dried droplet layer. The ablated samples were analysed using a quadrupole mass analyser.

Samples of drinking water were analysed for Ni, Cd and Pb in this way using a separate set of standards, standard additions calibration and isotope dilution calibration. The latter two methods produced results consistent with solution nebulisation, but the first method

* Nd:YAG lasers can be homogenised to produce flat beam profiles to minimise this effect. Most (if not all) commercially available Nd:YAG laser ablation systems use a homogenised beam.

produced significantly lower results, possibly due to matrix effects. Potentially, this method can be used for very small liquid samples as an alternative to graphite furnace atomic absorption spectroscopy, where problems with atomisation and carbide formation can occur.

1.5.1 MALDI Mapping

In 2004, Chaurand *et al.*^[28] explored the use of MALDI as sampling tool for mass spectrometric imaging of histological tissue slices. To achieve this, both optical images of the tissue slice and protein analysis via MALDI-MS have to be efficient. The usual stains used for histology, *i.e.* haematoxylin and eosin, were found to interfere with the MALDI matrix, compromising the efficiency of the MALDI experiment.

Additionally, insulating target plates were found to induce a localised charging effect on the sample molecules, resulting in a noticeable time shift in ToF mass analysers, ultimately altering the observed mass. Conducting targets, such as metal plates and glass coated with indium-tin oxide (ITO), reduce this effect, and are ideal for mass spectrometry. The team evaluated the use of different stains and target plates for the best combination of optical microscopy and mass spectrometry.

For the mass spectrometry, two adjacent 12 μm thick mouse liver sections were mounted on gold-coated stainless steel and ITO-coated glass targets respectively. Droplets of sinapinic acid (SA) were deposited on the surfaces of the sections and allowed to dry. The samples were then analysed by MALDI-ToF-MS using a 337 nm nitrogen laser (20 Hz repetition rate) and -25kV accelerating voltage through the flight tube. No significant difference was found between mass spectra obtained on the metal target and mass spectra obtained on the glass target.

Five different stains were evaluated for interference with MALDI matrices: Methylene Blue, Terry's Polychrome, Cresyl Violet, Nuclear Fast Red and Toluidine Blue. These stains bind preferentially to DNA and nuclear molecules, thereby reducing interference with protein analysis. It was found that the lowest distortion of protein signals was obtained using Methylene Blue and Cresyl Violet, Cresyl Violet giving the best contrast. To test the combined analyses, 12 μm thick histological samples of mouse coronal cerebellum were stained using Cresyl Violet and optically imaged. These samples were subsequently sprayed with SA and mapped using a 337 nm nitrogen laser (20Hz, 1 s per pixel). The resulting protein maps could then be overlaid on the optical slices and the positions of the proteins related to identifiable sites within the samples, thus identifying morphologically-linked changes in protein concentrations/locations.

1.5.2 Atmospheric Pressure MALDI Interfaces

Interfaces for MALDI that operate at atmospheric pressure (AP) have been developed to extend the use of MALDI to wider fields. In 2000, Laiko *et al.*^[29] developed an AP-MALDI interface consisting of a target probe, a parallel nitrogen gas flow and a vacuum interface (see Figure 1.15 across). A voltage is applied to the probe tip to push the ions off the target surface, and the use of the (nitrogen) gas flow makes this interface pneumatically assisted (PA).

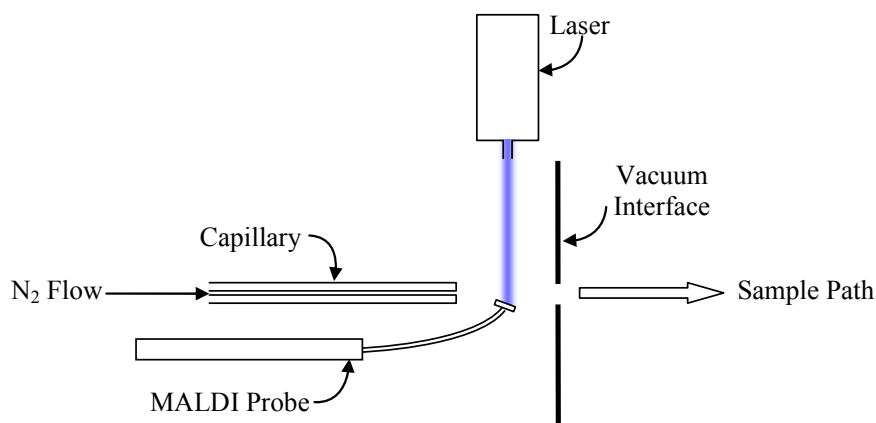


Figure 1.15: Schematic of an AP MALDI Interface

The resultant ions are transported into the vacuum section of the mass spectrometer by a combination of the probe tip potential, the dry stream of nitrogen and the pressure gradient through the vacuum interface, without the use of ion optics. This transport, however, is not as efficient as transport within a vacuum using ion optics. On comparison with such a vacuum system, the laser had to be tracked across the entire sample area (approximately 1.5×2.5 mm) to achieve a spectrum comparable to a vacuum MALDI system, where the sample taken was from a $500 \mu\text{m}$ diameter laser spot.

In 2004, O'Connor *et al.*^[30] developed a so-called ‘high-pressure’ interface for FT-ICR-MS that is capable of sampling from oversized samples such as thin layer chromatography (TLC) microtitre plates. Note, ‘high-pressure’ can refer to atmospheric pressure or just above, owing to the fact the inlet is at a much higher pressure than that of the mass analyser. In this case, the gas pressures involved were estimated to reach up to 1 kPa.

In this system, a plate containing a collar of gas jets set at 45° to the sample surface was used to extract ions released by an oblique laser. The system employed a dual wavelength setup, where the user could select UV-MALDI at 355 nm (Nd:YAG, 1 mJ/5 ns pulse, 20Hz) or IR-MALDI at 2940 nm (Er:YAG, 7 mJ/100 ns pulse, 5 Hz). The target was mounted on a 10×10 cm translation XY translation stage, which was housed inside a vacuum chamber. Inside this vacuum chamber is the gas channel plate (see Figure 1.16 below), which extracts the ions into an FT-ICR cell using 16 jets of high-pressure gas.

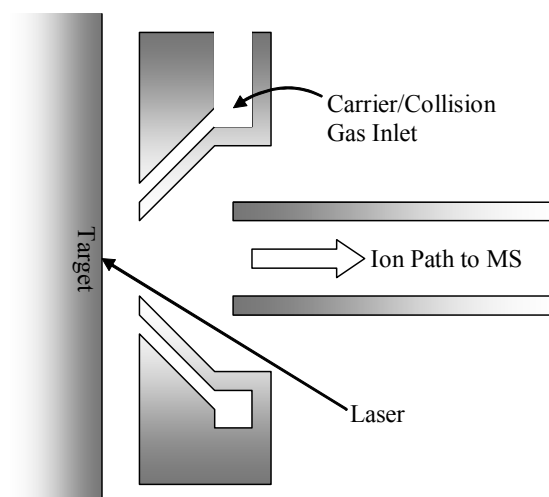


Figure 1.16: Simple Schematic of the Gas Channel Plate Used by O'Connor *et al.*^[30]

The target plates were charged at +3V DC to help lift off the positive ions produced by the laser and send them through the MS inlet. The chosen laser wavelength was fired at the target surface, followed by a pulse of high-pressure gas. In addition to being a simple transport mechanism for the ions, the gas can be used to stabilise large molecules and prevent fragmentation by collisional cooling processes. This high-pressure pulse picks up the stabilised sample plume and transports it through a series of hexapole ion-optics into the FT-ICR cell, where the analyte masses are analysed.

Tan *et al.*^[31] improved the sample transport through the vacuum interface by developing an electrode programme for the probe tip, called pulsed dynamic focussing (PDF). A high-voltage potential is applied to the probe tip after a time delay to improve the rate at which ions left the sample surface. The orientation of the setup was also altered, eliminating the need for pneumatic assistance (see Figure 1.17 below)

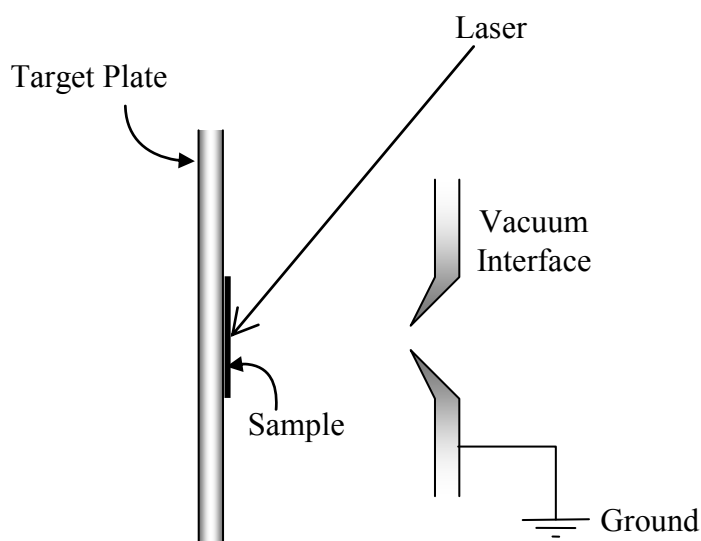


Figure 1.17: Schematic of an Improved AP-MALDI Interface Adapted for PDF

The voltage is applied to the target plate during the laser pulse, and subsequently switched off when the pulse has finished. This allows ions initially to be pushed away from the target by the electrostatic field, and then through the vacuum interface with the aid of the pressure gradient once the voltage is switched off. This prevents the ions following the electric field lines to the sides of the sample chamber and discharging. Comparative studies showed a two-fold increase in sensitivity compared to the first generation, non-pulsed AP-MALDI interface.

A commercial device has been produced using this technology by MassTech Inc. (Maryland, USA).^[32] It consists of a removable metal box housing a stage holder and fibre optics for the laser system and a viewing camera (see Figure 1.18 below). This box bolts onto the front end of many commercially available mass spectrometers, and is easily interchangeable with an ESI source.

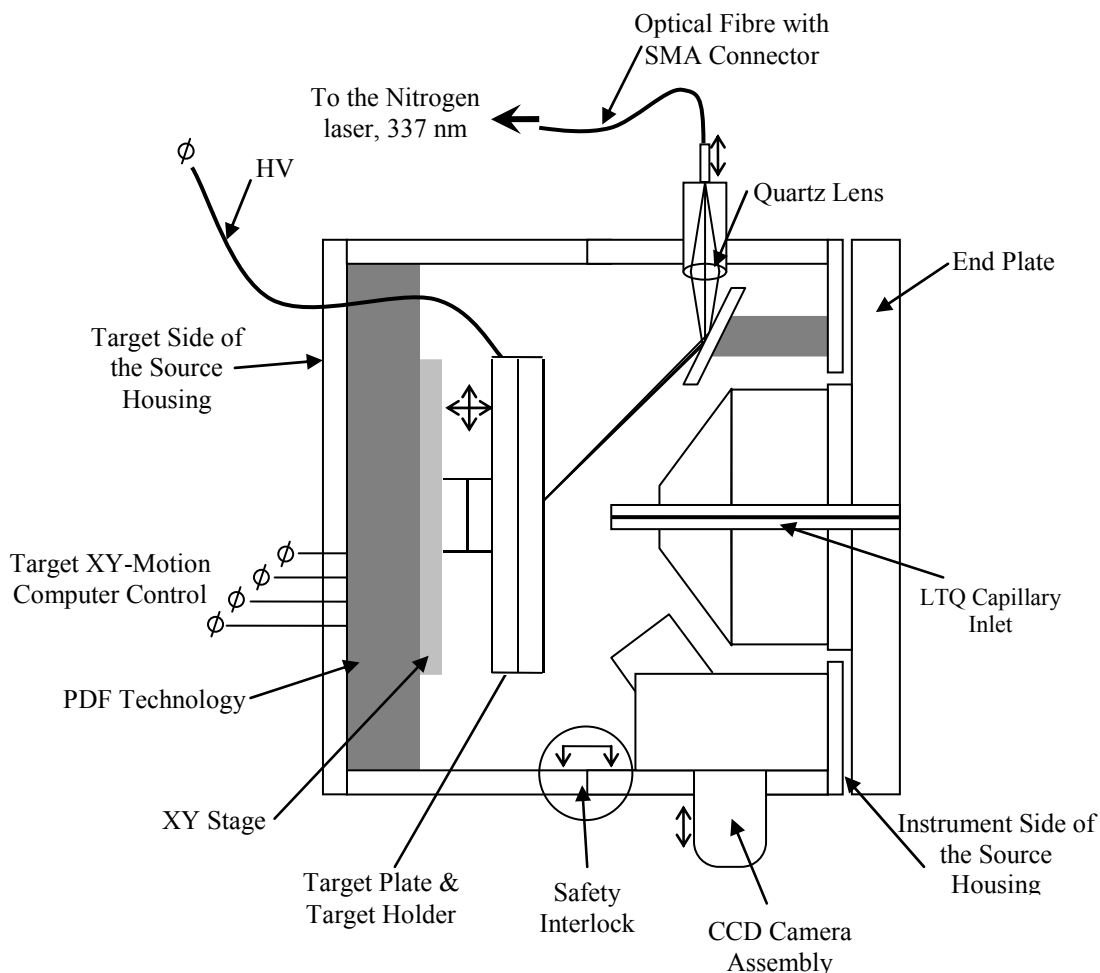


Figure 1.18: Simplified Schematic of the MassTech AP-MALDI PDF Source Installed on a Thermo Scientific LTQ-Trap Mass Spectrometer^[32] – © MassTech Inc. 2004

Taranenko *et al.*^[33] used the AP-MALDI interface coupled to an ion trap mass analyser to analyse a range of phosphopeptides. The phosphopeptides were obtained from tryptic digests of phosphorylated β -caesin, mixed with α -cyano-4-hydroxycinnamic acid (CHCA) matrix and desorbed using a 337 nm nitrogen laser. From the positive ion spectra, the sequence of amino acids was elucidated and the sites of phosphorylation identified.

In 2005, Kellersberger *et al.*^[34] used an AP-MALDI interface coupled to an FT-ICR mass analyser to see differences between normal and chemically modified RNA. RNA samples were created *in vitro* by transcription from commercially available, synthetic DNA templates. The RNA samples were treated with solvent accessibility reagents that are typically used in structural studies of RNA and protein-RNA complexes. The superior mass resolution of the ICR analyser allowed samples differing by as little as 0.04 Da to be fully resolved at masses up to 6.4 kDa, with little to no metastable decay.

Schneider *et al.*^[35] compared vacuum MALDI systems with AP-MALDI systems. Even though the ion transport is twice as efficient in vacuum systems, there are advantages to the AP-MALDI systems, not least being the ability to change samples without breaking vacuum. Because of the presence of gas molecules around the MALDI plume, the ions produced lose energy through collisions and therefore are less likely to fragment. This means higher laser energies can be used, increasing the number of ions initially produced per unit time.

Additionally, AP-MALDI systems can accept samples that are unstable in vacuum environments, such as electrophoresis gels and polymer membranes. The main disadvantage, however, is increased cluster formation between the analyte and matrix molecules, especially at low laser energies close to the ionisation threshold. This requires input of thermal energy to cause the clusters to dissociate, possibly as a curtain gas flow.

The AP-MALDI interface has more parameters to consider when optimising, such as source gas flows, potentials and temperature. As a result, optimisation of the technique is more complex, but once completed the sensitivity of AP-MALDI can reach similar values to that of vacuum MALDI: it was found that the ion currents in vacuum MALDI were twice that of AP-MALDI, but the signal-to-noise ratios were comparable.

1.6 Laser Ablation Cell Development

At present, LA-ICP samples are limited by size. Atmospheric gases can make an ICP unstable and therefore extinguish the plasma. Coupled with safety issues, this has meant samples have to be enclosed in a sample chamber filled with argon or helium. To avoid difficulties with sample transport, and to avoid high running costs with gas consumption, the sample cells have tended to be relatively small. For larger samples, a different strategy has to be employed.

1.6.1 Large, Enclosed Cell Strategies

The main problem with simply producing a large chamber to enclose the sample is that the ablated aerosol can expand into a large volume, swept relatively slowly by the helium sweep gas. This effectively dilutes the sample aerosol and decreases the sensitivity of LA-ICP-MS.

Various transport strategies have been devised to improve the sample transport efficiency through a laser cell, some of which can be adapted to larger cell designs. For example, in 2005 Bleiner and Altorfer^[36] developed a gas inlet system to improve aerosol entrainment in a standard laser ablation cell, called a 'turbo inlet' system. This consisted of a rotating nozzle at the gas inlet made up of 4 eccentric holes set at 40°, two of which were 0.3 mm in diameter and diametrically opposed, the other two were 0.5 mm in diameter and diametrically opposed. Rotating this nozzle at 2500 rpm had the effect of decreasing sample washout times, increasing transmission efficiencies and decreasing elemental fractionation.

In 2006, Fliegel and Günther^[37] developed a low pressure laser ablation cell to minimise the effect of nucleation, condensation and agglomeration processes in the ablation plume. The authors found that by decreasing the pressure within the ablation cell to around 500 mbar, the Particle Size Distribution (PSD) was shifted significantly towards smaller particles due to increased plume expansion and a subsequent reduction in condensation/agglomeration processes. The cell was isolated from the ICP torch during ablation and operated under closed conditions, then flushed through with gas for transport to the plasma. The main

drawback of this system was that at these lower pressures, the absolute signal intensity decreased significantly. This was due to decreased sample transport efficiency within the cell as the plume expanded and deposited inside the ablation cell.

Pisonero *et al.*^[38] developed a cell for laser ablation with low washout times and high aerosol transport efficiencies, called the ‘High Efficiency Aerosol Dispersion’ (HEAD) cell. The cell consists of a ‘closed’ sample section, which housed the sample to be ablated, and an ‘open’ section above, which extracted the ablated aerosol and transported it to the ICP. The ‘open’ section was slotted into the ‘closed’ section and sealed with an o-ring to create an essentially completely closed cell. Helium was then pumped into the ‘closed’ section to entrain the aerosol, which then entered the ‘open’ section through a small orifice (see Figure 1.19 below).

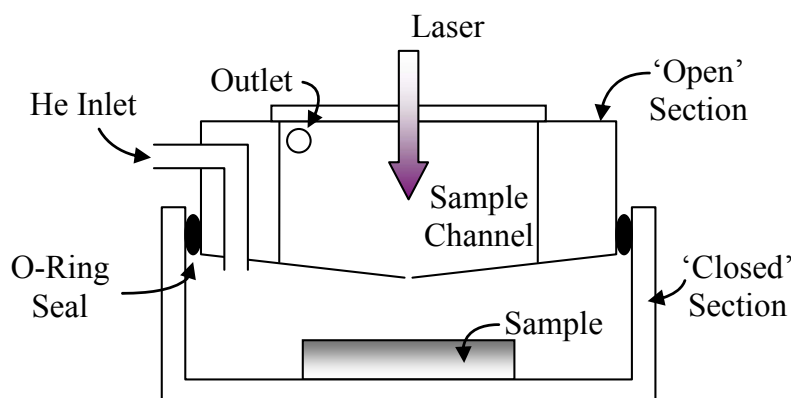


Figure 1.19: Side view of the HEAD cell, developed by Pisonero *et al.*^[38]

The aerosol was extracted into the cell through a small orifice. The gas flows were then accelerated and mixed by a cross-flow nebuliser, with an argon make-up flow being pumped orthogonal to the outlet from the cell (see Figure 1.20 below).

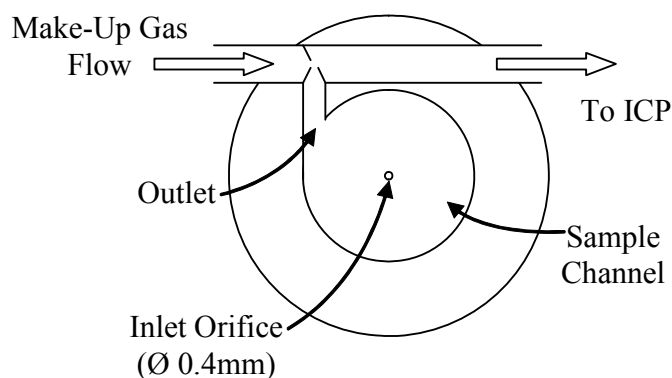


Figure 1.20: Top view of the HEAD cell developed by Pisonero *et al.*^[38]

With this cell, the authors found that the particle size distribution was shifted towards smaller particles (when using 266 nm Nd:YAG laser [LSX 500, CETAC Technologies, Omaha, NE, USA]) and there was reduced elemental fractionation in the plasma. This was achieved by using higher gas rates and entraining the ablated plume into a fast gas flow, reducing condensation processes. They also found that the stability of transient signals in the mass spectrometer was improved, reducing relative standard deviations (RSD's) from between 30 – 35% down to between 1 – 5%.

Feldmann *et al.*^[39] developed a cell to image hetero-atoms (*i.e.* any atom that is not carbon in an organic molecule, such as nitrogen, sulphur, phosphorous, oxygen, or halogens) in proteins blotted onto membranes. The cell developed consisted of a cylindrical polytetrafluoroethylene (PTFE, known commercially as Teflon®) roller (1.50" diameter) onto which the membrane was attached. The laser was then fired normal to the surface of the roller (see Figure 1.21 below).

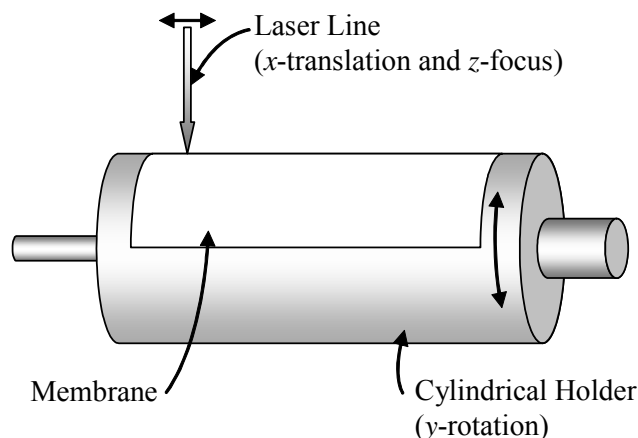


Figure 1.21: Schematic of the laser ablation cell developed by Feldmann *et al.*^[39]

This allowed access to all areas of the membrane without using a significantly large ablation cell, thereby maintaining the relatively short washout times of standard ablation cells. With this cell, the authors were able to create two-dimensional maps of proteins blotted onto membranes after electrophoresis using ^{31}P as an elemental marker.

In 2007, Guillong *et al.*^[40] developed an ablation cell for the analysis of highly radioactive samples. The main issue with analysing radioactive samples is that the instrumentation involved in such analyses can become contaminated and defects can occur, such as discolouration of optics. The ablation cell was housed within a stainless steel, lead-lined α -box with a dedicated microscope permanently in place. The beam generation system was then housed outside of this box and delivered to the microscope by an optical window in the α -box. The ablation cell was also permanently housed within this box, and consisted of a piston sample holder and a lid section.

Radioactive samples were loaded remotely, using a manipulator, into the ablation cell by means of the motorised piston (also for z -focus control). The piston moves 'bottom-up' into the lid section and is sealed with an o-ring forming a closed, shielded ablation cell. This was then connected to an ICP-MS through eight metres of flexible tubing. Cell performance was evaluated using an un-irradiated uranium dioxide sample, measuring the $^{235}\text{U}/^{238}\text{U}$ ratio. It was found that the system was capable of performing bulk analysis with high accuracy and sensitivity (RSD $\sim 0.3\%$); however, the large distance from the sample to the camera gave poor sample visualisation and the stick manipulator gave limited handling capabilities.

1.6.2 Non-Contact Cell Strategies

In 2007, Bleiner and Bogaerts^[41] reviewed a range of cells using computer simulations to assess gas flows and entrainment of the aerosol within the gas flow. The various cells were categorised into ‘closed’ and ‘open’ cells, where the ‘closed’ cell was defined as a sample chamber which fully enclosed the sample requiring little to no sample preparation and the ‘open’ cell used the sample as a final, closing wall. This required the sample to be polished to provide adequate sealing.

‘Open’ cells present advantages in terms of shortened washout times, as most of these cells have small volumes, and increased flexibility in terms of sample size. However, aerosol losses by impaction with the cell walls could increase and, alteration of the sample surface by the polishing method introduces uncertainty into the validity of the measurements.

To avoid polishing, the ‘open’ cell can be housed within an outer containment box. These types of cell are termed ‘two-volume’ cells, whereby the ablated plume expands into a secondary volume that is much smaller than the enclosure. Commercial examples of this type of cell are New Wave Research’s Large Format Cell,^[42, 43] Photon Machine’s HelEx Cell^[44] and Resonetics’ Laurin Cell.^[45]

These two-volume cells have all been developed after Barringer’s continuous ablation cell, first patented in 1980.^[46] This consisted of a reel of adhesive tape onto which the sample was spotted. The sample spots then passed under a ‘vaporization cell’, where the sample was ablated by the laser (see Figure 1.22 below).

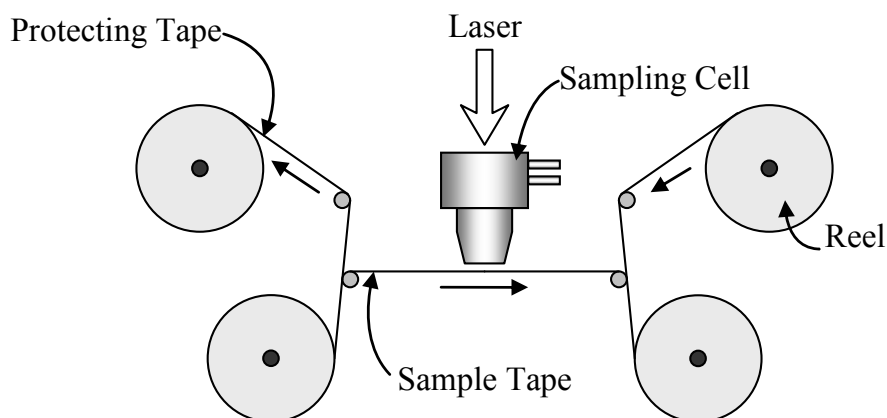


Figure 1.22: Schematic of the continuous ablation sampling cell developed by Barringer.^[46]

The tape consisted of an adhesive layer onto which the sample was spotted, covered by a protective PTFE tape layer. As the sample tape passed through the system, the protective tape was peeled back from the sample, allowing ablation to occur. Once past the sampling cell, another protective layer of PTFE tape was applied to protect any residual sample, ready for storage and subsequent analyses. The whole setup of reels and sampling cell sat inside an outer box pressurised with plasma support gas, which in this case was argon.

The sampling cell floated above the tape and entrained the ablated sample plume by means of an annular gas channel (see Figure 1.23 below). This channel was angled inwards to encourage gas to flow towards the internal space and out of the gas inlet.

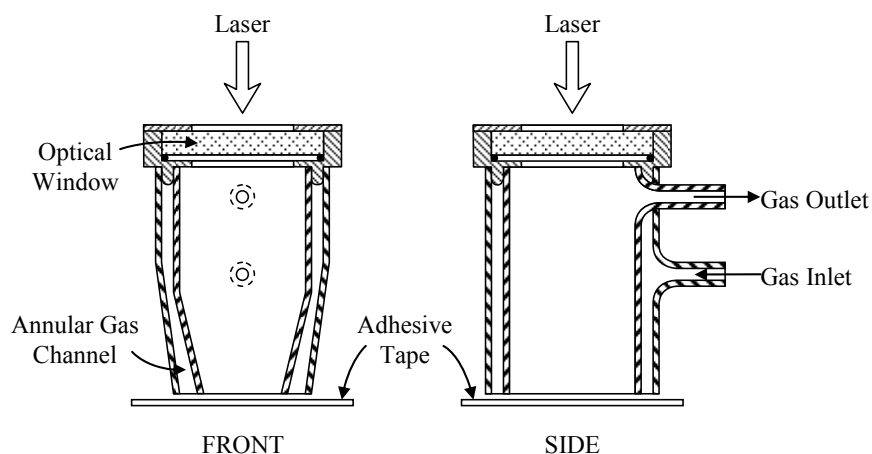


Figure 1.23: Front and side views of the 'Vaporization Cell' patented by Barringer. [47]

In 1988, Arrowsmith and Hughes^[47] adapted this design to a motorised stage capable of supporting large (10×10 cm) samples. The *xyz*-translation stage, the stepper motors and the sampling cell were all enclosed in a large outer box, pressurised with plasma support gas, again in this case argon. The cell was used as the sampling cell for a LA-ICP-MS system

Inlet gas was pumped in at volume flow rates of $5 - 10 \text{ l min}^{-1}$ and the outlet gas pumped out at rates of $1 - 2.2 \text{ l min}^{-1}$. Both flow rates were controlled by mass flow controllers. It was found that the optimum conditions for sample transport, ablation efficiency and ICP-MS signal occurred when the inlet gas flow was fixed at a very high flow of 10 l min^{-1} and the outlet gas flow was at approximately 1.5 l min^{-1} . The inlet gas flow was set at this level because it had to both purge the large outer box, to exclude atmospheric gases, and to entrain the sample.

In 1995, Shuttleworth *et al.*^[48] developed the design for the Barringer cell to add a second annular gas curtain. Dubbed the 'Hovercraft Cell', it used a rubber 'skirt' as an atmosphere exclusion device, the second annular gas curtain being used as a back-up exclusion system. It was further developed in 2000 by Boué-Bigne,^[49] working in this group, for use as a remote sampling unit for ICP-MS and removing the rubber skirt. The gas flows for this cell were optimised to an inlet flow of 1 l min^{-1} and an outlet flow of 0.4 l min^{-1} , using an ammonium chloride vapour generator. At these gas flows, the vapour was seen to rise vertically in thin stream in the centre of the cell and then bend sharply towards the exit channel.

In 1999, Devos *et al.*^[50] developed an open cell for the analysis of antique metal objects. Existing techniques at the time required removal of a visible fragment of the antique for either wet digestion or to fit into a sample cell for LA or X-Ray Fluorescence (XRF) analysis.

The study used a cylindrical borosilicate cell (4.2 cm in diameter with an adjustable height of 1.7 – 2.4 cm) with diametrically opposed lateral gas inlet and outlet tubes. The cell also had an exchangeable Plexiglas bottom, to adjust the sampling area, with central apertures of 5, 10 and 20 cm. The cell was sealed onto the antiques using modelling plasticine for irregular objects, or a flat rubber o-ring for flat objects.

Using this cell, various trace metals were characterised within references and the antiques. The results were in good agreement with established methods, and allowed *ante quem/post quem* dating (*i.e.* before or after 1850) for a range of silver antiques. The main advantage over the established techniques was the LA-ICP-MS method used three 100 μm spots that were barely visible to the naked eye as opposed to a visible fragment.

Most recently in 2010, Kovacs *et al.*^[51] removed the need for a laser ablation cell entirely, and used a gas exchange device^[52] to remove atmospheric gas and replace it with argon. The ablation was performed on the sample in ambient conditions, and the immediate ablation environment (including the aerosol) removed by means of a micro-diaphragm pump.

The aerosol was sent through the exchanger, which consisted of a porous silica tube within an outer borosilicate sheath. An argon counter-flow was introduced on the outside of the porous tube. The gas exchange mechanism is based on diffusion and was shown to be near 100% efficient, provided the sweep flow rate is 10 times greater than the aerosol flow rate.^[52] This allowed stable operation of the ICP and comparable performance to standard ablation cells.

For the analysis of large, planar samples and surface-sensitive samples, non-contact cell technology offers many advantages, the main being the ability to analyse a whole sample without alteration of the sample surface. The following pages in this thesis document the development of such a cell, with particular focus on the semiconductor industry where analysis of surface impurities in silicon wafers is important. ^[53, 54]

THIS PAGE IS INTENTIONALLY BLANK

2 Overarching Aim and Objectives

The goal of this project is to design and validate a laser ablation cell capable of sampling large, flat samples with high efficiency, sensitivity and little or no surface contact. This is to be employed in, but not limited to, *e.g.* a semiconductor fabrication plant for complete wafer analysis.

The cell should also be capable of being coupled simultaneously to more than one analytical device to provide multiple, simultaneous analyses for different aspects of the sample, *e.g.* identification of a biomarker through proteomic analysis using an organic mass spectrometer with simultaneous quantification using an ICP-MS system.

2.1 Design Brief

Requirements:

1. Low gas consumption

The main reason for the lack of interest in the design patented by Barringer is due to the high gas flows required to operate it in true non-contact conditions, meaning the existing design is not economically viable for commercial purposes and is restricted to research use.

2. Two concentric annular gas channels

Use of an outer flow of inert gas to drive away atmospheric gases from the plasma will extend the applicability of the proposed design to all flat surfaces without limitations on size, location and external atmosphere. The carrier channel will serve to pick up ablated material and introduce it to the ICP-MS.

3. Two sampling channels

By having two sampling (exit) channels, the proposed cell can be employed between an inorganic ICP mass spectrometer and a bio-organic mass spectrometer. This will provide dual analysis on a single sample, meeting one of the main objectives of this project.

4. Electrical grounding plane

MALDI requires an electrical pulse on the target plate to aid sampling of large, heavy molecules. To further aid the sampling, providing a grounding plane in the cell will help to 'pull' charged molecules towards the main sampling channel, improving efficiency.

5. Attachment to existing New-Wave™ Universal Platform

The Universal Platform is used for most of the New-Wave Research LA lasers. Coupling the cell to this system will make the cell available to a wider market of new and existing customers.

2.2 Performance

The most likely end-user for the ablation cell presented in this thesis will be using it to analyse semi-conductor samples for trace element contaminants. As an analytical tool, the laser ablation cell should have the following characteristics:

1. Efficient Transport/Sensitivity

Efficiency can be defined as a combination of both high mass flux and transport speed, *i.e.* the cell should be capable of transporting the ablated material to the analyser with minimal loss and/or dilution, and within the minimum time. A high mass flux will allow sensitive determination of low-levels analytes, whilst fast transport will allow for surface features to be spatially resolved.

2. Stability

The mass flux through the cell should be stable and not subject to fluctuations that will artificially induce apparent variability into the sample surface, *i.e.* any variability seen in the signals should be 'real' signal variability, not induced by the sample cell.

3. Reproducibility

Signal levels achieved for a particular set of laser and ICP settings must be achievable both during the analytical run and during a separate analytical run. In practice, this is difficult to show on a day to day basis using raw signals as the ICP is optimised daily, changing the optimum set of operating parameters.

3 Research Methodology

Scientific research is built upon proving or disproving published hypotheses within the acquired knowledge of a particular field of study.^[55, 56] This knowledge is based on shared assumptions in that particular scientific community, with established viewpoints on what determines valid research.

With this in mind, the research presented in this thesis has been designed to prove the objectives listed in Section 2.2 have been achieved within the bounds of accepted analytical performance of laser ablation cells, *i.e.* how laser cells ‘should’ perform, backed up with empirical quantitative data. Design considerations for the cell, outlined in Section 2.1 and detailed in Section 4.1, were approached purely theoretically. Existing hardware had to be considered to ensure the new design fitted existing platforms with room for modifications where necessary.

3.1 Validation Methodological Considerations

Published designs for laser ablation cells have been characterised for signal stability, reproducibility, speed of transport (wash-in/wash-out), spatial variability within the cell and elemental fractionation.^[38, 42, 43, 45] In this thesis, performance of the non-contact laser ablation cell is characterised by the following:

1. Gas dynamics and atmosphere exclusion
2. Transport efficiency, measured as wash-in/wash-out and elemental fractionation
3. Raw signal and elemental sensitivity
4. Signal stability and limits of detection

Since the cell is open, the end-user must be confident that the gases supplied are being vectored in the correct direction and that atmospheric gases (and possible contaminants) will not enter their analytical instrumentation. As mentioned earlier in Section 1.2.1.2, altering the composition of the central channel can alter the ionisation characteristics of the plasma; hence, a stable composition that conforms to established, validated methods is important to achieve. Simple physical flow studies, described in Section 4.6, aimed at characterising the flows through the cell and the composition of the output gas mixture were carried out to this effect.

Any ablation cell needs to be capable of transporting the ablated material through the cell with minimal losses and minimal alteration of the aerosol.^[38, 45, 57] The raw signal achieved by the cell and corresponding signal quality were compared to the UP standard cell for characterisation against certified reference materials (with well characterised compositions) and semiconductor materials, as described in Section 4.4 and 4.5.

THIS PAGE IS INTENTIONALLY BLANK

4 The Research Undertaken

This section provides a commentary on the design and test of the non-contact cell (NCC). The cell is based on an adaptation of the Barringer ‘vaporization cell’ by Boué-Bigne in 2000. The complete set of technical drawings for the final revision of the open, non-contact cell are included in Appendix D.

The ICP matching circuit is unstable when atmospheric gases, especially oxygen, are entrained into the central plasma channel at an excessive rate.^[51] Additionally, air has relatively low thermal conductivity, which can lead to larger particles being formed in the ablated aerosol through condensation/agglomeration processes.^[21] This can lead to both inefficient particle processing within the plasma (*i.e.* lowered sensitivity) and elemental fractionation.

To combat these effects, there are two concentric gas channels in the cell: an outer ‘curtain’ gas flow channel that provides a flow conduit for a shielding gas to exclude destabilising atmospheric gases (notably oxygen), and an inner ‘carrier’ gas flow channel that entrains the sample aerosol and conducts it to the plasma. The carrier gas in LA experiments is usually helium,^[21] as it is inert, of low density and has a relatively high thermal conductivity. These properties aid ablation and subsequent ICP analyses as they allow the plume to expand away from the ablation crater and minimise condensation and agglomeration processes.

The curtain gas chosen for use in this cell is either nitrogen or argon, as these gases are inert, stable and much heavier than helium. Either gas restricts the flow of destabilising atmospheric gases from entering the output channels of the cell, whilst also minimising the flow of the carrier gas out to atmosphere by providing an effective momentum barrier.

4.1 Design of the Non-Contact Cell

This sub-section should be read in tandem with Appendix A: Apparatus and Method for Laser Irradiation (Paper 1), which provides a full description of the form, function and intended use of the non-contact cell.

Design of the cell was carried out using a 3D computer aided design (CAD) package. Initial design was carried out using UGS SolidEdge, which is a CAD package available on an academic site license provided by Loughborough University. Once a concept and design (the 'alpha' system) was approved by the ESI Inc. engineering team, refinement was moved over to DSS SolidWorks, a CAD package used by ESI Inc. This was a commercially licensed system with integrated computational fluid dynamics (CFD) capabilities, allowing more thorough characterisation of the system.

Rendered images of the upper and lower surfaces are shown in Figure 4.1 and in Figure 4.2 respectively below.

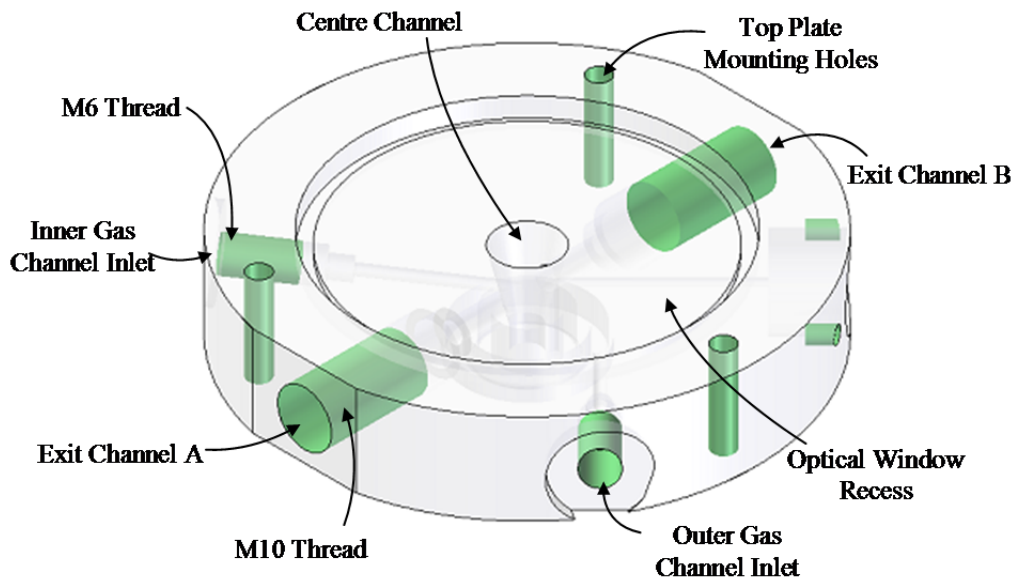


Figure 4.1: Rendered image of the non contact cell main body (upper surface – Revision G)

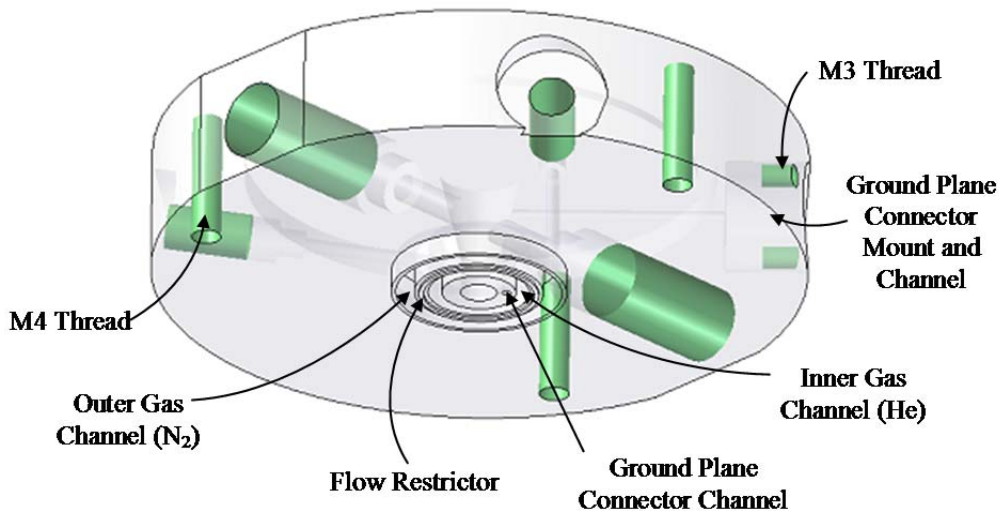


Figure 4.2: Rendered image of the non-contact cell (lower surface – Revision G).

The main body of the prototype cell was machined out of polymethylmethacrylate (PMMA), commercially known as Perspex® or Plexiglas®, by the Mechanical Engineering Workshop (Wolfson School of Mechanical Engineering, Loughborough University, Loughborough, UK). This was to allow the existing ring-lighting on the optics of the universal platform to be used, which floods the whole sample surface and provides even lighting; however, modifications to the cell described later meant a shadow was cast over the ablation site. Consequently, any lightweight material that provides good mechanical stability for manufacture, *e.g.* polyoxymethylene (POM, commercially known as Delrin®), can be used for the cell.

The gas fittings for this cell are based on commercially available VacuTight® seals (Upchurch Scientific Inc., Oak Harbor, WA, USA). The inlet channels are angled slightly to provide enough material for the fittings to tap into the threads. Note, M6 sized gas fittings (3 mm i.d.) are commercially available, but M10 fittings (6 mm i.d.) are not. These were manufactured with the cell by the Mech. Eng. Workshop.

The gas inlets for the carrier and curtain channels are tangential to the conduit geometry. This forces the gases to flow in helical paths, completely filling their respective channels. Once at the bottom of these channels, the gas flows encounter a fine nickel mesh (Micropore Technologies Ltd, Loughborough, UK). This mesh has 18 µm circular pores with an open area of ~1% of the total area, which creates stiff, vertical micro-jets of gas that, when combined, act as a curtain of high velocity gas using relatively low gas flows. To vector the gas flows in the desired direction, there is a concentric ridge included on the lower face to act as a radial flow restrictor.

A jet of gas can be said to be ‘stiff’ over a length ~20 times the diameter of the nozzle it originates from.^[58] From an 18 µm nozzle, this would equate to stiffness over 360 µm. For the two curtain gas to be effective, the cell must float above the sample at a ‘working distance’, *i.e.* the separation between the sample surface and the bottom of the flow restrictor, less than this; thus, 200 µm was chosen as a round figure that would ensure sufficient stiffness for effective operation.

It was the intention to use this cell as a simultaneous sampling device for both quantification and identification of (metallo)-biomolecules; consequently, two output channels are included, one for an ICP-MS and one for a bio-organic mass spectrometer. These channels are placed opposite each other to allow maximum separation of MALDI and LA, as LA samples could clog up MALDI instrumentation. Scoping studies were carried out to assess the viability of using a 213 nm UV LA laser for MALDI, as described later; however, much of the development of the cell focussed on elemental analysis using one output channel.

The laser beam is delivered to a sample through an anti-reflection coated optical window. To minimise development costs, window geometry was chosen that matches that used in the current NWR Universal Platform (UP) standard cell. The optical window has a diameter of 2 in. with a thickness of 1/8 in. (CVI Laser Llc., Albuquerque, NM, USA). A recess for the window in the top of the non-contact cell was thus built around these dimensions. Gas sealing was provided by two o-rings, one above and one below the window. The window is then held in place by the top plate, which is screwed into the top of the main body. A rendered exploded view is shown in Figure 4.3 below.

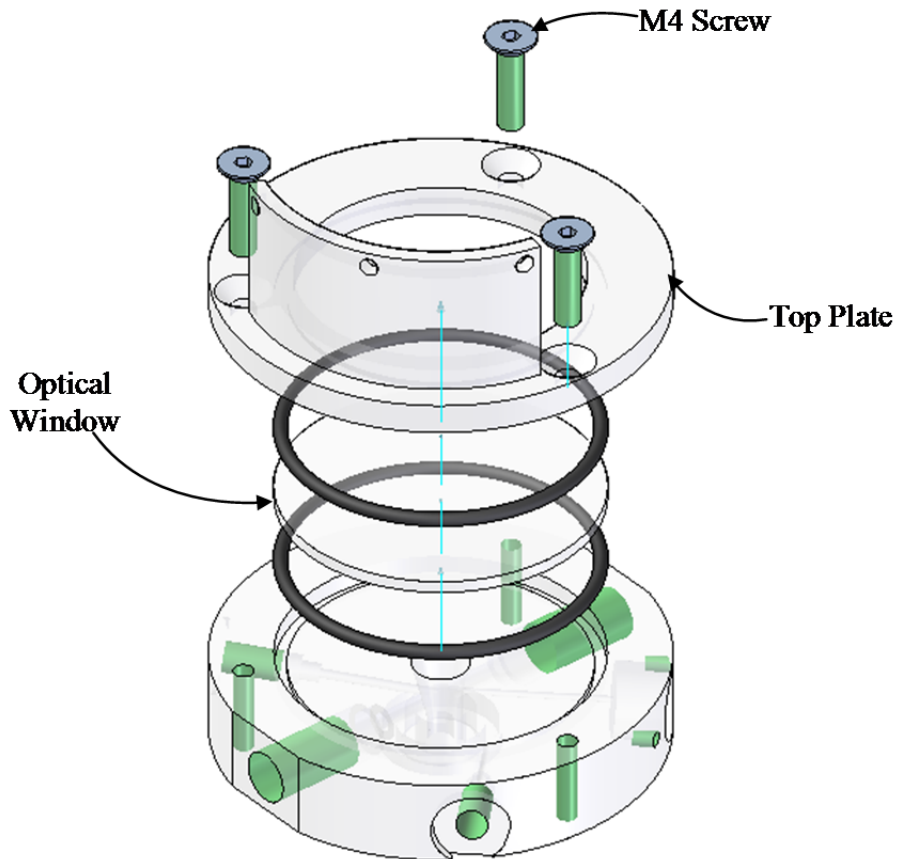


Figure 4.3: Rendered exploded view of the main body, top plate and optical window assembly

The top plate is the attachment point onto the UP laser ablation system. A modified objective lens mount was designed, incorporating a lip that accepts three M3 bolts through the three holes at the top of the vertical projection on the top plate. A rendered exploded view of this is shown in Figure 4.4 below.

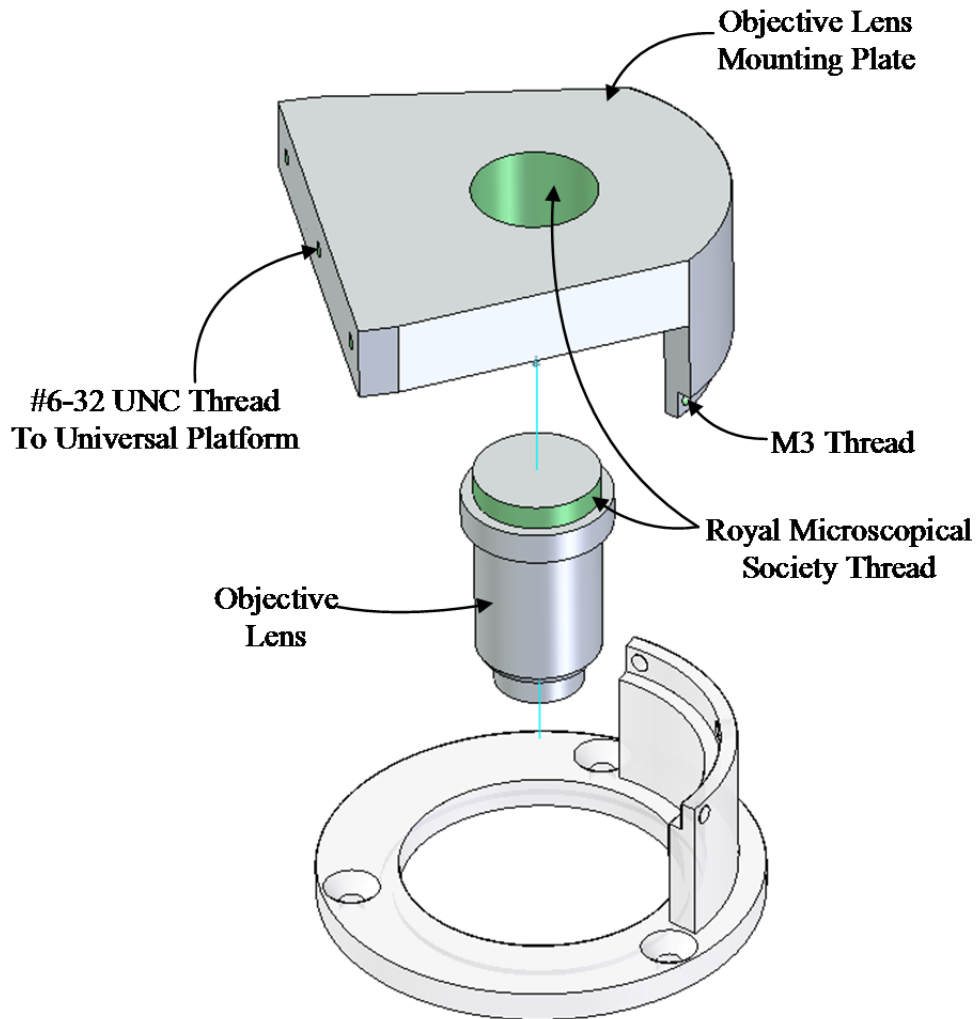


Figure 4.4: Rendered exploded view of the objective mount plate assembly

The objective lens used with the non-contact cell is an 8× zoom lens with a focal distance of 19.2 mm and a 29.5 mm body. The cell is designed to be mounted directly to the z-axis of the UP-213 platform, initially with the lower plane of the objective lens touching the upper plane of the optical window; however, this would have resulted in damage to the anti-reflection coating on the optical window by friction on assembly.

The heights of the attachment arms on the top plate and mounting plate were set to allow a 1.5 mm gap between the lens and the window; hence, this means the height main body is constrained to 16.7 mm allow a 200 μm gap between the lower plane of the flow restrictor and the sample surface. This means that the working distance can be set by focus rather than physical measurement.

It was desirable, however, to test more than one working distance, so an additional test top plate was manufactured from PMMA to increase the distance between the lens and the optical window. This window did not include a 1 mm window recess with an o-ring groove (shown in Appendix D, Page D-9), which raised the focal plane by 1 mm. By unscrewing the lens, the focal plane could be tuned to any working distance set by other means, *e.g.* a calibrated feeler gauge.

The meshes were initially tested for ease of assembly and cleaning. This involved applying a thin bead of silicone rubber gel (Bostik, Stafford, UK) to the main body of the cell. The meshes were then applied to the main body and left to set (see Figure 4.5 below).

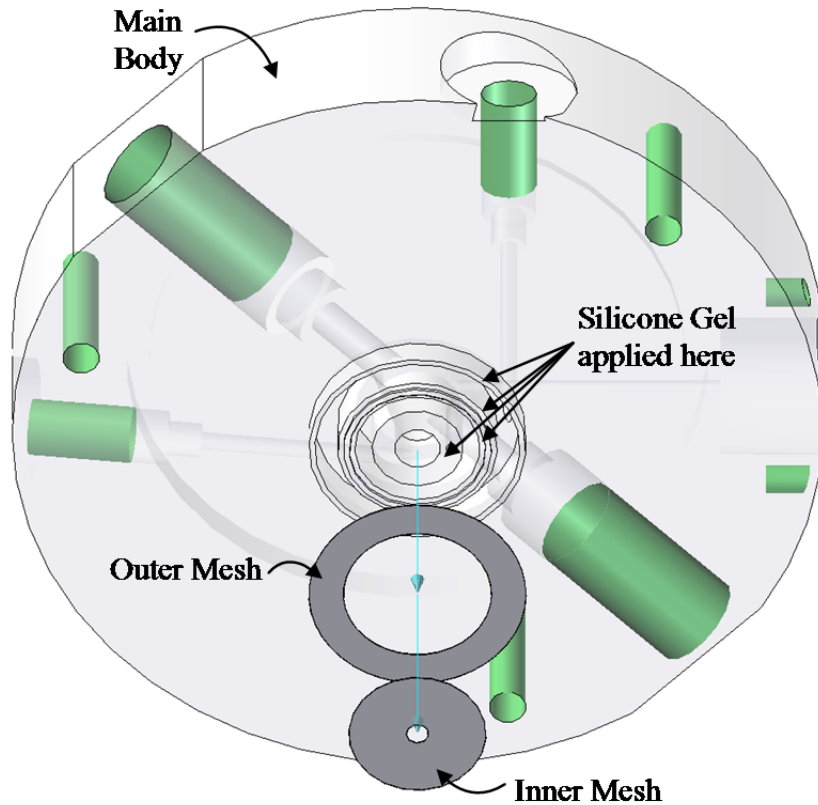


Figure 4.5: Main body of the non-contact cell showing installation of mesh components (revision G)

The assembly process was not reproducible and the meshes leaked around the joints. Removal of the mesh also proved difficult, resulting in bent meshes that exacerbated the leaks. For these reasons, the gas channel outlet area was redesigned to incorporate a screw thread on the outside of the channels that accepts a mesh permanently mounted to a screw-ring (see Figure 4.6 below).

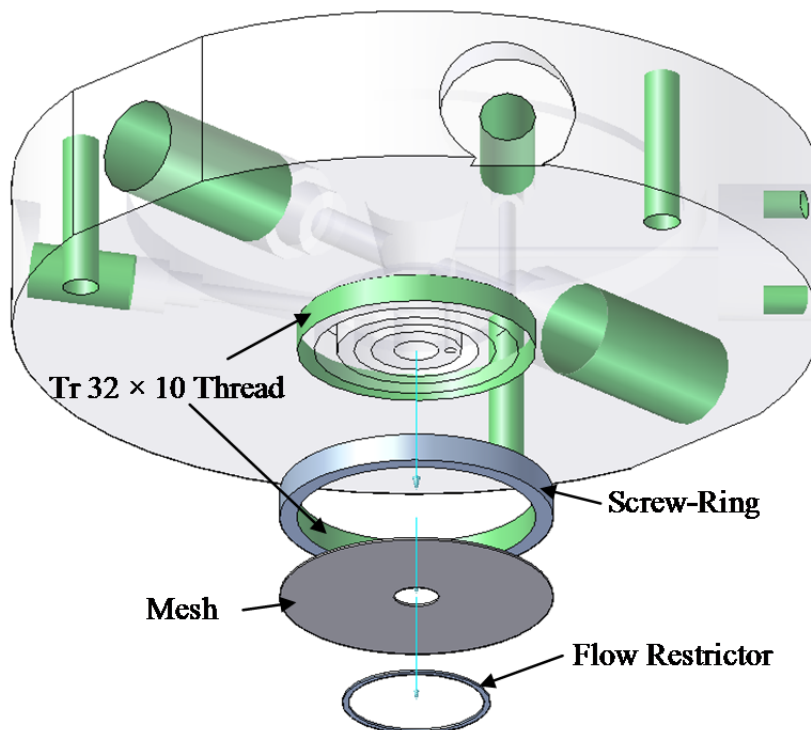


Figure 4.6: Rendered exploded view of the redesigned mesh assembly (revision H)

The main body was modified by gluing a metal ring, with the thread incorporated, to the main body around the channel outlet area using epoxy resin. The mesh and flow restrictor were both manufactured by Electro-Discharge Machining (EDM), also known as Wire Erosion (True Spark, Swadlincote, UK), and laser cutting (Preci-Spark Ltd, Loughborough, UK).

The flow restrictor was glued to the mesh using epoxy resin and a purpose built alignment tool.

Silicone rubber sealant was again used on the main body to seal the channels from each other, which provided adequate sealing and ease of disassembly for cleaning purposes.

To improve ion transmission in MALDI experiments, the option to electrically ground/bias the mesh is provided. The electrical connector is a Mini-BNC panel jack, chosen as the bayonet coupling provides a secure connection. With this connector, RF frequencies can also be sent along the connecting wire so a pulsed voltage program, such as the PDF program described by Tan *et al.*,^[31] can be used to further improve ion transmission.

The BNC connector is attached to the main body, within a recess, by a custom bracket. To keep the system gas-tight, a PTFE collar is used with the same diameter as the BNC recess, with a double o-ring gas seal. A rendered exploded view of this is shown in Figure 4.7 below.

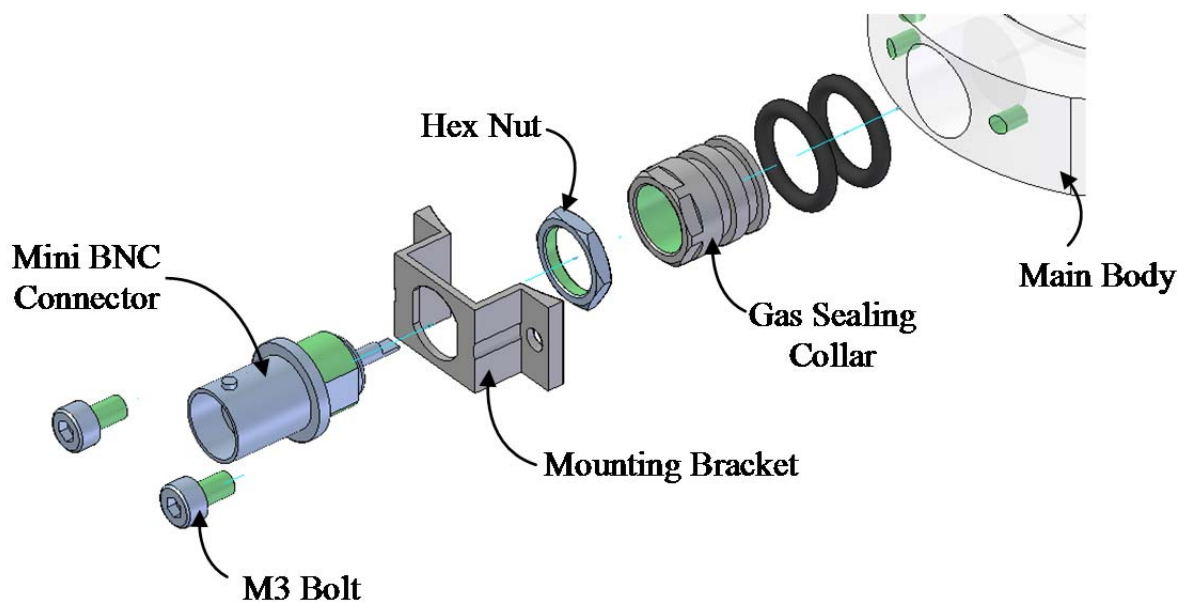


Figure 4.7: Rendered exploded view of the BNC ground plane connector assembly attached to the side of the non-contact cell

4.2 Principle of Operation of the Non-Contact Cell

An image of the cross section of the non-contact cell is shown in Figure 4.8 below.

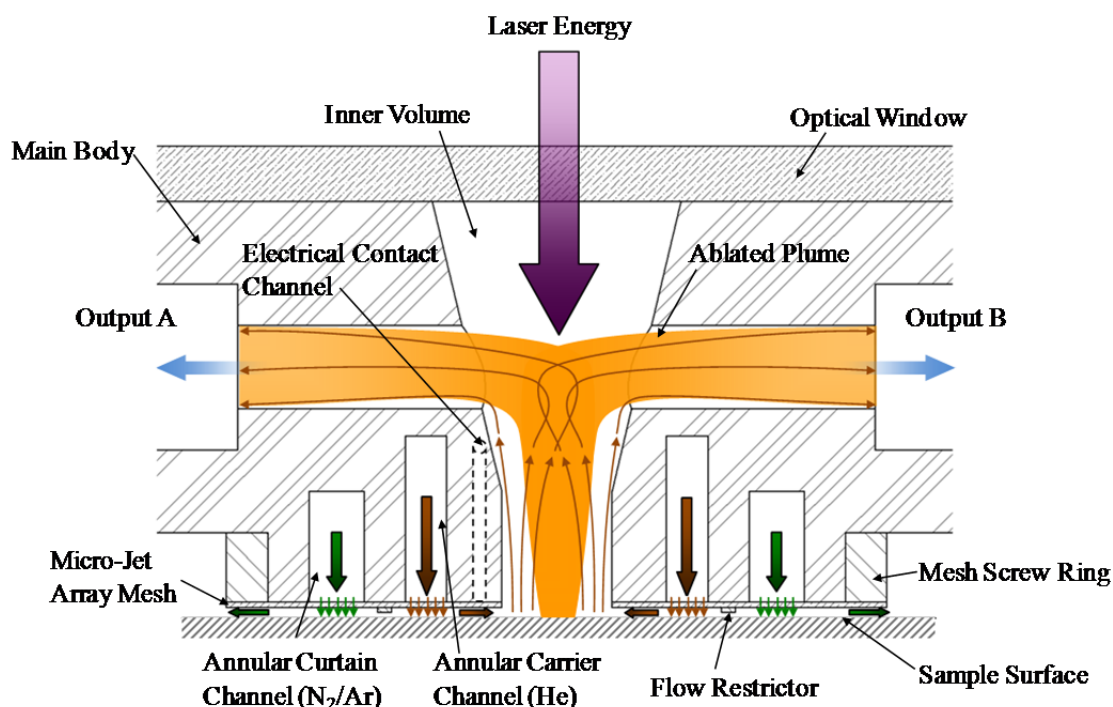


Figure 4.8: Cross section of the non-contact cell showing concentric inlet channels, inner cell volume, output channels and approximate direction of gas flow (Revision H).

The cell is floated above the sample surface and the lens of the laser ablation system is adjusted to focus an image of the aperture mask onto the surface. Imaging is preferred to focussing the the beam to a spot as different apertures can be used whilst maintaining constant fluence. Since the total height of the cell was calculated from the focal distance of the ablation system objective lens, having the sample in focus corresponds to a working distance of 200 μm .

Nitrogen (or argon) flows through the curtain channel and encounters the micro-jet array. Here, the nitrogen is forced through the 18 μm nozzles into high velocity micro-jets. The flow restrictor provides higher flow resistance radially inwards with respect to the curtain gas, so the nitrogen / argon flows radially outwards to atmosphere. This provides a momentum barrier to the atmosphere, and minimises its ingress into the central output channels.

Helium flows through the carrier channel and forms micro-jets through the micro-jet array nozzles. In this case, both the flow restrictor and the curtain gas provide higher flow resistance radially *outward* with respect to the carrier gas, so the helium flows radially inward into the inner volume of the cell.

The helium fills the inner volume (0.64 cm^3 effective volume in single channel mode, 0.86 cm^3 in dual channel mode) and flows through the output channel(s) to the analyser. Laser energy passes through the optical window to the sample surface and the subsequent ablated material is picked up by the helium and transported to the analyser.

4.3 Gas Dynamics through the Cell

The proceeding sections should be read in conjunction with Appendix B: An open, non-contact cell for laser ablation-inductively coupled plasma-mass spectrometry (Paper 2), which provides a description of the viability of the non-contact cell as an analytical tool.

The cell was mounted onto a UP-213 platform and tested for gas flows transmission and entrainment properties (see Figure 4.9 below). A plate of $20 \times 20 \times 0.4$ cm clear glass (to act as the sample – not shown below) was positioned underneath the cell at a distance of $200 \mu\text{m}$.

For initial testing, nitrogen was then passed independently through both channels at flow rates controlled by two independent Tylan mass flow controllers (Tylan General Inc, San Diego, CA, USA) and the output flow measured from one of the output channels using a soap film flow-meter (HP 0101-0113 – 1-10-100 graduated flow meter, Hewlett Packard Labs, Palo Alto, CA, USA). The gas output was measured in one output channel, with the other being blocked, as the cell will operate through one channel only in either ‘ablation’ mode or ‘MALDI’ mode.

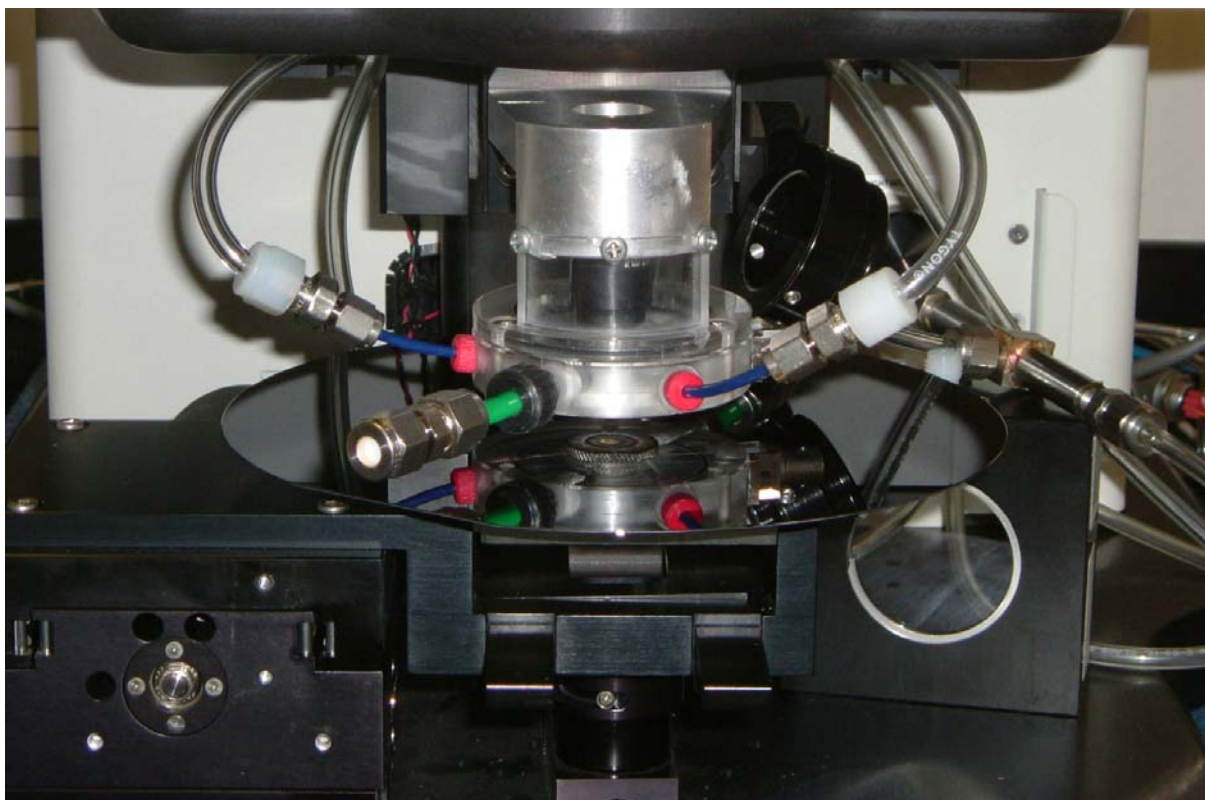


Figure 4.9: The prototype non-contact cell mounted on a New Wave Research UP-213 laser system floating above a 120 mm silicon wafer sample.

4.3.1 Effect of Input Flow Rate on Gas Transmission Efficiency

The sample-to-cell distance was set to 200 μm , measured from the bottom edge of the flow restrictor by feeler gauge, and the input flow rates altered. Three conditions were tested:

1. Dependence of output flow with carrier channel flow, curtain channel flow set to zero.
2. Dependence of output flow with curtain channel flow, carrier channel flow set to zero.
3. Dependence of output flow with both flows present.

4.3.1.1 Dependence of output flow with carrier channel flow, curtain channel flow set to zero.

The carrier channel flow rate was varied from 0.8 l min^{-1} to 1.6 l min^{-1} using a pressure regulator (Camozzi Series M non-relieving micro-regulator at 0 – 4 bar, Camozzi Pneumatics Ltd., Nuneaton, UK). As the input flow rate of the carrier channel was increased, the output flow rate increased, showing approximately 15% transmission of the carrier channel input (see Figure 4.10 below). The remainder of the gas vented radially to the atmosphere.

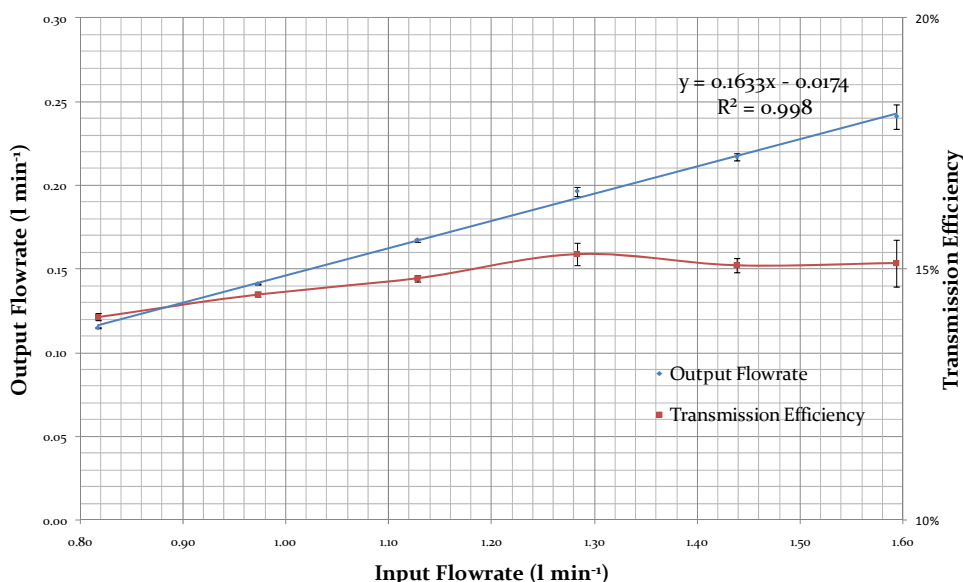


Figure 4.10: Output flow rate and transmission efficiency (relative to carrier channel flow rate) vs. carrier channel flow rate for the non-contact cell set at 200 μm above a planar sample surface and curtain channel flow set to zero. The output flow is consistently shown to be approximately 15% of the input flow rate from the carrier channel. (Error bars = 3σ)

4.3.1.2 Dependence of output flow with curtain channel flow, carrier channel flow set to zero.

The curtain channel flow rate was run at higher flow rates, varying from 1.6 l min⁻¹ to 2.5 l min⁻¹, which is typical of those that might be required to exclude atmospheric gases. Again, as the input flow rate of the curtain channel was increased, the output flow rate increased; however, the transmission efficiency in this case is only approximately 5% of the curtain channel input (see Figure 4.11 below). The preferred flow route for this gas is a radial flow outwards to the atmosphere.

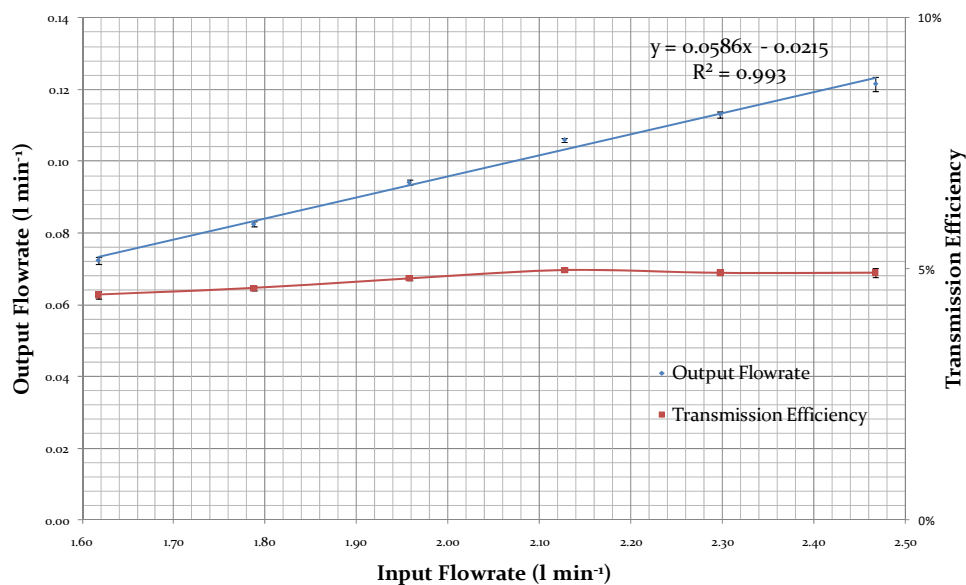


Figure 4.11: Output flow rate and transmission efficiency (relative to curtain channel flow rate) vs. curtain channel flow rate for the non-contact cell set at 200 μm above a planar sample surface and carrier channel flow set to zero. The output flow rate is approximately 5% of the input flow rate from the curtain channel. (Error bars = 3σ)

4.3.1.3 Dependence of output flow with both flows present.

The output of the cell using both flows is shown in Figure 4.12 below. With both channels delivering gas to the cell, the output of the cell ranged from 0.26 to 0.42 l min⁻¹. Using both flows, the efficiency was increased to between 24% and 36% of the carrier channel input flow (see Figure 4.13 below) for the 200 μ m working distance.

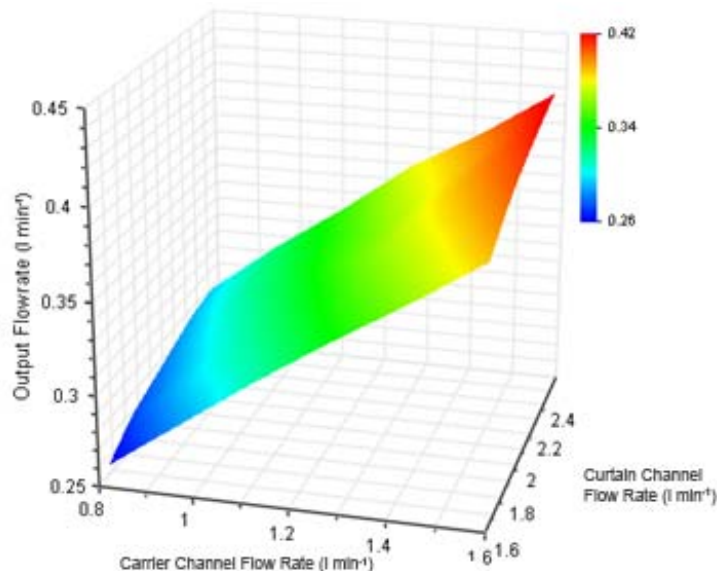


Figure 4.12: Output flow rate *vs.* carrier channel flow rate and curtain channel flow rate for the non-contact cell set at 200 μ m above a planar sample surface.

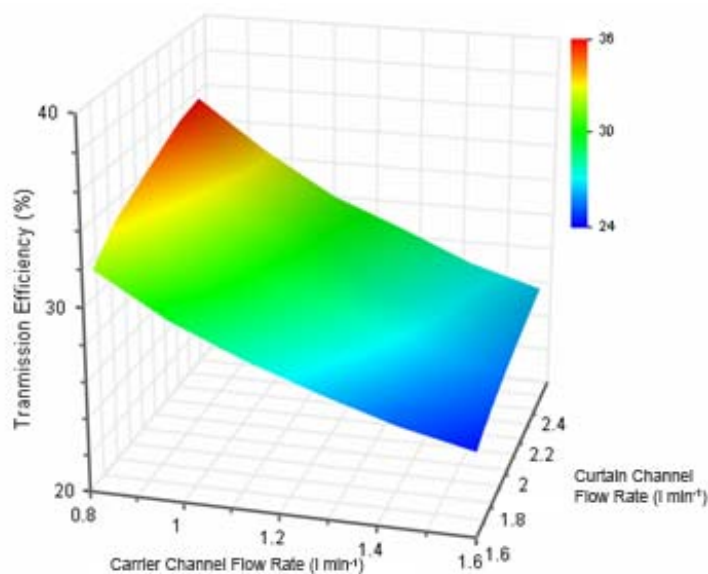


Figure 4.13: Transmission efficiency relative to total input flow *vs.* carrier channel flow rate and curtain channel flow rate for the non-contact cell set at 200 μ m above a planar sample surface.

The shape of both plots shows that the curtain channel flow promotes vectoring of the carrier channel flow through the sample chamber by increasing the flow resistance in the radial direction to atmosphere. However, an alternative explanation is that the apparent increase in efficiency was due to the 5% of curtain channel flow that was shown to enter the sample compartment when the central channel flow was zero.

To test this hypothesis, the output flow rates obtained when each channel was operated independently were added together at six chosen pairs of input flow rates (termed the ‘theoretical transmission’). The gas channels were then set to match these pairs and the output flow rates measured for comparison (termed the ‘measured transmission’). Figure 4.14 below shows the theoretical transmission versus the measured transmission.

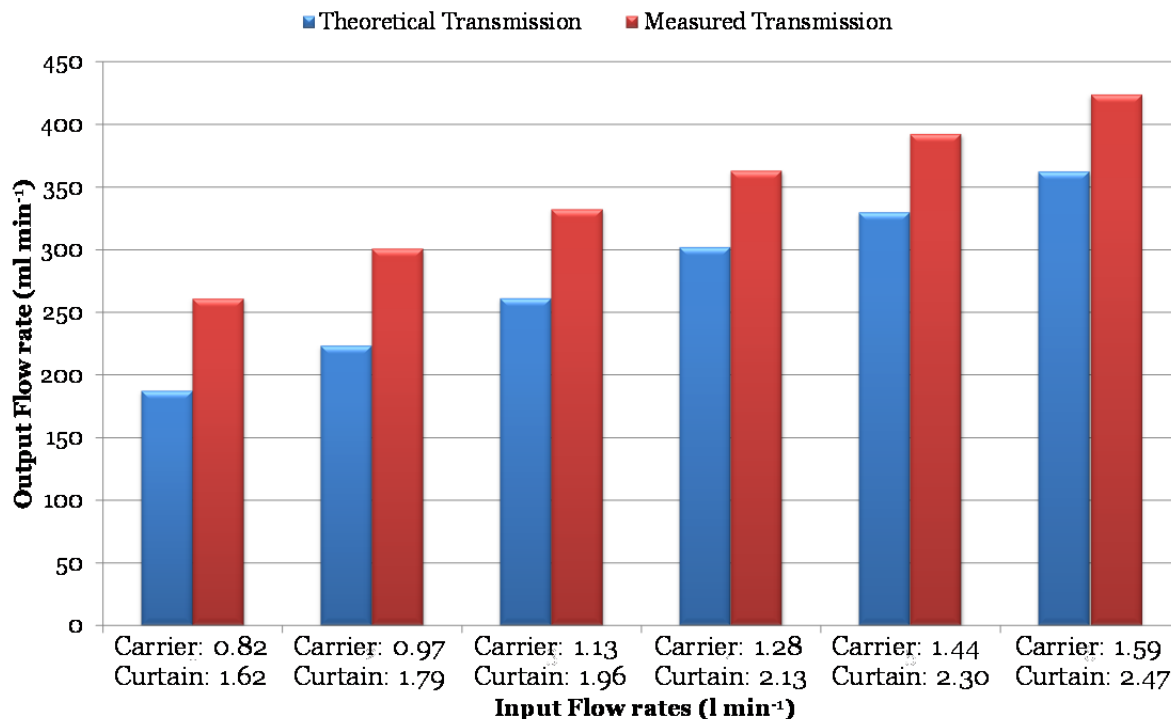


Figure 4.14: Theoretical and measured transmission through the non-contact cell at six pairs of curtain and carrier channel flow rates. Theoretical figures were calculated by choosing six curtain and six carrier flow rates, then adding together the output flow rates achieved when each channel was operated independently.

The measured transmission achieved through the NCC whilst both carrier and curtain flows were enabled was consistently higher than the calculated theoretical transmission. This indicates that whilst the curtain channel still may flow through the sample compartment, it does promote vectoring of the carrier channel flow by increasing flow resistance to atmosphere.

4.3.2 Gas Flow Composition Study

Since the increase in transmission efficiency demonstrated in Section 4.1.1 may have been in part due to the addition of curtain channel gas flow into the output channel, a gas mass spectrometer (Cirrus quadrupole Gas MS, MKS Instruments UK Ltd., Altrincham, Cheshire, UK) was used to determine the fractions of the output gas that were derived from the carrier channel, the curtain channel and atmospheric gases.

The carrier channel was fed with argon, since the gas mass spectrometer was not calibrated for helium, and the curtain channel with nitrogen to distinguish between the two channels. The partial pressures of nitrogen, argon and oxygen were then measured, which gave the fractions coming from the curtain channel, the carrier channel and atmospheric gases respectively.

Initially, the carrier channel was varied from 0.8 to 1.6 l min⁻¹ with the curtain channel fixed at 2.5 l min⁻¹. The fraction of nitrogen and oxygen being entrained into the output channel was found to be less than 0.04 % for nitrogen, and less than 0.005 % for oxygen. This shows that rather than significantly adding to the output flow, the curtain channel flow increases the radial flow resistance hence assisting the carrier channel flow through the sample compartment and to the output channel. Entrainment of the curtain channel may occur at higher flow rates through momentum exchange in the turbulent flow created at the interface between the gas flows and the sample surface.

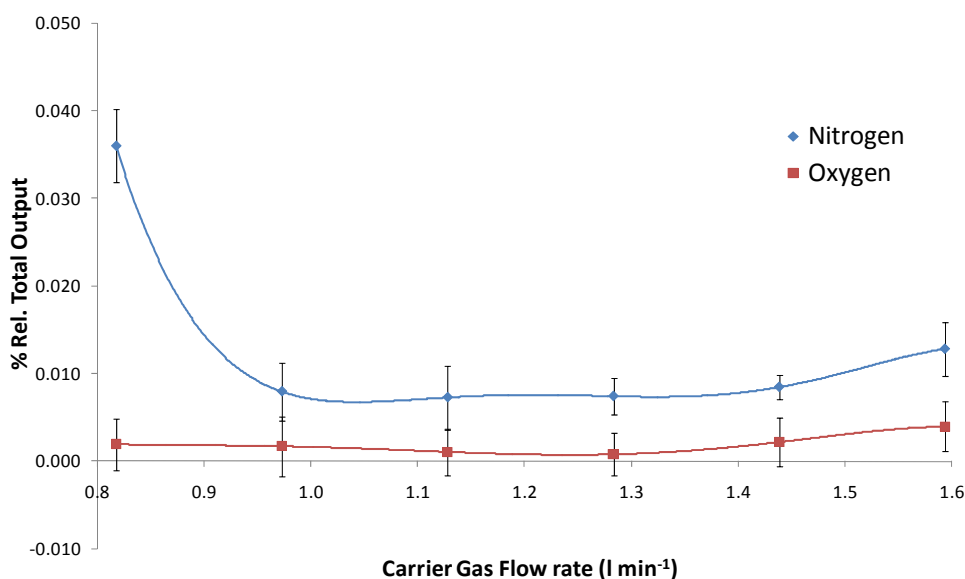


Figure 4.15: Nitrogen and oxygen content of the output flow *vs.* carrier channel flow rate for the non-contact cell set at 200 μm above a planar sample surface and the curtain channel set to 2.5 l min⁻¹.

Fixing the carrier channel input flow to 1.6 l min^{-1} and increasing the curtain channel flow rate showed that the amount of nitrogen entrained in the output flow reached significant levels at curtain channel flow rates above 6 l min^{-1} (see Figure 4.16 below). The amount of oxygen entrained remained negligible. Combined with Figure 4.15, this suggests the cell excludes atmospheric gases from the system through a large input flow rate range. As the cell is unlikely to be run at curtain channel flow rates above 3 l min^{-1} , this also shows the separation between inner and curtain channels is sufficient to ensure nitride generation in the plasma is kept at low levels.

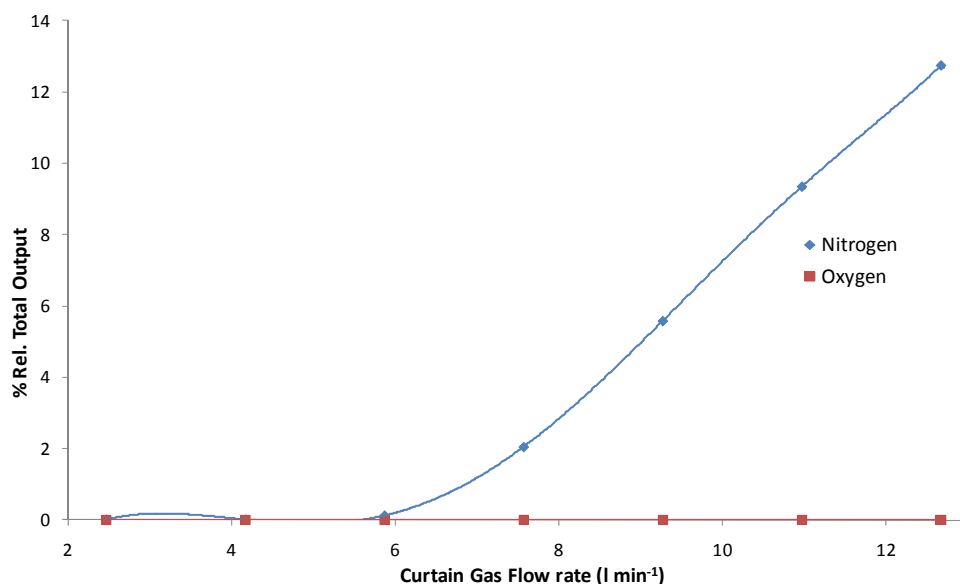


Figure 4.16: Nitrogen and oxygen content of the output flow *vs.* curtain channel flow rate for the non-contact cell set at $200 \mu\text{m}$ above a planar sample surface and the carrier channel set to 1.6 l min^{-1} .

Helium is a much lighter gas than argon and ingress of nitrogen is likely to occur at lower curtain channel flow rates; however, it must be noted at this stage that in 1994 Durrant^[59] reported enhancement of elemental signals in LA-ICP-MS using nitrogen in the cell sweep gas. Using a Ruby laser at 1 Hz coupled to a prototype quadrupole ICP-MS system, it was found that addition of approximately 12.5% N_2 into the cell sweep gas resulted in around 150% increase in signal intensity for cerium response.

Hirata and Nesbitt^[60] also reported an ‘increase in sensitivity’ measuring U-Pb ratios in zircons by adding nitrogen to cell sweep gas, using a 266 nm Nd:YAG laser at 6.5 Hz coupled to a quadrupole instrument, although the degree of enhancement was not reported. Whilst too much nitrogen may destabilise the plasma, total exclusion may not be necessary as signal enhancement could occur.

4.3.3 Effect of Cell Distance to Sample on Gas Transmission Efficiency

The distance between the sample and the cell was varied from 200 μm down to 38 μm using feeler gauges to assess the effect on gas transmission efficiency. The output flow rate was measured under two conditions:

1. Carrier channel input flow rate varied from 0.8 to 1.6 l min^{-1} with the Curtain channel switched off
2. Carrier channel input flow rate varied from 0.8 to 1.6 l min^{-1} with the Curtain channel Flow rate switched on and set to 2.5 l min^{-1}

The output flow rate increased as the sample-to-cell distance decreased (see Figure 4.17 below). As the cell approached the surface of the work piece, the efficiency of the flow restrictor in preventing radial flow of the carrier channel flow to atmosphere (and probably curtain channel flow leakage in to the carrier channel flow) increased.

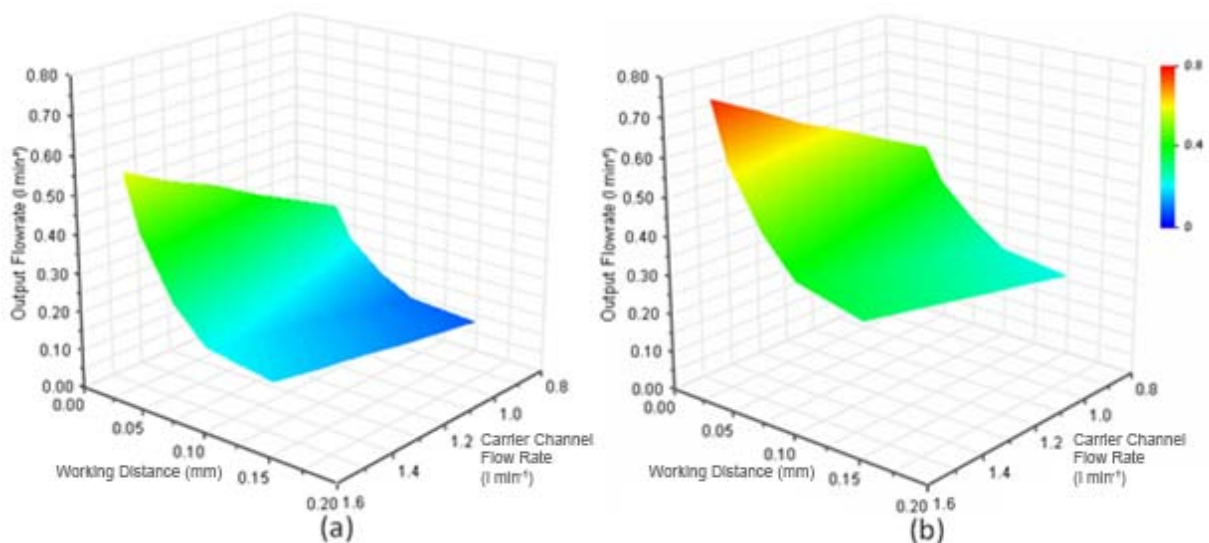


Figure 4.17: Output flow rate vs. carrier channel flow rate and sample-to-cell distance with (a) curtain channel switched off and (b) curtain channel switched on at 2.5 l min^{-1} .

With the flow assistance afforded by the curtain channel, the output flow again increased significantly. A surface plot of transmission efficiencies (see Figure 4.18 below) shows that the level of assistance varied with carrier channel flow rate. With higher carrier channel flow rates, the carrier channel gas was able to overcome some of the extra resistance provided by the curtain channel flow rate, thus resulting in the slight curvature in the surface plot.

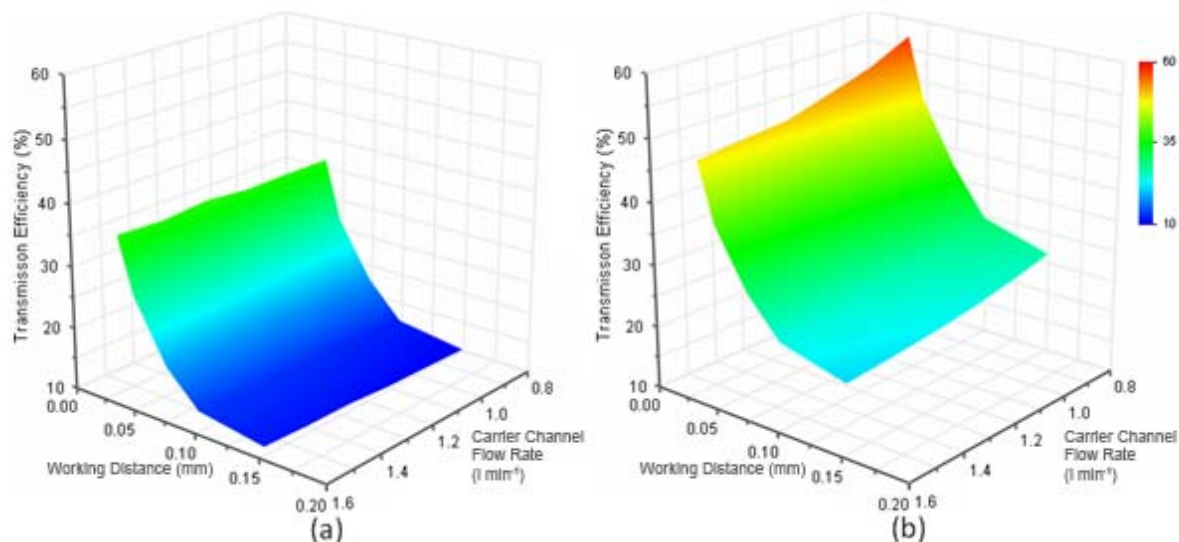


Figure 4.18: Transmission efficiency (relative to total flow) *vs.* carrier channel flow rate and sample-to-cell distance with (a) curtain channel switched off and (b) curtain channel switched on at 2.5 l min⁻¹.

To increase the transmission efficiency of the inner gas flow through the sample compartment, assistance downstream from the cell arising from a pressure gradient was considered. The device used to create this pressure gradient could also be used to mix the cell gas with argon make-up gas before entry into the ICP torch, much like the cross-flow nozzle arrangement in the Pisonero HEAD cell.^[38] For this reason, a nebuliser driven by argon was considered.

The nebuliser chosen was a Conikal Nebuliser with a 1 ml min⁻¹ liquid uptake capacity (Glass Expansion, Melbourne, Victoria, Australia), but here with the liquid intake capillary connected to the output port of the non-contact cell. The pressure of argon gas supplied to the nebuliser was varied and the output of the cell measured. The optimum settings for the cell were chosen, i.e. cell height above the work piece was set at 38.1 μm and the inner and outer gas flows set to 1.6 and 2.5 l min⁻¹ respectively.

The nebuliser was tested under three conditions:

- Driven by argon with the uptake channel blocked to assess the amount of gas in the output provided by the driving gas (nebuliser flow)
- Driven by argon with the uptake channel open to atmosphere to assess the free entrainment of the uptake channel (nebuliser flow + free entrainment flow)
- Driven by argon with the uptake channel connected to the cell output to assess the effect of the nebuliser on the cell output (nebuliser flow + cell output flow)

Figure 4.19 shows the flow from the nebuliser under the three conditions.

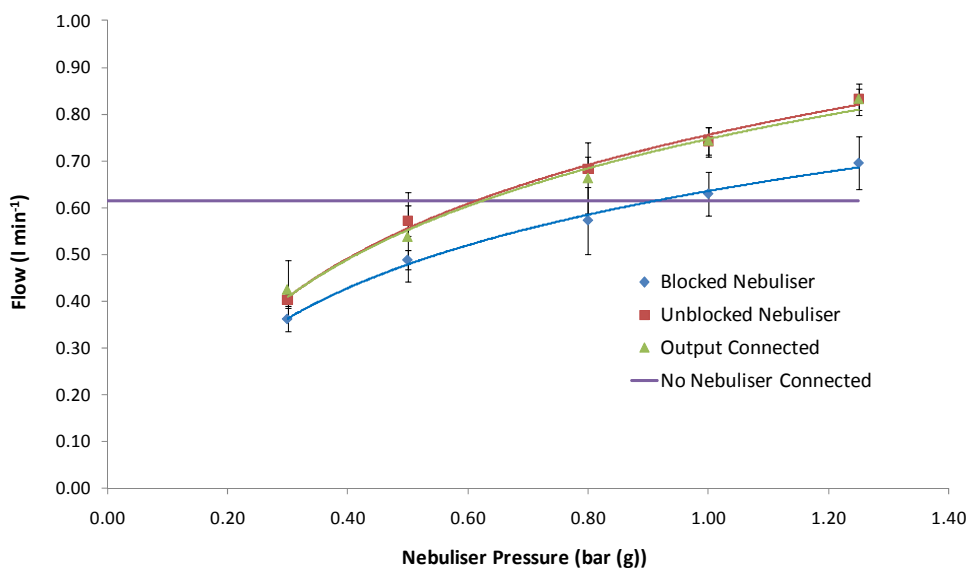


Figure 4.19.: Output flow rate vs. nebuliser driving pressure for a Conikal nebuliser with a 1 ml min⁻¹ liquid uptake capacity.

Under the conditions chosen, the cell normally has an output of approximately 615 ml min^{-1} (unassisted cell output flow). With the nebuliser in place downstream of the cell, the output flow is forced to match the free entrainment flow of the nebuliser and the flow through the cell is restricted to about 100 ml min^{-1} , this being the maximum flow conductance of the nebuliser central channel before significant back pressure is produced in the cell chamber. This is illustrated in Figure 4.20 below.

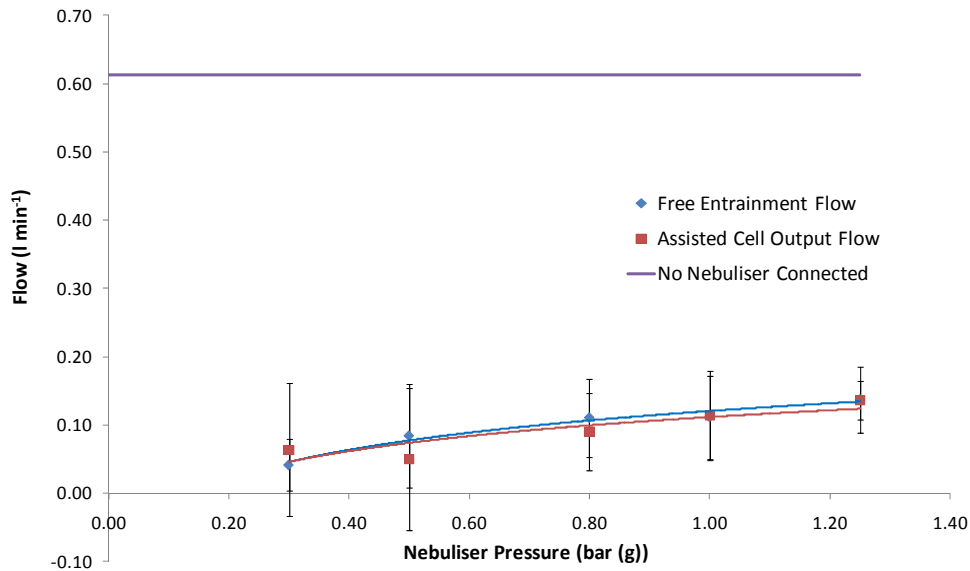


Figure 4.20: Adjusted output flow rate *vs.* nebuliser driving pressure for a Conikal nebuliser with a 1 ml min^{-1} liquid uptake capacity.

An additional drawback of using a concentric nebuliser as a gas pump is the high probability of inducing a blockage in the system when conducting ablated material through the narrow central channel. To circumvent this, a 'micro jet-pump' was used. This consists of a free turbulent jet of gas being directed into a throat, this being followed by a diffuser (see Figure 4.21 below). The purpose of the throat is to ensure that the gas entrained into the free turbulent jet comes from the output of the cell, as without the throat driving gas can be re-entrained from further down the output channel by small reverse flow eddy currents.

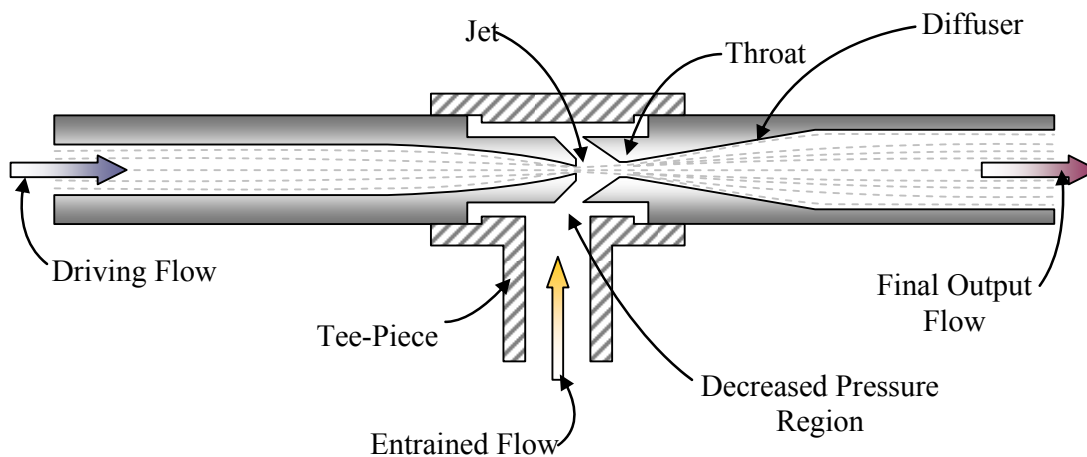


Figure 4.21: Schematic of a cross flow jet-pump.

The jet used originates from an orifice 0.254 mm in diameter, using argon as the driving gas. This was chosen as it is the normal gas used in the ICP and conveniently is the heaviest gas out of nitrogen, helium and argon (the three gases to be used in the cell setup), and as such, using the principle of conservation of momentum, should enable a significant amount of helium to be entrained by the jet-pump.

The resultant pressure gradient produced by the free turbulent jet is dependent on both the driving flow input pressure and the distance between the jet and the throat. Initially, the pressure gradient was measured at varying orifice-to-throat separations using a simple mercury manometer at varying input pressures. A surface plot of the negative pressure difference relative to atmospheric pressure in the free jet region is shown in Figure 4.22 below. The plot shows an optimum separation of approximately 3.5 mm in reference to where the two halves of the jet-pump touch.

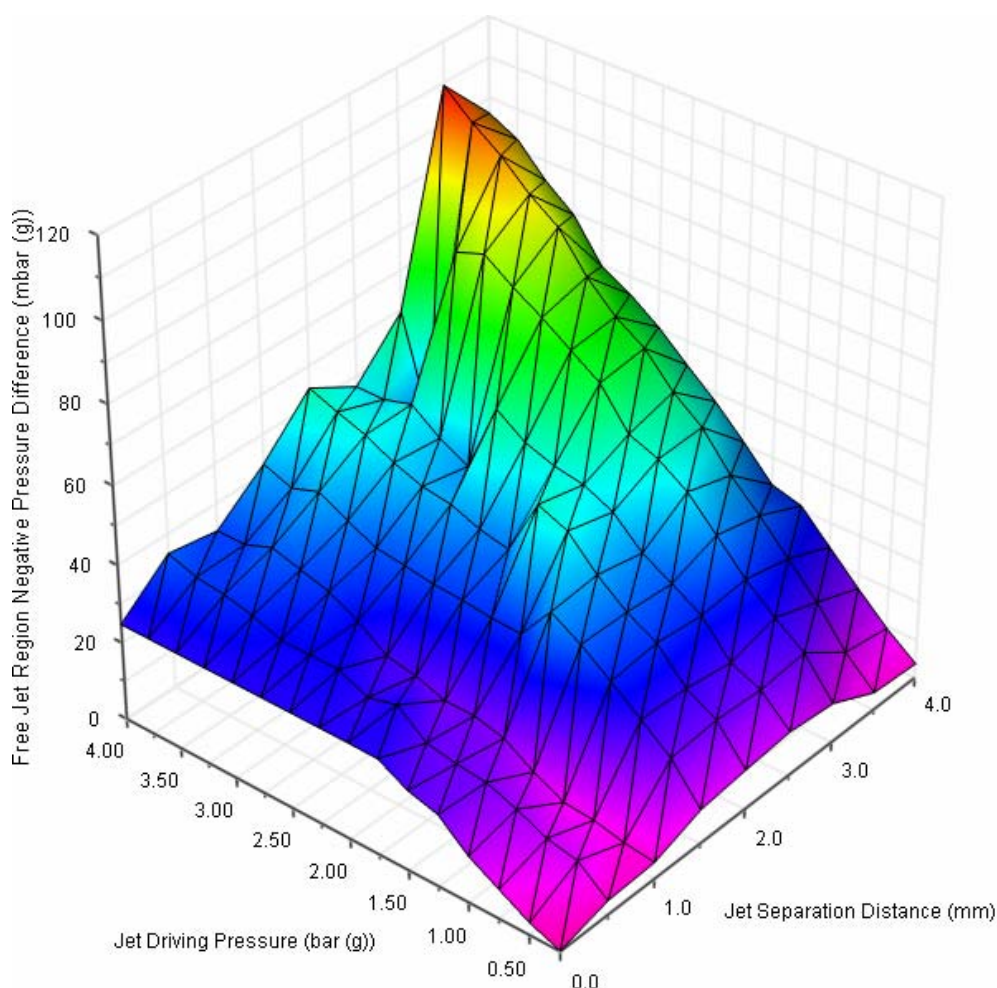


Figure 4.22: Jet-pump negative pressure difference vs. argon driving flow pressure and jet-to-throat separation using a 254 μm jet nozzle.

It is of interest to note that there are regions where the jet pressure drops as the driving pressure increases. The pressures at which these occur are dependent on the separation of the jet-pump pieces, and are accompanied by an audible change in tone of the free jet. This is due to the throat being positioned in the centre of a 'zone of silence', created by shockwaves in the free turbulent jet. There are many of these zones in the turbulent jet, as investigated previously by Sharp,^[58] and varying the input pressure varies the position and size of the zones relative to the jet orifice.

For constant flow and entrainment potential, the separations and pressures used must be unaffected by a zone of silence, which appears to occur at approximately 3.5 mm separation relative to the two parts of the jet-pump touching. This corresponds to an absolute jet-to-orifice separation of 5.30 mm.

The cell was setup with the optimum flow conditions and the jet-pump assessed for flow assistance, similar to the concentric nebuliser. The conditions tested were:

1. Driven by argon with the uptake channel blocked to assess the amount of gas in the output provided by the driving gas (free jet flow)
2. Driven by argon with the uptake channel open to an atmosphere of helium* to assess the free entrainment of the jet-pump (free jet flow + free entrainment flow)
3. Driven by argon with the uptake channel connected to the cell output to assess the effect of the jet-pump on the cell output (free jet flow + cell output flow)

Figure 4.23 below shows the total output flow rates under the three conditions.

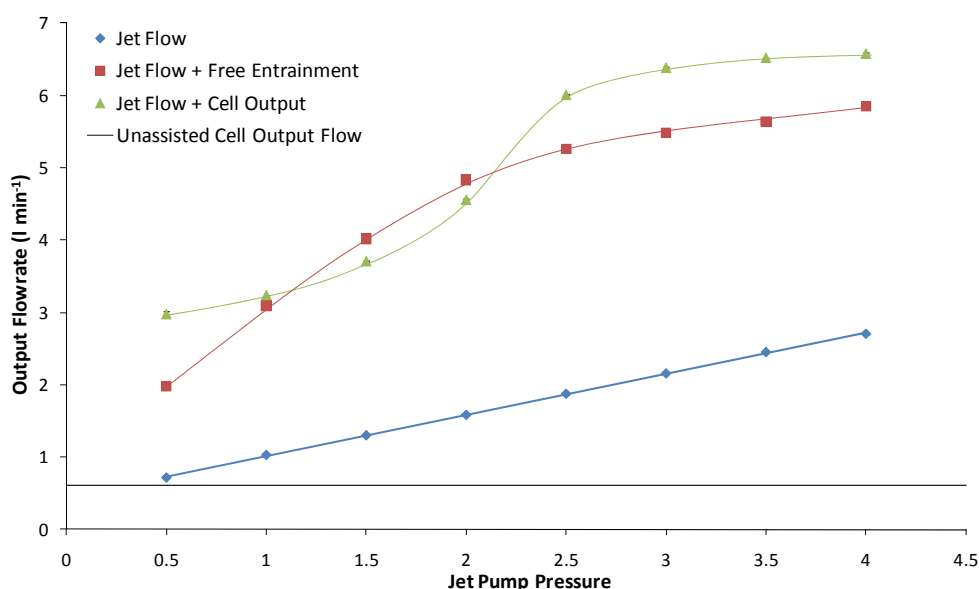


Figure 4.23: Output flow rate vs. jet-pump driving pressure for a jet-pump with a 254 μm nozzle.

Again, the NCC has an unassisted output flow rate of approximately 615 ml min⁻¹. Attaching the cell to the jet-pump increases the output of the cell to between 3 and 6.5 l min⁻¹. The entrainment flows are shown in Figure 4.24 overleaf. The free entrainment of helium shown yields an optimum jet-pump operating pressure of approximately 2.5 bar (g).

After this point, two possible effects are evident. The eddy currents produced by the turbulent jet cause the entrainment efficiency to decrease as they both disrupt the position of shockwaves in the tee-piece of the micro jet-pump and leak argon into the uptake entrainment channel counter-flow to the cell output.

* The helium atmosphere was provided from a 2 l volumetric flask. The flask was filled with helium, inverted and the neck submerged under water. The uptake channel of the micro jet-pump was connected *via* a ball valve to a long piece of polyurethane tubing, which was inserted into the flask via the neck to sample from the top. As the volume of helium decreased, water was drawn into the flask, thereby reducing the volume and keeping the pressure constant (at 1 atm).

For the cell output, for operating pressures above 2.5 bar (g), the same trend is followed. Below this there is a slow increase in entrained helium with operating pressure, which then suddenly jumps exponentially to a maximum at around 2 – 2.5 bar(g).

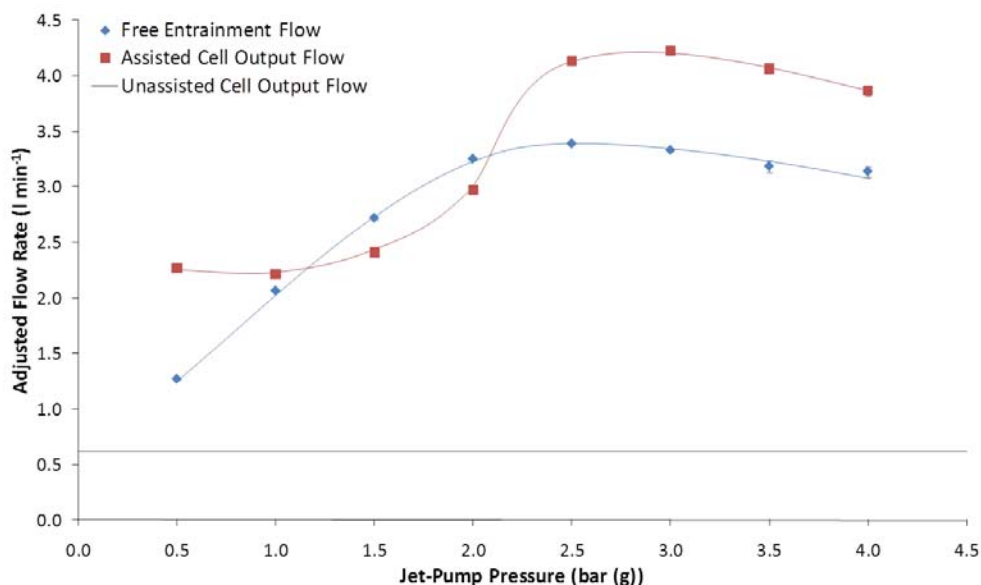


Figure 4.24: Adjusted output flow rate vs. jet-pump driving pressure for a jet-pump with a 254 μm nozzle.

The unexpected shape of the assisted cell output flow can be attributed to the fact that the entrained flow under these conditions is a mixture of helium and nitrogen instead of pure helium as in the free entrainment flow. The propagation of sonic shockwaves (and hence, the zones of silence) is dependent on the driving pressure and gas composition, and for every combination of these parameters there will be an optimum separation of the free jet and the throat.

Since the separation of the jet-pump was optimised and set under a helium atmosphere, the optimum separation between the jet and the throat is different under the assisted cell output conditions. It is likely that the difference in density between the two conditions results in a difference in the negative pressure achieved in the body of the micro jet-pump, and consequently a difference in the amount of cell flow ultimately entrained.

The unassisted cell output of 615 ml min^{-1} corresponds to a transmission efficiency of 15% of the total input flow (nitrogen and helium). At the lower jet-pump driving pressures, the assisted flow showed an increase to 55% of the total input flow. As the helium flow itself only corresponds to 40% of the total input flow, this suggests all of the carrier channel helium was entrained in the output channel, with additional flow from the nitrogen being entrained (approximately 25% of the nitrogen input). At the higher jet-pump driving pressures, this efficiency increases to approximately 105% of the total input flows of helium and nitrogen, which suggests the jet-pump was entraining all of the helium, all of the nitrogen and some atmospheric gases.

The usual flow rate in the central channel of an ICP torch is $\sim 800 \text{ ml min}^{-1}$. To run at similar flow rates, the jet-pump will be run at 0.25 – 0.5 bar (g), which will provide 100% transmission of the carrier channel and 25% of the curtain channel. The consequential total flow will be in a turbulent flow regime, which brings a possibility of destabilising the ICP

torch. To combat this, the flow will have to be converted into a laminar flow by passing through a conduit before entering the central channel of the torch, *i.e.* a short length of tubing. In practice this is provided by the delivery tubing and the capillary injector (typically 30 x 1.8 mm) in the ICP torch.

4.4 Performance Testing: Transport Efficiency and Raw Signal Intensity

To compare the non-contact laser ablation cell with the New Wave Research Universal Platform Standard Cell, a UP-213 Laser Ablation system (New-Wave Research, Fremont, CA, USA) was fitted with the non-contact cell and coupled to a High Resolution Element XR Sector Field (SF) ICP-MS (Thermo Scientific, Bremen, DE). The cell was tested using a National Institute of Standards and Technology Certified Reference Material (NIST CRM-613: Trace Elements in Glass), and a section of silicon wafer.

The NIST CRM was tested for ^{232}Th , ^{238}U and their respective oxides. Both elements are present in the CRM at a certified level of approximately 35 ppm. There are no isobaric interferences for these elements, but they do form oxides in the ICP. The oxide levels are therefore a good indication of how much oxygen is being entrained by the cell, and how much signal is being lost to oxide formation. A silicon wafer section was screened for ^{31}P , as this is a major element of interest in the semiconductor industry. Because ^{31}P has a major molecular interference from $^{31}\text{NOH}^+$, this was analysed at medium resolution ($m/\delta m = 4000$).

4.4.1 NIST CRM-613

The CRM was initially tested using the standard cell, followed by testing using the non-contact cell set at a distance of 200 μm above the sample surface. The optimised instrument settings used are summarised in Table 4.1 below.

Table 4.1: LA-ICP-MS Settings for the validation of the non-contact cell on the UP-213 laser ablation system.

ICP-MS Settings				
<i>Torch Settings</i>		<i>High Resolution Lens Voltages</i>		
Cool Gas Flow	15.5 l min ⁻¹	Rotation Quad 1	0.37 V	0.22 V
Auxiliary Gas Flow	0.88 l min ⁻¹	Rotation Quad 2	0.22 V	2.60 V
Plasma Power	1250 W	Focus Quad 1	-0.07 V	-8.00 V
		Focus Quad 2	0.12 V	0.12 V
	<i>Standard Cell Non-Contact Cell</i>			
Sample Gas Flow	0.80 l min ⁻¹	0.64 l min ⁻¹	<i>Detector Voltages</i>	
Torch x-position	5.1 mm	5.2 mm	Matsuda Plate	60.01 V
Torch y-position	2.6 mm	3.1 mm	SEM-Deflection	700 V
Torch z-position	-1.2 mm	-0.4 mm	SEM	1700 V
<i>Lens Voltages</i>				
Extraction Lens	-2000 V			
Focus Lens	-1536 V			
X-Deflection	-2.23 V			
Y-Deflection	-2.24 V			
Shape	120 V			
Laser Ablation Settings				
	<i>Standard Cell</i>	<i>Non-Contact Cell</i>	Laser power	
Sweep Gas	0.42 l min ⁻¹	N/A	85 %*	
Inner Channel Gas	N/A	1.59 l min ⁻¹	Laser head output	
Outer Channel Gas	N/A	2.45 l min ⁻¹	2.5 mJ	
Jet-Pump Pressure	N/A	0.25 bar g	Laser Warm-up time	
Laser Spot Size	65 μm		5 s	
Frequency	20 Hz		Line-Scan Scan-rate	
			20 $\mu\text{m s}^{-1}$	
			Spot-Line Dwell Time	
			10 s	
			Spot-Line Intersite Pause	
			30 s	
			Manual Trigger Offset	
			10 s	

* This system did not have a real-time energy meter; hence, there was no reading for surface fluence.

From Figure 4.23, applying 0.5 bar (g) to the driving flow of the micro jet-pump results in a total central channel flow of approximately 3 l min⁻¹. This high flow can cause both instability in the plasma and also cool the central channel, thereby reducing the ionisation efficiency of the ICP. An acceptable central channel flow for LA-ICP-MS experiments uses a total flow of approximately 1.2 l min⁻¹, comprising 50% - 60% helium.

With this particular jet-pump configuration, it was decided that a minimum driving flow would be sufficient to efficiently entrain the cell output flow at the required level. For this reason, the jet-pump pressure was set at a minimum to give a stable jet flow, which was at 0.25 bar (g) with the regulator in use (Camozzi Series M non-relieving micro-regulator at 0 – 4 bar, Camozzi Pneumatics Ltd., Nuneaton, UK); however, this still resulted in a central channel flow totalling approximately 1.8 l min⁻¹.

The laser power was tuned for ablation yielding the highest sensitivity using the standard cell with the above settings. The signal intensity and relative standard deviations for ²³²Th and ²³⁸U were measured at differing laser power. The results of the tune are shown in Figure 4.25 below.*

The chart shows the greatest signal achieved was in the region of 80% to 90% full power. A compromise between absolute sensitivity and the relative standard deviations for both uranium and thorium was chosen at 85% full power. This laser power was to be used for all subsequent analyses of the NIST glass.

The wash-in and wash-out times of the non-contact cell were compared to the standard cell by tracking six lines across the sample and taking an average (see Figure 4.26 across). One port of the non-contact cell was blocked off, as in this case only the ICP-MS was coupled as a detector.

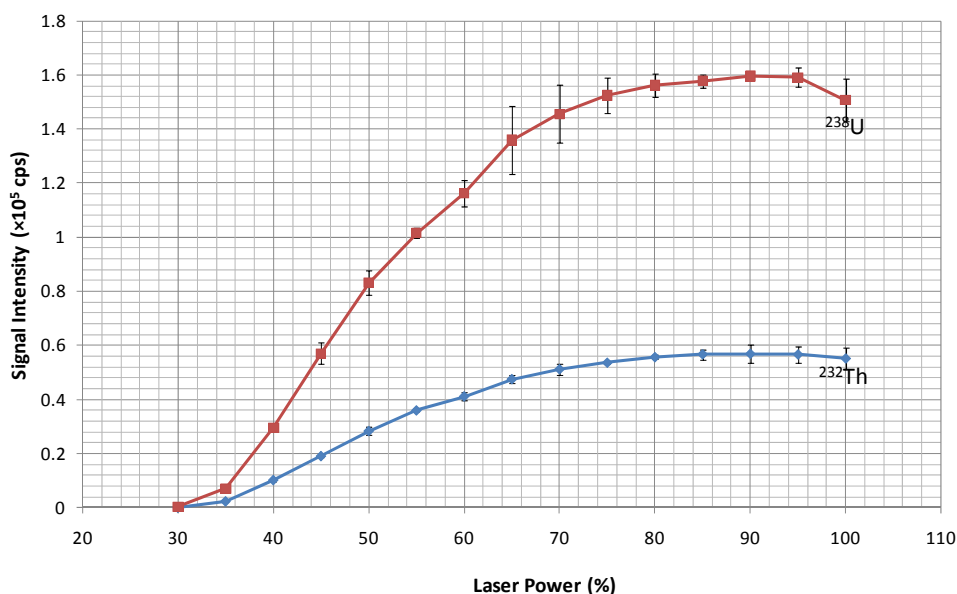


Figure 4.25: Signal intensity vs. laser power for NIST CRM-613 in the standard New Wave Research sampling cell using a UP-213 laser ablation system.

* Note, for NIST CRM-613 the signals for ²³²Th and ²³⁸U should be approximately equal. In this case, laser- and transport-induced fractionation is apparent. The initial test, however, was for wash-in and wash-out, which is independent of fractionation, and since the analytical performance of the non-contact cell was unknown, this was ignored.

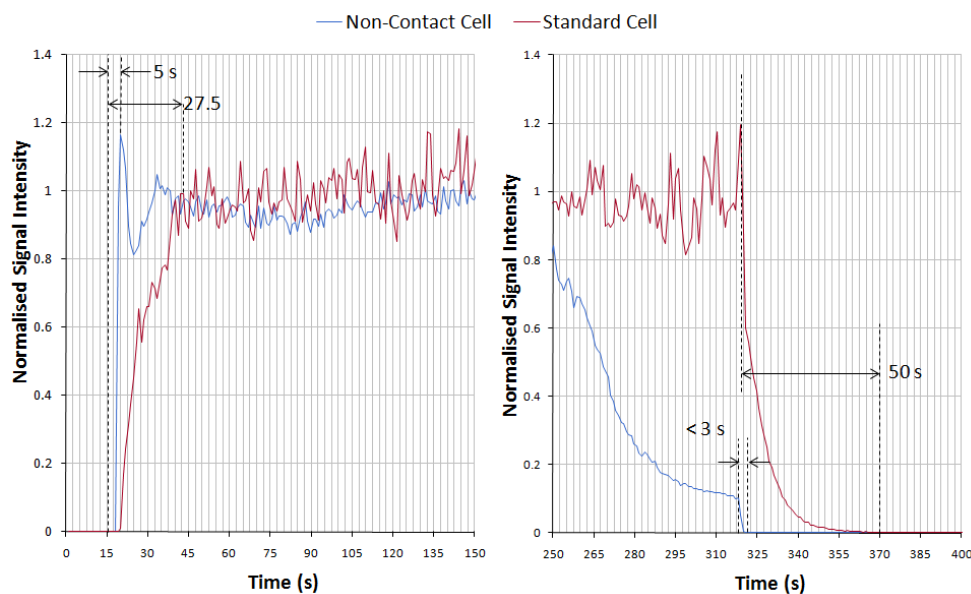


Figure 4.26: Normalised ^{232}Th signals *vs.* time for a 5 min line scan on NIST CRM-613 showing wash-in and wash-out times for the standard cell (sweep gas of 0.42 l min^{-1}) and the non-contact cell (inner and curtain channel flows at 1.6 and 2.5 l min^{-1} respectively, 0.25 bar jet-pump driving pressure and $200 \mu\text{m}$ above the sample surface). The gradual downward slope before the washout period for the NCC is from an ‘edge effect’ explained in the following pages.

The wash-in and wash-out times for the standard cell were approximately 27.5 and 50 s respectively, compared to approximately 5 s and < 3 s respectively for the non-contact cell. This is mainly due to the smaller volume of the cell, which is 0.64 cm^3 for the non-contact cell with one port closed (0.86 cm^3 with both ports open) compared to 33.8 cm^3 for the standard cell (possible as the non-contact cell does not need to physically enclose the sample) and the higher gas flows transmitted through the system.

There was an apparent enhancement in signal at the end of the track seen with the non-contact cell, followed by a drop-off. This can be attributed to an ‘edge-effect’ as the cell tracked across the surface. Initially, as the outer nitrogen channel fell off the edge of the sample there was a signal enhancement. This was followed by a drop in signal as the inner helium channel then fell off the edge of the sample and transport efficiency suffered (see Figure 4.27 and Figure 4.28 below).

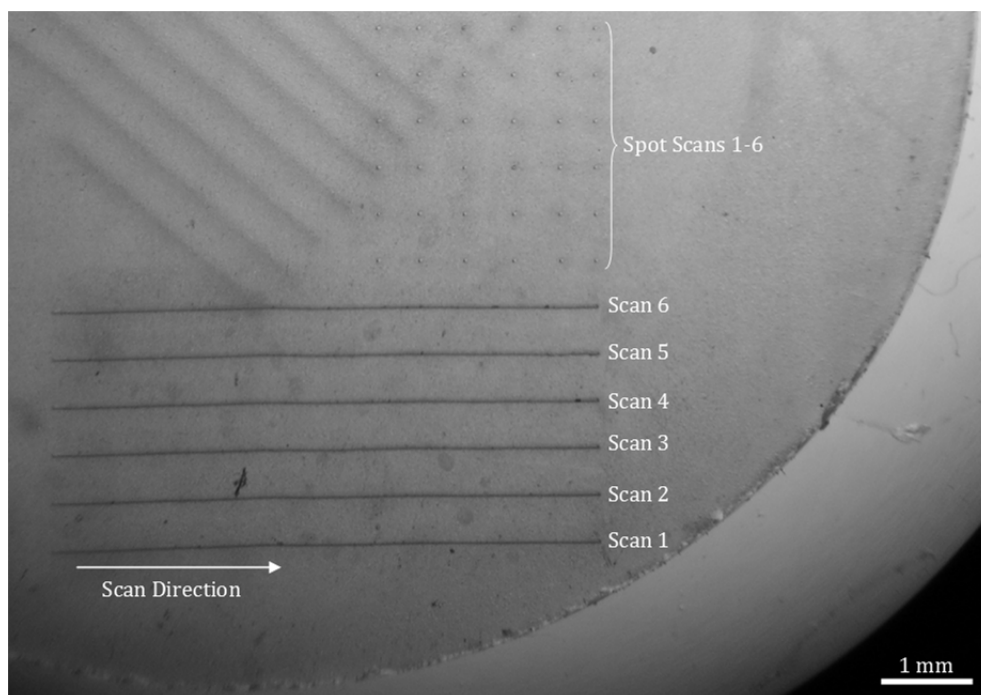


Figure 4.27: NIST CRM-613 post ablation by the non-contact cell showing line scan and spot scan positions.

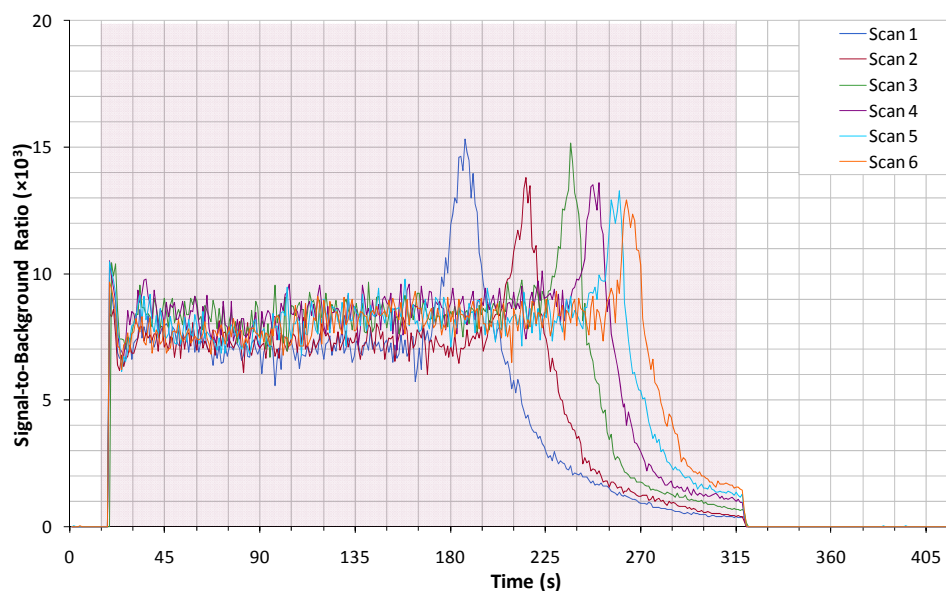


Figure 4.28: Signal intensity vs. time scans for ^{232}Th from 5 min line scans on NIST CRM-613 using the non-contact cell (inner and curtain channel flows at 1.6 and 2.5 l min⁻¹ respectively, 0.25 bar jet-pump driving pressure and 200 μm above the sample surface). The shaded area in the above figure represents the time at which the laser was firing at the sample surface. This pattern was also observed in the ^{238}U signals.

As mentioned previously, there could have been an enhancement effect occurring from the addition of nitrogen to the plasma.^[59, 60] As the cell tracked towards the edge of the sample, turbulent flow regimes may have come into play and caused an increase in the amount of nitrogen in the composition of the cell output gas. This may have caused an enhancement in the signals by enhancing energy coupling to the analytes in the plasma. It has also been suggested that the additional nitrogen can reduce elemental oxide formation by favourably combining with oxygen in the plasma, acting like an oxygen scavenger in the plasma.

However, here this increased flow of nitrogen was accompanied by an increase in oxygen entrainment, and therefore an increase in oxide formation (see Figure 4.29 below). The loss in sensitivity due to oxide formation was counteracted by the enhancement in signal afforded by the nitrogen addition, which ultimately resulted in the signal increase seen in the time-resolved scan above. Note the start point for the enhancement changes because of the edge curvature of the NIST sample disc.

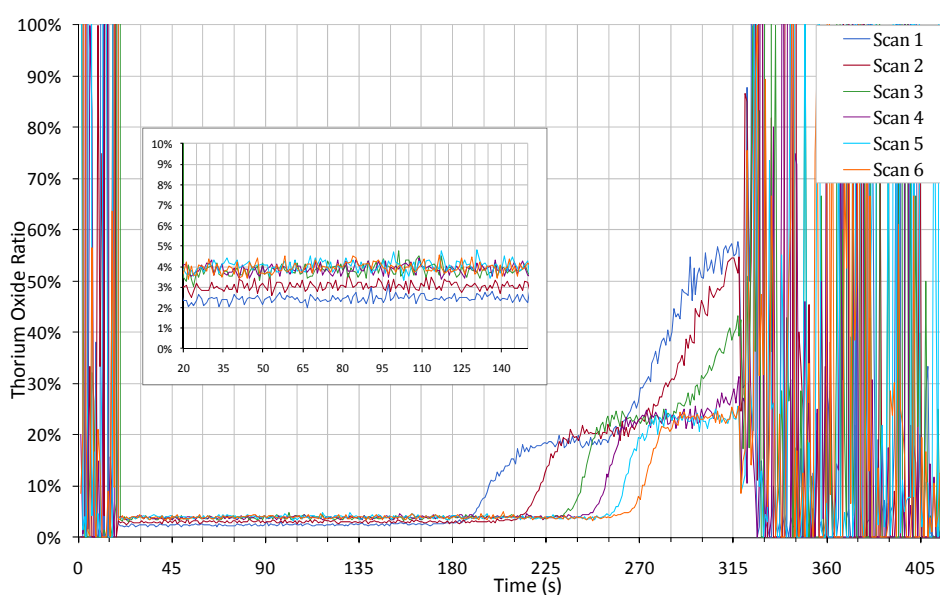


Figure 4.29: $^{232}\text{Th}^{16}\text{O}$ ratio vs. time from 5 min line scans on NIST CRM-613 using the non-contact cell (inner and curtain channel flows at 1.6 and 2.5 l min⁻¹ respectively, 0.25 bar jet-pump driving pressure and 200 μm above the sample surface).

Once the outer nitrogen channel had moved far enough away from the sample edge, the flow no longer added to the output channel, which resulted in the loss in signal intensity. This was accompanied by an increase in oxide levels that can be attributed to both increased oxygen levels in the output channel, as there was less resistance afforded by the nitrogen channel, and less nitrogen being present.

The ratio between ^{232}Th and ^{238}U can be an indicator of elemental fractionation effects. The ratio is shown in Figure 4.30 below.

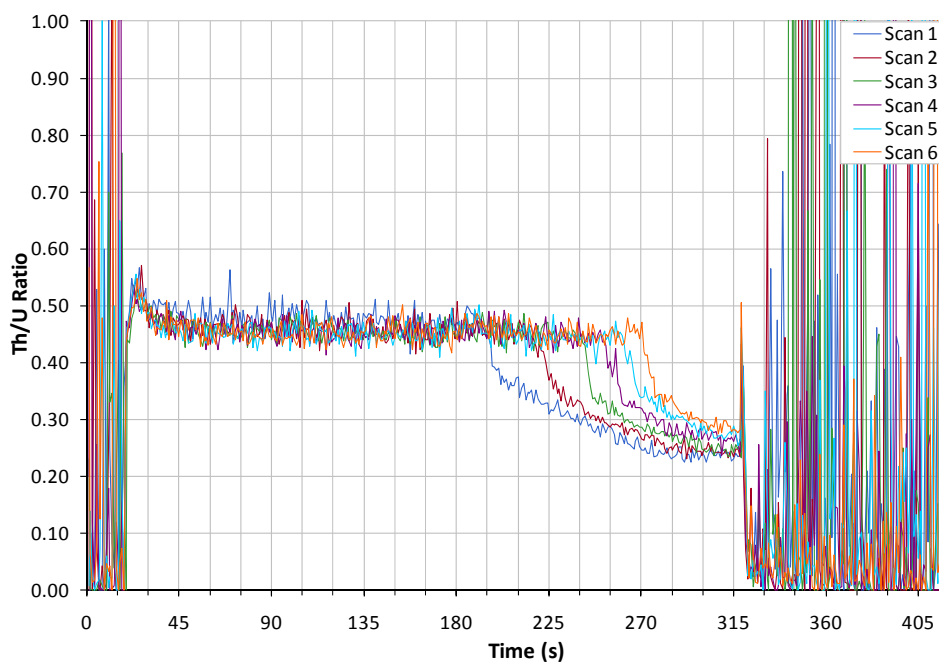


Figure 4.30: $^{232}\text{Th}/^{238}\text{U}$ ratio vs. time from 5 min line scans on NIST CRM-613 using the non-contact cell (inner and curtain channel flows at 1.6 and 2.5 l min⁻¹ respectively, 0.25 bar jet-pump driving pressure and 200 μm above the sample surface).

The expected ratio is 1.02, which suggests there were some fractionation processes occurring. This was the same for both the standard cell and the non-contact cell, therefore they are most likely to have been due to ablation and in-torch processes. The ratio, however, remained stable until the helium channel dropped off the edge of the sample, which indicates that further elemental fractionation started to occur at this point. This may have been due to less efficient ablation producing larger particles, or higher oxide levels. The average oxide levels for both thorium and uranium are summarised in Table 4.2 below, including the raised levels that occurred when the nitrogen and helium channel dropped off the edge of the sample.

Table 4.2: Oxide levels from thorium and uranium in NIST-613 for both the standard and non-contact cells.

Oxide Levels:	Standard Cell Average (%)	Non-Contact Cell		
		Average (%)	Curtain channel Off Sample Edge (%)	Both Channels Off Sample Edge (%)
Thorium Oxide	0.46 ± 0.22	3.54 ± 0.63	22.02 ± 2.19	54.77 ± 2.19
Uranium Oxide	0.28 ± 0.12	0.71 ± 0.11	4.52 ± 0.77	28.66 ± 1.48

The oxide levels are shown to be higher in the non-contact cell than in the standard cell, which is to be expected as the system was open to atmosphere. The gas MS data obtained previously suggested there was very little oxygen entrained into the output channel unassisted. With the jet-pump giving a total flow of approximately 3 l min^{-1} , the level of oxygen in the cell flow must be much larger, which indicates that the jet-pump was running too strongly in this configuration.

This level of oxides, however, was lower than the oxide levels seen in solution mode on the same instrument. This suggests that the inner and curtain channels working in conjunction were excluding atmospheric oxygen, but there is a limit to how close the cell can scan to the edge of the sample.

The average shot-to-shot reproducibility of the system with both the standard cell and the non-contact cell can be seen in Figure 4.31 and Figure 4.32 below and overleaf. The shorter wash-in and wash-out times can again be seen, with a peak height of approximately 25×10^3 cps with the standard cell, enhanced to 9×10^6 cps with the non-contact cell (shaded areas again represent ablation time).

The enhancement in signal (360 times in this case) can mainly be attributed to better mass transport through the non-contact cell compared to the standard ablation cell owing largely to the very small inner volume of the NCC, which is swept much more efficiently than the standard ablation cell.

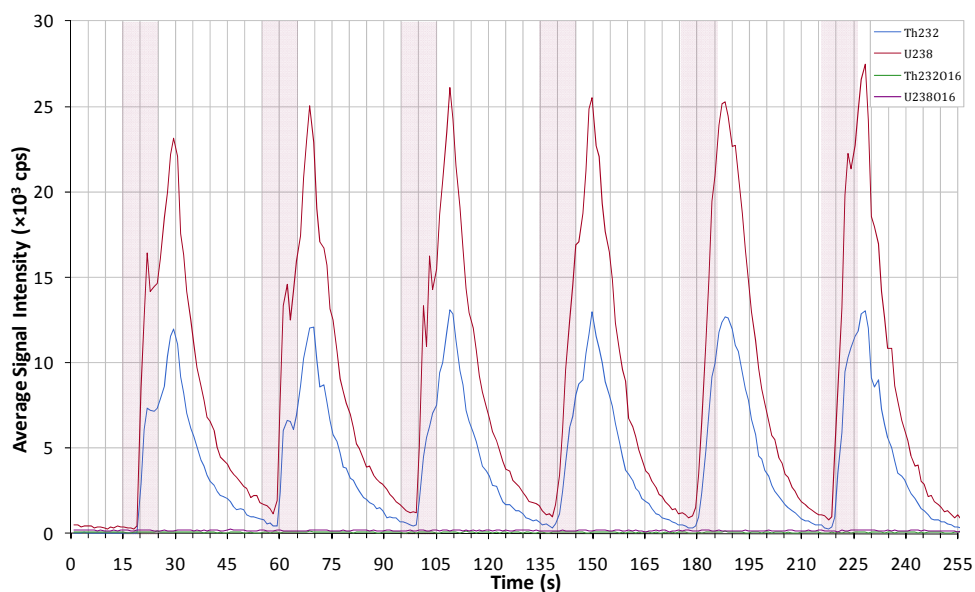


Figure 4.31: ^{232}Th , ^{238}U , ^{248}ThO and ^{254}UO signal intensity *vs.* time from spot-line scans (6 spots, 10s dwell time, 30s inter-site pause) on NIST CRM-613 using the standard sampling cell (sweep gas set at 0.42 l min^{-1}).

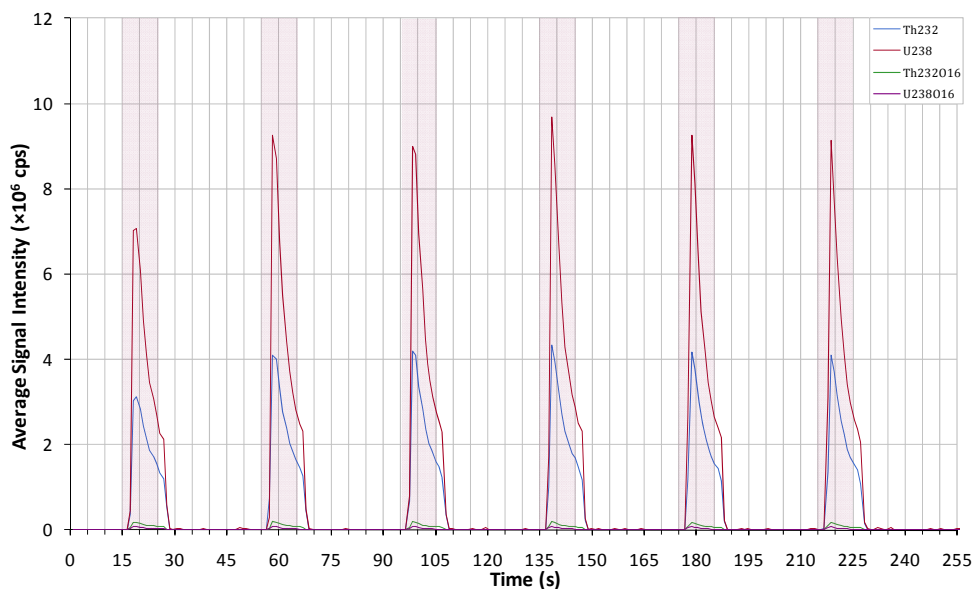


Figure 4.32: ^{232}Th , ^{238}U , ^{248}ThO and ^{254}UO signal intensity vs. time from spot-line scans (6 spots, 10s dwell time, 30s intersite pause) on NIST CRM-613 using the non-contact cell (inner and curtain channel flows at 1.6 and 2.5 l min⁻¹ respectively, 0.25 bar jet-pump driving pressure and 200 μm above the sample surface).

4.4.2 Silicon Wafer

The tests were repeated measuring phosphorous on the surface of a section of silicon wafer. The sample was scanned whole by the non-contact cell, but had to be sub-sampled for the standard cell due to size restrictions (see Figure 4.33 below). The picture was taken post ablation showing that the amount of ablated material left on the sample surface by the non-contact cell was lower than the amount left by the standard cell, which suggests the transport efficiency was greater for the non-contact cell. Additionally, the colour of the ablated material suggests the silicon is converted from crystalline silicon (blue-grey metallic colour) to amorphous silicon (brown powder), indicating melting and recombination through condensation has occurred.

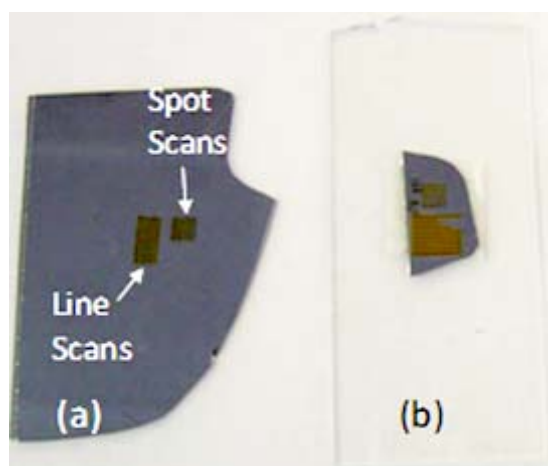


Figure 4.33: Si Wafer samples post ablation sampled by (a) the non-contact cell and (b) the standard cell, showing amorphous silicon (brown powder) on the surface of the crystalline wafer. There is less amorphous silicon evident after ablation using the non-contact cell compared to using the standard ablation cell, which indicates better mass transport efficiency.

The wash-in and wash-out times were again measured (see Figure 4.34 below). Once again, the wash-in and wash-out times of < 5 s and < 2.5 s respectively for the non-contact cell were lower than the wash-in and wash-out times of approximately 30 s and 45 s respectively for the standard cell.

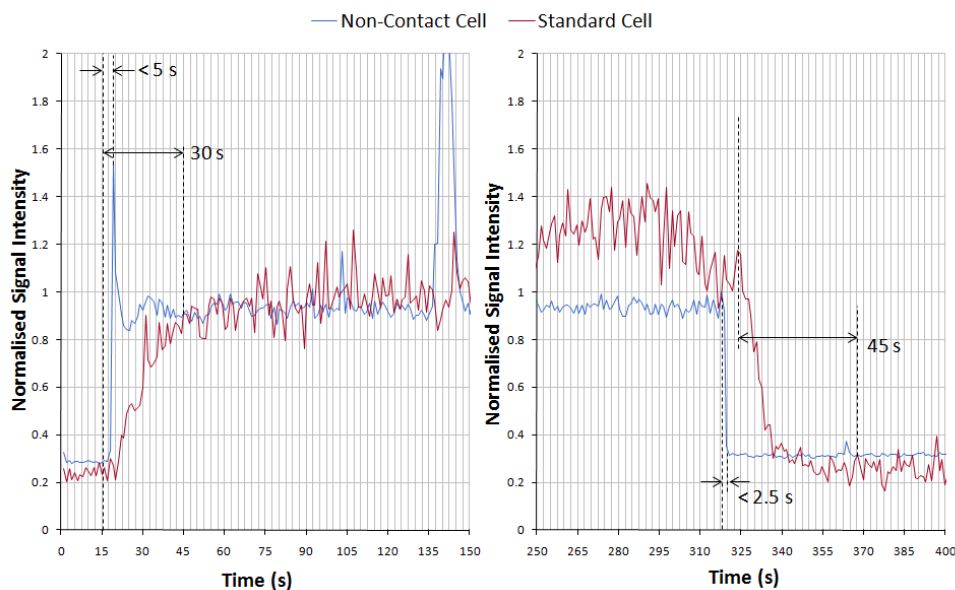


Figure 4.34: Normalised ^{31}P signal intensity vs. time for a 5 min line scan on a silicon wafer sample showing wash-in and wash-out times for the standard cell (sweep gas of 0.42 l min^{-1}) and the non-contact cell (inner and curtain channel flows at 1.6 and 2.5 l min^{-1} respectively, 0.25 bar jet-pump driving pressure and $200 \mu\text{m}$ above the sample surface).

The silicon wafer was large enough that the scanned area fell completely underneath the non-contact cell sampling area, so there was no edge effect seen in this case. The large peak seen at around 135 s in the non-contact cell trace can be attributed to an increase in signal intensity in the area scanned, indicating inhomogeneity in the sample surface. As this data was acquired at medium resolution, this was most probably due to an increase in phosphorous levels in the sample.

The shot-to-shot reproducibility is shown in Figure 4.35 and Figure 4.36 overleaf. The transient phosphorous signals appear to be as stable as those obtained with the standard cell; however, the intensity was enhanced from 70 cps to 7,000 cps.

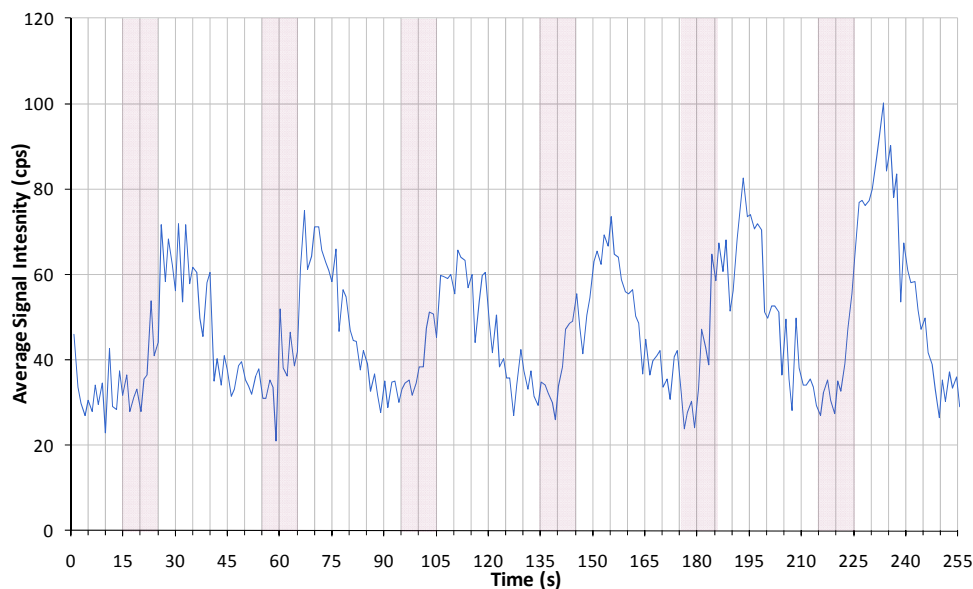


Figure 4.35: ^{31}P signal intensity *vs.* time from spot-line scans (6 spots, 10s dwell time, 30 s inter-site pause) on silicon wafer using the standard sampling cell (sweep gas set at 0.42 l min^{-1}).

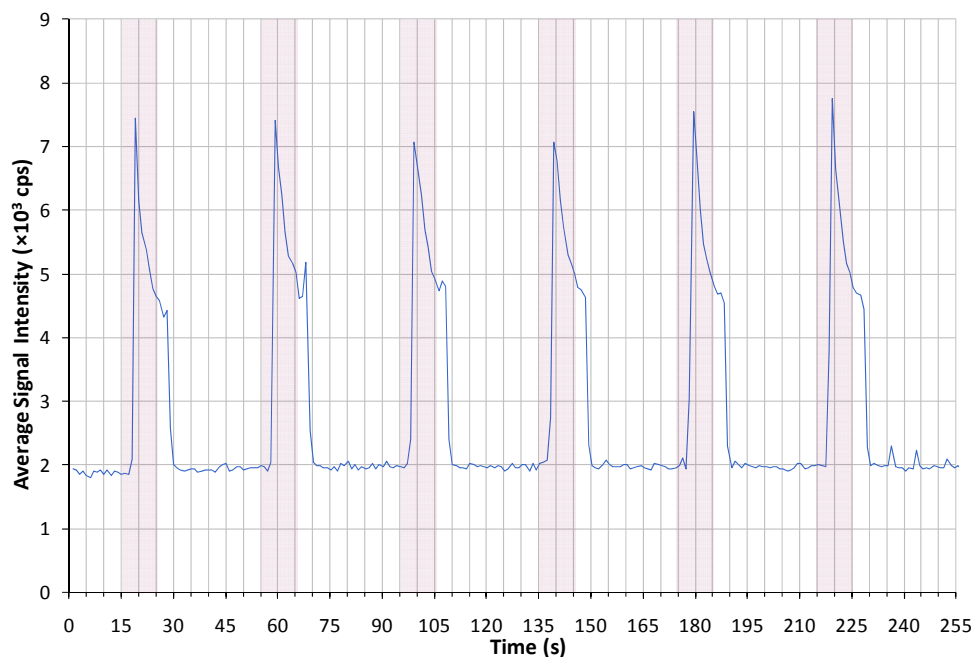


Figure 4.36 ^{31}P signal intensity *vs.* time from spot-line scans (6 spots, 10s dwell time, 30s inter-site pause) on silicon wafer using the non-contact cell (inner and curtain channel flows at 1.6 and 2.5 l min^{-1} respectively, 0.25 bar jet-pump driving pressure and $200 \mu\text{m}$ above the sample surface).

The enhancement in signal in this case (100 times greater peak signal using the NCC) is lower than that obtained when sampling NIST glass. This difference can be attributed to the ablation characteristics of the two materials. Pure silicon has a much lower ablation threshold than glass since it has a smaller bond energy (52 kcal mol^{-1} *vs.* $110 \text{ kcal mol}^{-1}$ respectively). Additionally, silicon has a smaller band-gap than glass (1.11 eV *vs.* 8.9 eV respectively); hence, it is likely that photon energy is used to excite electrons into the conduction band more easily with pure silicon.

Relaxation of these excited electrons dissipates energy as heat, causing melting at the ablation site. The brown, amorphous silicon left on the sample surface is indicative of melting followed by rapid cooling, whereby the atoms do not have enough time to arrange themselves into extended crystalline structures before freezing.

This can cause ablated particles to coalesce through agglomeration (partially melted particles sticking together), condensation (vapour phase cooling by solidifying) and assimilation (trapping of smaller particles in large melt droplets), ultimately becoming more difficult to transport.

The NCC has sufficient pull from the micro jet-pump to transport these heavier particles, whereas the standard ablation cell does not; however, some of the largest particles are still lost and the signal enhancement is not as great when compared to sampling of NIST glass.

4.5 Performance Testing: Molecular Ion Formation, Time Resolved Reproducibility and Signal Stability

The testing of the non-contact cell was repeated on a New Wave Research UP-193 laser ablation system. This system has better energy coupling into NIST glass than the UP-213 system as a result of the shorter laser wavelength used, which means laser induced fractionation should be minimised. Traditionally, fractionation in the ICP torch is tuned out *via* the torch sample depth (residence time in the plasma) and balancing the helium carrier gas and argon make-up gas flow rates (plasma composition and residence time in the plasma). In the case of the non-contact cell, the gas flows to be balanced are the curtain gas, the carrier gas, the micro jet-pump motive flow rate and a make-up gas flow rate.

The comparative data in this experiment was used to investigate ion formation in a wide range of elements, from ^{11}B through to ^{238}U , looking at the selected metal ion (M^+), the nitride (MN^+), the oxide (MO^+) and the doubly charged species (M^{2+}). Unfortunately, there was a technical error with the ICP-MS resulting in loss of signals at elements below ^{85}Rb , therefore the following results will only look at the reduced range from ^{85}Rb upwards.

This also means the signal intensities are not a reliable indicator of the relative signal intensities achieved by each cell in this case, as the error occurred after completing the standard cell reference data (time restrictions did not allow repeat measurements for the standard ablation cell); however, as only ratios between the metal ion and the related daughter ions were needed the data was deemed fit-for-purpose.

Initially, the jet-pump was redesigned to allow negative pressure comparable to that obtained in the testing with the UP-213 system, but with much lower flow rates. This was done by altering the size of the jet nozzle down from $254\ \mu\text{m}$ to $127\ \mu\text{m}$, which allowed comparable entrainment at flows ranging from $0.1\ \text{l min}^{-1}$ to $0.4\ \text{l min}^{-1}$.

With the standard cell fitted, the laser system was optimised for absolute signal level by measuring ^{232}Th and ^{238}U signal intensities at different laser powers. The optimum signal level with low RSD was achieved at 70% of the full laser power (approximately $10\ \text{J cm}^{-2}$).

The settings used in the LA-ICP-MS experiment are summarised in Table 4.3 below. The actual value for the laser power was not recorded, but was kept constant throughout the investigation. The standard cell was optimised with a He sweep gas flow rate of 0.61 l min⁻¹, giving a total flow of 1.41 l min⁻¹ through the central channel of the ICP torch when combined with the argon ‘sample gas’ from the ICP.

The flows from the jet-pump and the ‘sample gas’ were adjusted to give a total flow of 0.40 l min⁻¹ of argon. The non-contact cell gives roughly 0.60 to 0.70 l min⁻¹ of gas from the output (which consists of helium essentially doped with nitrogen), which then results in a flow rate through the central channel of the ICP torch comparable to that achieved with the standard sampling cell. This means the expected signal levels should be similar, depending on flow entrainment and instrument performance.

Table 4.3: LA-ICP-MS settings for the validation of the non-contact cell on the UP-193 laser ablation system.

<u>ICP-MS Settings</u>				
<i>Torch Settings</i>		<i>Lens Voltages</i>		
			<i>Low Resolution</i>	<i>Medium Resolution</i>
Cool Gas Flow	15.5 l min ⁻¹	Rotation Quad 1	0.37 V	0.22 V
Auxiliary Gas Flow	0.88 l min ⁻¹	Rotation Quad 2	0.22 V	2.60 V
Plasma Power	1250 W	Focus Quad 1	-0.07 V	-8.00 V
		Focus Quad 2	0.12 V	0.12 V
	<i>Standard Cell</i>	<i>Non-Contact Cell</i>		
Sample Gas Flow	0.80 l min ⁻¹	0.4 – 1 min ⁻¹	<i>Detector Voltages</i>	
Torch x-position	5.1 mm	5.2 mm	Matsuda Plate	60.01 V
Torch y-position	2.6 mm	3.1 mm	SEM-Deflection	700 V
Torch z-position	-1.2 mm	-0.4 mm	SEM	1700 V
<i>Lens Voltages</i>				
Extraction Lens	-2000 V			
Focus Lens	-1536 V			
X-Deflection	-2.23 V			
Y-Deflection	-2.24 V			
Shape	120 V			
<u>Laser Ablation Settings</u>				
	<i>Standard Cell</i>	<i>Non-Contact Cell</i>	Laser Power	70 %
Sweep Gas	0.61 l min ⁻¹	N/A	Laser Irradiance	1.58 GW cm ⁻²
Inner Channel Gas	N/A	1.59 l min ⁻¹	Laser Warm-up time	5 s
Outer Channel Gas	N/A	2.45 l min ⁻¹	Line-Scan Scan-rate	20 μm s ⁻¹
Jet-Pump Flow	N/A	0.1 – 0.4 l min ⁻¹	Spot-Line Dwell Time	10 s
Laser Spot Size	100 μm		Spot-Line Intersite Pause	30 s
Frequency	10 Hz		Manual Trigger Offset	10 s

With the jet-pump set at 0.40 l min^{-1} , the signal levels for ^{232}Th and ^{238}U were measured at differing sample-to-cell distances of the non-contact cell. As the non-contact cell was moved closer towards the sample surface, the signal intensity increased following an exponential relationship (see Figure 4.37 below).

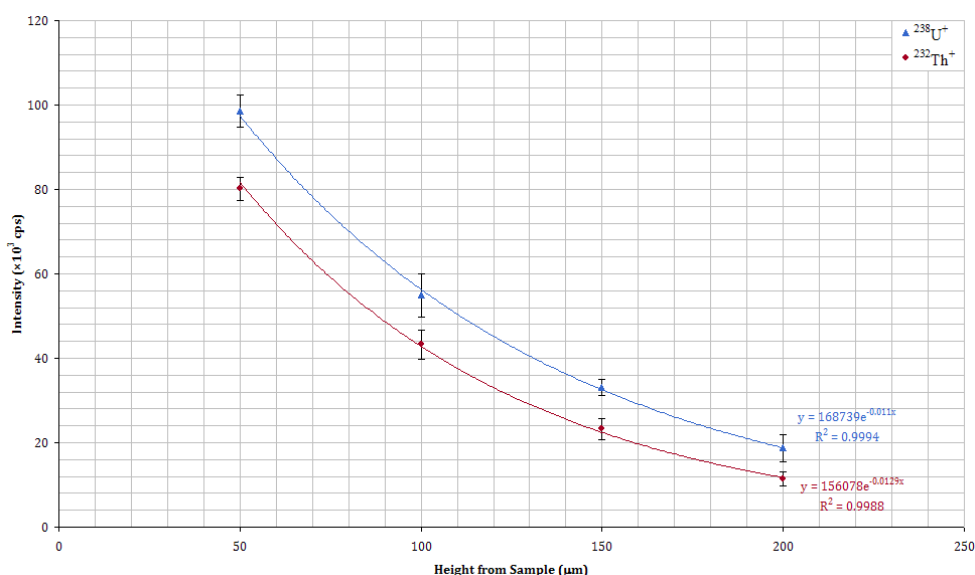


Figure 4.37: Signal intensity *vs.* height from sample for NIST CRM-613 using the non-contact cell on a UP-193 laser ablation system.

During this experiment, the laser was focused on the sample surface when the non-contact cell was floating $200 \mu\text{m}$ above the sample surface. As the cell was moved in closer to the sample surface, the focal plane consequently moved below the sample surface and defocused the laser spot image on the sample surface, thereby decreasing the fluence. This means with new focusing at each height, the signals could potentially increase further.

The mixture of helium and nitrogen coming from the output channel changes with height, smaller sample-to-cell separations containing relatively more helium than nitrogen. Because of this, the position of shockwaves will change depending on the flow rate of the driving gas (in this case, argon). The simplest method for altering the position of the shockwaves is to alter the overall density of the free jet expansion region in the jet-pump housing. This is easily achieved by altering the flow rate of the argon motive flow, higher flow rates being needed at the smaller sample-to-cell separations

Signals levels for ^{232}Th and ^{238}U were measured at different flow rates of the jet-pump at the different sample-to-cell heights. The optimum jet-pump flow rates are summarised in Table 4.4 below.

Table 4.4: Optimum jet-pump flow rates for different sample-to-cell heights of the non-contact cell. At smaller sample-to-cell heights, more argon is needed position the shockwaves correctly.

Sample-to-cell height (μm)	Jet-pump flow rate (l min^{-1})
40	0.30
80	0.30
120	0.20
160	0.20
200	0.15

4.5.1 Sensitivity and Molecular Ion Formation

To compare the signal levels and the relative nitride, oxide and doubly charged species formation in the non-contact cell to the standard New Wave Research sampling cell, signal levels for ⁸⁵Rb were measured together with the nitride, oxide and doubly charged ion in both the standard sampling cell and the non-contact cell at low resolution. Rubidium was chosen since it is free of major isobaric interferences from other elements in NIST 613 glass. The rubidium concentration is 31.02 ppm, obtained from the GeoReM website.^[61]

When using the non-contact cell, molecular ions are shown to have increased relative to the total counts of the M⁺, MN⁺, MO⁺ and M²⁺ ions obtained in each run (see Figure 4.38 below). This is expected as the system is open to atmosphere and entrained gases (especially nitrogen) lead to changes in the plasma composition, which can ultimately change the ionisation performance characteristics.

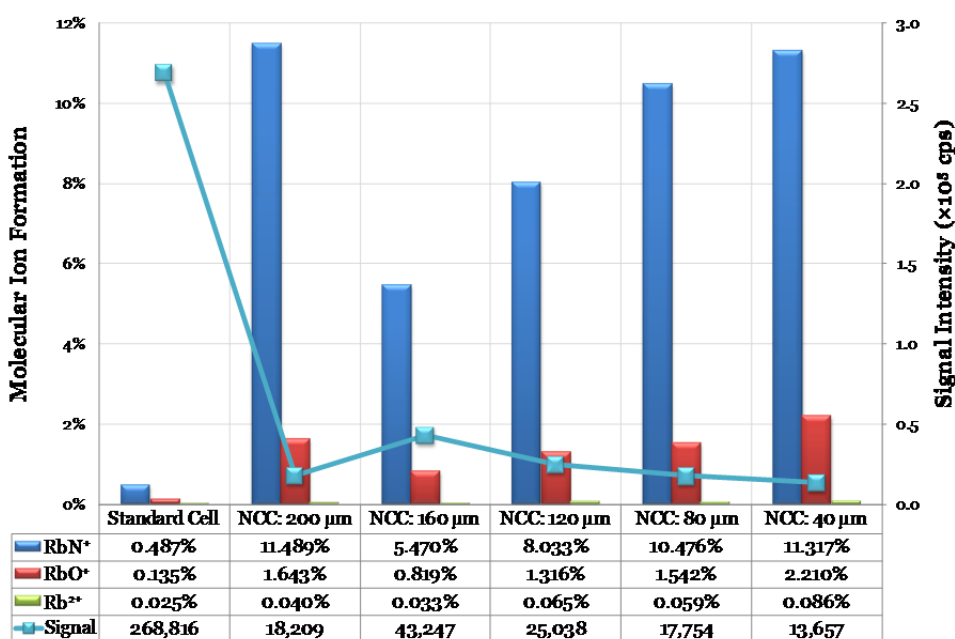


Figure 4.38: Signal variation and molecular ion formation for ⁸⁵Rb in both the standard sampling cell and the non-contact cell (at various heights).

From the signal intensities, there appears to be an optimum level at which the non-contact cell performs giving the best signal intensity for ⁸⁵Rb at 160 μm above the sample surface. This could indicate a trade-off between entraining sufficient nitrogen for signal enhancement and ultimate transport efficiency, due to sample-to-cell distance. Note, comparing the signal intensities for the standard cell and the non-contact cell is not appropriate in this study since the ICP-MS had a technical error lowering overall sensitivity.

For measurement of oxide formation, the usual element of choice is ^{140}Ce , with its oxide measured at $m/z = 156$ in low resolution, as it forms a strong oxide bond. The source of oxygen in wet plasma conditions is usually the solvent; therefore, a low $^{140}\text{Ce}^{16}\text{O}/^{140}\text{Ce}$ ratio (expressed as a percentage) is used to indicate robust plasma operating conditions. Typically the user aims to tune these conditions to reduce the CeO/Ce ratio to $< 1\%$, indicating the plasma is able to desolvate and process the liquid droplets effectively.

For laser ablation, the oxygen source is typically oxides in the sample matrix, impurities in the sweep gas and atmospheric oxygen entrainment through air leaks or diffusion through the plasma. As a consequence, measurement of the oxide levels is important to assess whether the plasma is processing the ablated particles effectively as well as checking for leaks and/or entrainment.

NIST 612 (which is the standard of choice for optimising ablation and plasma parameters prior to a run) contains 37.3 ppm ^{156}Gd . This means the CeO signal suffers from a significant isobaric interference and cannot be used as a reliable oxide indicator. As a result, the indicators used during laser ablation are both $^{232}\text{Th}^{16}\text{O}/^{232}\text{Th}$ and $^{238}\text{U}^{16}\text{O}/^{238}\text{U}$. Since thorium and uranium are the two heaviest ‘major’ trace elements in NIST 612, their oxides are relatively free of significant isobaric interferences.

For thorium, the nitride levels rise slightly as expected since this is a product of entrained curtain gas into the plasma central channel (see Figure 4.39 below). The levels do not rise more than 0.200 %; therefore, the plasma is still able to process most formed nitrides effectively. Signal levels show an optimum at 160 μm above the sample surface, confirming the pattern seen with ^{85}Rb .

The oxide levels, however, appear to *decrease*. This could be due to either reduced oxygen entrainment into the plasma central channel, or an overall reduction in formation of ThO from the entrainment of nitrogen into the plasma – Durrant^[59] theorised the nitrogen could act as an oxygen ‘scavenger’, reducing the amount of oxygen available to form oxides.

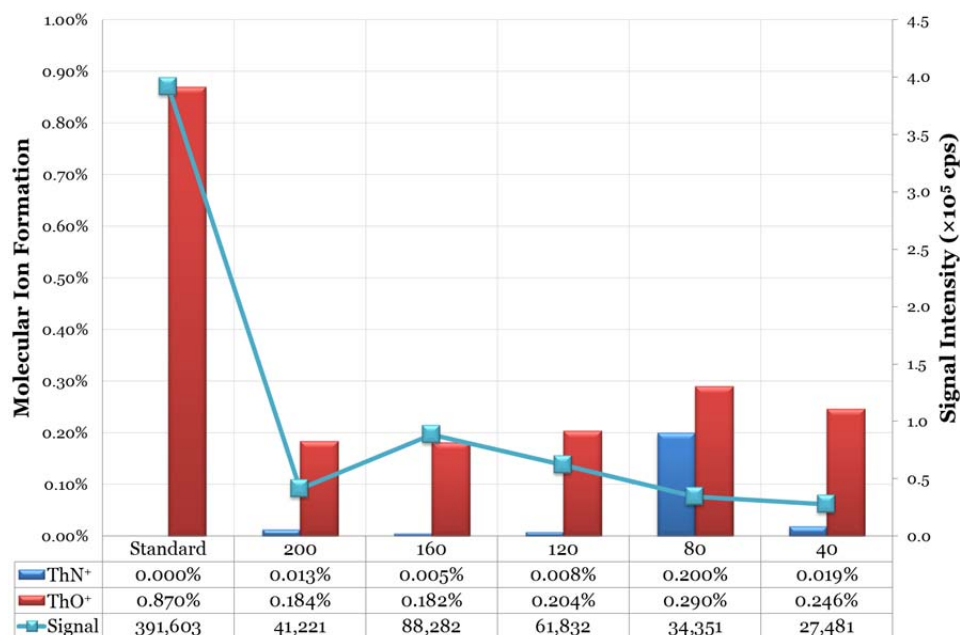


Figure 4.39: Signal variation, nitride and oxide formation for ^{232}Th in both the standard sampling cell and the non-contact cell (at various heights).

For uranium, the signal intensity and nitride rise is seen again (see Figure 4.40 below). The nitride levels (as %) increase to a maximum as the distance to the sample surface decreases, all significantly higher than formed using the standard ablation cell (although still relatively low at 1.3 %). This could be an effect of background signals contributing more significantly to the nitride signal as the overall signal intensity decreases.

Oxide formation is decreased slightly, again indicating either less entrained oxygen or reduction in oxide formation; however, for uranium the oxide levels increase to levels similar to those formed using the standard cell as the cell moves closer to the sample surface. Again, this could be a mathematical artefact of increased significance of background levels to a lower overall signal intensity.

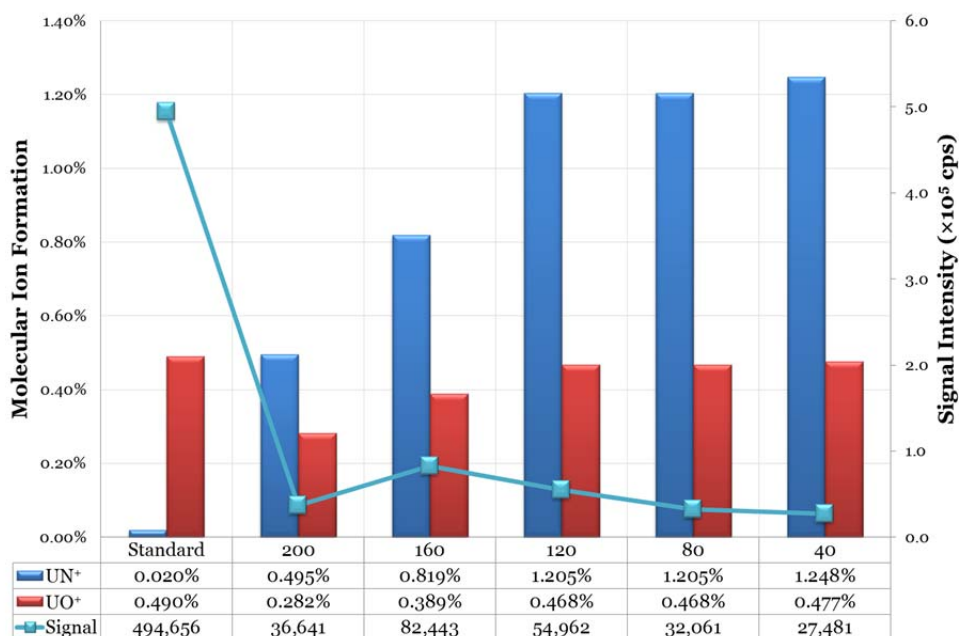


Figure 4.40: Signal variation, nitride and oxide formation for ²³⁸U in both the standard sampling cell and the non-contact cell (at various heights).

4.5.2 Time-resolved Reproducibility

The shot-to-shot reproducibility of the standard sampling cell and the non-contact cell at various heights was tested. The wash-in and wash-out times were measured for both cells and compared by running line-of-spot scans with six spots with a dwell time of 10 seconds and an inter-site pause of 30 seconds. As the standard sampling cell on the UP-193 system uses a higher sweep gas flow rate than the same cell on the UP-213 system, the wash-in and wash-out times are shorter at 10 s and 15 s respectively (see Figure 4.41 below). Using the non-contact cell, the wash-in and wash-out times were reduced to approximately 5 s and 7.5 s respectively (see Figure 4.42 across). This was mainly due to the smaller cell volume of the non-contact cell.

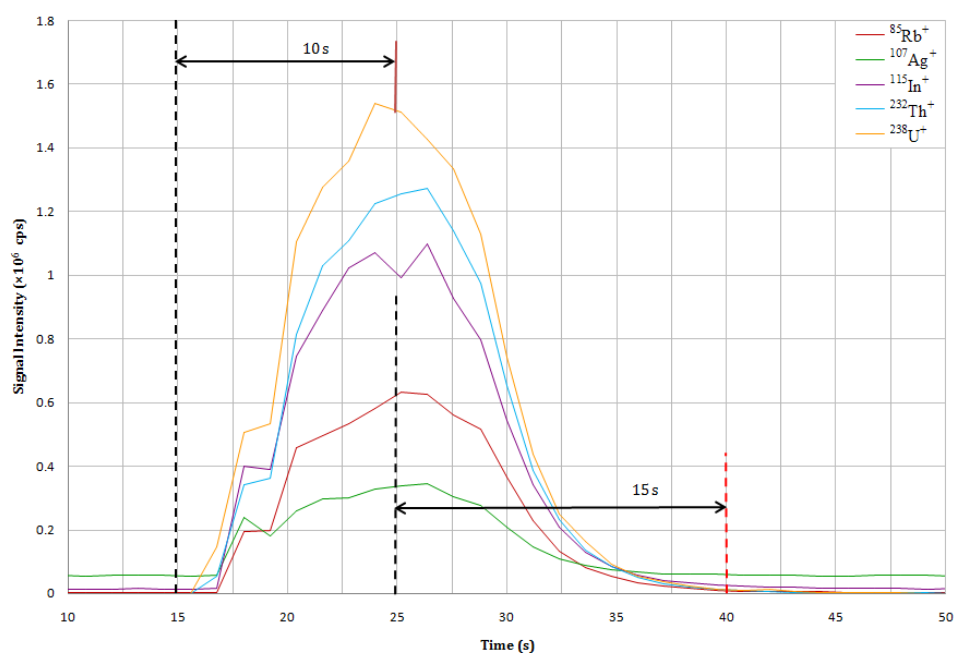


Figure 4.41: Signal intensity *vs.* time for NIST CRM-613 using the standard sampling cell on a UP-193 laser ablation system showing a wash-in time of approximately 10 s and a wash-out time of approximately 15 s.

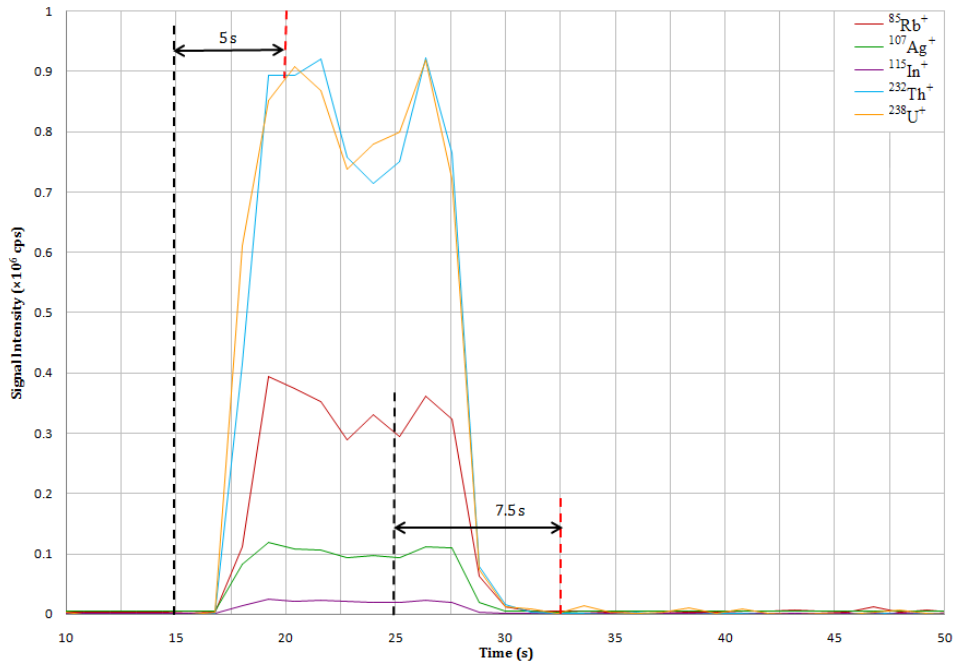


Figure 4.42: Signal intensity *vs.* time for NIST CRM-613 using the non-contact cell on a UP-193 laser ablation system showing a wash-in time of 5 s and a wash-out time of 7.5 s.

The non-contact cell exhibited reproducibility comparable to that of the standard sampling cell (see Figure 4.43 below and Figure 4.44 overleaf), with reduced wash-in and wash-out times. This shows that there were no time-resolved effects that could alter an analysis, and that total run time can be marginally reduced for an assay that requires sampling single shots at multiple repetitions.

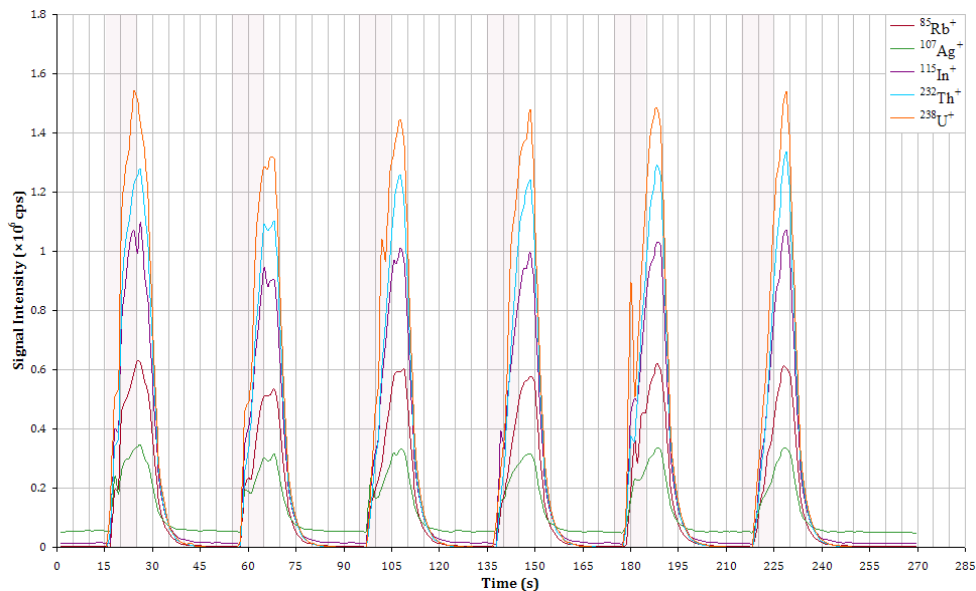


Figure 4.43: Signal intensity *vs.* time for NIST CRM-613 using the standard sampling cell on a UP-193 laser ablation system showing signal reproducibility for six sequential laser shots.

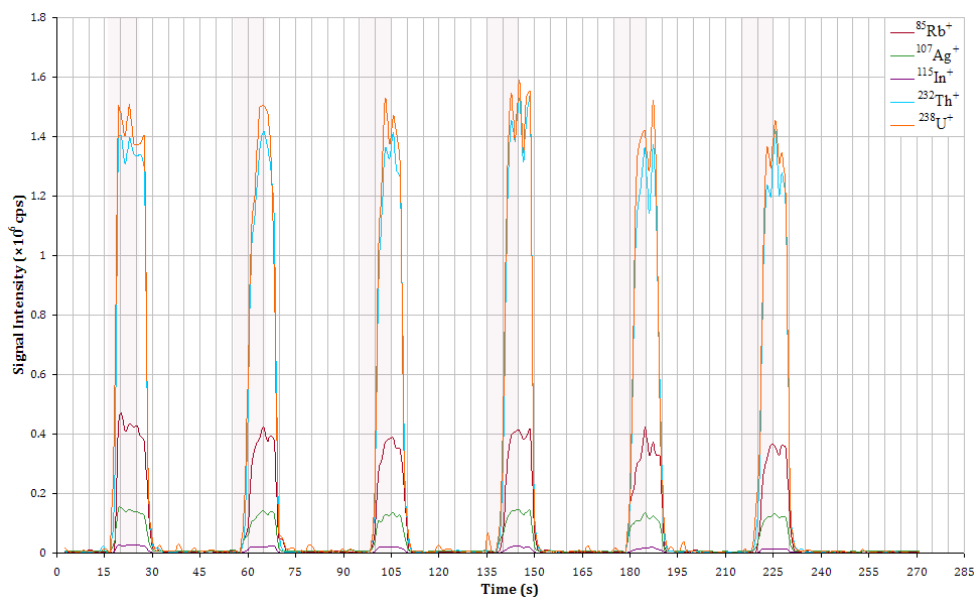


Figure 4.44: Signal intensity vs. time for NIST CRM-613 using the non-contact cell on a UP-193 laser ablation system showing signal reproducibility for six sequential laser shots.

The signal intensity for ^{115}In appears to have decreased dramatically when switching to the non-contact cell, which is an artefact of the ICP problems faced whilst obtaining the non-contact cell data. Of interest to note is that the isotope ratio for $^{232}\text{Th}/^{238}\text{U}$ moved closer to 1.02 (the correct value) when switching from the standard sampling cell to the non-contact cell, which suggests the cell was providing an ablated plume that minimised fractionation effects.

4.5.3 Time-resolved Stability

As the laser drills down into a sample, the irradiance decreases as the laser spot defocuses which leads to decreased signal intensity. The optics of the laser system provides a flat beam profile, so a drilled hole should have a flat base with vertical walls. If the ablated material is not removed efficiently from the sample surface, the profile of the drilled hole begins to resemble an inverted cone, and the area irradiated by the laser increases (termed ‘coning’). This further reduces the irradiance and causes the signal intensity to be decreased.

A two minute single spot drill on NIST CRM-613 using a 100 μm spot was run on both cells to compare the signal stability afforded by both cells. For the standard cell, the final signal intensity was approximately 20 – 35% of the peak intensity (see Figure 4.45 below).

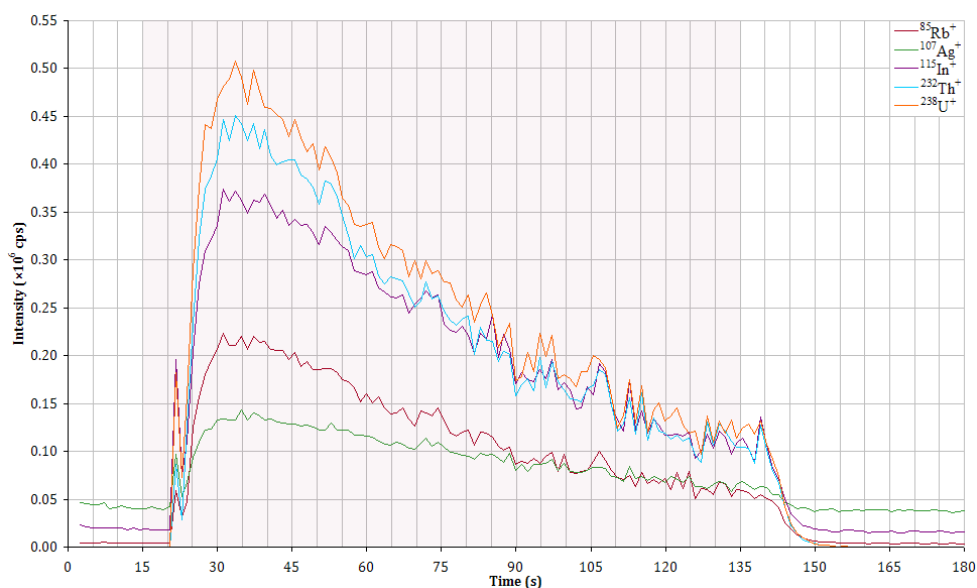


Figure 4.45: Signal intensity *vs.* time of NIST CRM-613 using the standard sampling cell on a UP-193 laser ablation system for a 2 minute single 100 μm spot drill.

The non-contact cell showed a similar response (see Figure 4.46 below) with a final signal intensity of approximately 15 – 25% of the initial signal intensity.

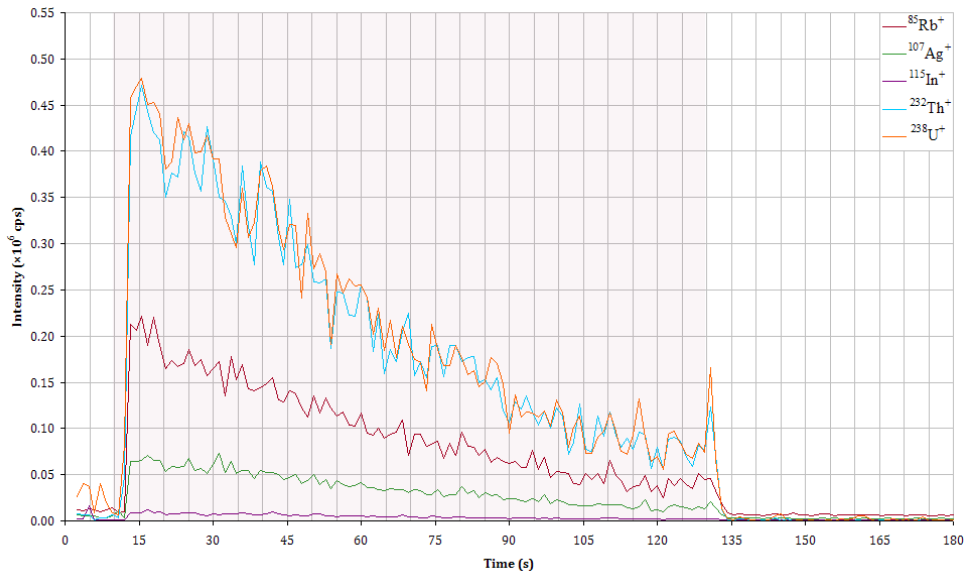


Figure 4.46: Signal intensity vs. time of NIST CRM-613 using the non-contact cell on a UP-193 laser ablation system for a 2 min single 100 μm spot drill.

Comparing the two cells, the degree of signal depletion is very similar (see Figure 4.47 below). This indicates the drilling process is probably identical, with ablated material clearing at similar rates.

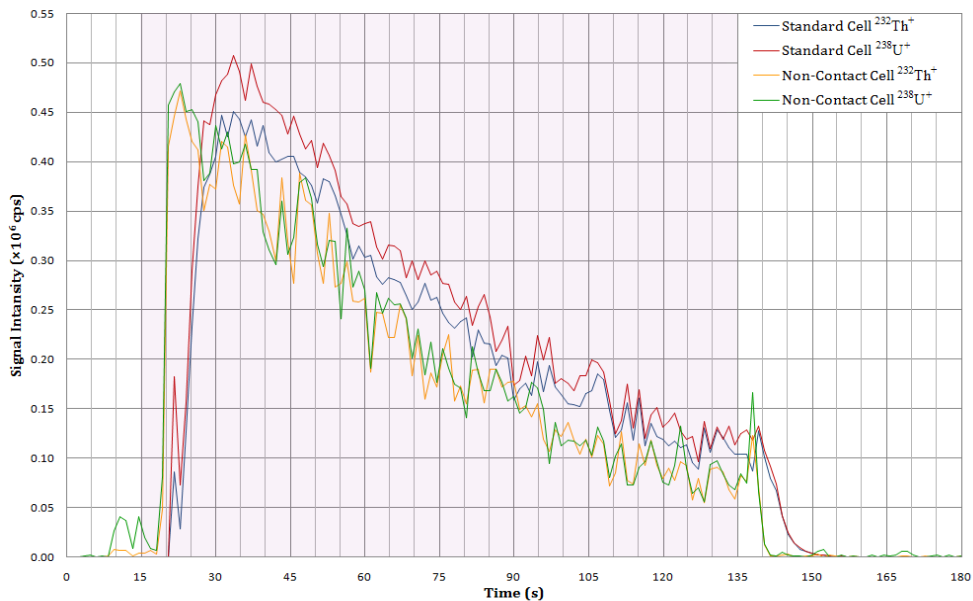


Figure 4.47: Signal intensity vs. time of NIST CRM-613 using both the standard sampling cell and the non-contact cell on a UP-193 laser ablation system for a 2 min single 100 μm spot drill.

4.6 Numerical Simulations: Gas Flow Paths

This section should be read in conjunction with Appendix C: Numerical simulations of gas flows through an open, non-contact cell for LA-ICP-MS (Paper 3).

Following on from the empirical data obtained in the preceding sections, an attempt was made to numerically characterise the gas flow paths through the NCC. The main aim of this study was to assess the effect of the micro-jet array on exclusion of atmospheric gas from the sample surface below the NCC. Additionally, velocity data generated during the calculation was used to estimate particle transit times through the central volume of the cell. Flow calculations were performed using the Computational Fluid Dynamics (CFD) add-on package available for SolidWorks called 'Flow Simulation'.

4.6.1 Governing Equations

Flow Simulation solves the Navier-Stokes equations for laminar and turbulent fluid flows, which describe the mass, momentum and energy conservation laws for fluid flows.^[62] These equations are modified by additional equations defining the fluid state and describing dependencies of density, viscosity and thermal conductivity on environment temperature.

A particular engineering problem is specified by defining geometry (by building a mesh using the CAD model), the fluid type, initial conditions and boundary conditions (*i.e.* definition of mass flow inlets, static pressures, wall conditions *etc.*). Non-Newtonian fluids can also be simulated in this package; however, these fluids are beyond the scope of this thesis so will not be considered in the proceeding discussion.

Turbulence in a flow can be predicted by calculating the Reynolds number (Re) for the fluid flow, which is defined as the ratio of the inertia (drag) in a flow and the viscous force. It can be applied to both fluids and particles.

$$Re = \frac{\rho u^2}{L} \quad (4.1)$$

Where:

- ρ : fluid/particle density
- u : flow velocity
- L : characteristic scalar dimension (*e.g.* pipe diameter)

The Reynolds number provides an indication for the relative damping of eddy currents by the viscous forces within the flow. Large values of Re indicate the viscous forces are too small to damp the eddy currents in the flow; hence, for high Reynolds number ($> \sim 4000$), the flow is said to be turbulent, and low Reynolds number flows ($< \sim 2300$) are said to be laminar. In the region between these two boundaries, the fluid flow streamlines can be both laminar and turbulent.

Flow Simulation was developed to solve engineering problems that are usually in the turbulent flow regime. To predict these flows, the Favre-averaged Navier-Stokes equations are used. In these equations, the time averaged effects of flow turbulence are considered for the flow parameters, whereas other time-dependent flow effects are taken into account directly in the fluid. Due to these considerations, extra terms appear in the equations known as the Reynolds stresses, and extra information must be supplied. To close the system of equations, the program uses the $K-\varepsilon$ model to apply transport equations for the turbulent kinetic energy and its dissipation rate.

4.6.1.1 The Conservation Laws

The conservation laws for mass, angular momentum and energy in a Cartesian coordinate system (rotating about an axis passing through the model's origin) can be written as*:

$$\frac{\partial \rho}{\partial t} + \frac{\partial}{\partial x_i} (\rho u_i) = 0 \quad (4.2)$$

$$\frac{\partial u_i}{\partial t} + \frac{\partial}{\partial x_j} (\rho u_i u_j) + \frac{\partial P}{\partial x_i} = \frac{\partial}{\partial x_j} (\tau_{ij} + \tau_{ij}^R) + S_i \quad (4.3)$$

$$\frac{\partial \rho H}{\partial t} + \frac{\partial \rho u_i H}{\partial x_i} = \frac{\partial}{\partial x_i} (u_j (\tau_{ij} + \tau_{ij}^R) + q_i) + \frac{\partial p}{\partial t} - \tau_{ij}^R \frac{\partial u_i}{\partial x_j} + \rho \varepsilon + S_i u_i + Q_H \quad (4.4)$$

$$H = h + \frac{u^2}{2} \quad (4.5)$$

Where:

- P : system pressure
- τ : viscous shear stress tensor
- τ^R : Reynolds stress tensor
- S : mass distributed external force
- q : diffusive heat flux
- Q_H : heat flux from a heat source/sink (solid materials)
- h : thermal enthalpy

The mass distributed external force is a combination of force exerted by porous media in the gas flow path, buoyancy and rotation of the coordinate system. Rotation was not used in this study, so the force term takes into account the other two forces only. Additionally, heat conduction through solids was not considered.

For Newtonian fluids, the viscous shear stress tensor is defined as:

$$\tau_{ij} = \mu \left(\frac{\partial u_i}{\partial x_j} + \frac{\partial u_j}{\partial x_i} - \frac{2}{3} \delta_{ij} \frac{\partial u_K}{\partial x_K} \right) \quad (4.6)$$

Where: μ : the dynamic viscosity coefficient.

Following the Boussinesq assumption[†], the Reynolds stress tensor is given by:

$$\tau_{ij}^R = \mu_t \left(\frac{\partial u_i}{\partial x_j} + \frac{\partial u_j}{\partial x_i} - \frac{2}{3} \delta_{ij} \frac{\partial u_K}{\partial x_K} \right) - \frac{2}{3} \rho K \delta_{ij} \quad (4.7)$$

Where:

- μ_t : the turbulent eddy viscosity coefficient
- K : turbulent kinetic energy
- δ_{ij} : Kronecker delta function[‡]

* Note for all equations in this section, ∂x_i and ∂x_j refer to changes in distance along two generic axes i and j in the Cartesian coordinate system. These can take values of 1, 2 or 3.

† This assumption states that the momentum transfer induced by eddy currents can be modelled using an eddy viscosity, analogous to how momentum transfer induced by molecular motion can be modelled using molecular viscosity.^[63, 64]

‡ Mathematical shorthand stating that when $i = j$, $\delta_{ij} = 1$ and for all other conditions, $\delta_{ij} = 0$. This factor ensures turbulent energy is accounted for along a given reference axis.

For laminar flows, μ_t and K are both zero; hence, the Reynolds stress tensor is zero and simplifies equations (4.3) and (4.4). Using the K - ε model for turbulent flow, the turbulent viscosity is given by:

$$\mu_t = f_\mu \frac{C_\mu \rho K^2}{\varepsilon} \quad (4.8)$$

Where: f_μ : turbulent viscosity factor
 C_μ : constant – defined empirically for each specific fluid with a typical value of 0.09
 ε : turbulent dissipation

The viscosity factor is given by:

$$f_\mu = [1 - e^{-0.025R_y}]^2 \cdot \left(1 + \frac{20.5}{R_T}\right) \quad (4.9)$$

$$R_y = \frac{\rho \sqrt{K} y}{\mu}, \quad R_T = \frac{\rho K^2}{\mu \varepsilon}$$

Where: y : the distance from the model wall

In the above equation, R_T and R_y allow the turbulence intensity within the fluid flow in the Reynolds transition range ($2300 < Re < 4000$) to be estimated.

To describe the turbulent energy (K) and the turbulent dissipation (ε), two further transport equations are used:

$$\frac{\partial \rho K}{\partial t} + \frac{\partial}{\partial x_i} (\rho u_i K) = \frac{\partial}{\partial x_i} \left(\left(\mu + \frac{\mu_t}{\sigma_K} \right) \frac{\partial K}{\partial x_i} \right) + S_K \quad (4.10)$$

$$\frac{\partial \rho \varepsilon}{\partial t} + \frac{\partial}{\partial x_i} (\rho u_i \varepsilon) = \frac{\partial}{\partial x_i} \left(\left(\mu + \frac{\mu_t}{\sigma_\varepsilon} \right) \frac{\partial \varepsilon}{\partial x_i} \right) + S_\varepsilon \quad (4.11)$$

Where: σ_K : constant, typical value = 1
 σ_ε : constant, typical value = 1.3

The force terms S_K and S_ε are defined as:

$$S_K = \tau_{ij}^R \frac{\partial u_i}{\partial x_j} - \rho \varepsilon + \mu_t + P_B \quad (4.12)$$

$$S_\varepsilon = C_{\varepsilon(1)} \frac{\varepsilon}{K} \left(f_1 \tau_{ij}^R \frac{\partial u_i}{\partial x_j} + \mu_t C_B P_B \right) - C_{\varepsilon(2)} f_2 \frac{\rho \varepsilon^2}{K} \quad (4.13)$$

$$P_B = -\frac{g_i}{\sigma_B} \frac{1}{\rho} \frac{\partial \rho}{\partial x_i}, \quad f_1 = 1 + \left(\frac{0.05}{f_\mu} \right)^3, \quad f_2 = 1 - e^{-R_T^2}$$

Where: P_B : represents turbulent generation from buoyancy forces
 $C_{\varepsilon(1)}$: constant, typical value = 1.44
 C_B : constant, = 1 when $P_B > 0$, otherwise 0
 $C_{\varepsilon(2)}$: constant, typical value = 1.92
 g_i : component of gravity in the direction i
 σ_B : constant, = 0.9

To take into account heat transfer through the fluid and assuming a Lewis number (Le , the ratio of heat diffusion-to-fluid diffusion) of 1, the diffusive heat flux is defined as:

$$q_i = \left(\frac{\mu}{Pr} + \frac{\mu_t}{\sigma_c} \right) \frac{\partial h}{\partial x_i} \quad (4.14)$$

Where: Pr : the Prandtl number (the ratio of momentum diffusivity to thermal diffusivity)
 σ_c : constant, = 0.9

4.6.1.2 Equations of State

The system of Navier-Stokes conservation laws, equations (4.2) to (4.5), is supplemented by definitions for the thermophysical properties (specific heat ratio, thermal conductivity, viscosities, *etc.*) and state equations for the chosen fluids. The program simulates gas and liquid flows with density, thermal conductivity, specific heat and fluid diffusivities as functions of pressure, temperature and concentration (in the case of mixtures).

Modelling the fluids flowing through the non-contact cell as incompressible ideal gases simplifies the required equation of state and drastically reduces the amount of computing power required to solve the Navier-Stokes equations, and this assumption holds true unless the system approaches the gas-liquid transition point, either by cooling or increasing pressure. As such, the equation of state takes the form:

$$\rho = \frac{P}{RT} \quad (4.15)$$

$$R = R_{univ} \sum_m \frac{[F]_M}{M_M}$$

Where: R : the gas constant for a given mixture
 R_{univ} : the universal gas constant
 $[F]_M$: the concentration of fluid component 'M'
 M_M : the molecular mass of fluid component 'M'

4.6.1.3 Mass Transfer

Mass transfer in fluid mixtures is governed by species conservation equations, and the equations that describe the concentrations of the individual components of the mixture are:

$$\frac{\partial \rho [F]_M}{\partial t} + \frac{\partial}{\partial x_i} (\rho u_i [F]_M) = \frac{\partial}{\partial x_i} \left((D_{MN} + D_{MN}^t) \frac{\partial [F]_N}{\partial x_i} \right) + S_M \quad (4.16)$$

Where: $[F]_N$: the concentration of fluid component 'N'
 D_{MN} : molecular diffusion matrix between component 'M' and 'N'
 D_{MN}^t : turbulent diffusion matrix between component 'M' and 'N'
 S_M : rate of production/consumption of fluid component 'M'

4.6.1.4 Porous Media

A useful approximation to save computer resources is to set the micro-jet array as a porous medium.^[65] The characteristic dimension of the holes in the array (18 μm) is much smaller than the next closest dimension (3 mm for the sweep/curtain inlet conduits). This can cause excessive splitting in the generated mesh for the calculation, increasing the calculation time.

Porous media are treated as distributed flow resistances, and as such contribute to the mass distributed external force terms S_i and $S_i u_i$ in equations (4.3) and (4.4). (If heat conduction in solids is considered by the software, then the porous medium also contributes to Q_H .) The external force component related to porous media is given by:

$$S_i^{porous} = -S_{Res} \delta_{ij} \rho u_j \quad (4.17)$$

Where: S_{Res} : the resistance vector of the porous medium

In the region of the porous medium, turbulence disappears and only laminar flow remains. Additionally, in this region the density of the fluid mixture in equations (4.2) to (4.4) is multiplied by the porosity, which is defined as the volume fraction of the pores with respect to the total medium volume.

The resistance vector, S_{Res} , is calculated depending on the definition of the porous medium. For the micro-jet array, an appropriate definition is of a unidirectional porous medium. From this, the resistance vector is given by:

$$S_{Res} = \frac{\Delta P A_C}{\dot{m} L} \quad (4.18)$$

Where: ΔP : the pressure drop through the medium
 A_C : the cross sectional area of the medium
 L : the length of the medium
 \dot{m} : the mass flux of the fluid through the medium

The pressure drop for the mesh was calculated using a single repeat unit for the mesh geometry. Repeat unit consisted of a parallelogram with 400 μm sides, with four 18 μm holes spaced 200 μm apart in a regular equilateral triangular pattern. This yields a porosity of 0.07 (or 7 % v/v). The details for this unit are shown in Appendix C.

A flow of air was simulated from 0.1 to 1.0 l min^{-1} , and the resultant pressure drop across the two faces of the repeat unit was calculated. The trend can be seen in Figure 4.48 overleaf. The results for the calculation were applied to the micro-jet array component in the CAD assembly, and the software was able to scale the pressure drop according to the dimensions of the final model.

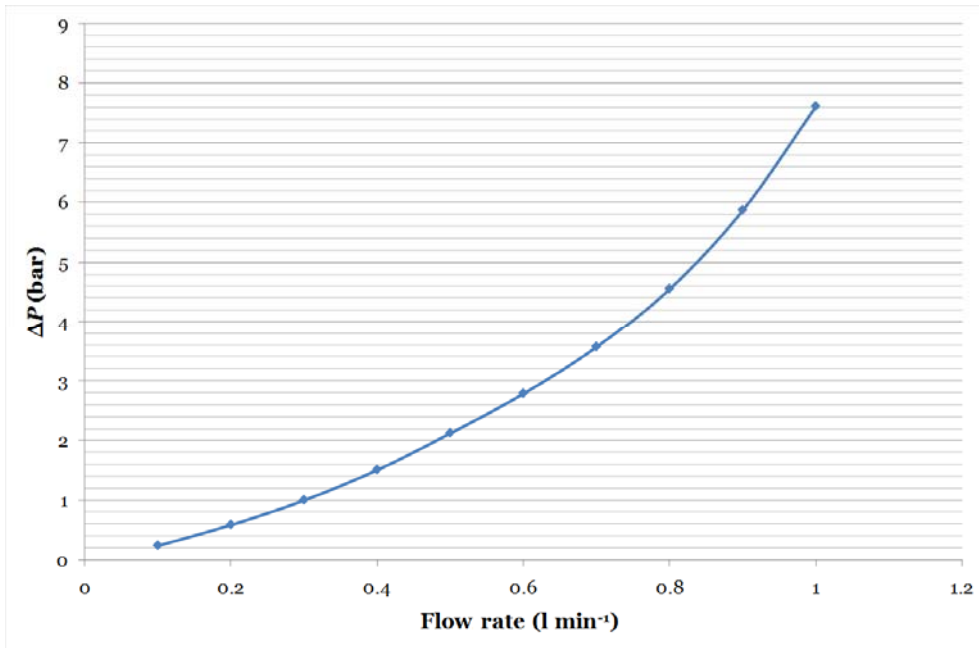


Figure 4.48: Pressure drop *vs* volumetric flow rate for air through the micro-jet array repeat unit. The results of this calculation were inputted into the Flow Simulation database and scaled to the correct area for the array used in the final CAD model geometry.

4.6.1.5 Particle Flow within the Fluid Flow

Flow Simulation has the ability to simulate particles flows for spherical particles in a steady-state flow field. It can only simulate dilute particle flows, where the influence of the particle flux on the fluid parameters (*e.g.* temperature) is negligible. This is defined as a particle mass flux less than 30% of the fluid mass flux.

The particles are assumed to be spherical, of constant mass and material. Reflections on model surfaces are governed by the two particle restitution coefficients, which is dependent on particle material:

$$e_n = \frac{V_{2(n)}}{V_{1(n)}} \quad (4.19)$$

$$e_\tau = \frac{V_{2(\tau)}}{V_{1(\tau)}} \quad (4.20)$$

Where: V represents the velocity component before (1) and after (2) reflection

As a result of impingement on the model surfaces, the rate of particle erosion and accretion are determined as:

$$R_{\Sigma(erosion)} = \sum_{i=1}^N \int_{M_{pi}} K_i V_{pi}^b f_{1i}(\alpha_{pi}) f_{2i}(d_{pi}) \cdot d\dot{m}_{pi} \quad (4.21)$$

$$R_{\Sigma(accretion)} = \sum_{i=1}^N M_{pi} \quad (4.22)$$

Where:

- N : number of particle injections (user specified)
- i : injection number
- M_{pi} : particle mass impinging on the model walls for injection i
- K_i : impingement erosion coefficient for injection i
- V_{pi} : particle impingement velocity for injection i
- b : velocity exponent ($b = 2$)
- $f_{1i}(\alpha_{pi})$: dimensionless function of particle impingement angle α_{pi}
- $f_{2i}(d_{pi})$: dimensionless function of particle diameter d_{pi}
- \dot{m}_{pi} : particle fraction mass flux

4.6.2 Numerical Solution Setup

The numerical solution technique used by Flow Simulation is based on the Finite Volumes (FV) iterative approach. The fluid model of the volume is split into discrete cells (cubes with planar faces parallel to the Cartesian axes), which are smaller at fluid/surface boundaries than in 'open space', collated together to form a mesh. The values for all the physical variables are stored in the centres of each discrete cell, and their effects on neighbouring cells are calculated. Generally, the more cells a mesh has, the more accurate the numerical results; however, this increases the strain on computational resources. An appreciation of how Flow Simulation generates the mesh can allow the user to streamline the efficiency of the calculation.

Since the mesh is rectangular in nature and the model's surface may be curved, special cells are employed at fluid/surface boundaries (termed 'partial' cells), where the solid volume intersects the discrete cell volume, that treat mass and heat flux properly. Flow Simulation can calculate fluid flows for both closed systems, where the fluid volume is implicitly bounded by boundary 'lids', and open systems, where fluids flow throughout the entire system.

Initially a computational domain is specified that encompasses the fluid volume the fluid flows will pass through. From here, a basic mesh is generated that splits the computational domain into equal volumes.

When setting up the mesh, the user can define the 'minimum gap size', which defines the smallest size of fluid cells to be generated. At the solid/fluid interface, the basic mesh cells are split into 8 equal volume child cells. Each of the child cells lying in a solid/interface region is then further split into 8 cells and the process repeated until the specified minimum cell size is reached.

Cells in the interface region are then tested for surface curvature, and if the maximum angle between the surface normals is exceeded, the cell is split. If a cell does not contain surface normals that exceed this maximum angle, it is merged with neighbouring cells and re-tested. This allows the generated mesh to efficiently follow the curvature of the fluid volume in the CAD model without excessive cell generation.

Finally, cells in a fluid region bounded by a so-called 'narrow channel', *i.e.* those regions where the mesh cell size is of the order of the gap, are split into 8 child cells to ensure there is a minimum number of cells spanning the gap. This parameter is set internally by the software.

Once the mesh procedure is finalised, it is advisable for the user to inspect the mesh to ensure all major features are modelled. Since the meshing procedure is carried out before the calculation is started, some mesh refinement may have to be performed in the middle of the calculation. This can be set manually to run after a preset time, or automatically by the software to refine after certain criteria are met.

After the mesh has been generated to a satisfactory level, the initial conditions for the fluids are applied to the cell centres, in terms of velocity vectors and concentrations. A proprietary iterative algorithm is then applied to solve equations (4.2) to (4.5). This process continues until the 'stopping criteria' are met, which could be either a specific iteration number or, more usually, when a particular variable has stabilised, *e.g.* pressure.

4.6.3 Non-Contact Cell Mesh Generation and Boundary Definitions

The model geometry was set so the cell is floating about the wafer by 200 μm between the top plane of the wafer and the bottom plane of the flow restrictor, as chosen in previous empirical tests.

The mesh generated to solve the CFD problem defined is shown in Figure 4.49 below. The cells generated describe the geometry of the non-contact cell well, with good resolution at the thin gaps. The cell is made up of 683,502 cells, comprising 358,219 fluid cells, 158,716 solid cells and 166,567 partial cells. The remaining cells are termed ‘trimmed’ cells, which are cells generated in cavities without flow conditions, and are excluded from the calculation to save time. In this case, these are located in the o-ring seal groove between the optical window and the main body.

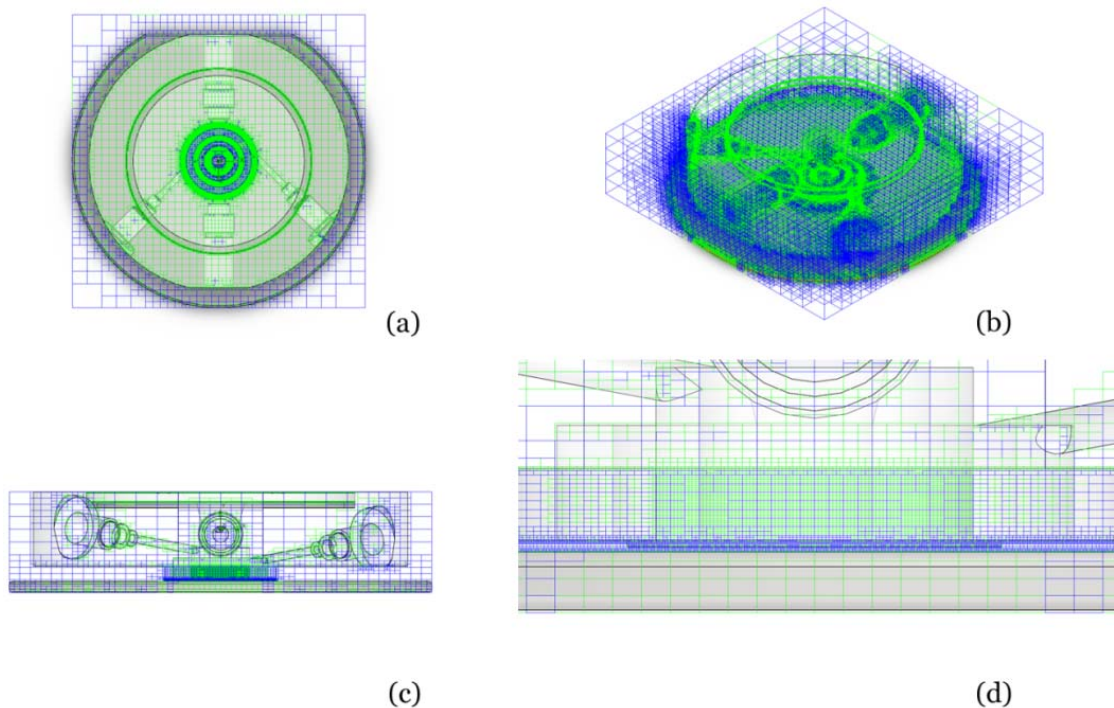


Figure 4.49: Mesh used to simulate the gas flows through the non-contact cell, showing fluid (blue) cells and partial (green) cells in (a) top, (b) isometric, (c) front and (d) zoomed front views.

Initial conditions were set so the model existed in an air atmosphere at the start of the calculation. Boundary conditions were applied as shown in Figure 4.50 across. The sweep gas inlet was set at $1.2 \text{ l min}^{-1} \text{ He}$ ($2.00 \times 10^{-5} \text{ m}^3 \text{ s}^{-1}$), and the curtain gas inlet at $2.5 \text{ l min}^{-1} \text{ N}_2$ ($4.17 \times 10^{-5} \text{ m}^3 \text{ s}^{-1}$).

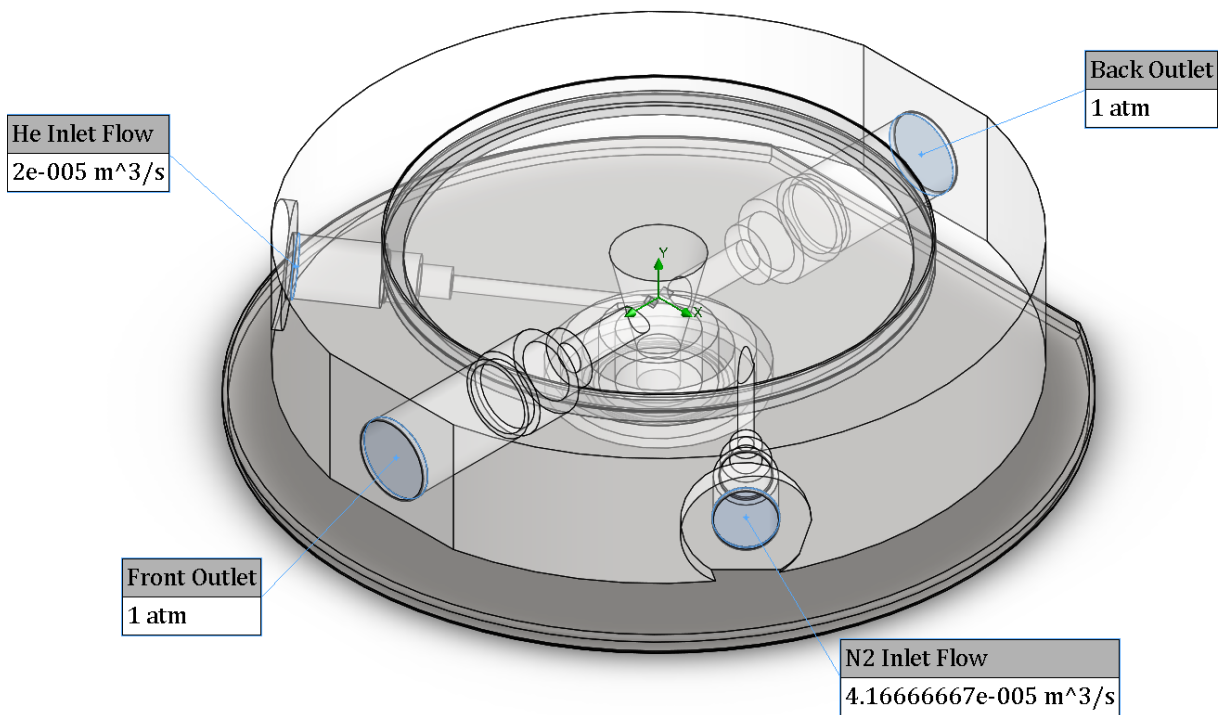


Figure 4.50: Position and values for boundary conditions used in numerical simulations for the non-contact cell.

The faces of the outlets were set as environment pressure, which means the pressure decays as close to ambient as possible without any flow assistance (*e.g.* the micro jet-pump). The micro jet-pump was left out of the calculation to separate out its effect from that of the micro-jet array.

2 models were solved – one with and one without the micro-jet array. In each case, the flow restrictor is present to keep its effects on gas flow constant. When the micro-jet array was present, it was modelled as a unidirectional porous medium with 7 % porosity in the axis perpendicular to the wafer surface (defined as the *y*-axis in the model above).

4.6.4 Gas Flow Patterns

The calculated field flows were characterised as false colour images on the wafer surface, indicating the efficiency of air exclusion. Air exclusion is shown for both models in Figure 4.51 below. The volume fraction of air across the wafer surface is uniform as close to zero when the micro-jet array is in use. Without it, there is no back-pressure experienced by the inlet helium or nitrogen flows; hence, they swirl and mix across the sample surface.

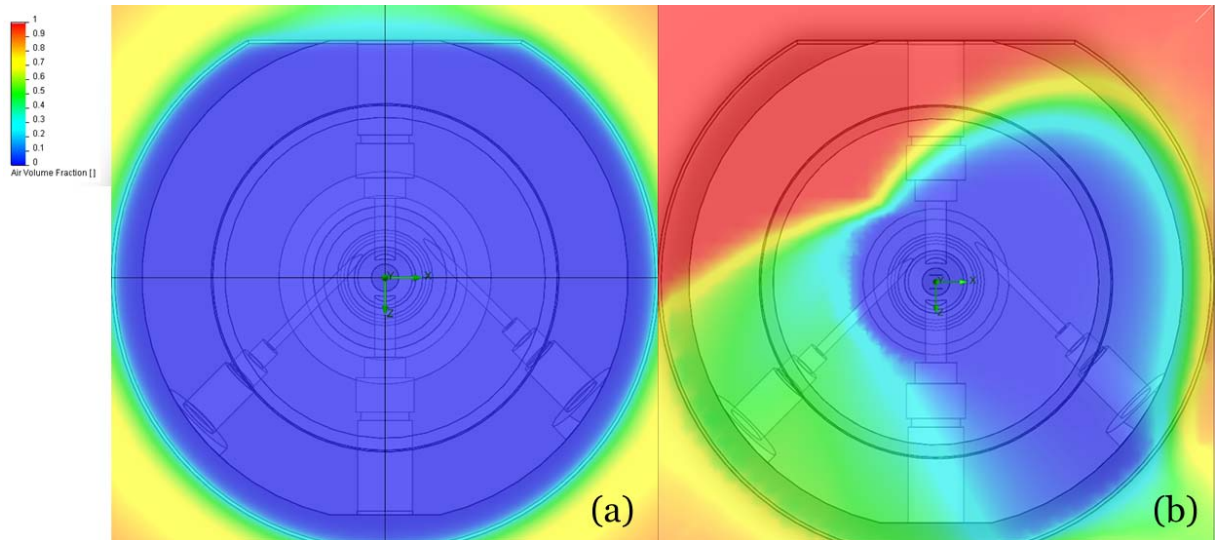


Figure 4.51: False colour images showing volume fraction of air across the wafer surface (a) with and (b) without the micro-jet array

Looking at helium and nitrogen independently, it is apparent that when the micro-jet array is not in place, the nitrogen flow entrains the helium flow away from the central volume of the NCC. This is also apparently circumventing the flow restrictor, and under these conditions it is ineffective. This is because the helical flows of nitrogen and helium are relatively ‘floppy’ and are able to mix together more freely.

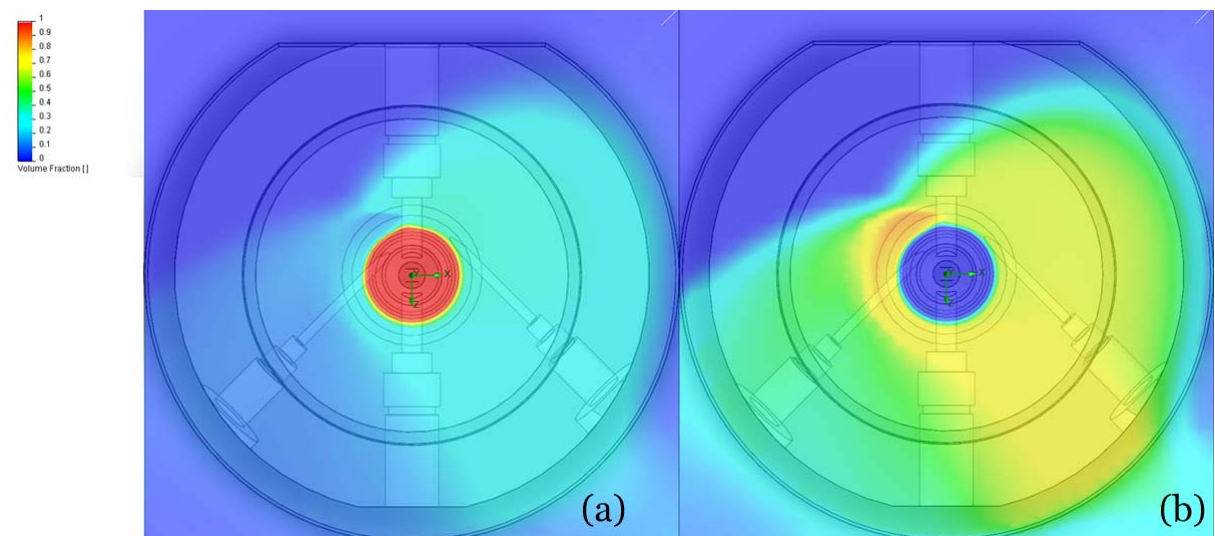


Figure 4.52: False colour images of (a) helium and (b) nitrogen volume fraction across the sample surface without the micro-jet array

The helium flow also shows entrainment into the curtain gas channel, indicating the flow is back-diffusing and mixing. This can be seen more clearly in Figure 4.53 below. The flow trajectories shown are coloured with nitrogen volume fraction, and can be see mixing in the curtain gas outlet channel.

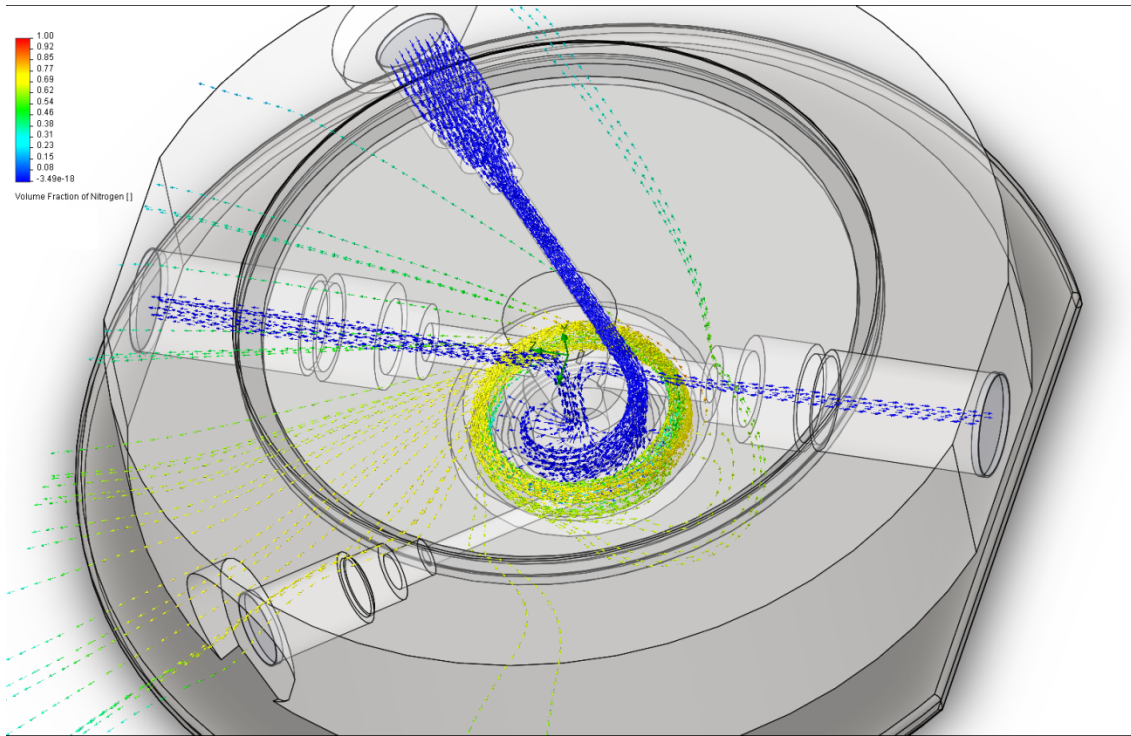


Figure 4.53: Flow trajectories from the sweep gas inlet, showing entrainment of the sweep gas into the curtain gas channel.

In contrast, with the micro-jet array in place the independent false colour images for helium and nitrogen show good separation of the two channels (see Figure 4.54 below). Nitrogen is spread across the sample surface uniformly and shows only minimal ingress into the central volume of the ablation cell.

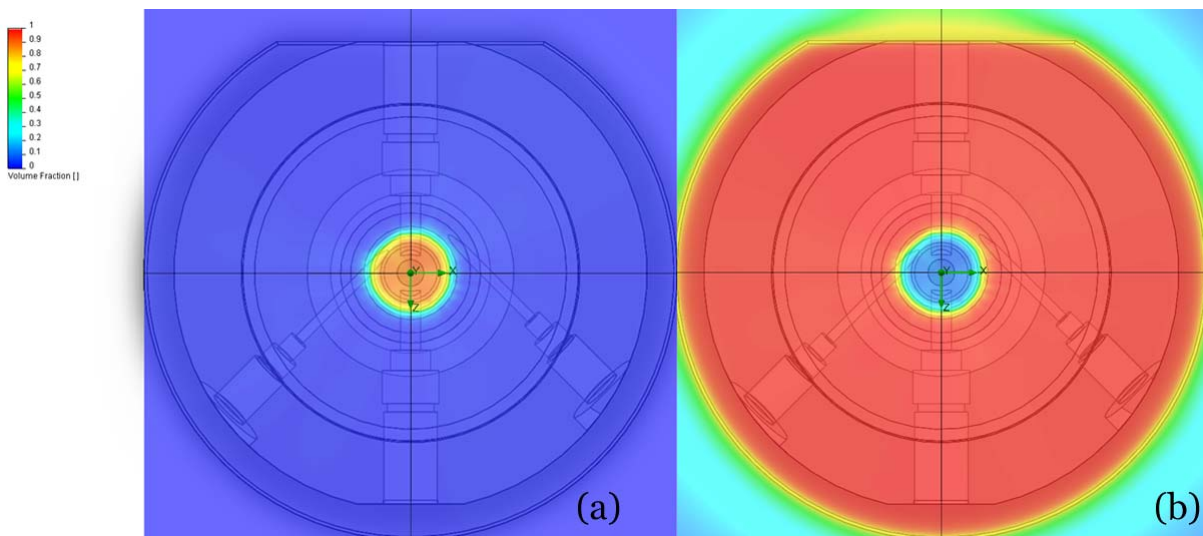


Figure 4.54: False colour images of (a) helium and (b) nitrogen volume fraction across the sample surface with the micro-jet array in place.

The flow trajectories for the sweep gas are also confined to the sweep gas channel, as shown in Figure 4.55 below. Due to the stiffness and the velocity of the gases at the exit plane of the micro-jet array, the sweep gas cannot physically diffuse and mix with the curtain channel before the curtain gas has exited the micro-jet array.

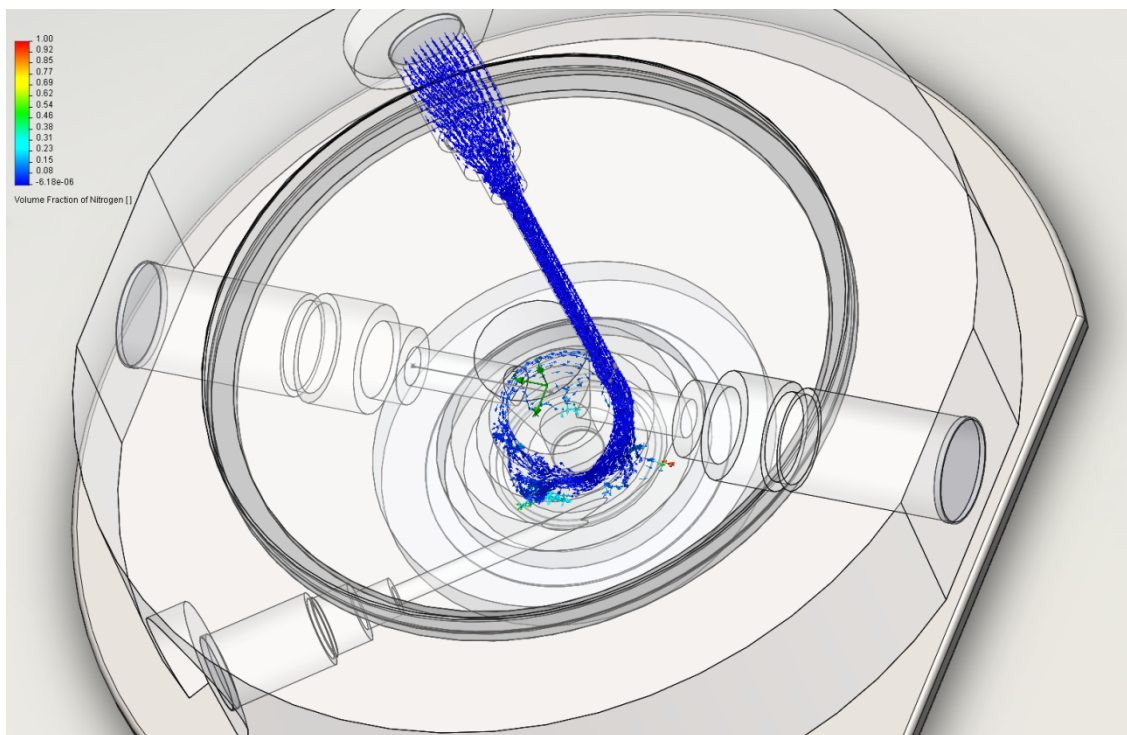


Figure 4.55: Flow trajectories for the sweep gas channel with the micro-jet array in place, showing flow separation and increased independence from the curtain gas channel.

The false colour images seem to suggest good air exclusion with and without the micro-jet array in place. However, the images do not show any information relating to volumetric flow rate. The flow rate was calculated at the front exit port boundary and the results are summarised in Table 4.5 below. The relative air exclusion is very similar in both cases; however, crucially the volumetric flow rate is approximately 4 times higher when the micro-jet array is in place.

Table 4.5: Summary of numerical results obtained by CFD for the non-contact cell

Condition	Density (kg m ⁻³)	Volumetric Flow rate (l min ⁻¹)	He (%)	N ₂ (%)	Air (%)
<i>No Micro-Jet Array</i>	0.166492	0.231	99.98	0.01	0.01
<i>Micro-Jet Array</i>	0.262586	0.944	79.71	20.29	0.00

The level of nitrogen present in the output flow when the micro-jet array is in use is diluted by the make-up flow or micro jet-pump flow. In most cases, this will be on the order of 0.400 – 0.600 l min⁻¹. Factoring this in to the volumetric flow rate, this equates to a final nitrogen concentration of 12 – 14%, shown to be beneficial to analyte sensitivity in previous studies.^[59]

4.6.5 Particle Transport

Particle transport through the cell was estimated for both conditions. The material chosen was glass, as this matches the standard reference materials measured in the preceding sections. The mass flux was estimated by assuming a laser track 100 μm in diameter, scanned at a rate of 10 $\mu\text{m s}^{-1}$. This means in 1 min during a line scan, the laser will track 600 μm , as illustrated in Figure 4.56 below. The leading and trailing edges of the track have the same geometry; hence, this laser track can be approximated to a $100 \times 600 \mu\text{m}$ rectangle.

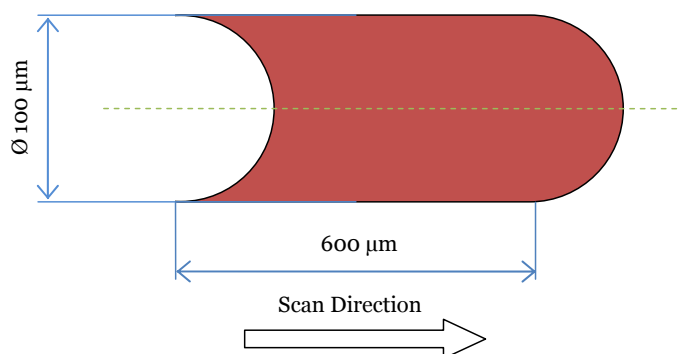


Figure 4.56: Shape of a transient 100 μm laser track.

Ablation depth was measured empirically using the optical focus on a UP-213 LA system after ablating a 600 μm track in NIST glass. This was estimated to be approximately 35 μm . The volume of this track multiplied by the density of glass (2320 kg m^{-3}) yields an ablated mass of approximately 5 ng in one minute, so this mass flux rate was defined in the particle injection parameters. The particle diameter was also defined as 1 μm , as this represents the upper limits for an ‘ideal’ ablation particle size distribution; hence, a ‘worst case scenario’.

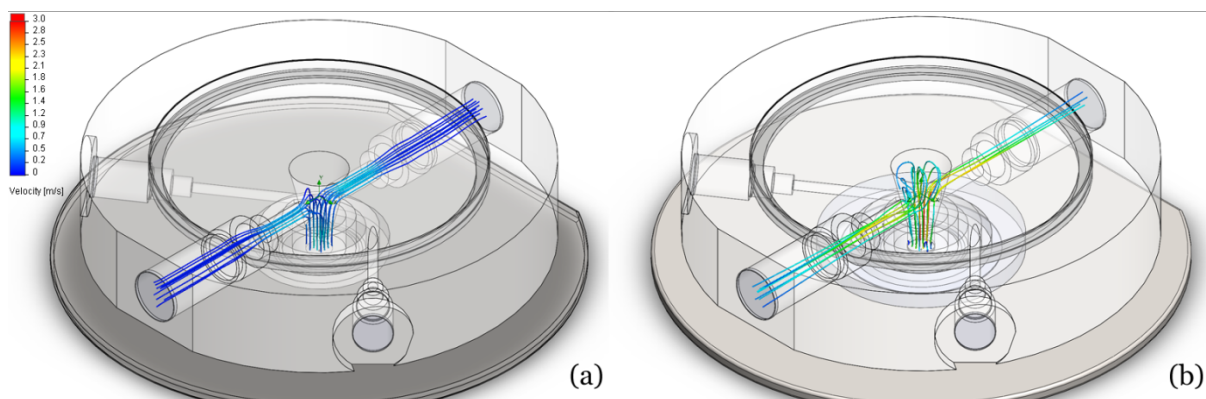


Figure 4.57: Particle flow trajectories for 1 μm glass particles ($\dot{m} = 5 \text{ ng min}^{-1}$) through the non-contact cell both (a) without and (b) with the micro-jet array. Trajectories are coloured with particle velocity.

The resulting particle trajectories for 20 particles spaced equally along the face of the central chamber volume closest to the sample surface are shown in Figure 4.57 above. The trajectories show that the particle velocity is faster through the cell when the micro-jet array is in place. This is due to the increased volumetric flowrate (and hence, linear velocity) of the gas flow through the cell, which imparts more momentum to the particles when the micro-jet array is in place. However, this increased gas velocity (and hence, gas momentum) causes eddy currents to form at the connecting point between the inner volume of the cell and the exit ports.

Consequently, the additional momentum transferred to the particles combined with the eddy currents means that the particles swirl at the connecting point between the inner volume of the NCC and the exit ports, which increases the trajectory length. This indicates the particles will impact the cell window, which is seen as predicted when running softer biological materials (see Figure 4.58 below). The material impacts the cell window and is burnt into the window coating by successive laser pulses.



Figure 4.58: Deposition of soft, biological material on the non-contact cell window. In this figure, the material has been burnt into the window coating.

The increased trajectory length can be seen more easily in the velocity profiles for the particle trajectories, shown in Figure 4.59 below. The increased particle swirl also means that more particles may impact on the surface of the optical window and be lost from the solid aerosol during transport.

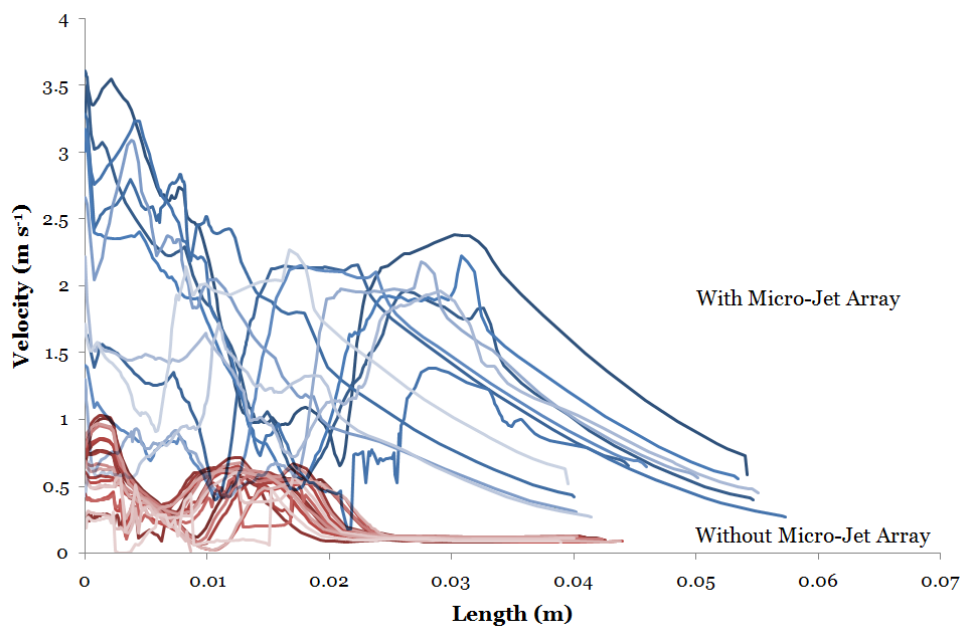


Figure 4.59: Calculated velocity profiles of trajectories for 1 μm spherical particles through the NCC with (blue) and without (red) the micro-jet array in place.

Integrating the inverse of these velocities with respect to trajectory length gives the total transit time for 1 μm spherical glass particles. This equates to 116.2 ± 13.3 ms without the micro-jet array and 49.2 ± 12.1 ms with the micro-jet array in place. This suggests the increased velocity is sufficient to sweep the particles through the inner volume of the non-contact cell with the micro-jet array in use approximately twice as fast as without, despite the apparent eddy currents increasing the trajectory length.

The algorithms used by Flow Simulation do not, however, take into account random particle-particle motion or collisions during transport, such as a Markov chain Monte-Carlo algorithm used by other, more sophisticated CFD packages. This type of algorithm assigns random movement to the particle at each iteration of the calculation, consequently accepting or rejecting the motion based on the probability of that motion occurring. Using such an algorithm may produce a more accurate answer for particle transport times, but only if the number of trajectories calculated was sufficiently large.

5 Parallel Research

This section of the thesis outlines work done to achieve ‘satellite objectives’ that are loosely related to the main focus of the research. These are:

1. Development of a vacuum interface for particle transport
2. Development of a matrix-assisted laser desorption-electrospray ionisation method for the identification of biomolecules
3. Development of a single-point calibration method for semi-conductor samples

In all cases, the research shows promise; however, ultimately there is a substantial amount of further work required for these objectives to be fulfilled. Completion of these objectives will be beneficial to the industry as a whole, which will be discussed in the proceeding sub-sections.

5.1 Aerosol Lens Stacks for Particle Transport

For operation in MALDI mode, soft desorption of large biomolecules leads to a charged plume expanding away from the sample surface at atmospheric pressure. Mass analysis, as shown in Section 1.2.2 previously, occurs under vacuum; hence, a vacuum interface is required to allow both sections of the technique to work effectively.

Current vacuum interfaces for sample introduction to mass spectrometers consist of at least one cone with a small orifice. This can lead to sample losses as the gas carries sample around the cone as opposed to into the instrument through the orifice (see Figure 5.1 below), thereby reducing the sensitivity of the chosen method.

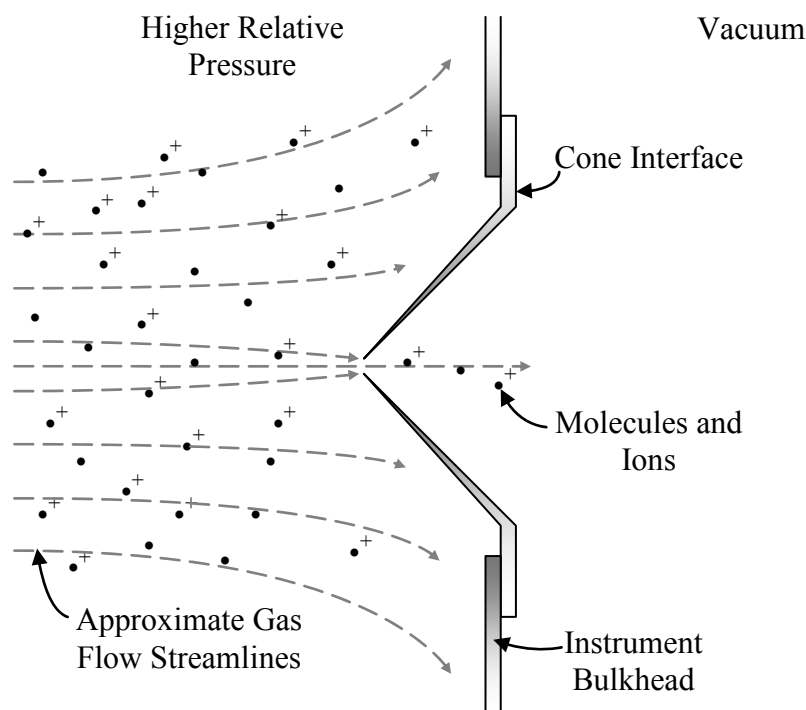


Figure 5.1: A single cone vacuum interface illustrating losses in sampling

It is possible to reduce the diameter of a particle flow by reducing the diameter of the space that contains it; however, the particle concentration is not increased and therefore, problems with sensitivity can still be apparent with time resolved techniques.^[66]

Use of a flow concentrator can increase the amount of sample entering the vacuum region, which at this stage should be purely ions. These include virtual impactors and aerodynamic lenses.^[67]

Virtual impactors consist of an accelerating nozzle, through which the particle flow is passed. A receiving tube, placed coaxially and directly after the nozzle, collects a small fraction of the flow containing particles larger than a certain aerodynamic size (see Figure 5.2 below). This is the preferred interface for most organic mass spectrometers; however, this collected fraction only represents between 5% and 20% of the total number of particles in the flow, which means a loss in sensitivity still arises.

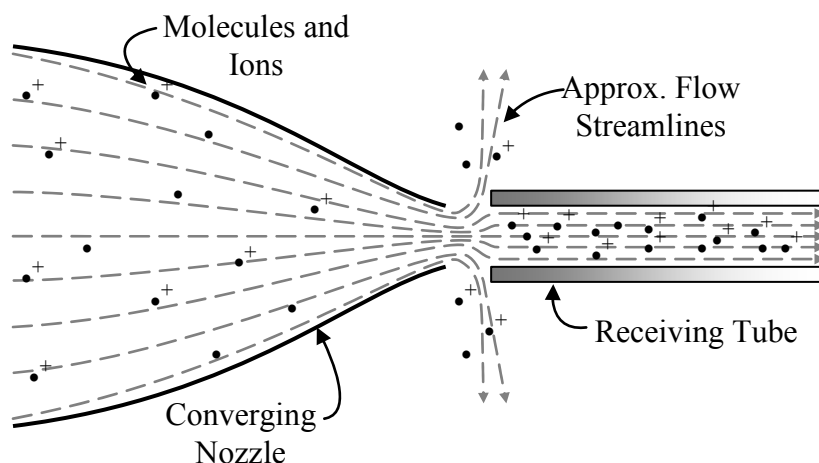


Figure 5.2: Action of a virtual impactor flow concentrator showing increased particle concentration

Aerodynamic lenses create concentrated particle beams by converging streamlines within the flow by forcing the flow through a small pinhole or nozzle (see Figure 5.3 below).^[68-70] This creates a shift in the particle velocity and, depending on the particle inertia, can lead to focusing of the particles. The sample fraction passing through this system is significantly greater than that passing through a virtual impactor; hence, an aerodynamic lens is more feasible as a flow concentrator.

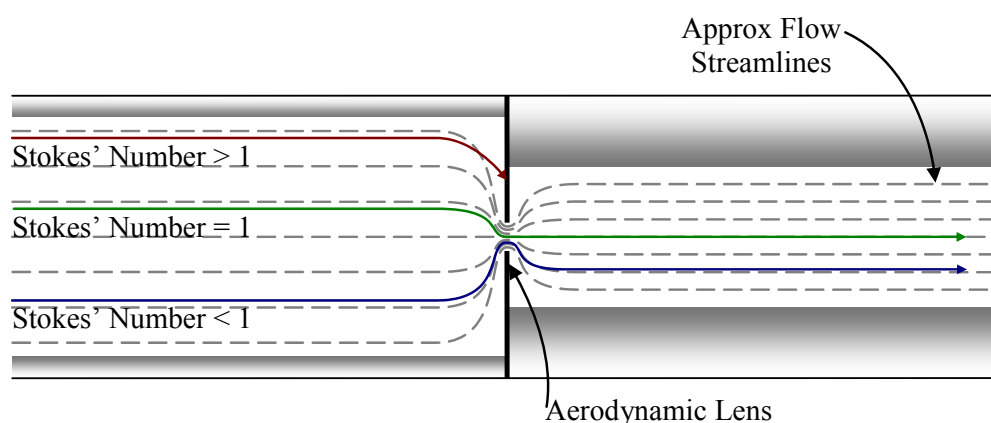


Figure 5.3: An aerodynamic lens system showing carrier gas streamline contraction and approximate particle streamlines dependent on Stokes' number

The degree of focusing is governed by particle Stokes' Number (St) and particle Reynolds' Number (Re). Particles with Stokes' Number significantly greater than 1.0 leave the streamlines of the carrier gas and are lost by impaction, those with Stokes' Number significantly lower than 1.0 follow the gas streamlines implicitly and those with Stokes' Number equal to 1.0 are focused along the centreline of the lens.

5.1.1 Selected Applications for Aerodynamic Lenses

This section covers a few applications of aerodynamic lenses that highlight their use in analytical chemistry, and why they would be useful integrated into the transport system between the NCC and an organic mass analyser.

In 2006, Alfarra *et al.*^[71] used an Aerodyne Aerosol Mass Spectrometer (AMS) to detect and quantify volatile organic compounds (VOC's) related to daily mortality/morbidity rates and adverse health effects. Looking at just the hardware alone, the Aerodyne AMS focuses the sample aerosol using an aerodynamic lens stack^[72], which comprises six lenses under vacuum, and measures the particle size distribution in the aerosol by means of a ToF system.^[72] The particles are then flash vaporised on a heated block, ionised with an electron ionisation source and detected using a quadrupole mass spectrometer.

In 2007, Harris *et al.*^[73] modified a PolarisQ Ion Trap Mass Spectrometer (ThermoFinnigan, Austin, TX) to incorporate an aerodynamic lens as the sample inlet. The lens itself was based on the design by Liu *et al.*^[68, 69] in 1995, which was a five-lens stack under vacuum, focusing particles to a beam less than one millimetre in diameter. Aerosol particles from chemical-warfare related species were desorbed from samples of house dust and injected into the ionisation source of the mass spectrometer *via* the aerodynamic lens stack. Since the mass analyser was an ion trap, tandem MS was possible enabling detection and identification of chemical warfare agents.

Spencer *et al.*^[74] coupled a Differential Mobility Analyser (DMA) to an AMS through an aerodynamic lens stack, operating at an inlet pressure of 2.1 Torr. By coupling the DMA to the AMS, the information gathered by the AMS was expanded from chemical composition and vacuum particle size to include particle effective density, which is a combination of particle density and aerodynamic shape. In this study, it was found that the chemical composition of ambient atmospheric aerosols varies greatly with time for the same effective density and is highly sensitive to changes in ambient humidity.

In all cases above, the aerodynamic lens was operated at sub-atmospheric pressures, usually around the 2 Torr region. The lens stack was used to focus particles for sizing experiments, using light scattering from the particle beam to measure the particle size distribution. Because the stack operates at low pressures, it can also be used as a vacuum inlet, which may be of use in this project for coupling to organic mass spectrometers that require such an interface.

5.1.2 Aerodynamic Lenses as Particle Size Selectors

Precedence has been set for the aerodynamic lens to be used as a vacuum interface; however, one property that may be useful to LA-ICP-MS is the ability for a lens to reject large particles from the aerosol stream, *i.e.* those particles where the Stokes' number is significantly greater than 1.0.

Section 1.4.2 highlights the problem of elemental fractionation during a LA-ICP-MS, with the major contributing factor being the particle size distribution. Large particles are inefficiently processed in the plasma, trapping non-volatile and refractory elements and decreasing the ultimate signal intensity for those elements, *e.g.* for efficient ionisation of glass particles, the maximum particle size has been reported to be around 150 nm.^[75]

Volatile elements, however, escape from the large particle more readily and suffer from lower reductions in ultimate sensitivity; hence, isotope ratios between elements of sufficiently different volatility can be inaccurate.

5.1.3 Design Calculations

The calculations required to select the correct orifice size and spacer dimensions for the lens housing system are very complex. Additionally, most applications of the aerodynamic lens system are performed under vacuum conditions, where the inlet pressure to the lens is frequently in the order of 1×10^{-3} bar and below. The LA step is performed at atmospheric pressure, so any lenses chosen have to be able to cope with the supplied gas load with minimal back-pressure.

Wang and McMurry^[76-78] provide a free calculator based on their modelling work available through their departmental website called The Aerodynamic Lens Calculator. The following discussion describes the mathematics used in this calculator and how the calculator can be applied to ICP-MS.

The lens system typically consists of an inlet, the aerodynamic lens stack and the outlet nozzle. The lens stack itself consists of a number of orifice plates in sequence separated by regions of free space, termed 'spacers' (see Figure 5.4 below). The lens system described in this work, however, has a single lens in the lens stack; hence, the particle transmission characteristics of the lens were considered as the main priority.

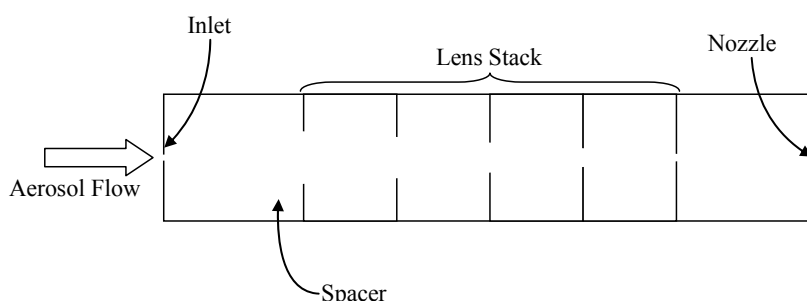


Figure 5.4: Typical configuration of a focusing aerodynamic lens system

For the calculator used, particles are assumed to spherical and neutral whilst the flow is assumed to be laminar, continuum and subsonic. For the flow to be laminar, the Reynolds Number has to be below a critical value, which is dependent on the diameter of the orifice and the length of the spacer behind it, such that:^[79]

$$Re = \frac{\rho_1 u d_f}{\mu} = \frac{4\dot{m}}{\pi \mu d_f} \leq 200 \quad (5.1)$$

Where: ρ_1 : carrier gas density upstream of the lens (kg m⁻³)
 u : carrier gas velocity upstream from the lens (m s⁻¹)
 d_f : aerodynamic lens orifice diameter (m)
 μ : carrier gas viscosity (Pa s)
 \dot{m} : carrier gas mass flow rate (kg s⁻¹)

The $\rho_1 u d_f$ term in Equation (5.1) represents dynamic forces within the fluid flow, whilst the viscosity term is a measure of the ability of the fluid to generate shear forces.^[58] In the case of laminar flow, the viscous (shear) forces dominate the characteristics of the flow, and heating by shear friction results in the loss of mechanical work done by the carrier gas, *i.e.* reduced turbulence. For the use of the lens calculator, Wang and McMurry^[77] recommend using a Reynolds Number of 200 or less.

In the free molecular flow regime, the particle inertia is greater than the drag force and no focusing, or indeed filtering, will occur.^[78] For this reason, the flow is restricted to the continuum regime by ensuring that the flow Knudsen Number (Kn) is below 0.1, such that:

$$Kn = \frac{2\lambda_1}{d_f} < 0.1 \quad (5.2)$$

Where: λ_1 : mean free path of gas molecules upstream from the lens (m)

To avoid the influence of shockwaves and compressibility on the flow streamlines, the flow has to be restricted to subsonic speeds. This means the lens Mach number is limited to be less than the Mach number corresponding to choked flow through the final lens element. Choked flow occurs when the pressure ratio reaches a critical value, whereby any subsequent decrease in downstream pressure has no effect on volumetric flow rate, hence there is a limit to the linear gas velocity.^[58] This critical pressure ratio is given by:

$$\frac{p^*}{p_1} = \left(\frac{2}{\gamma + 1} \right)^{\frac{\gamma}{\gamma - 1}} \quad (5.3)$$

Where: p^* : critical pressure for choked flow downstream of the lens (= p_2 = downstream pressure (Pa))
 p_1 : pressure upstream of the lens (Pa)
 γ : carrier gas specific heat ratio

The Mach number (Ma) corresponding to choked flow is given by:^[80]

$$Ma = \frac{u}{c} = \left[1 - (0.410 + 0.350\beta^4) \cdot \frac{\Delta p}{p_1 \gamma} \right] C_d \sqrt{\frac{2\Delta p}{p_1 \gamma}} \quad (5.4)$$

Where: c : local speed of sound in the carrier gas (m s^{-1})
 β : ratio of lens diameter to spacer diameter (constriction ratio)
 Δp : drop in pressure through the lens ($= p_2 - p_1$ (Pa))
 C_d : lens discharge coefficient

The lens discharge coefficient is a term describing how closely the flow follows inviscid, incompressible flow, i.e. it is the ratio of actual viscous flow rate to theoretical inviscid flow rate. This ratio is dependent on the flow Reynolds Number, such that:^[78]

$$C_d = \begin{cases} 0.1373\sqrt{Re} & \text{for } Re < 12 \\ 1.118 - 0.8873[\ln Re] + 0.3953[\ln Re]^2 \\ -0.07081[\ln Re]^3 + 0.005551[\ln Re]^4 & \text{for } 12 \leq Re < 5000 \\ -0.0001581[\ln Re]^5 & \\ 0.59 & \text{for } Re \geq 5000 \end{cases} \quad (5.5)$$

From Equations (5.3), (5.4) and (5.5) it is possible to calculate the maximum upstream Mach number for choked flow at any given mass flow rate. As mentioned previously, this is restricted to subsonic speeds to avoid supersonic shock effects downstream of the lens.

5.1.3.1 Particle Stokes' Number

The particle contraction factor (η) is the ratio of final to initial beam diameters through the lens, and is strongly dependent on the Stokes' number of the particle. When the Stokes' number is much smaller than 1.0, the contraction factor is approximately equal to 1. This means the beam diameters through a lens are equal, i.e. there is no focusing occurring through the lens.

As the Stokes' number approaches an optimal value, which is around $St = 1$ for most spherical particles, the contraction factor tends to zero, which means there is an optimal Stokes' number at which the final beam diameter is theoretically zero and the particle field is perfectly focused.

Beyond this limit, i.e. as St grows, the contraction factor increases again, which means the degree of focusing decreases. At a certain value of St , the magnitude of η grows larger than 1, which means the particle beam is defocused and grows at the exit of the lens.

The contraction factor depends on the Reynolds number, the Mach number and the Stokes' Number. This can only be estimated by numerical simulation, an account of which is discussed by Wang and McMurry.^[81, 82]

As Reynolds Number increases (*i.e.* higher mass flow rates, lighter carrier gases or smaller lenses), the Stokes' Number at which defocusing occurs decreases, which means the particle size at which defocusing starts to occur decreases. For focused particles through a lens, the particle Stokes number is given by:

$$St = \frac{\tau u}{d_f} = \frac{2\rho_p d_p^2 C_C \dot{m}}{\pi \rho_1 \mu d_f^3} \quad (5.6)$$

Where τ : particle relaxation time (s)
 ρ_p : average particle density (kg m⁻³)
 d_p : particle diameter (m)
 C_C : Cunningham slip correction factor

The Cunningham slip correction factor is used to correct for effects of molecular slip, which occurs when the particles are on the same size scale as the distance between gas molecules. In this case, the particles move along the flow without experiencing any drag from the gas molecules. The value of the Cunningham slip correction factor is given by:

$$C_C = 1 + Kn_p \left(1.257 + 0.4e^{\left(-\frac{1.1}{Kn_p}\right)} \right) \quad (5.7)$$

Where Kn_p : particle Knudsen number $\left(\frac{\lambda_1}{d_p}\right)$

Hence, for the optimal Stokes' Number, given by the relationship with the contraction factor, and for a particular particle diameter the size of lens required for focusing to occur is given by rearranging Equation (5.6):

$$d_f = \sqrt[3]{\frac{2\rho_p d_p^2 C_C \dot{m}}{\pi \rho_1 \mu St_0}} \quad (5.8)$$

The optimal Stokes' Number is dependent on flow Reynolds number, Mach number and lens geometry, which takes into account the constriction ratio (β). It has been shown by Liu *et al.*^[68] and by Zhang *et al.*^[83] that the dependence of Stokes' Number on β in thin plate orifices becomes weak when $\beta \leq 0.25$; hence, the constriction ratio is constrained within the calculator to less than this value to keep the optimal Stokes' Number around $St_0 = 1.0$.

As can be seen in Equation (5.4), the reduction in β then reduces the effect of lens geometry on the Mach number such that the maximum operating upstream Mach number is increased. This in turn reduces its effect on the optimal Stokes' Number. The effect of initial particle radial location becomes increasingly significant on the contraction factor as the Stokes' Number increases, and significant losses by impaction occur when $St > 10$.

5.1.3.2 Operating Pressures

The pressure upstream of the lens affects many factors that govern the lens diameter, so it needs to be estimated accurately.^[81, 82] The pressure is dependent on the mass flow rate such that:

$$\dot{m} = \frac{A_f C_d Y p_1}{\sqrt{1 - \beta^4}} \sqrt{\frac{2M_r}{RT_1} \cdot \frac{\Delta p}{p_1}} \quad (5.9)$$

Where:

- A_f : area of the lens (m²)
- Y : expansion factor $\left(1 - (0.410 + 0.350\beta^4) \frac{\Delta p}{\gamma p_1}\right)$
- M_r : molecular mass of the carrier gas (kg mol⁻¹)
- R : ideal gas constant (8.314 J K⁻¹ mol⁻¹)
- T_1 : upstream temperature (K)

Equation (5.9) can be rearranged to find the pressure drop such that:

$$\left(\frac{\chi}{\gamma p_1}\right)^2 \Delta p^3 - \frac{2\chi}{\gamma p_1} \Delta p^2 + \Delta p - \frac{\dot{m} R T_1 (1 - \beta^4)}{2A_f C_d^2 M_r} = 0 \quad (5.10)$$

Where: $\chi = (0.410 + 0.350\beta^4)$

The operating (downstream) pressure of the lens should be large enough for the flow through the lens to be continuum and subsonic to avoid both compressibility and shock effects. The minimum pressures for continuum flow (p_{Kn}) and subsonic flow (p_{Ma} , from a rearrangement of Equation (5.9)) are given as:

$$p_{Kn} = \frac{2}{d_f Kn^*} \cdot \frac{\lambda_r p_r T_1^2 (T_r + S)}{T_r^2 (T_1 + S)} \quad (5.11)$$

$$p_{Ma} = \frac{\dot{m} \sqrt{1 - \beta^4}}{C_d Y A_f} \cdot \sqrt{\frac{RT_1}{2M_r x_c}} \rightarrow \frac{\dot{m}}{C_d Y A_f} \cdot \sqrt{\frac{RT_1}{2M_r x_c}} \quad (5.12)$$

Where λ_r , p_r and T_r are reference values of λ , p and T according to Sutherland's Law

- Kn^* : critical particle Knudsen number
- S : Sutherland Constant for the carrier gas
- x_c : critical pressure drop ratio $\left(1 - \frac{p^*}{p_1}\right)$

Note, as $\beta \leq 0.25$, $\sqrt{1 - \beta^4}$ tends to 1, hence disappears for Equation (5.12).

Each combination of particle size and lens diameter has a characteristic focusing pressure (p_{focus}), which is given by the following:

$$p_{focus} = \frac{2\rho d_p^2 C_c \dot{m} R T_1}{9\pi\mu d_f^3 M_r St_0} \quad (5.13)$$

The maximum downstream pressure for any given particle size is dependent on the lens diameter, and the minimum operating pressures given by Equations (5.11) and (5.12). For small particles in the 500 nm range, p_{Ma} tends to be larger than p_{Kn} ; therefore, the lens size at which focusing is optimised occurs when the lines for p_{focus} and p_{Ma} intersect. In such cases, the following equation can be applied:

$$p_{Max} = \frac{648\dot{m}\mu^2 St_0^2}{\mu(C_d Y_d)^3 (d_p^2 \rho_p C_c)^2} \cdot \sqrt{\frac{M_r}{2RT_1 x_c^3}} \quad (5.14)$$

In the case where p_{Ma} and p_{focus} do not intersect, any pressure larger than p_{Kn} can be used to efficiently focus particles. However, as the pressure is increased the Reynolds number also increases, which means the Reynolds number then limits the maximum operating pressure of any lens.

Once the operating pressures have been calculated, it is then possible to calculate the particle size range that will be focused, the maximum inlet pressure with the corresponding volumetric flow rate and the overall dimensions of the lens setup.

5.1.3.3 Lens Performance

The three main important parameters for assessing lens performance are particle terminal velocities, particle beam widths and particle transmission efficiencies. All of the parameters need extensive numerical simulations to be estimated accurately, but a close approximation is easy to obtain.

Terminal Velocity

Assuming the downstream pressure out of the accelerating nozzle (see Figure 5.4) is low enough to avoid gas-particle collisions and that the particles are in thermal equilibrium with the carrier gas, the beam divergence can be estimated from the particle radial terminal velocity, given by the Maxwell-Boltzmann distribution. The particle radial velocity distribution is assumed to be frozen during the downstream expansion;^[68] therefore:

$$f(v_{pr}) \cdot dv_{pr} = \frac{m_p}{2\pi k T_{pF}} \cdot e^{-\left(\frac{m_p v_{pr}^2}{2k T_{pF}}\right)} \cdot 2\pi v_{pr} \cdot dv_{pr} \quad (5.15)$$

Where:

- v_{pr} : particle radial velocity (m s⁻¹)
- m_p : particle mass (kg)
- k : Boltzmann constant (1.38 × 10⁻²³ J K⁻¹)
- T_{pF} : particle frozen temperature downstream of the exit nozzle (K)

The particle terminal axial velocities (u_p) depend on a number of factors, including particle size, shape, nozzle geometry, pressure ratio and carrier gas. Using experimental data and numerical simulations, Wang and McMurry^[78] developed a fitted curve for use in their calculator that closely follows all data:

$$\frac{u_p}{c} = \frac{0.939 + 0.09St}{1 + 0.543St} \quad (5.16)$$

Beam Width

This is defined as the beam diameter in which 90% of the particle flux is contained. This is governed by the contraction factor through each lens and by diffusion broadening, which can be estimated using the root mean square displacement (x_{rms}):

$$x_{rms} = \sqrt{2Dt} \quad (5.17)$$

Where D : particle diffusion coefficient
 t : particle residence time (s)

Assuming the flow is fully developed upstream of the inlet (lens 0) and the particles are homogeneously distributed across the entire flow cross section, the initial beam diameter is ~83% of the inlet spacer diameter ($d_{s(0)}$). The particle beam diameter (d_B) before reaching the lens is then:

$$d_{B(0)} = 0.827d_{s(0)}\eta_0 + x_{rms(0)} \quad (5.18)$$

Where η_0 : contraction factor (
 The beam diameter at stage i in a multi-lens system is given by:

$$d_{B(i)} = d_{B(i-1)}\eta_i + x_{rms(i)}, i = 1 \text{ to } n \quad (5.19)$$

The beam diameter may be calculated to be larger than the spacer diameter, in which case those particles are assumed to be lost and the value for $d_{B(i-1)}$ is set to $0.827d_{s(i)}$.

Taking into account the Maxwell-Boltzmann distribution of radial velocities, the beam width at lens $i + 1$ (set at a distance L downstream of the lens i) can be estimated by:

$$d_{B(i+1)} = d_{B(i)}\eta_{i+1} + \frac{3.04L}{u_p} \sqrt{\frac{2kT_{pF}}{m_p}} \quad (5.20)$$

Note, η_{i+1} is a rough estimate of contraction factor at low exit pressure, as the contraction factor is invalid at these conditions.

Particle Transmission Efficiency

Losses through the lens system arise from impaction, both on the lens plate and the spacer walls, and from diffusion.

The lens can be viewed as an impactor plate. Particles with large Stokes' Numbers will leave carrier gas streamlines and impact on the surface of the plate; therefore, it is appropriate to use the spacer Stokes' Number (St_s) to characterise particle impaction. The characteristic velocity of the system is now the average flow velocity upstream of the lens (U_s) and the characteristic length of the system is now the spacer diameter (d_s); hence,

$$St_s = \frac{\tau U_s}{d_s} = \frac{4\tau Q}{\pi d_s^3} \quad (5.21)$$

Where Q : volumetric flow rate ($\text{m}^3 \text{s}^{-1}$)

Significant particle losses are seen to occur when St_s is in the range of 0.1 – 1, asymptotically tending to a value for transmission efficiency (φ_t) of $\varphi_t = 2 \left(\frac{d_f}{d_s}\right)^2 - \left(\frac{d_f}{d_s}\right)^4$ for very large Stokes' Numbers ($St_s > 1$), which corresponds to geometric blocking of the lens.^[83]

At any chosen flow Reynolds Number, there exists a cut-off Stokes' Number for which $\varphi = 0.5$, which is termed $St_{s(50)}$. Impaction particle losses are steep, dependent on the cut-off Stokes' Number:

$$\varphi_{t(lens)i} = \begin{cases} 1 & \text{for } St_s < St_{s(50)} \text{ or } d_{B(i-1)} \leq d_{f(i)} \\ 2 \left(\frac{d_{f(i)}}{d_{s(i-1)}}\right)^2 - \left(\frac{d_{f(i)}}{d_{s(i-1)}}\right)^4 & \text{for } St_s \geq St_{s(50)} \text{ or } d_{B(i-1)} > d_{f(i)} \\ 2 \left(\frac{d_{B(i-1)}}{d_{s(i-1)}}\right)^2 - \left(\frac{d_{B(i-1)}}{d_{s(i-1)}}\right)^4 & \end{cases} \quad (5.22)$$

Defocused particles will be lost on the walls of the lens system when $\eta < -1$ through any lens, in which case the particle radial position upstream of this lens is defined by r_i :

$$r_i = \frac{d_{s(i)}}{2\eta_i} \quad (5.23)$$

The transmission efficiency can now be estimated as the ratio of particle flux within this diameter to the total flux in that stage:

$$\varphi_{t(spacer)i} = \begin{cases} 1 & \text{for } d_{B(i)} \leq d_{s(i)} \\ 2 \left(\frac{d_{s(i)}}{d_{s(i-1)}\eta_i}\right)^2 - \left(\frac{d_{s(i)}}{d_{s(i-1)}\eta_i}\right)^4 & \text{for } d_{B(i)} > d_{s(i)} \\ 2 \left(\frac{d_{B(i-1)}}{d_{s(i-1)}}\right)^2 - \left(\frac{d_{B(i-1)}}{d_{s(i-1)}}\right)^4 & \end{cases} \quad (5.24)$$

Transmission losses due to diffusion are accounted for by the Gormley-Kennedy equation:

$$\varphi_{t(GK)i} = \begin{cases} 1 - 5.50\sqrt[3]{\xi^2} + 3.77\xi & \text{for } \xi < 0.009 \\ 0.819e^{-11.5\xi} + 0.975e^{-70.1\xi} & \text{for } \xi \geq 0.009 \end{cases} \quad (5.25)$$

$$\xi = \frac{D_i l_{s(i)}}{Q_i}$$

Where ξ : dimensionless diffusion deposition coefficient
 $l_{s(i)}$: spacer length
 Q_i : volumetric flow rate through lens i

Equation (5.25) assumes fully developed, stable laminar flow. Because the lens moves streamlines and particles away from the walls for the lens spacer, the actual diffusion losses is less than that predicted by Equation (5.25).^[82] The following simplified equation is used in the calculator:

$$\varphi_{t(diff)i} = \begin{cases} \frac{\varphi_{t(GK)i} + 1}{2} & \text{for } d_{B(i)} < d_{s(i)} \\ \varphi_{t(GK)i} & \text{for } d_{B(i)} \geq d_{s(i)} \end{cases} \quad (5.26)$$

The total particle transmission efficiency is the product of all transmission efficiencies associated with the lens system:

$$\varphi_t = \varphi_{t(lens)n+1} \cdot \prod_{i=0}^n [\varphi_{t(lens)i} \cdot \varphi_{t(spacer)} \cdot \varphi_{t(diff)i}] \quad (5.27)$$

Where $\varphi_{t(lens)n+1}$: the transmission efficiency through the exit nozzle.

5.1.4 Simulations

For a range of lenses, the transmission efficiencies were evaluated with an aim to estimate approximate particle size upper limits. The lenses chosen were 0.0018” (0.045 mm) and 0.0016” (0.041 mm) ruby straight orifices (Bird Precision, Waltham, MA, USA), 0.8 mm and 0.06” (1.5 mm) stainless steel orifices (in-house manufacture).

The dimensions of the single lens system are shown in Figure 5.5 below. The lens housing is set up with a relaxation chamber upstream from the lens to allow the pressure to stabilise to the operating pressure of the lens.

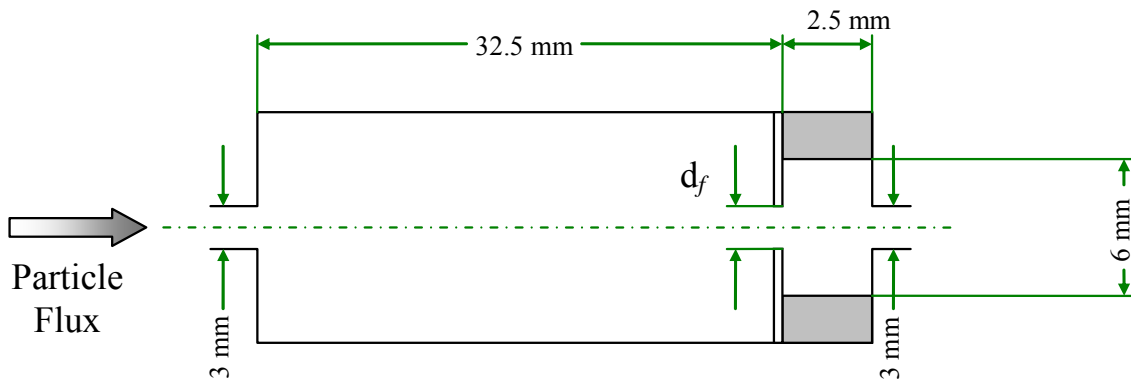


Figure 5.5: Dimension of the single lens setup

Setting a flow rate of 0.1 l min^{-1} , an operating pressure for the lens of 1.2 bar and a nozzle exit pressure at approximately 1 bar in The Aerodynamic Lens Calculator^[76-78], transmission efficiencies through these selected orifices were estimated (see Figure 5.6 below). As the lens size decreases, the upper size limit of the lens decreases. Note, the graphs for the 0.041 and 0.045 mm lenses overlap and have reduced transmission throughout the particle size range. This is because the lenses may experience geometric blocking effects, making it difficult for particles to pass through the system.

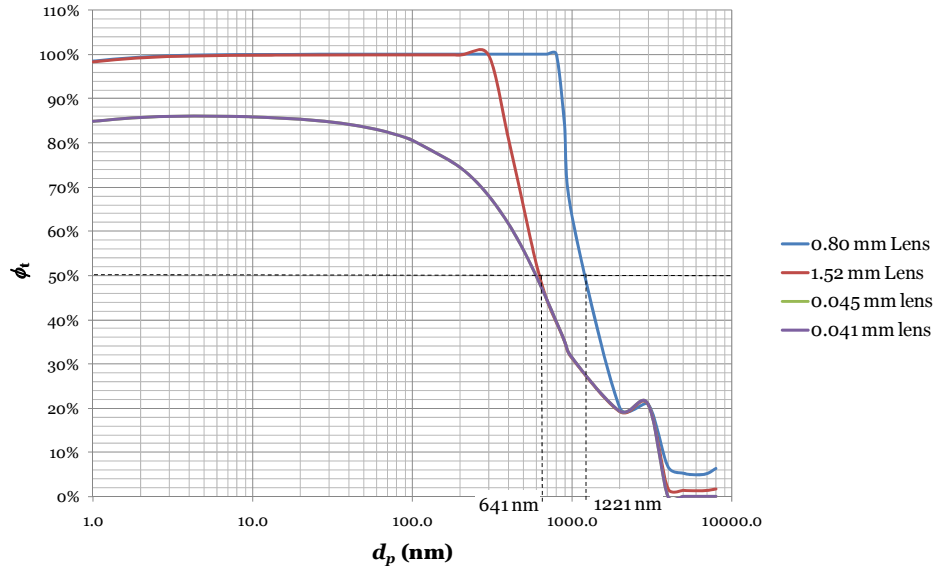


Figure 5.6: Particle transmission efficiency vs. particle size for four different lens sizes

The contraction factors shown in Figure 5.7 below illustrate the focusing ability of each lens. As discussed above, values such that $0 < |\eta| < 1$ show focusing of particles onto the centre line of the lens*; values such that $|\eta| > 1$ conversely show defocusing in the system. All lenses exhibit large defocusing effects for $d_p > 1000 \text{ nm}$, which implies there are significant impaction losses downstream in the spacer.

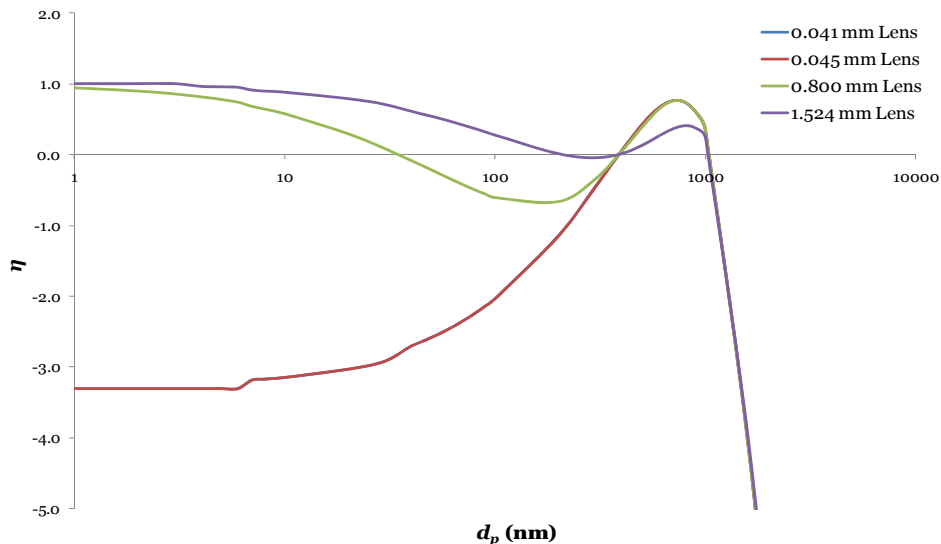


Figure 5.7: Contraction factors vs. particle size for four different lens sizes. The smaller lenses have contraction ratios that overlap, and these show focussing only for particles with diameters greater than $\sim 400 \text{ nm}$ up to $\sim 1000 \text{ nm}$.

* A negative value of η indicates the particle will cross the centreline during focusing.

5.1.5 Testing

To test the performance of the lenses as particle separators, isotope ratios were measured using ^{206}Pb , ^{207}Pb , ^{238}U and ^{232}Th . By setting up an ablation process designed to produce significant fractionation effects, the ratios are expected to be significantly different from theoretical values based on the sample used. With the lenses in place, this ratio should improve and approach the expected ratios.

Each lens was tested individually, downstream from the output from a UP-213 Laser Ablation System (New Wave Research, Huntingdon, UK). This was then coupled to an Element 2 XR ICP-MS (Thermo Scientific, Bremen, DE). The system employed argon make-up gas, tee'd in after the aerodynamic lens (see Figure 5.8 across).

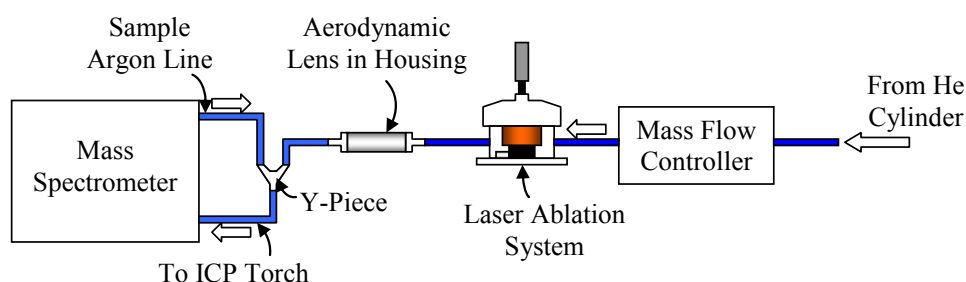


Figure 5.8: Schematic layout of the sample introduction system for LA-AL-ICP-MS

The sample used was NIST SRM 613: Trace Elements in Glass (NIST, Gaithersburg, MD, USA), certified to around 50 mg kg^{-1} for each of the measured elements. The ICP-MS and LA systems were configured to the settings shown in Table 5.1 below.

Table 5.1: LA-AL-ICP-MS Settings.

<i>Element 2 XR ICP-MS</i>			
Scanning Time	0.0105 s	Cool Gas	15.26 l min ⁻¹
Scan Type	EScan	Auxiliary Gas	0.82 l min ⁻¹
Runs	3	Sample Gas (make-up)	1.2 – 1.45 l min ⁻¹
Passes	27	RF Forward Power	1235 W
Resolution	Low		
Sample Time	2 min		
<i>UP-213 LA system</i>			
Line Scan Rate	10 $\mu\text{m s}^{-1}$	Fluence	85% (22.71 J cm ⁻¹)
Spot Size	65 μm	He Flow (sweep gas)	0.05 – 0.30 l min ⁻¹
Rep. Rate	20 Hz		

The total He and Ar gas flow entering the torch was kept constant at total 1.5 l min^{-1} at all times to maintain the residence time of ablated material in the plasma

As shown in Figure 5.9 below, the ion counts generally decreased as the lens size decreased. However, for the two smallest lenses (0.045 and 0.041 mm), the counts are of the same order as blank levels, so cannot be distinguished from noise levels. For this reason, isotope ratios calculated for these lenses cannot be considered to be representative of the sample.

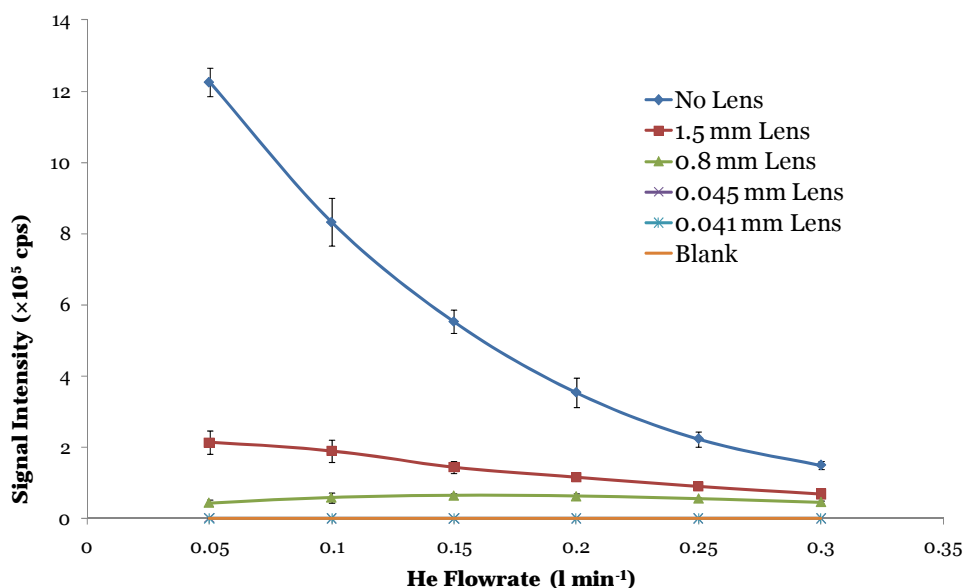


Figure 5.9: Signal intensity vs. volumetric He flow rate for ²⁰⁷Pb

Additionally, it is clear that the counts decrease as the volumetric flow rate of helium passing through the ablation cell increases. This is due to a number of effects introduced into the plasma characteristics as a result of changing the gas flow. The most obvious effect is that as the flow rate increases, the kinetic energy of the ablated particles increases. This reduces the particle residence time in the plasma, and hence reduces the amount of sample atomised and ionised. This is not a proportional effect, and has been highlighted previously by Mermet.^[84]

More importantly as the gas flow is increased, the characteristics of the whole plasma are altered, with respect to central channel width, zone structure, temperature, ionisation characteristics and effective sampling depth. This results in changes in signal intensity, the degree and direction of which are dependent on the element being measured. In practice, once the correct gas flow is established, the torch sampling depth would be tuned to compensate for these factors.

Theoretical nuclide ratios can be calculated from the natural abundances, certified concentrations and ionisation efficiencies of each nuclide in the plasma, ionisation efficiency being calculated using the Saha equation as detailed in Section 1.2.1.2 previously. The concentrations of each nuclide theoretically reaching the detector (adjusted concentrations) are calculated by multiplying the three values together. The adjusted concentrations are shown in Table 5.2 below:

Table 5.2: Adjusted concentrations for elements used in LA-AL-ICP-MS experiment, based on an electron density of $1.6 \times 10^{15} \text{ cm}^{-3}$ and a 6800 K plasma temperature. [8]

Isotope	Natural Abundance (%)	Ionisation Efficiency (%)	Certified Concentration (mg kg^{-1})	Adjusted Concentration (mg kg^{-1})
^{207}Pb	22.10	99.76	38.57 ± 0.20	08.50 ± 0.04
^{208}Pb	52.40	99.76	38.57 ± 0.20	20.16 ± 0.10
^{232}Th	100.00	99.91	37.79 ± 0.08	37.76 ± 0.08
^{238}U	99.27	99.92	37.38 ± 0.08	37.07 ± 0.08

Theoretical nuclide ratios can then be calculated by dividing the adjusted concentrations by each other, *e.g.*:

$$\frac{^{207}\text{Pb}}{^{208}\text{Pb}} = \frac{8.50}{20.16} = 0.422 \text{ (3 s.f.)}$$

The theoretical nuclide ratios are summarised in Table 5.3 below.

Table 5.3: Theoretical nuclide ratios between lead, thorium and uranium isotopes.

$\frac{^{207}\text{Pb}}{^{208}\text{Pb}} = 0.422$	$\frac{^{207}\text{Pb}}{^{238}\text{U}} = 0.229$	$\frac{^{208}\text{Pb}}{^{238}\text{U}} = 0.544$
$\frac{^{207}\text{Pb}}{^{232}\text{Th}} = 0.225$	$\frac{^{208}\text{Pb}}{^{232}\text{Th}} = 0.534$	$\frac{^{232}\text{Th}}{^{238}\text{U}} = 1.019$

Nuclide ratios of $^{207}\text{Pb}/^{208}\text{Pb}$, $^{207}\text{Pb}/^{232}\text{Th}$, $^{207}\text{Pb}/^{238}\text{U}$, $^{208}\text{Pb}/^{232}\text{Th}$, $^{208}\text{Pb}/^{238}\text{U}$ and $^{232}\text{Th}/^{238}\text{U}$ were calculated for no lens in place, and for the 0.8 mm and the 1.5 mm aerodynamic lenses for various helium flow rates. The $^{207}\text{Pb}/^{232}\text{Th}$ ratio (see Figure 5.10 across) shows a general decrease in value as the volumetric flow rate is increased for both lenses and the empty chamber. This may be due to the changes in the plasma characteristics mentioned above, *e.g.* the decreased residence time of the particles in the plasma may reduce the time for partitioning to occur in larger particles. This may also be a result of instrument response being altered by the many changes in plasma characteristics brought about by the increase in helium flow rate.

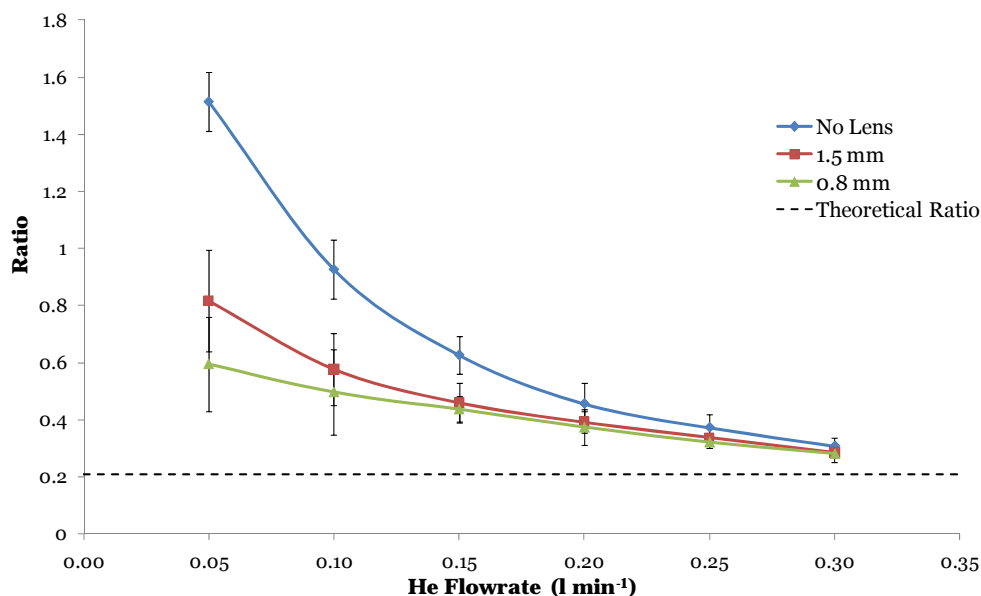


Figure 5.10: $^{207}\text{Pb}/^{232}\text{Th}$ ratio *vs.* volumetric He flow rate. As the flow rate through the ablation cell increases, the ratio tends towards the theoretical value. Additionally, the ratio decreases with aerodynamic lens size indicating ^{232}Th is enriched in larger particles and is lost within the plasma through incomplete processing.

Additionally, the increased gas flow in the laser plume expansion region increases the amount of collisional plume cooling by the sweep gas, and decreases cooling by condensation processes. The transport tubing in the laser ablation system may also act as a particle separator at higher sweep gas flow rates, making the aerodynamic lens further down the line redundant. The trends suggest that even higher flow rates will improve the ratio towards the theoretical even more.

The $^{207}\text{Pb}/^{232}\text{Th}$ ratio also shows a trend towards the theoretical value as the lens size decreases, notably at lower flow rates where the effects described above are less important. This suggests an optimal lens size for the reduction of elemental fractionation in NIST glass samples for this ratio.

This end result is a reduction in apparent elemental fractionation. This could be due to the effects of the altered plasma characteristics, which suggests the particles reaching the plasma are still large and susceptible to fractionation effects, or that the PSD was shifted to lower particle sizes as the volumetric flow rate increased. To be able to distinguish which effect is greater, the PSD will have to be measured.

Similar trends are seen with the other isotope ratios. This is especially important for geochronology of zircons, where the lead-uranium nuclide ratios are used to determine the age of the zircon (and hence, surrounding rock).^[60]

The ideal performance of the lens systems would be for the isotope ratios to remain constant with varying volumetric helium flow rate. The trends suggest a decrease in the effect of volumetric flow rate on isotope ratio with decreasing lens diameter, which in turn suggests that an optimal lens diameter with an independent response against flow rate might be achievable.

There is one major issue with this approach for correcting elemental fractionation: how can the end user be sure that, by altering the ablated plume prior to analysis, the ablated aerosol is stoichiometric and still representative of the sample?^[85] Because there was not a readily available method of testing this hypothesis, this research was put on hold.

5.2 Single-Point Calibration Strategy for the Analysis of Silicon Wafers by Laser Ablation-Inductively Coupled Plasma-Mass Spectrometry

This section outlines a short investigative study into a single-point calibration method for silicon samples using ICP-MS. Consumers of microelectronic devices are demanding smaller and more powerful components that work quickly and efficiently, consequently increasing the need for characterisation of trace metal impurities in the manufacturing process at lower concentrations.^[53, 54] Currently, the best practice is Surface Metal Extraction analysis, where the silicon wafer is exposed to a digestion medium, which comprises hydrofluoric acid (HF) and hydrogen peroxide (H₂O₂) in the vapour phase. Once condensed onto the wafer surface, this digestion medium is collected by use of a 250 µl droplet (either HF or ultrapure water) scanned across the surface. This is then submitted for analysis, usually by ICP-MS.

Whilst offering low detection limits, providing the reagents used are ultrapure, this method is time consuming and uses highly corrosive and toxic reagents, namely HF. Methods that do not utilise HF include Total X-Ray Fluorescence (TXRF) and Neutron Activation Analysis (NAA). TXRF can provide semi-quantitative analyses of bulk materials, and can be relatively insensitive to trace impurities (especially light elements).^[27] NAA is much more sensitive and accurate; however, the technique requires access to a nuclear reactor and is very time consuming, so it cannot be used routinely.

The non-contact cell, described in Section 4 previously, is ideal for sampling silicon wafers, since the wafer is a large, smooth planar form factor. In this study, the cell was operating with a single output, with the micro jet-pump being coupled to this outlet to help extract the ablated aerosol, provide mixing of the aerosol with the injector flow of the ICP and to isolate the cell from downstream conditions in the injector flow.

5.2.1 Calibration Strategy

Currently, LA-ICP-MS requires a matrix matched calibration reference material, since laser energy interactions differ between matrices and results in differing sample mass loading of the plasma. In a 'dry' LA experiment (i.e. there is no solvent in the aerosol), these small differences in mass load are significant showing up as large errors in analysis.

Traditional 'wet' ICP-MS analysis, where the bulk of the aerosol is solvent, does not suffer from this problem as the nebulised aerosol provides enough total mass load so that small variations in mass load with respect to the analyte are not significant. This is termed 'a robust plasma'.

Under robust plasma conditions, a single dominant species is present (e.g. water in a wet plasma). Robust plasma conditions such as these can be achieved by adding approximately 10% nitrogen to the aerosol stream in a dry LA experiment, which causes nitrogen to form the dominant species.^[59]

Here, instrumental sensitivity is not significantly affected by small changes in mass load, and those changes in mass load can be corrected for by selection of a suitable internal standard element:

$$C_S = \left(\frac{I_R^I}{I_S^I}\right) \cdot \left(\frac{C_S^I}{C_R^I}\right) \cdot \left(\frac{I_S}{I_R}\right) \cdot C_R \quad (5.28)$$

Where:

- C_S : Concentration of the analyte in the sample
- C_S^I : Concentration of the internal standard in the sample
- C_R : Concentration of the analyte in the reference
- C_R^I : Concentration of the internal standard in the reference
- I_S : Intensity of the analyte in the sample
- I_S^I : Intensity of the internal standard in the sample
- I_R : Intensity of the analyte in the reference
- I_R^I : Intensity of the internal standard in the reference

In the case of calibrating a wafer against a silicate glass, the amount of silicon present in the wafer is much greater than the concentration of any other species, and can be approximated to an atom density of 5.0×10^{22} atoms cm^{-3} . Silicate glasses contain approximately 1.7×10^{22} atoms cm^{-3} silicon, which is in the same order of magnitude as the wafer; hence, Si can be used as an internal standard.

5.2.2 Experimental

This section summarises experimental conditions used for the analysis of wafer materials. Mass Spectrometry was performed using an Element 2 XR sector-field ICP-MS (Thermo Scientific, Bremen, DE). Laser ablation was performed using a New Wave Research UP-213 Nd:YAG laser (New Wave Research, Huntindgdon, Cambs, UK), operating 213 nm wavelength. Samples were scanned using an open, non-contact cell with a sampling height of 200 μm , set by the focal plane of the UP-213 optical system. The operating conditions used are summarised in Table 5.4.

Table 5.4: Operating conditions for LA-ICP-MS experiments. During the plasma lighting sequence, the output from the non-contact cell was vented to atmosphere and make-up gas introduced to achieve ‘punch-through’ in the plasma. Once lit and established, the make-up flow was gradually reduced and the non-contact cell output introduced.

<i>Element 2 XR ICP-MS</i>		
Coolant gas	15.50	l min ⁻¹
Auxiliary gas	0.80	l min ⁻¹
Sample (make-up) gas	0.35	l min ⁻¹
Sampling depth	-1.40	mm
Forward power	1250	W
Interface cones	Platinum	
Resolution	4000	(Medium)
Mass window	120	%
Peak time	144	ms
<i>Non-contact cell on UP-213</i>		
Carrier gas flow	1.20	l min ⁻¹
Curtain gas flow	2.50	l min ⁻¹
Micro jet-pump flow	0.40	l min ⁻¹
Energy density	8.12	J cm ⁻² (NIST glass)
	1.72	J cm ⁻² (Silicon wafer)
Spot size	100	μm
Laser repetition rate	10	Hz
Scan speed (XY Stage)	10	$\mu\text{m s}^{-1}$
Transport tubing	Tygon® 1/4" outer diameter, ~ 1.5 m long	

Reference and sample data were acquired by ablating lines across the sample surface. Gas blanks were acquired prior to the sample being scanned, and subsequent data was blank corrected before being processed.

5.2.3 Results and Discussions

A set of nine reference wafers, previously characterised by 4-point probe resistivity measurements, were scanned by LA-ICP-MS. Limits of Detection are presented in Table 5.5, and calculated concentrations are summarised in Table 5.6 below.

Table 5.5: Limits of Detection obtained for LA-ICP-MS. Limits were calculated from 3σ of 10 gas blank runs.

Element	Limit of Detection		Element	Limit of Detection	
	(ppm)	(atoms cm ⁻³)		(ppm)	(atoms cm ⁻³)
B	13.2 ± 6.5	(1.71 ± 0.85) × 10 ¹⁸	In	6.7 ± 2.3	(8.2 ± 2.9) × 10 ¹⁶
Na	440 ± 330	(2.7 ± 2.0) × 10 ¹⁹	Sn	3.2 ± 1.2	(3.7 ± 1.4) × 10 ¹⁶
Mg	22 ± 12	(1.25 ± 0.70) × 10 ¹⁸	Sb	1.1 ± 0.57	(1.26 ± 0.65) × 10 ¹⁶
Al	86 ± 44	(4.5 ± 2.3) × 10 ¹⁸	Te	11 ± 3.5	(1.22 ± 0.38) × 10 ¹⁷
Si	3100 ± 1500	(1.53 ± 0.74) × 10 ²⁰	Ba	10.0 ± 3.6	(1.02 ± 0.37) × 10 ¹⁸
P	19.8 ± 8.4	(8.9 ± 3.8) × 10 ¹⁷	Ce	0.43 ± 0.14	(4.3 ± 1.4) × 10 ¹⁵
Ti	0.64 ± 0.28	(1.87 ± 0.84) × 10 ¹⁶	Nd	2.8 ± 1.2	(2.7 ± 1.2) × 10 ¹⁶
V	1.01 ± 0.40	(2.8 ± 1.1) × 10 ¹⁶	Eu	1.05 ± 0.36	(9.7 ± 3.4) × 10 ¹⁵
Cr	1.13 ± 0.55	(3.1 ± 1.5) × 10 ¹⁶	Gd	2.4 ± 1.4	(2.1 ± 1.2) × 10 ¹⁶
Mn	1.47 ± 0.53	(3.8 ± 1.4) × 10 ¹⁶	Dy	1.35 ± 0.69	(1.17 ± 0.59) × 10 ¹⁶
Ni	7.5 ± 2.6	(1.80 ± 0.62) × 10 ¹⁷	Ho	0.39 ± 0.23	(3.4 ± 2.0) × 10 ¹⁵
Co	2.52 ± 0.91	(6.0 ± 2.1) × 10 ¹⁶	Yb	1.14 ± 0.46	(9.2 ± 3.8) × 10 ¹⁵
Cu	2.65 ± 0.93	(5.9 ± 2.1) × 10 ¹⁶	Lu	0.49 ± 0.19	(4.0 ± 1.5) × 10 ¹⁵
Zn	8.4 ± 4.0	(1.79 ± 0.85) × 10 ¹⁷	Hf	0.79 ± 0.40	(6.2 ± 3.1) × 10 ¹⁵
Ga	3.7 ± 1.8	(7.4 ± 3.6) × 10 ¹⁶	Ta	0.37 ± 0.14	(2.9 ± 1.1) × 10 ¹⁵
Ge	6.4 ± 1.8	(1.23 ± 0.34) × 10 ¹⁷	W	0.65 ± 0.28	(5.0 ± 2.2) × 10 ¹⁵
As	3.2 ± 1.4	(6.0 ± 2.6) × 10 ¹⁶	Re	0.30 ± 0.10	(2.24 ± 0.77) × 10 ¹⁵
Sr	5.8 ± 1.9	(9.4 ± 3.0) × 10 ¹⁶	Pt	26.6 ± 8.0	(1.92 ± 0.57) × 10 ¹⁷
Zr	0.83 ± 0.36	(1.27 ± 0.56) × 10 ¹⁶	Au	1.50 ± 0.47	(1.07 ± 0.33) × 10 ¹⁶
Nb	0.32 ± 0.11	(4.9 ± 1.7) × 10 ¹⁵	Hg	722 ± 278	(5.0 ± 1.9) × 10 ¹⁸
Mo	1.26 ± 0.46	(1.85 ± 0.67) × 10 ¹⁶	Tl	0.56 ± 0.26	(3.8 ± 1.8) × 10 ¹⁵
Rh	0.47 ± 0.18	(6.4 ± 2.5) × 10 ¹⁵	Pb	0.62 ± 0.26	(4.2 ± 1.8) × 10 ¹⁵
Pd	1.47 ± 0.69	(1.94 ± 0.91) × 10 ¹⁶	Bi	0.32 ± 0.19	(2.2 ± 1.3) × 10 ¹⁵
Ag	1.32 ± 0.35	(1.72 ± 0.45) × 10 ¹⁶	Th	0.22 ± 0.09	(1.31 ± 0.53) × 10 ¹⁵
Cd	1.43 ± 0.58	(1.78 ± 0.72) × 10 ¹⁶	U	0.22 ± 0.12	(1.29 ± 0.72) × 10 ¹⁵

Table 5.6: Dopant densities obtained by LA-ICP-MS compared to 4-point probe resistivity. Limits of detection were (1.71 ± 0.85) × 10¹⁸ atoms cm⁻³ for boron and (8.9 ± 3.8) × 10¹⁷ atoms cm⁻³ for phosphorous.

Sample No.	Dopant	Dopant Density by Resistivity (atoms cm ⁻³)	Dopant Density by LA-ICP-MS (atoms cm ⁻³)	Recovery (%)
1	B	(1.70 ± 0.17) × 10 ²⁰	(1.26 ± 0.45) × 10 ²⁰	74.17
2	B	(3.78 ± 0.14) × 10 ¹⁸	(5.04 ± 1.26) × 10 ¹⁸	133.45
3	B	(4.56 ± 1.14) × 10 ¹⁵	(8.16 ± 3.31) × 10 ¹⁷	<LOD
4	B	(1.21 ± 0.01) × 10 ¹⁴	(7.38 ± 5.65) × 10 ¹⁷	<LOD
5	B	(7.00 ± 0.23) × 10 ¹³	(6.29 ± 3.54) × 10 ¹⁷	<LOD
6	P	(7.38 ± 3.69) × 10 ¹⁹	(3.50 ± 0.60) × 10 ¹⁹	41.75
7	P	(9.64 ± 2.41) × 10 ¹⁴	(2.80 ± 0.91) × 10 ¹⁸	<LOD
8	P	(6.14 ± 0.05) × 10 ¹³	(2.27 ± 0.93) × 10 ¹⁸	<LOD
9	P	(2.65 ± 0.01) × 10 ¹³	(4.24 ± 1.20) × 10 ¹⁸	<LOD

The limits of detection (LOD's) for this method, calculated from 3σ of the averaged blanks, were $(1.72 \pm 0.85) \times 10^{18}$ atoms cm^{-3} and $(8.93 \pm 3.80) \times 10^{17}$ atoms cm^{-3} for boron and phosphorous respectively, which corresponds to 13.2 and 19.8 ppm respectively. Conversion of the atom densities to ppm show that only references 1, 2 and 6 have dopant concentrations above these calculated LOD's (1310 ± 131 ppm B, 29.1 ± 1.0 ppm B and 1629 ± 814 ppm P respectively).

The calculated values for dopant density by LA-ICP-MS for samples 1, 2 and 6 were found to be statistically no different from those values measured by 4-point probe resistivity, using a 2-tailed unpaired *t*-test assuming unequal variance.

A general observation was that the ablated material tended to aggregate in relatively large particles and drop out of the gas streams onto the sample surface (see Figure 5.11 below). This could contribute to the relatively high LOD's as this indicates insufficient mass transport. This could occur due to silicon's small band-gap (1.12 eV at 300 K), which could promote transfer of laser energy through the sample surface in thermal processes rather than ablation processes. To provide better ablation, a femtosecond laser system could be employed as the shorter pulses promote ablation processes over thermal processes and the silicon wafer would ablate in a similar manner to silicate glass.^[86]

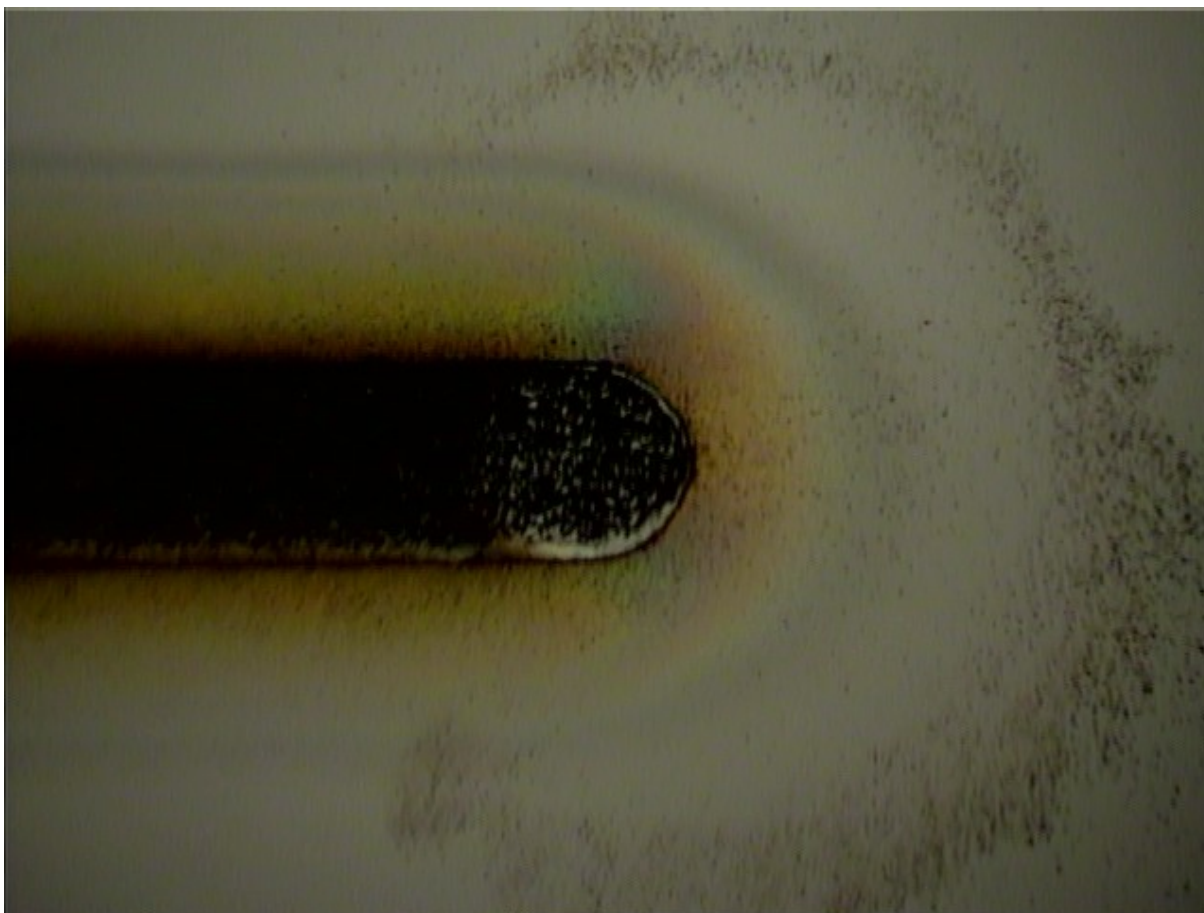


Figure 5.11: Microscope image of an ablated track through a silicon wafer. The ablation depth was measured to be $25 \mu\text{m}$ by focus. Ablated material is seen to have condensed/aggregated and dropped out of the gas stream, thereby reducing the mass transport through the laser ablation system through to the central channel of the ICP-MS.

5.2.4 Conclusions and Further Work

A single-point, non-matrix matched reference strategy for the quantification of minor components on silicon wafer surfaces (*i.e.* elements other than silicon) has been demonstrated using an open, non-contact cell for laser ablation. However, limits of detection are currently too high for the semiconductor industry and trace contaminants cannot be quantified.

The limits of detection need to be reduced to be of value to the semiconductor industry, and a repeat of the experiment in a clean room environment would be beneficial. The mass transport efficiency of the silicon wafers suffer from significant thermal processes in the ablation mechanism, which can be probably be minimised by using a femtosecond laser for ablation.

The question of elemental fractionation has not been answered in this study, *i.e.* are the laser conditions chosen for the silicon wafer appropriate to minimise/negate elemental fractionation processes? The amount of deposited material suggests not; however, a method that could verify this is to perform an online-additions calibration method.^[87]

In this method, a nebulised aerosol is added to the ablated aerosol. A general calibration function for any instrument can be written as:

$$I = CS_{met} \quad (5.29)$$

Where: I intensity
 C concentration
 S_{met} method sensitivity

The gradient of the generated calibration slope is a measure of the method sensitivity. This sensitivity can be split into 2 terms, namely:

$$S_{met} = S_{inst}\dot{m} \quad (5.30)$$

Where: S_{inst} instrument sensitivity
 \dot{m} analyte mass flux

For a liquid sampling method, the instrument response from equation (5.29) becomes:

$$I_A^L = \dot{m}_A^L S_{A(inst)}^L C_A^L \quad (5.31)$$

Where the 'L' superscript denotes 'liquid' and the 'A' subscript denotes the analyte.

For a substrate where an ablated aerosol is added to a liquid aerosol, the instrument response is given by:

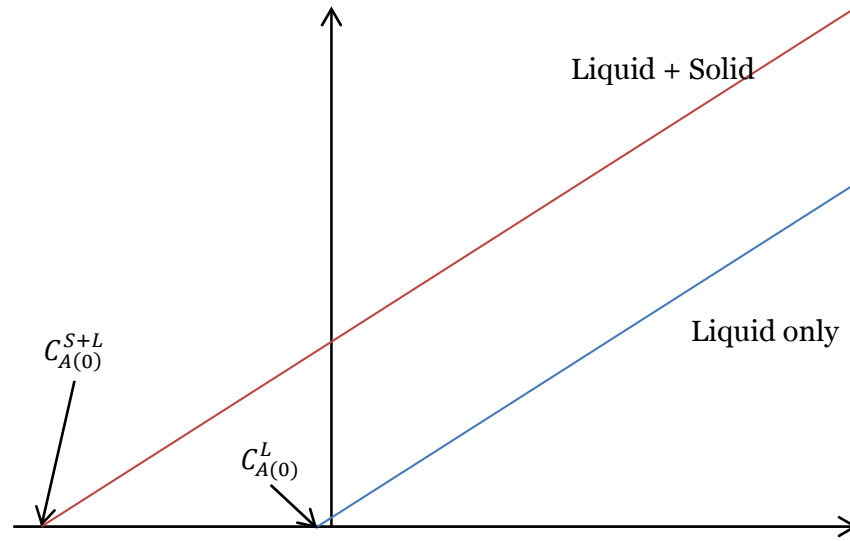
$$I_A^{S+L} = (\dot{m}_A^L + \dot{m}_A^S) S_{A(inst)}^{S+L} C_A^L + \dot{m}_A^S S_{A(inst)}^{S+L} C_A^S \quad (5.32)$$

Under normal ablation conditions, $\dot{m}_A^S \ll \dot{m}_A^L$; hence, $(\dot{m}_A^L + \dot{m}_A^S) S_{A(inst)}^{S+L} \rightarrow \dot{m}_A^L S_{A(inst)}^L$

Equation (5.32) becomes:

$$I_A^{S+L} = \dot{m}_A^L S_{A(inst)}^L C_A^L + \dot{m}_A^S S_{A(inst)}^{S+L} C_A^S \quad (5.33)$$

The combined calibration performance for a particular analyte will have the following approximate trends:



When $I = 0$, $C_A^L = -(C_{A(0)}^{S+L} - C_{A(0)}^L) = -C_{y=0}$. Substituting this condition into equation (5.33) yields:

$$\begin{aligned}
 0 &= -\dot{m}_A^L S_{A(inst)}^L C_{y=0} + \dot{m}_A^S S_{A(inst)}^{S+L} C_A^S \\
 \dot{m}_A^S S_{A(inst)}^{S+L} C_A^S &= \dot{m}_A^L S_{A(inst)}^L |C_{y=0}| \\
 C_A^S &= \left(\frac{\dot{m}_A^L}{\dot{m}_A^S} \right) \cdot \left(\frac{S_{A(inst)}^L}{S_{A(inst)}^{S+L}} \right) \cdot |C_{y=0}| \quad (5.34)
 \end{aligned}$$

The gradients for the two slopes are given by differentiating equations (5.31) and (5.32) with respect to C_A^L :

$$\nabla I_A^L = \dot{m}_A^L S_{A(inst)}^L \quad (5.35)$$

$$\nabla I_A^{S+L} = (\dot{m}_A^L + \dot{m}_A^S) S_{A(inst)}^{S+L} \rightarrow \dot{m}_A^L S_{A(inst)}^{S+L} \quad (5.36)$$

Taking the ratio of gradients (*i.e.* equation (5.35) \div (5.36)):

$$\frac{\nabla I_A^L}{\nabla I_A^{S+L}} = \frac{\dot{m}_A^L S_{A(inst)}^L}{\dot{m}_A^L S_{A(inst)}^{S+L}} = \frac{S_{A(inst)}^L}{S_{A(inst)}^{S+L}} = R_S^A \quad (5.37)$$

Hence, the ratio of the gradients of the two lines gives the ratio of sensitivities. Substituting into equation (5.34):

$$C_A^S = \left(\frac{\dot{m}_A^L}{\dot{m}_A^S} \right) \cdot \left(\frac{\nabla I_A^L}{\nabla I_A^{S+L}} \right) \cdot |C_{y=0}| \quad (5.38)$$

To find the mass flux ratio, an internal standard of known concentration has to be used. This can be determined empirically from stoichiometry or by another technique, and is available for most substrates (*e.g.* silicate as the major constituent element in a rock or glass, calcium in a coral *etc.*).

Taking the concentrations of internal standards into account and substituting into equation (5.38):

$$C_I^S = \left(\frac{\dot{m}_A^L}{\dot{m}_A^S} \right) \cdot R_S^I \cdot |C_{y=0}^I| \quad (5.39)$$

$$\left(\frac{\dot{m}_A^L}{\dot{m}_A^S} \right) = \frac{C_I^S}{R_S^I |C_{y=0}^I|} = R_M \quad (5.40)$$

Elemental fractionation, as discussed previously in Section 1.4.2, is mostly dependent on the particle size distribution of the ablation aerosol. Excessive amount of matrix suppression and/or fractionation effects from large particles will lead to the apparent instrument sensitivity for a particular analyte to decrease. This means the gradient for the combined aerosol will be shallower than that for the liquid standards alone; hence, if no matrix suppression or elemental fractionation effects are occurring, the ratio of sensitivities for all elements (R_S^A) will be equal to 1.

To minimise mutual matrix effects, a low-flow nebuliser should be utilised with a flow below 100 $\mu\text{l min}^{-1}$. This was not available in the timeframe of this study, so effects of fractionation weren't investigated and cannot be confidently ruled out.

5.3 MALDI sampling using the non-contact cell

One of the key features included in the design of the NCC is the ability to have multiple output ports (two in this prototype) that allow simultaneous analysis of a laser-generated plume. This would be useful in metallo-proteomic studies, whereby the sample is desorbed using a low irradiance laser mode. This would allow desorption of the intact bio-molecule and identification through fragmentation analysis on an organic mass spectrometer, whilst at the same time quantifying the protein using ICP-MS.

ICP-MS analysis of proteins can be achieved by using ^{13}C signals (high backgrounds), hetero atoms such as ^{32}S or ^{31}P (high $^{16}\text{O}_2$ backgrounds and low ionisation efficiency respectively), or metal ions present in metallo-proteins. The best option is to use metal ions, since these can either be present in the case of metallo proteins, or added by attaching a chelating ligand to one end of the protein, such as cyclic diethylenetriaminepentaacetic anhydride (cDTPA).^[88]

Currently, MALDI matrices are tailored towards nitrogen lasers (337 nm) since they are relatively inexpensive and easy to maintain compared to Nd:YAG systems. For a balance between ablation performance and cost, the most effective harmonic for an Nd:YAG system is at 213 nm. An ideal MALDI matrix to facilitate the use of the NCC in a simultaneous MALDI and LA experiment would be an organic acid that absorbs efficiently at 213 nm.

A suitable choice would appear to be vanillic acid, as this is a simple organic acid that absorbs effectively at 217 nm ($\epsilon_{217} = 22\,900 \text{ l mol}^{-1} \text{ cm}^{-1}$), and has been shown to increase the efficiency of laser ablation in previous work by O' Connor *et al.*^[89] In this work, the authors showed that a 60:40 mix of sample:vanillic acid provided better quality analytical data than sample alone, and demonstrated that adding an 'absorbing binder' to a pressed powder disc ensures the mass flux for all samples is equivalent, ensuring the ablation characteristics and plasma effects are equivalent between standards and samples. This means that any variation in a chosen internal standard would be affected more by instrument drift rather than the laser-

sample interaction. The authors also demonstrated the possibility of using the technique of Matrix Assisted Laser Ablation (MALA) to perform external calibration where the sample and reference standard are not matrix matched.

5.3.1 Experimental

To initially test the effectiveness of low power ablation, vanillic acid (SigmaAldrich UK Ltd., Gillingham, Dorset, UK) discs spiked with an indium internal standard, cyanocobalamin and haemoglobin were made up. The indium internal standard was present to give an indication that the disc was being physically ablated, since the indium would only be adsorbed onto vanillic acid crystals. Cyanocobalamin was chosen as it is a low molecular weight protein (1355.28 g mol⁻¹) with an existing cobalt centre, and haemoglobin as it is a high molecular weight protein (~65706 g mol⁻¹) with existing iron centres.

To avoid handling very small amounts of each component, each disc was spiked to contain metal concentrations in line with NIST SRM 610, *i.e.* 400 ppm of each metal. Initial mixtures were made up to weigh 0.6 g and homogenised using a Retsch MM-200 ball mill (Retsch UK Ltd., Castleford, West Yorkshire, UK) at 30 Hz for 20 mins. Each mixture was lubricated with 250 µl of trace-metals grade MeOH (Romil, Cambridge, UK).

Four mixtures, each made up to be 0.6 g total mass with a 240 µl indium spike (1000 ppm in 2% HNO₃, Ultra Scientific *via* LGC, Teddington, Middlesex, UK) were made up with the following compositions:

Table 5.7: Composition by weight of four mixtures used to investigate the viability of MALDI using a 213 nm laser ablation system.

Component	Spike (g)	Cyanocobalamin (g)	Haemoglobin (g)	Mixed (g)
Vanillic Acid	0.6059	0.5920	0.5363	0.5245
Cyanocobalamin (4.35 % Co w/w in 50:50 MeOH:H ₂ O)	0.0	0.0056	0.0	0.0057
Haemoglobin (0.35 % Fe w/w in 50:50 MeOH:H ₂ O)	0.0	0.0	0.0760	0.0711

A portion of each mixture (0.3 g) was transferred to a hydraulic IR press (Specac Ltd., Orpington, Kent, UK) and compressed using a 13 mm die set with 10 tonnes of pressure for 10 minutes. Additionally, 0.3 g of pure vanillic acid was pressed into a disc to serve as a matrix blank.

The laser ablation system used was a service spare UP-213 platform. The samples were scanned initially using the standard ablation cell (sweep gas 0.56 l min⁻¹ He, make-up gas 0.41 l min⁻¹ Ar) to try and establish proof-of-concept. The cell was purged for 30 minutes prior to analysis to ensure the transport tubing had degassed sufficiently. Laser power was varied from 8 – 17.5 % in 0.5 % increments. At each power level, the fitted energy meter reported the fluence as 0.04 J cm⁻²; hence, actual fluence is not reported in this section.

Signals for ¹³C, ⁵⁶Fe, ⁵⁹Co and ¹¹⁵In were monitored in medium resolution on the Element XR ICP-MS. ¹³C was used as an internal standard element to correct for mass flux differences, *i.e.* at each power setting, the analyte signals (I_A) were divided by ¹³C signals (I_C). Figure 5.12

across shows the response of the analyte signals with varied laser power for the blank disc. For each sampling point, a 0.6 mm line was ablated at $10 \mu\text{m s}^{-1}$ (60 s total ablation time). Each data point is an average of 10 spectra obtained during the ablation.

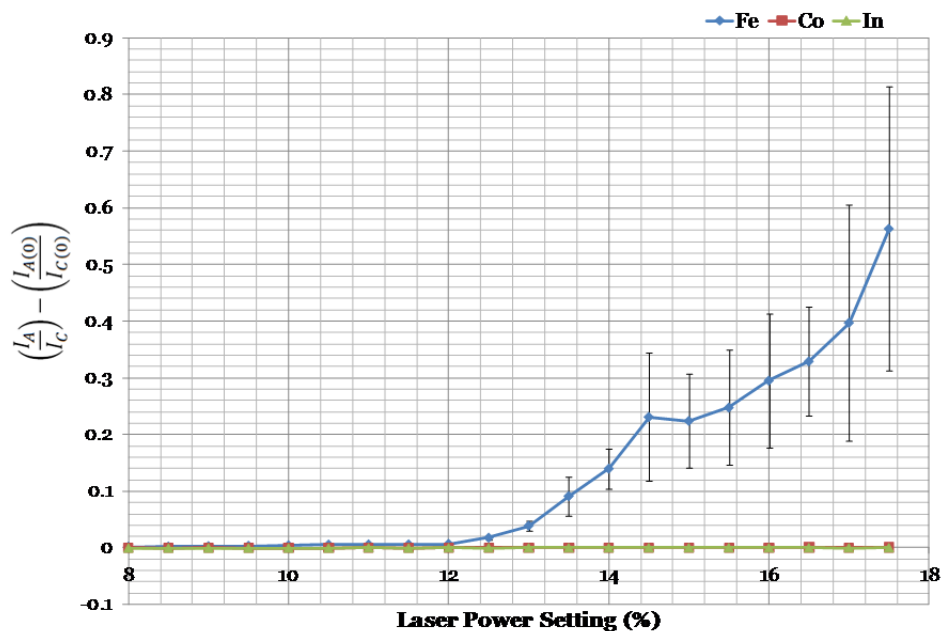


Figure 5.12: Background and drift corrected signal dependence on laser power for iron, cobalt and indium in a matrix blank vanillic acid disc.

The blank disc should have provided background signals for all analytes; however, transfer of iron from the stainless steel dies used to press the discs is shown as rising signals from 12 % incident power upwards indicating blank contamination.

Figure 5.13 below shows the signal response for the analytes with increasing laser power on the spiked vanillic acid disc. The figure shows a large spike for 14.5 % and 15 % laser power. Since each line was arranged in series, this suggests inhomogeneity on the sample surface from incomplete mixing.

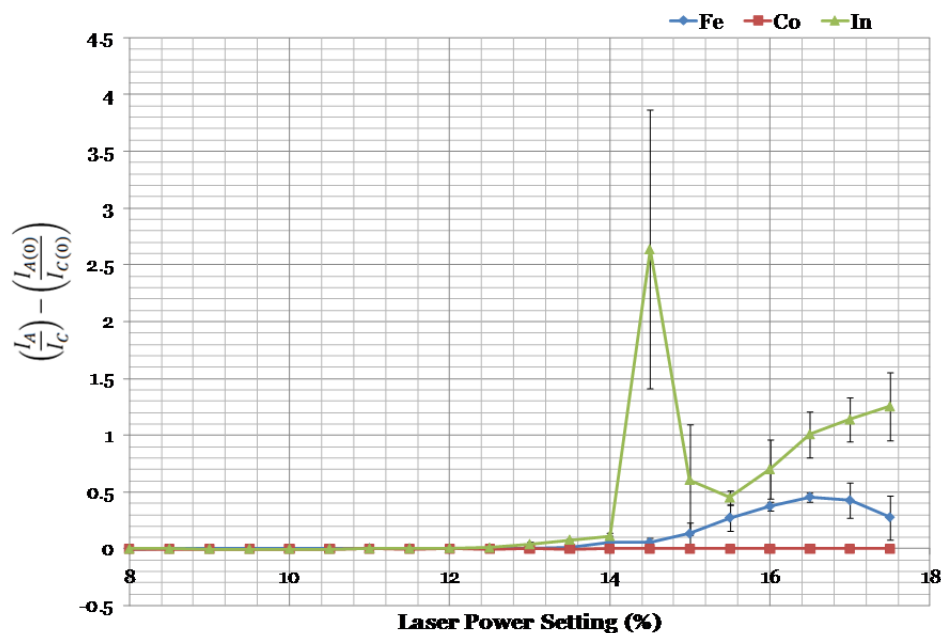


Figure 5.13: Background and drift corrected signal dependence on laser power for iron, cobalt and indium in an indium spiked vanillic acid disc

Vanillic acid is insoluble in aqueous media (such as 2 % HNO_3) and it is possible that the small volume of indium stock solution was poorly mixed within the sample. The indium signal appears to rise after 13 % laser power, with visible ablation occurring at 14.5 %, suggesting the ablation threshold for a vanillic acid disc is approximately 13 % on this laser system. The rise in Fe signals is consistent with that seen in the blank.

Figure 5.14 below shows the signal response for the cyanocobalamin doped disc. The rise in Co signal is coincident with the In signal, suggesting either the disc has to be ablated to see metallo-protein signals, or that some In exchanged with Co during homogenisation.

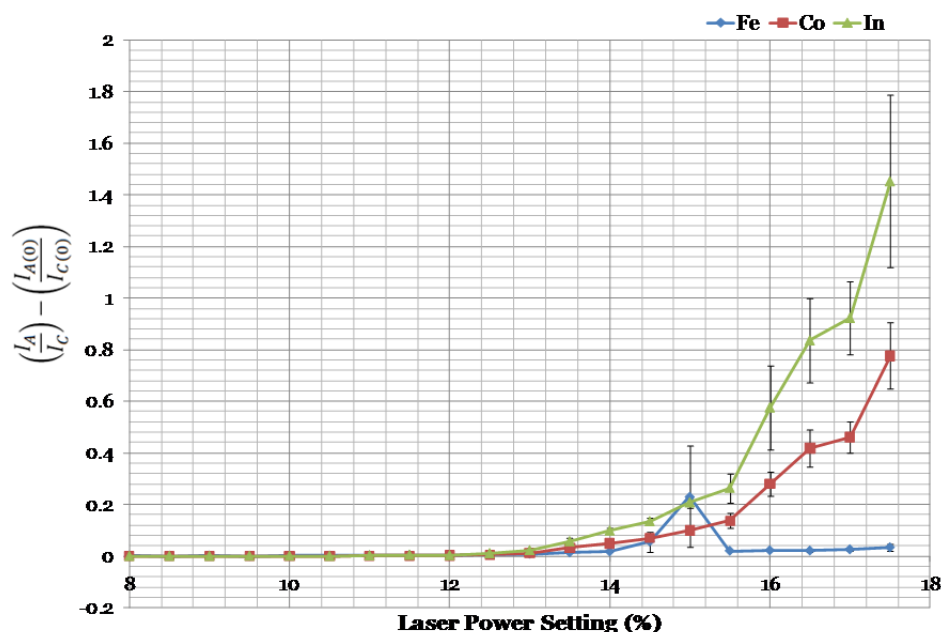


Figure 5.14: Background and drift corrected signal dependence on laser power for iron, cobalt and indium in a cyanocobalamin doped, indium spiked vanillic acid disc.

In either case, these tests only suggest MALA processes, not MALDI. To see if MALDI was occurring, the NCC was set-up with the output connected to a LTQ Liner Ion Trap Organic Mass Spectrometer (Thermo Scientific, San Jose, CA, USA). The NCC was run without a curtain gas in this case, as the LTQ interface is designed to accept atmospheric gas. The He sweep gas was set to 0.8 l min^{-1} and the micro jet-pump set to 0.3 l min^{-1} Ar to provide pneumatic assistance for transport. Since this has a metallic body, it was grounded to assist transport.

The laser output was transported to the inlet capillary of the LTQ using a length of Tygon tubing terminating in a glass dropping pipette (i.d. 1.5 mm). The laser experiment outlined above was repeated with all the discs and the m/z range 150 – 2000 monitored for cyanocobalamin and vanillic acid.

Intermittent cyanocobalamin signals were seen during tuning the system, but the signal at 1355 Da (for cyanocobalamin) was not stable enough for an effective tune. The system was therefore tuned using a liquid cyanocobalamin mixture ($\sim 1 \text{ mg ml}^{-1}$ in 0.1 % acetic acid in methanol, run through the ESI interface on the LTQ) to ensure the ion lenses would be set correctly for the 1355 Da peak. This was done with the helium flow through the NCC switched off.

After tuning, no signals were seen throughout the experiment, which suggests either:

- There was insufficient cyanocobalamin in the disc to be detected by the mass spectrometer.
- The singly charged molecules were discharging in the transport tubing (*i.e.* on the micro jet-pump body)
- The ablated plume was swept from the sample surface too quickly for charge transfer to occur.
- Vanillic acid is not an effective MALDI matrix.

To aid the generation of charged ions, the plume can be sprayed by the output from an electrospray nozzle. This technique is referred to as 'Matrix Assisted Laser Desorption ElectroSpray Ionisation', or MALDESI.^[90] In this study, the output from the laser was combined with the charged ESI plume from the LTQ's ESI interface using 0.1 % acetic acid in 50:50 MeOH:H₂O at a flow rate of $10 \text{ } \mu\text{l min}^{-1}$. This was tried, initially with some partial success; however, signals were so intermittent that during 20 attempts to record the signal, no peaks for vanillic acid (168 Da) or cyanocobalamin were seen.

Most MALDI/MALDESI experiments house the sample in a vacuum chamber close to the inlet on the mass spectrometer, and the sample is desorbed by an oblique laser. This setup does not require gas for transport, whereas the non-contact cell does. It could be that the gas used to transport the ablated plume has one of (or a combination of) three effects:

1. The plume expands rapidly from the tip of the glass pipette used in the interface, thereby lowering the transmission efficiency of the interface.
2. The gas overloads internal space of the mass spectrometer, destabilising ions within the ion trap and suppressing signals.
3. The exit velocity of the ablation cell output from the glass pipette tip is too high for the ESI spray to charge the sample molecules.

The intermittent cyanocobalamin peaks at 1355 Da shows some promise; however, since the signal stability is poor it can be said that, under these conditions, vanillic acid is a poor MALDI matrix. Another matrix will have to be used to facilitate MALDI analysis using the NCC. Unfortunately, time constraints meant further investigation could not be undertaken within the scope of this thesis.

THIS PAGE IS INTENTIONALLY BLANK

6 Findings & Implications

In this thesis, a design for an open, non-contact cell for laser ablation has been presented. This cell shows good analytical performance with respect to analyte sensitivity and sample transport; however, numerical simulations show eddy formation in the central volume of the cell. Optimisation of this inner volume to smooth the gas flows will improve sample transport and cell performance.

The advantage of using a micro-jet array plate for lowering consumption of input gases, improving atmosphere exclusion and improving sample transport has been demonstrated by numerical simulation. The array provides stiff micro-jets of gas that restricts lateral entrainment and diffusion of atmosphere into the central volume of the ablation cell. Additionally, the stiff curtain gas restricts lateral outward vectoring of the sweep gas and improves transport through the central volume.

Addition of a micro jet-pump on the cell outlet provides not only pneumatic transport assistance but also efficient turbulent mixing between the cell output and the make-up flow used in laser ablation experiments. The design of the micro jet-pump is still in its infancy, and improvements in internal geometry can improve efficiency and ease of use.

6.1 Implications for New Wave Research and Relevant Industries

Sample preparation is the limiting factor in most laser ablation studies. The concept of this cell minimises sample preparation times by eliminating the need to cut large, planar samples (over 4" × 4" – currently covered by the Large Format Cell) to fit an enclosed chamber. The pneumatic assistance provided by the micro jet-pump should also minimise the need to optically polish surfaces for best plume transport, provided the laser still couples into the sample surface efficiently.

The concept of the non-contact cell is also useful for breaking into the semiconductor market segment. At present, wafer analysis is performed reliably by vapour-phase decomposition, which is time consuming and uses harsh chemicals. The cell could be used on-line during the etching/scribing process to analyse content on the fly. Individual wafers can be scanned instead of a representative batch, which would allow less wastage (individual wafers discarded instead of whole batches) and failures (defective wafers can be missed in sub-sampling).

In laser welding/cutting applications, the cell can be used to provide an inert atmosphere for the cutting process to occur, minimising potentially noxious fumes being generated. Extraction through the outlet ports can also be used on those same fumes, providing a means of both environmental monitoring (for waste gas release) and quality control (elemental composition of the ablated material can indicate quality of the product).

6.2 Critical Evaluation and Further Research

The research progressed well, but was initially hampered by technical failures on the ICP-MS and unavailability of a laser ablation platform for continuous testing. The system used for this project was a roving demonstration system, moving to customer sites for evaluations. Since field demonstrations generate profit, they are obviously a priority to the company.

Unfortunately on some occasions when the laser was available for testing, there were downtime problems with the ICP-MS. These problems took months to troubleshoot and repair. Despite this, the experimental designs implemented meant that key performance indicators of the cell were well characterised.

The present 'alpha' design is accepted as being limited to flat, smooth surfaces, and for a complete characterisation of the performance of the cell, the degree of sample curvature and roughness that the cell is able to effectively scan and analyse must be assessed. This will provide vital information concerning the range of samples that can be handled and the relevant commercial markets for its use.

The geometry of the flow restrictor was not changed in this project. An appreciation of the effects of the flow restrictor thickness on the efficiency of the ablation cell will allow the gas flows to be further optimised.

The micro-jet pump used in this project is a first implementation, and computing power to formally model the internal flow dynamics was not available. As stated previously, optimisation of the geometry will improve its transport efficiency and ease of use.

The molecular ion formation data was deemed fit-for-purpose by ESI management to maintain project funding; however, this needs to be repeated to get a fair comparison of signals between the NCC and standard cell.

Currently, the cell is undergoing re-design by the ESI-NWR engineering team to finalise a beta-product for testing with technical partners. At this point, application development for relevant industries will be performed by those technical partners, hopefully including development of calibration strategies for semi-conductor materials.

7 References

1. E. De Hoffman, J. Charette and V. Stroobant, *Mass Spectrometry: Principles and Applications*, John Wiley & Sons, New York, 1999.
2. J. Mora, S. Maestre, H. V and J. L. Todoli, *Trends in Analytical Chemistry*, 2003, **22**, 123-132.
3. R. E. Russo, X. L. Mao, H. C. Liu, J. Gonzalez and S. S. Mao, *Talanta*, 2002, **57**, 425-451.
4. A. Vertes, R. Gijbels and F. Adams, *Laser Ionisation Mass Analysis*, John Wiley & Sons, New York, 1993.
5. M. Barber, B. N. Green and K. R. Jennings, *Rapid Communications in Mass Spectrometry*, 1987, **1**, 80-83.
6. J. A. Dean, *Practical inductively coupled plasma spectroscopy*, Wiley, Hoboken, NJ, 2005.
7. F. F. Chen and J. P. Chang, *Lecture notes on principles of plasma processing*, Kluwer Academic/Plenum Publishers, New York, 2003.
8. R. S. Houk and Y. Zhai, *Spectrochimica Acta Part B: Atomic Spectroscopy*, 2001, **56**, 1055-1067.
9. H. Bradt, in *Astrophysics Processes: the Physics of Astronomical Phenomena*, Cambridge University Press, Cambridge, UK, 2008, pp.SE1-SE13.
10. J. H. Gross, *Mass Spectrometry: A Textbook*, Springer-Verlag, 2004.
11. *Finnigan™ ELEMENT GD Glow Discharge Mass Spectrometer*, © Thermo Electron Corp. 2005, Brochure.
12. C. Steel and M. Henchman, *Journal of Chemical Education*, 1998, **75**, 1049-1054.
13. A. Makarov, in *Practical Aspects of Trapped Ion Mass Spectrometry, Volume IV*, ed. ed. R. E. March and F. J. Todd, CRC Press, Boca Raton, FL, USA, 2010, pp.251-272.
14. *Finnigan Element XR: Extended Dynamic Range High Resolution ICP-MS*, © Thermo Electron Corp. 2005, Technical Note No: 30064, 1-4
15. B. Salle, D. A. Cremers, S. Maurice and R. C. Wiens, *Spectrochimica Acta Part B-Atomic Spectroscopy*, 2005, **60**, 479-490.
16. B. Hattendorf, C. Latkoczy and D. Gunther, *Analytical Chemistry*, 2003, **75**, 341A-347A.
17. M. Guillong, H. R. Kuhn and D. Gunther, *Spectrochimica Acta Part B-Atomic Spectroscopy*, 2003, **58**, 211-220.
18. D. Gunther and C. A. Heinrich, *Journal of Analytical Atomic Spectrometry*, 1999, **14**, 1369-1374.
19. I. Horn, M. Guillong and D. Gunther, *Applied Surface Science*, 2001, **182**, 91-102.
20. V. Margetic, A. Pakulev, A. Stockhaus, M. Bolshov, K. Niemax and R. Hergenroder, *Spectrochimica Acta Part B-Atomic Spectroscopy*, 2000, **55**, 1771-1785.
21. I. Horn and D. Gunther, *Applied Surface Science*, 2003, **207**, 144-157.
22. D. Witkowska, M. Mieszala, A. Gamian, M. Staniszevska, A. Czarny, A. Przondo-Mordarska, M. Jaquinod and E. Forest, *Fems Immunology and Medical Microbiology*, 2005, **45**, 221-230.
23. C. Ruiz-Romero, M. J. Lopez-Armada and F. J. Blanco, *Proteomics*, 2005, **5**, 3048-3059.

24. G. Marko-Varga, H. Lindberg, C. G. Lofdahl, P. Jonsson, L. Hansson, M. Dahlback, E. Lindquist, L. Johansson, M. Foster and T. E. Fehniger, *Journal of Proteome Research*, 2005, **4**, 1200-1212.
25. I. H. Hwang, *Asian-Australasian Journal of Animal Sciences*, 2004, **17**, 1296-1302.
26. S. A. Watmough, T. C. Hutchinson and R. D. Evans, *Environmental Science & Technology*, 1998, **32**, 2185-2190.
27. L. Yang, R. E. Sturgeon and Z. Mester, *Analytical Chemistry*, 2005, **77**, 2971-2977.
28. P. Chaurand, S. A. Schwartz, D. Billheimer, B. G. J. Xu, A. Crecelius and R. M. Caprioli, *Analytical Chemistry*, 2004, **76**, 1145-1155.
29. V. Laiko, M. A. Baldwin and A. L. Burlingame, *Analytical Chemistry*, 2000, **72**, 652-657.
30. P. B. O' Connor, B. A. Budnik, V. B. Ivleva, P. Kaur, S. C. Moyer, J. L. Pittman and C. E. Costello, *Journal of the American Society for Mass Spectrometry*, 2004, **15**, 128-132.
31. P. V. Tan, V. Laiko and V. M. Doroshenko, *Analytical Chemistry*, 2004, **76**, 2462-2469.
32. *AP/MALDI™ PDF Source for Thermo Finnigan LTQ Linear Ion Trap Mass Spectrometers, Installation, Operation and Maintenance Manual*, © MassTech Inc. 2004.
33. N. Taranenko, V. M. Doroshenko, A. K. Shukla and M. M. Shukla, *American Laboratory*, 2004, **36**, 34-+.
34. K. A. Kellersberger, E. T. Yu, S. I. Merenbloom and D. Fabris, *Journal of the American Society for Mass Spectrometry*, 2005, **16**, 199-207.
35. B. B. Schneider, C. Lock and T. R. Covey, *Journal of the American Society for Mass Spectrometry*, 2005, **16**, 176-182.
36. D. Bleiner and H. Altorfer, *J. Anal. At. Spectrom.*, 2005, **20**, 754-756.
37. D. Fliegel and D. Gunther, *Spectrochimica Acta Part B-Atomic Spectroscopy*, 2006, **61**, 841-849.
38. J. Pisonero, D. Fliegel and D. Gunther, *J. Anal. At. Spectrom.*, 2006, **21**, 922-931.
39. I. Feldmann, C. U. Koehler, P. H. Roos and N. Jakubowski, *J. Anal. At. Spectrom.*, 2006, **21**, 1006-1015.
40. M. Guillong, P. Heimgartner, Z. Kopajtic, D. Gunther and I. Gunther-Leopold, *J. Anal. At. Spectrom.*, 2007, **22**, 399-402.
41. D. Bleiner and A. Bogaerts, *Spectrochimica Acta Part B-Atomic Spectroscopy*, 2007, **62**, 155-168.
42. Hutchinson, R. W., Ryan, E., Graham, S., Elkin, K., Green, D. A., O'Connor, C. J. P. and Colucci, M., *Poster at the 9th European Workshop on Laser Ablation in Elemental and Isotopic Analysis*, 2008, Prague.
43. R. W. Hutchinson, E. Ryan, S. Graham, K. Elkin, D. A. Green, C. J. P. O'Connor and M. Colucci, *New Wave Research Application Note*, 2007, **No. QL200 Rev. 8**.
44. *Photon Machines: Sample Cells*, © Photon Machines Inc. 2009, (URL: http://www.photon-machines.com/sample_cells.html), accessed January 2011.
45. W. Muller, M. Shelley, P. Miller and S. Broude, *J. Anal. At. Spectrom.*, 2009, **24**, 209.
46. A. R. Barringer, *US. Pat.*, Pat. N°: 4220414, 1980.
47. P. Arrowsmith and S. K. Hughes, *Appl. Spectrosc.*, 1988, **42**, 1231-1239.
48. S. Shuttleworth. M. R. Chandratillake, V. J. Robinson, *WO. Pat. (Application)*, Pat. N°: 1995/027986 A1, 1995.

49. F. Boué-Bigne, Doctoral Thesis, Loughborough University, 2000.
50. W. Devos, C. Moor and P. Lienemann, *J. Anal. At. Spectrom.*, 1999, **14**, 621-626.
51. R. Kovacs, K. Nishiguchi, K. Utani and D. Gunther, *J. Anal. At. Spectrom.*, 2010, (DOI:10.1039/b924425e).
52. K. Nishiguchi, K. Utani and E. Fujimori, *J. Anal. At. Spectrom.*, 2008, **23**, 1125.
53. J. Takahashi and K. Youno, *Characterization of Trace Impurities in Silicon Wafers by High Sensitivity Reaction Cell ICP-MS*, 5988-9529EN, Agilent Technologies, Agilent Technologies Literature Library, 2006.
54. T. Gluodenis, *Characterization of Surface Metal Contamination on Silicon Wafers Using Surface Metal Extractions Inductively Coupled Plasma Mass Spectrometry (SME-ICP-MS)*, 5988-4602EN, Agilent Technologies, Agilent Technologies Literature Library, 2001.
55. T. S. Kuhn, *The Structure of Scientific Revolutions*, University of Chicago Press, 1962.
56. Pajares, F., *The Structure of Scientific Revolutions: A Synopsis from the original by Professor Frank Pajares*, 2009, 1-4 (URL: <http://www.des.emory.edu/mfp/kuhnsyn.html>), accessed March 2011.
57. I. Kroslakova and D. Gunther, *J. Anal. At. Spectrom.*, 2007, **22**, 51-62.
58. B. L. Sharp, *J. Anal. At. Spectrom.*, 1988, **3**, 613-652.
59. S. F. Durrant, *Fresenius J. Anal. Chem.*, 1994, **349**, 768-771.
60. T. Hirata and R. W. Nesbitt, *Geochim. Cosmochim. Acta*, 1995, **59**, 2491-2500.
61. GeoReM database of Reference Materials, *Max Planck Institut fur Chemie, Otto-Hahn Institut*, 2010, <http://georem.mpch-mainz.gwdg.de/>, accessed multiple times between May 2006 and July 2009.
62. DSS Operating Manual, *SolidWorks Flow Simulation 2010: Technical Reference*, Dassault Systemes, 2010.
63. J. Boussinesq, *Essai sur la théorie des eaux courantes*, Mémoires présentés par divers savants à l'Académie des Sciences, Paris, 1877.
64. F. Schmitt, *Comptes Rendus Mécanique*, 2007, **335**, 617-627.
65. DSS Operating Manual, *SolidWorks Flow Simulation 2010: Solving Engineering Problems*, Dassault Systemes, 2010.
66. J. W. Lee, M. Y. Yi and S. M. Lee, *J. Aerosol. Sci.*, 2003, **34**, 211-224.
67. J. Goo, *J. Aerosol. Sci.*, 2002, **33**, 1493-1507.
68. P. Liu, P. J. Ziemann, D. B. Kittelson and P. H. McMurry, *Aerosol Science and Technology*, 1995, **22**, 293-313.
69. P. Liu, P. J. Ziemann, D. B. Kittelson and P. H. McMurry, *Aerosol Science and Technology*, 1995, **22**, 314-324.
70. X. L. Wang, P. H. McMurry and F. E. Kruis, *US Patent*, Pat. N°: US 2006/0102837 A1, May 18, 2006.
71. M. R. Alfarra, D. Paulsen, M. Gysel, A. A. Garforth, J. Dommen, A. S. H. Prevot, D. R. Worsnop, U. Baltensperger and H. Coe, *Atmospheric Chemistry and Physics*, 2006, **6**, 5279-5293.
72. J. L. Jimenez, J. T. Jayne, Q. Shi, C. E. Kolb, D. R. Worsnop, I. Yourshaw, J. H. Seinfeld, R. C. Flagan, X. F. Zhang, K. A. Smith, J. W. Morris and P. Davidovits, *Journal of Geophysical Research - Atmospheres*, 2003, **108**, 8425.
73. W. A. Harris, P. T. A. Reilly and W. B. Whitten, *Anal. Chem.*, 2007, **79**, 2354-2358.

74. M. T. Spencer, L. G. Shields and K. A. Prather, *Environ. Sci. Technol.*, 2007, **41**, 1303-1309.
75. H. R. Kuhn, M. Guillong and D. Gunther, *Analytical and Bioanalytical Chemistry*, 2004, **378**, 1069-1074.
76. X. L. Wang and P. H. McMurry, 2006, *The Aerodynamic Lens Calculator – MS Excel spreadsheet*, http://www.me.umn.edu/~wxl/documents/061109_Calculator_v1.4.1.xls, accessed February 2006.
77. X. L. Wang and P. H. McMurry, *Aerosol Science and Technology*, 2006, **40**, 1-10.
78. X. L. Wang and P. H. McMurry, *Aerosol Science and Technology*, 2006, **40**, 320-334.
79. F. J. Gómez-Moreno, J. Rosell-Llompart and J. Fernández de la Mora, *Journal of Aerosol Science*, 2002/3, **33**, 459-476.
80. X. L. Wang, F. E. Kruis and P. H. McMurry, *Aerosol Sci. Technol.*, 2005, **39**, 611-623.
81. X. L. Wang and P. H. McMurry, *International Journal of Mass Spectrometry*, 2006, **258**, 30-36.
82. X. L. Wang, A. Gidwani, S. L. Girshick and P. H. McMurry, *Aerosol Science and Technology*, 2005, **39**, 624-636.
83. X. F. Zhang, K. A. Smith, D. R. Worsnop, J. Jimenez, J. T. Jayne and C. E. Kolb, *Aerosol Science and Technology*, 2002, **36**, 617-631.
84. J. M. Mermet, *Spectrochimica Acta Part B-Atomic Spectroscopy*, 1989, **44**, 1109-1116.
85. Gunther, D., Fleigel, D. and Bogaerts, A., personal discussions at the European Winter Conference for Plasma Spectrochemistry, *Taormina, Sicily.*, 2007.
86. E. G. Gamaly, A. V. Rode, B. Luther-Davies and V. T. Tikhonchuk, *Phys Plasmas*, 2002, **9**, 949-957.
87. C. O' Connor, B. L. Sharp and P. Evans, *J. Anal. At. Spectrom.*, 2006, **21**, 556-565.
88. P. Patel, P. Jones, R. Handy, C. Harrington, P. Marshall and E. H. Evans, *Anal. Bioanal Chem.*, 2008, **390**, 61-65.
89. C. O' Connor, M. R. Landon and B. L. Sharp, *J. Anal. At. Spectrom.*, 2007, **22**, 273.
90. J. S. Sampson, A. M. Hawkridge and D. C. Muddiman, *J. Am. Soc. Mass Spectrom.*, 2006, **17**, 1712-1716.

* * * * *

Appendix A Apparatus and Method for Laser Irradiation (Paper 1)

Dhinesh Asogan,^{a,b} Barry L. Sharp,^a Ciaran J. P. O' Connor,^c

US Patent Application No: US 2010/0207038 A1

Filed: Feb. 13, 2009

Published: Aug. 19, 2010

^a *Centre for Analytical Science, Department of Chemistry, Loughborough University, Loughborough, Leicestershire, UK LE11 3TU, e-mail: B.L.Sharp@lboro.ac.uk*

^b *Centre for Innovative and Collaborative Engineering, Department of Civil and Building Engineering, Loughborough University, Loughborough, Leicestershire, UK LE11 3TU*

^c *Electro Scientific Industries Europe Ltd., New Wave Research Division, 8 Avro Court, Ermine Business Park, Huntingdon, Cambs, UK PE29 6XS*

ABSTRACT

An apparatus for laser irradiation including a housing wherein the housing defines at least a portion of a test volume; a first conduit configured to provide a first flow of gas into the test volume; a second conduit configured to remove the first flow of gas from the test volume; a third conduit configured to provide a second flow of gas; and a flow controller configured to provide a region of increased flow impedance between the first conduit and the third conduit so that the first flow of gas is directed towards the test volume and the second flow of gas is directed away from the first flow of gas so as to restrict gas external to the housing from coming into contact with the first flow of gas.

Keywords – N/A

Paper type – US Patent Application

1 Drawings

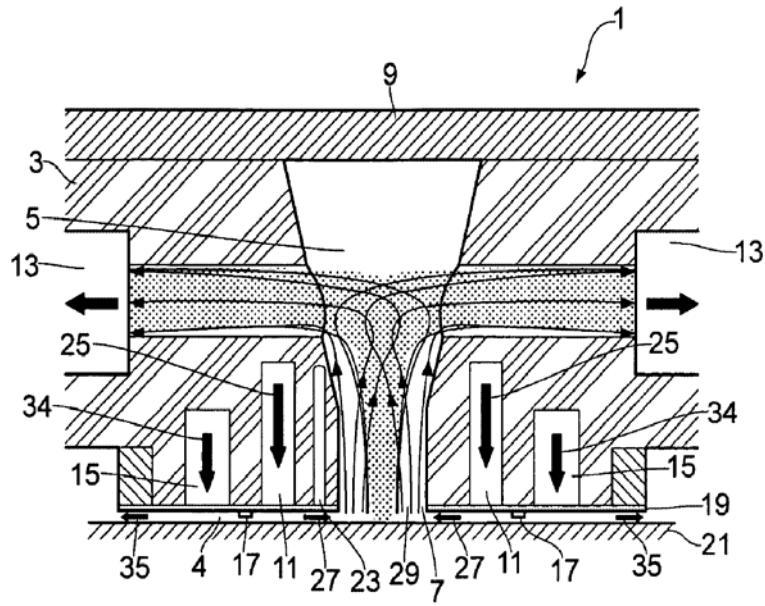


FIG 1

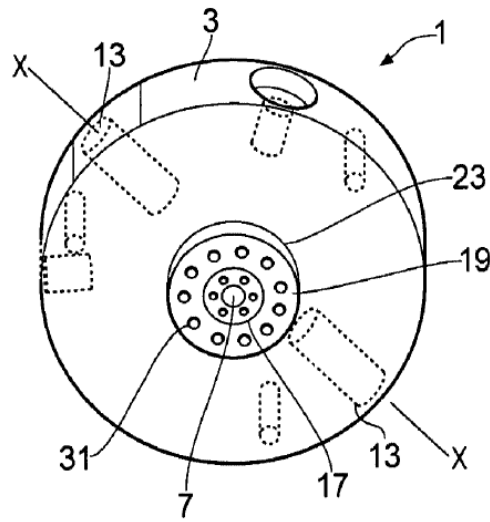


FIG 2

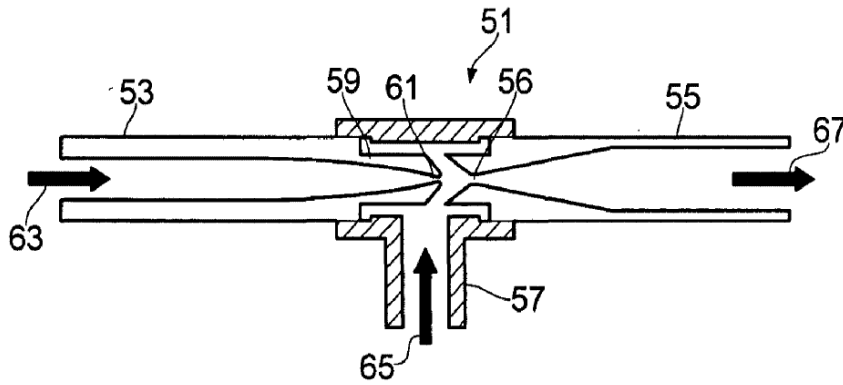


FIG 3

2 Field of the Invention

[0001] Embodiments of the present invention relate to an apparatus and method for laser irradiation. In particular, they relate to an apparatus and method for controlling the environment in which laser irradiation takes place.

3 Background to the Invention

[0002] Laser ablation is a method in which a sample is irradiated with a laser beam such that material is removed from the sample. Laser ablation has a wide range of uses in many different areas of technology. For example it may be used to remove material for analysis so that the chemical or structural composition of a sample may be determined. A laser may also be used to cut or drill into a sample or to scribe or etch into the surface of a sample. Laser ablation may also be used to remove any unwanted material from a sample, this may be useful for removing unwanted short circuits in an electrical circuit or for cleaning a sample by removing any impurities from the surface of the sample.

[0003] Matrix assisted laser desorption ionization (MALDI) is a method in which an analyte is held within a matrix. The matrix is then irradiated with a laser and absorbs the energy from the laser. Some of the energy from the laser is then transferred to the analyte so that the analyte is ionized and removed from the sample. The matrix enables energy to be transferred from the laser to the analyte.

[0004] In many applications of laser irradiation such as laser ablation and MALDI it is advantageous to be able to control the environment in which the laser ablation or MALDI takes place. For example, it may be advantageous to prevent the sample from coming into contact with ambient air as this may oxidize the sample or contaminate the material which has been removed from the sample.

[0005] Known methods of controlling the environment in which laser ablation or MALDI takes place involve placing the sample within a sealed container, however this limits the size of the samples which can be used as they must be able to fit inside the container. In some known methods a relatively large gas flow may be required to control the environment within the container.

4 Brief Description of Various Embodiments of the Invention

[0006] According to various, but not necessarily all, embodiments of the invention there is provided an apparatus for laser irradiation comprising: a housing wherein the housing defines at least a portion of a test volume; a first conduit configured to provide a first flow of gas into the test volume; a second conduit configured to remove the first flow of gas from the test volume; a third conduit configured to provide a second flow of gas; and a flow controller configured to provide a region of increased flow impedance between the first conduit and the third conduit so that the first flow of gas is directed towards the test volume and the second flow of gas is directed away from the first flow of gas so as to restrict gas external to the housing from coming into contact with the first flow of gas.

[0007] Embodiments of the invention provide the advantage that the second flow of gas is used to block the ingress of other gases into the first flow of gas and the test volume where the laser irradiation is taking place. This prevents the sample from coming into contact with ambient air or other gases external to the housing so it is not necessary to place the apparatus in a sealed box or to create a vacuum around the apparatus.

[0008] Also the use of a flow controller between the first conduit and the third conduit ensures that the first flow of gas may be independent from the second flow of gas. This enables the amount of gas flow required to control the laser irradiation environment to be reduced.

[0009] In some embodiments of the invention the apparatus may comprise an optical transmitter configured to enable a laser to be transmitted into the test volume. The optical transmitter may be, for example, an optical window or an optical fibre.

[0010] In some embodiments of the invention the apparatus may comprise a plurality of second conduits configured to remove the first flow of gas from the test volume. Such embodiments of the invention provide the advantage that the flow of gas from each of the second conduits may be provided to a different output. For example, the flow from one conduit may be provided to a first type of analytical apparatus such as an inductively coupled plasma mass spectrometry (ICP-MS) apparatus or MALDI mass spectrometer while the flow from another conduit may be provided to a different type of analytical apparatus such as an apparatus for inductively coupled plasma optical emission spectrometry (ICP-OES) or any other suitable type of optical detector.

[0011] In some embodiments of the invention a jet pump may be coupled to at least one second conduit. Such embodiments of the invention provide the advantage that the jet pump enables the proportion of gas from the first flow of gas which enters the test volume to be controlled.

[0012] In some embodiments of the invention the first conduit may comprise a grating. In some embodiments of the invention the third conduit may comprise a grating. Such embodiments of the invention reduce the amount of turbulence in the flows of gas.

[0013] In some embodiments of the invention the apparatus comprises an electrical connection configured to provide an electrical charge to the grating.

[0014] In some embodiments of the invention the flow controller may be coupled to the grating.

[0015J] In some embodiments of the invention the gas removed from the test volume may comprise particles of solid or liquid dispersed within the flow of gas.

[0016] According to various, but not necessarily all, embodiments of the invention there is provided a method of laser irradiation comprising: positioning a housing over a sample wherein the housing defines at least a portion of a test volume; directing a laser beam toward the sample; directing a first flow of gas into the test volume; removing the first flow of gas from the test volume; and directing a second flow of gas away from the first flow of gas so that the second flow of gas restricts gas external to the housing from coming into contact with the first flow of gas.

[0017J] In some embodiments of the invention the laser beam may be directed through an optical transmitter into the test volume.

[0018] In some embodiments of the invention a plurality of conduits may be provided for extracting gas from the test volume. In some embodiments of the invention a jet pump may be used to extract gas from the test volume.

[0019] In some embodiments of the invention the method may also comprise directing the first flow of gas through a grating. In some embodiments of the invention the method may also comprise directing the second flow of gas through a grating. In some embodiments of the invention an electrical charge may be provided to the grating.

[0020] In some embodiments of the invention a flow controller may be coupled to the grating and configured to direct the first flow of gas into the test volume and direct the second flow of gas away from the first flow of gas.

[0021] In some embodiments of the invention the first flow of gas may comprise helium or argon. In some embodiments of the invention the second flow of gas may comprise nitrogen or argon.

[0022] According to various, but not necessarily all, embodiments of the invention there is provided an apparatus comprising: a housing wherein the housing defines at least a portion of a test volume; a first conduit configured to provide a first flow of gas into the test volume; a second conduit configured to remove the first flow of gas from the test volume; a third conduit configured to provide a second flow of gas; and a flow controller configured to provide a region of increased flow impedance between the first conduit and the third conduit so that the first flow of gas is directed towards the test volume and the second flow of gas is directed away from the first flow of gas so as to restrict gas external to the housing from coming into contact with the first flow of gas.

[0023] According to various, but not necessarily all, embodiments of the invention there is provided a jet pump comprising: an inlet conduit configured to direct a flow of motive fluid into the jet pump wherein the inlet conduit comprises a constriction configured to increase the velocity of the motive fluid; a connector configured to enable the jet pump to be connected to a conduit of a test volume of a laser irradiation apparatus such that gas extracted from the test volume of the laser irradiation apparatus is drawn into the jet pump;

and an outlet conduit configured to discharge the motive fluid and the gas extracted from the test volume of the laser irradiation apparatus from the jet pump.

[0024] In some embodiments of the invention the constriction may comprise a sapphire nozzle. In some embodiments of the invention the nozzle may have a diameter of 160 micrometres.

[0025] In some embodiments of the invention the outlet conduit of the jet pump may comprise a first portion and a second portion where the first portion has a narrower diameter than the second portion and is configured to prevent gas flowing from the outlet conduit towards to the inlet conduit.

5 Brief Description of the Drawings

[0026] For a better understanding of various examples of embodiments of the present invention reference will now be made by way of example only to the accompanying drawings in which:

[0027] FIG. **1** is a schematic illustration of a cross section of an apparatus according to embodiments of the invention;

[0028] FIG. **2** is a perspective view of an apparatus according to an embodiment of the invention in which the grating and flow controller are visible; and

[0029] FIG. **3** is a schematic illustration of a jet pump according to embodiments of the invention.

6 Detailed Description of Various Embodiments of the Invention

[0030] The Figures illustrate an apparatus **1** for laser irradiation comprising: a housing **3** wherein the housing **3** defines at least a portion of a test volume **5**; a first conduit **11** configured to provide a first flow of gas into the test volume **5**; a second conduit **13** configured to remove the first flow of gas from the test volume **5**; a third conduit **15** configured to provide a second flow of gas; and a flow controller **17** configured to provide a region of increased flow impedance between the first conduit **11** and the third conduit **15** so that the first flow of gas is directed towards the test volume **5** and the second flow of gas is directed away from the first flow of gas so as to restrict gas external to the housing **3** from coming into contact with the first flow of gas.

[0031] In the following description, unless expressly stated otherwise, the words "connect" and "couple" and their derivatives mean operationally connected or operationally coupled. It is to be appreciated that any number or combination of intervening components can exist including no intervening components.

[0032] FIG. **1** schematically illustrates a cross section through an apparatus **1** for laser irradiation according to an embodiment of the invention. The cross section is taken through the line X-X as indicated in FIG. **2**. FIG. **2** is a perspective view of the apparatus in which the grating **19** and flow controller **17** are visible.

[0033] The apparatus **1** may be configured to enable a method such as laser ablation to be used for any of a plurality of different purposes, including, but not limited to, analysis of a sample, cutting of a sample, scribing or etching of a sample or repair of samples such as electronic circuits. In other embodiments of the invention the apparatus **1** may be configured for MALDI.

[0034] The apparatus **1** comprises a housing **3**. The housing is configured to overlay a sample **21** so that, in the illustrated embodiment, a gap **4** is provided between the housing **3** and the sample **21**. In some embodiments of the invention some portions of the housing **3** may contact the sample **21**. The width of the gap **4** may be up to 1 mm. The width of the gap **4** used may depend upon the application of the laser irradiation and the gas flows being used.

[0035] The housing **3** defines at least a portion of a test volume **5**. In the illustrated embodiment the test volume **5** is funnel shaped, that is, it comprises a truncated cone portion and a cylindrical portion at the narrower end of the cone. Other shapes of test volume **5** may be used in other embodiments of the invention.

[0036] The test volume **5** is not sealed and comprises an opening **7** at the narrow end. The opening **7** enables a first flow of gas to enter to the test volume **5**. The laser may also be directed through the opening **7** onto the sample **21**.

[0037] In the illustrated embodiment an optical window **9** is provided at the wider end of the test volume **5**. The optical window **9** is configured to enable a laser to be transmitted into the test volume **5**. It is to be appreciated that in other embodiments of the invention other optical transmitters may be used, for example, an optical fibre.

[0038] The optical window **9** seals this end of the test volume **5** and prevents gas external to the housing **3** from entering the test volume **5** but enables a laser to enter the test volume **5**. The optical window **9** may comprise a means for focussing the laser such as a lens.

[0039] The apparatus **1** also comprises a first conduit **11**. The first conduit **11** is configured to provide a first flow of gas into the test volume **5**. In the illustrated embodiment the first conduit **11** is annular and extends around the test volume **5**. The first conduit **11** is configured such that, in use, a flow of gas from the first conduit **11** will be directed towards to the test volume **5**.

[0040] At least one second conduit **13** is provided. The second conduit **13** extends from the test volume **5** and out of the housing **3** and enables the first flow of gas from the first conduit **11** to be removed from the test volume **5**. The flow of gas through the second conduit **13** may comprise solid or liquid particles dispersed within the flow of gas. In some embodiments of the invention the flow of gas may comprise an aerosol.

[0041] In the illustrated embodiment two second conduits **13** are provided. The two second conduits **13** are provided in the side walls of the test volume **5**. In the illustrated embodiment the two second conduits **13** are located at the same height within the test volume **5** and are positioned diametrically opposite each other. It is to be appreciated that in other embodiments of the invention more than two second conduits **13** may be provided and these may be arranged around the test volume **5** in any suitable configuration. Similarly, in other embodiments of the invention there may only be one second conduit **13** provided.

[0042] The second conduits **13** may be coupled to another apparatus so that the gas which has been extracted from the test volume **5** is provided to the another apparatus. For example, in embodiments of the invention where laser ablation is being used to analyse the sample **21** the second conduit **13** may provide the gas to an apparatus for analysing the material removed from the sample **21**. The apparatus for analysing the sample **21** may be any means which enables the structure or composition of the sample **21** to be determined for example, a mass spectrometer such as an ICP-MS instrument or an apparatus for ICP-OES.

[0043] In some embodiments of the invention the second conduit **13** may provide the gas to a control means which may then provide feedback to control the laser. The control means may be any means which is configured to detect an event and, in response to the detection of the event, provide feedback to control the laser. Such events may be, for example, the detection of a material or type of material in the gas flowing through the second conduit **13** or the detection that a certain volume of gas has passed through the second conduit **13**.

[0044] In some embodiments of the invention the material which may be removed from the sample **21** by the laser may be toxic or harmful, in such cases the second conduits **13** may enable the toxic or harmful fumes to be safely removed.

[0045] In embodiments where a plurality of second conduits **13** are provided the second conduits **13** may provide the gas to a plurality of different apparatus.

[0046] The apparatus **1** also comprises a third conduit **15** which is positioned adjacent to the first conduit **11** and is configured to provide a second flow of gas. In the illustrated embodiment the third conduit **15** is annular and extends around the first conduit **11**. The third conduit **15** is configured so that, in use, the second flow of gas is directed away from the test volume **5**.

[0047] A flow controller **17** is provided between the first conduit **11** and the third conduit **15**. The flow controller **17** extends around the perimeter of the first conduit **11**. In the illustrated embodiment the flow controller is a ring which projects out of the surface of grating **19** so that, in use, the flow controller **17** is the closest part of the apparatus **1** to the sample **21**. The flow controller **17** increases the impedance to gas flow between the first conduit **11** and the third conduit **15** because the gap **4** between the flow controller **17** and the sample **21** is smaller than the gap **4** between the sample and other parts of the housing **3**. By positioning the flow controller **17** between the first conduit **11** and the third conduit **15** the flow of gas from the first conduit **11** is directed in an opposite direction to the flow of gas from the third conduit **15**.

[0048] It is to be appreciated that in other embodiments of the invention other configurations of flow controller **17** may be used. For example the flow controller **17** may have a different shape or there may be more than one flow controller **17**.

[0049] The apparatus **1** also comprises a grating **19**. In the illustrated embodiment the grating **19** extends over the first conduit **11** and the third conduit **15** so that the flows of gas from the two conduits **11**, **15** pass through the grating **19**. As can be seen in FIG. **2**, in the illustrated embodiment the grating **19** comprises a single annular disc which extends over both the first conduit **11** and the third conduit **15**. In other embodiments of the invention a different grating **19** may be provided for each of the different conduits **11**, **15**.

[0050] The grating **19** comprises an array of small holes **31**. The holes **31** divide the flows of gas from the conduits **11**, **15** from a single large jet into a plurality of smaller jets. This makes the flows of gas quasi-laminar and less turbulent. As the flows of gas are less turbulent this decreases the amount of gas external to the housing **3** which is drawn into the flows of gas and reduces the amount of gas necessary to control the laser irradiation environment.

[0051] In the illustrated embodiment the holes **31** only cover a small proportion of the surface area of the grating **19**. For example, in some embodiments of the invention the holes **31** may cover approximately 1 percent of the surface area. In other embodiments of the invention the holes **31** may cover a different percentage of the surface area. Covering only a small proportion of the surface area of the grating **19** with holes provides an improved performance of the grating **19**.

[0052] In some embodiments of the invention the grating may be made from a metal such as nickel.

[0053] In the illustrated embodiment the flow controller **17** is attached to the grating **19**. This makes the apparatus **1** simple to assemble as it reduces the number of parts which are required. In other embodiments of the invention more than one grating **19** may be provided and the flow controller **17** may be attached either to one of the gratings **19** or directly to the housing **3**.

[0054] In some embodiments of the invention an electrical connection **23** may be provided to the grating **19**. The electrical connection **23** may provide an electrical charge to the grating **19** so that, in use, the grating **19** is electrically biased with respect to the sample **21**. This may enable ions which have been removed from the sample **21** by the laser to escape the surface of the sample **21** more easily.

[0055] When the apparatus **1** is in use the housing **3** is positioned over a sample **21** so that the test volume **5** overlays the sample **21**. The sample **21** may be any item from which material is to be removed by a laser. For example the sample **21** may be a piece of material which is to be analysed or it may be an item such as an electrical circuit which is to be repaired.

[0056] In the illustrated embodiment the housing **3** is positioned close to but not touching the sample **21** so that there is a gap **4** between the housing **3** and the sample **21**. As mentioned above, the gap **4** between the housing **3** and the sample **21** may be up to 1 mm. The narrowest part of the gap **4** is the point between the flow controller **17** and the sample **21**. In other embodiments of the invention the housing **3** may contact the sample **21**.

[0057] A laser is directed through the optical window **9** and the test volume **5** to the sample **21**. The laser causes material to be removed from the sample **21**. The material is then extracted from the sample by the gas flow through the test volume **5** as will be described below.

[0058] A first flow of gas is provided through the first conduit **11**. In the illustrated embodiment the flow of gas through the first conduit **11** is provided downwards towards the sample **21** in the direction indicated by the arrows **25**.

[0059] The gas used in the first flow of gas may depend on the application of the laser irradiation. In some embodiments of the invention the gas used may be helium. Helium may be a suitable gas to use because it is inert so it will not contaminate the sample **21** or the material removed from the sample **21**. Helium also has a low density which makes it easier for material to escape the surface of the sample **21** and a high thermal conductivity which prevents the build up of heat which may affect the efficiency of the laser irradiation. Helium also has a high ionization potential which prevents the gas from forming a plasma which might scatter the laser and affect the nature of the laser interaction with the sample **21**. In other embodiments of the invention other gases may be used such as argon.

[0060] The first flow of gas through the first conduit **11** may be controlled by a mass flow controller or any other apparatus which enables the flow of gas to be accurately controlled.

[0061] In some embodiments of the invention the first conduit **11** may be configured so that the first flow of gas enters the first conduit **11** tangentially. This ensures a good distribution of gas around the perimeter of the first conduit **11** so that there is an even distribution of gas through the grating **19**.

[0062] The first flow of gas flows through the grating **19** and into the gap between the sample **21** and the housing **3**. The first flow of gas is then directed towards the test volume **5** by the flow controller **17** so that the first flow of gas flows along the gap **4** to the test volume **5** in the direction of arrows **27**.

[0063] The first flow of gas then enters the test volume **5** through the opening **7** where the material removed from the sample **21** by the laser is entrained within the first flow of gas. The first flow of gas then flows upwards through the test volume **5** toward the second conduits **13** as indicated by the arrows **29** in FIG. 1.

[0064] The first flow of gas and the material entrained within the gas then flows through the second conduits **13** and so is removed from the test volume **5**. As described above, the second conduits **13** may be coupled to other apparatus so that the flow of gas is provided to other apparatus.

[0065] A second flow of gas is provided through the third conduit **15**. In the illustrated embodiment the flow of gas through the third conduit **15** is provided downwards towards the sample **21** in the direction indicated by the arrows **34**. The second flow of gas through the third conduit **15** is parallel to the first flow of gas through the first conduit **11**.

[0066] The gas used in the second flow of gas may depend on the application of the laser irradiation. In some embodiments of the invention the gas used may be nitrogen as this may provide cost benefits. In some embodiments of the invention the gas used in the second gas flow may be argon as this may also be used for ICP-MS.

[0067] The second flow of gas through the third conduit **15** may be controlled by a mass flow controller or any other apparatus which enables the flow of gas to be accurately controlled.

[0068] In some embodiments of the invention the third conduit **15** may be configured so that the second flow of gas enters the third conduit **15** tangentially. This ensures a good distribution of gas around the perimeter of the third conduit **15** so that there is an even distribution of gas through the grating **19**.

[0069] The second flow of gas flows through the grating **19** and into the gap **4** between the sample **21** and the housing **3**. The second flow of gas is then directed in the opposite direction to the first flow of gas by the flow controller **17** so that the second flow of gas flows along the gap **4** away from the test volume **5** and towards the edge of the housing **3** as indicated by the arrows **35**.

[0070] The second flow of gas acts as a barrier to the first flow of gas and prevents other gases, external to the apparatus, from coming into contact with the first flow of gas. The apparatus **1** may be configured so that only the gas from the first conduit **11** enters the test volume **5**. This enables the environment in the test volume **5** to be controlled so that it is suitable for the laser irradiation. Using a second flow of gas to prevent external gases from entering the test volume **5** means that it is not necessary to place the apparatus **1** in a sealed container so the apparatus **1** may be used for any size of sample **21**.

[0071] Also the two flows of gas maybe independently controlled which means that the overall gas flow may be reduced.

[0072] In some embodiments of the invention a jet pump **51** may be connected to one or more of the second conduits **13**. An example of a jet pump **51** which may be used in embodiments of the invention is illustrated in FIG. **3**.

[0073] The jet pump **51** comprises an inlet conduit **53**, an outlet conduit **55** and a connector **57**.

[0074] The inlet conduit **53** is configured to be connected to a supply of motive fluid at one end and connected to the jet pump **51** at the other end.

[0075] The inlet conduit **53** comprises a constriction **59** at the end connected to the jet pump **51**. At the constriction **59** the cross sectional area of the inlet conduit **53** is gradually decreased. The constriction **59** terminates in a nozzle **61**. The nozzle **61** may have a very small diameter. In some embodiments of the invention the diameter of the nozzle **61** may, be approximately **160** micrometers.

[0076] The nozzle **61** may be made of any suitable material for example sapphire.

[0077] The outlet conduit **55** is configured to be connected to the jet pump at one end. The second end may be connected to another apparatus such as an ICP-MS apparatus.

[0078] The outlet conduit **55** is positioned relative to the inlet conduit **53** so that the gas flow from the inlet conduit **53** flows into the outlet conduit **55**.

[0079] The portion of the outlet conduit **55** connected to the jet pump **51** comprises a narrow throat **56** which has a small cross sectional area. In the illustrated embodiment the cross sectional area of the outlet conduit **55** gradually increases from the narrow throat **56** until the cross sectional area of the outlet conduit **55** is greater than the cross sectional area of the inlet conduit **53**. It is to be appreciated that in other embodiments of the invention the outlet conduit **55** and the inlet conduit **53** may have the same cross sectional area or the inlet conduit **53** may have a greater cross sectional area than the outlet conduit **55**.

[0080] The connector **57** is configured so that one end may be connected to a second conduit **13** of the laser irradiation apparatus **1** and the other end may be connected to the jet pump **51**. The connector **57** enables the flow of gas removed from the test volume **5** to be provided to the jet pump **51**.

[0081] In use a motive fluid is provided to the jet pump **51** as indicated by the arrow **63**. The motive fluid used may depend upon the application of the invention. In some embodiments of the invention the motive fluid used may be argon as this may be used for ICP-MS.

[0082] As the motive fluid flows through the constriction **59** the velocity of the fluid increases because the cross sectional area of the inlet conduit is decreasing **59**. The jet of fluid which exits inlet conduit at the nozzle **61** may have a very large velocity. In some embodiments of the invention the velocity of the jet may be close to or faster than the speed of sound in the motive fluid.

[0083] The fluid leaving the inlet conduit **53** has a very high velocity. The jet pump may be configured so that fluid leaving the inlet conduit **53** has a low pressure region. The low pressure region may be on the axis of symmetry of the jet. This draws the gas from the connector **57** into the jet pump **51** as indicated by the arrow **65**. This enables the flow of gas from the test volume **5** to be drawn out of the test volume **5** and into the jet pump **51**.

[0084] As the jet of fluid exiting the inlet conduit **53** has a very high velocity it is also very turbulent. The turbulence and viscous drag on the surrounding fluid mean that the jet of fluid is strongly entraining which provides another mechanism by which gas from the test volume **5** is drawn out of the test volume **5** and into the jet pump **51**. This also enables the gas flowing in through the connector **57** to be efficiently mixed with the motive fluid and carried into the outlet conduit **55**. Therefore the jet pump **51** provides an efficient means for mixing the gas from the test volume **5** with another fluid.

[0085] The mixture of the motive fluid and the flow of gas from the test volume **5**, then enters the outlet conduit **55** where it flows along the outlet conduit **55** away from the jet pump **51** as indicated by the arrow **67**.

[0086] The narrow throat **56** of the outlet conduit **55** prevents fluid from the outlet conduit from flowing back down the outlet conduit towards the inlet conduit **53**. The increasing cross section of the outlet conduit **55** acts as a diffuser and decreases the velocity of the flow of gas in the conduit.

[0087] Therefore the jet pump **51** provides a means for controlling the proportion of flow of gas from the first conduit **11** which flows into the test volume **5**. This provides an improved control over the environment in which the laser irradiation takes place. The jet pump **51** also enables the gas to be efficiently removed from the test volume **5**.

[0088] Although embodiments of the present invention have been described in the preceding paragraphs with reference to various examples, it should be appreciated that modifications to the examples given can be made without departing from the scope of the invention as claimed. For example in the above described embodiments a laser is used to provide energy to the sample in order to remove material from the sample. In other embodiments of the invention an energy source other than a laser such as a supersonic aerosol stream or a spark for a conducting sample may be used.

[0089] Also in the illustrated embodiments the flow controller **17** increases the impedance to gas flow between the first conduit **11** and the third conduit **15** by decreasing the cross sectional area of the gap **4** between the first conduit **11** and the third conduit **15**. It is to be appreciated that other means of providing increased impedance to gas flow may be used in addition to or instead of the reduced cross sectional area of the gap **4**. For example, the flow of gas through the first conduit **11** and the third conduit **15** may be controlled so that there is a larger flow of gas through the third conduit **15**, the apparatus **1** may be configured so that the impedance to gas flow into the surrounding atmosphere is less than the impedance to gas flow through the second conduit **13**, the grating **19** may be configured to control the stiffness and direction of the flow of gas etc.

[0090] Features described in the preceding description may be used in combinations other than the combinations explicitly described.

[0091] Although functions have been described with reference to certain features, those functions may be performable by other features whether described or not.

[0092] Although features have been described with reference to certain embodiments, those features may also be present in other embodiments whether described or not.

[0093] Whilst endeavoring in the foregoing specification to draw attention to those features of the invention believed to be of particular importance it should be understood that the Applicant claims protection in respect of any patentable feature or combination of features hereinbefore referred to and/or shown in the drawings whether or not particular emphasis has been placed thereon.

1. An apparatus for laser irradiation comprising:
 - 1.1. a housing wherein the housing defines at least a portion of a test volume;
 - 1.2. a first conduit configured to provide a first flow of gas into the test volume;
 - 1.3. a second conduit configured to remove the first flow of gas from the test volume;
 - 1.4. a third conduit configured to provide a second flow of gas; and
 - 1.5. a flow controller configured to provide a region of increased flow impedance between the first conduit and the third conduit so that the first flow of gas is directed towards the test volume and the second flow of gas is directed away from the first flow of gas so as to restrict gas external to the housing from coming into contact with the first flow of gas.
2. An apparatus as claimed in claim 1 wherein the apparatus comprises an optical transmitter configured to enable a laser to be transmitted into the test volume.
3. An apparatus as claimed in claim 1 wherein the apparatus comprises a plurality of second conduits configured to remove the first flow of gas from the test volume.
4. An apparatus as claimed in claim 1 wherein a jet pump is coupled to at least one second conduit.
5. An apparatus as claimed in claim 1 wherein the first conduit comprises a grating.
6. An apparatus as claimed in claim 1 wherein the third conduit comprises a grating.

7. An apparatus as claimed in claim 5 comprising an electrical connection configured to provide an electrical charge to the grating.
8. An apparatus as claimed in claim 5 wherein the flow controller is coupled to the grating or the housing.
9. A method of laser irradiation comprising:
 - 9.1. positioning a housing over a sample wherein the housing defines at least a portion of a test volume;
 - 9.2. directing a laser beam toward the sample;
 - 9.3. directing a first flow of gas into the test volume;
 - 9.4. removing the first flow of gas from the test volume; and
 - 9.5. directing a second flow of gas away from the first flow of gas so that the second flow of gas restricts gas external to the housing from coming into contact with the first flow of gas.
10. A method as claimed in claim 9 wherein the laser beam is directed through an optical transmitter into the test volume.
11. A method as claimed in claim 9 wherein a plurality of conduits are provided for extracting gas from the test volume.
12. A method as claimed in claim 9 wherein a jet pump is used to extract gas from the test volume.
13. A method as claimed in claim 9 further comprising directing the first flow of gas through a grating.
14. A method as claimed in claim 9 further comprising directing the second flow of gas through a grating.
15. A method as claimed in claim 13 comprising providing an electrical charge to the grating.
16. A method as claimed in claim 13 wherein a flow controller is coupled to the grating or the housing and configured to direct the first flow of gas into the test volume and direct the second flow of gas away from the first flow of gas.
17. A method as claimed in claim 9 wherein the first flow of gas comprises helium or argon.
18. A method as claimed in claim 9 wherein the second flow of gas comprises nitrogen or argon.
19. An apparatus comprising:
 - 19.1. a housing wherein the housing defines at least a portion of a test volume;
 - 19.2. a first conduit configured to provide a first flow of gas into the test volume;
 - 19.3. a second conduit configured to remove the first flow of gas from the test volume;
 - 19.4. a third conduit configured to provide a second flow of gas; and
 - 19.5. a flow controller configured to provide a region of increased flow impedance between the first conduit and the third conduit so that the first flow of gas is

directed towards the test volume and the second flow of gas is directed away from the first flow of gas so as to restrict gas external to the housing from coming into contact with the first flow of gas.

20. A jet pump comprising:

- 20.1. an inlet conduit configured to direct a flow of motive fluid into the jet pump wherein the inlet conduit comprises a constriction configured to increase the velocity of the motive fluid;
 - 20.2. a connector configured to enable the jet pump to be connected to a conduit of a test volume of a laser irradiation apparatus such that gas extracted from the test volume of the laser irradiation apparatus is drawn into the jet pump; and an outlet conduit configured to discharge the motive fluid and the gas extracted from the test volume of the laser irradiation apparatus from the jet pump.
21. A jet pump as claimed in claim 20 wherein the constriction comprises a sapphire nozzle.
22. A jet pump as claimed in claim 20 wherein the nozzle has a diameter of 160 micrometres.
23. A jet pump as claimed in claim 20 wherein the outlet conduit comprises a first portion and a second portion where the first portion has a narrower diameter than the second portion and is configured to prevent gas flowing from the outlet conduit towards to the inlet conduit.

* * * * *

THIS PAGE IS INTENTIONALLY BLANK

Appendix B An open, non-contact cell for laser ablation-inductively coupled plasma-mass spectrometry (Paper 2)

Dhinesh Asogan,^{a,b} Barry L. Sharp,^a Ciaran J. P. O' Connor,^c Damon A. Green^c and Robert W. Hutchinson,^c *J. Anal. At. Spectrom.*, 2009, **24**, 917 – 923

^a *Centre for Analytical Science, Department of Chemistry, Loughborough University, Loughborough, Leicestershire, UK LE11 3TU, e-mail: B.L.Sharp@lboro.ac.uk*

^b *Centre for Innovative and Collaborative Engineering, Department of Civil and Building Engineering, Loughborough University, Loughborough, Leicestershire, UK LE11 3TU*

^c *Electro Scientific Industries Europe Ltd., New Wave Research Division, 8 Avro Court, Ermine Business Park, Huntingdon, Cambs, UK PE29 6XS*

DOI: 10.1039/B904850B

ABSTRACT

A novel, open, non-contact cell for laser ablation, capable of sampling: large planar samples, embedded planar samples, or samples of less than 2 mm mounted on a planar platform, without an outer containment enclosure, is described. This cell, when tested on NIST-613 CRM, exhibited rapid wash-out (<3.6 s for 99% signal reduction), low limits of detection and good signal precision in LA-ICP-MS. The cell uses a dual, annular, micro-jet gas flow array to exclude atmospheric gases and to entrain the ablated sample aerosol. The micro-jet array employed enabled a sampling height, between the sample surface and the lowest plane of the cell, of up to 200 µm. The micro-jet array has the facility to be electrically biased if the application demands it, *e.g.* extracting a charged plume in Matrix-Assisted Laser Desorption/Ionisation (MALDI) or Desorption Electrospray Ionisation (DESI) experiments. This particular implementation of the cell featured dual sample output channels, which could enable connection of the cell to more than one analyser. A micro jet-pump was coupled to the cell to extract the ablated aerosol from the low-volume inner ablation chamber, provide mixing of the aerosol with the injector flow of the ICP and to isolate the cell from downstream conditions in the injector flow. Potential applications of this cell include: analysis of silicon wafers, gel-plates/membranes, tissue samples, multiple sample analysis in high throughput facilities; and toxic fume removal and analysis in laser scribing, cutting and etching.

Keywords – laser ablation, cutting, etching, scribing, ICP-MS, large samples, multiple sample handling, gel-plates, membranes, tissue mapping, silicon wafers.

Paper type – Journal

1 Introduction

Laser ablation-inductively coupled plasma (LA-ICP) optical- and mass-spectrometry are currently limited by the size of the samples they can analyse. Ingress of atmospheric gases can make an ICP unstable, leading to extinction of the plasma, and the presence of these gases greatly enhances the abundance of unwanted molecular ions when mass spectrometric detection is employed. This has meant that samples have had to be enclosed in a sample chamber filled with argon or helium. To avoid difficulties with sample transport and excessive wash-in and wash-out times, the sample cells have tended to be relatively small.

In 2007, Bleiner and Bogaerts¹ studied a range of cell designs using computer simulations to assess gas flow patterns and the entrainment of the aerosol. The various cells were categorised into 'closed' and 'open' cells. The 'closed' cell was defined as a sample chamber which fully enclosed the sample, requiring little to no sample preparation, and the 'open' cell used the sample as a final, closing wall; this normally requires the sample to be polished to provide adequate sealing. The 'open' cells offer advantages in terms of shortened washout times (as most have small internal volumes) and increased flexibility in sample size. However, alteration of the sample surface by polishing is not viable for many samples; it may introduce contamination or remove features that could otherwise be studied by the LA technique.

Custom cells have been described for a variety of applications including closed cells for: low pressure ablation², ablation of gel plates and membranes³ and radionuclides⁴; and open cells for: continuous sampling⁵, flat plates⁶, solutions, polymers and steel⁷, antiques⁸ and large sample handling.⁹⁻¹¹

A key feature of all the cells described to date is that ultimately the sample is either contained in a box or contacts the sample for a final seal; this limits the sample size and complicates multi-sample or high throughput operation.

An open, 'non-contact' cell¹² that does not physically touch the sample would overcome many of the problems associated with existing cell designs and enable LA to be applied directly to samples of any arbitrary size or number. This paper describes such a cell.

2 LA cells using annular gas flows

Annular gas flows can be used to reduce the effective volume of an ablation cell and to entrain ablated material from the ablation site. Further, by maintaining a stable geometry relative to the laser beam, the ablation site remains in a reproducible gas flow environment.

A cell design, incorporating an annular flow of argon, intended for quasi-continuous sampling was patented by Barringer in 1980.⁵ This consisted of a reel of adhesive tape onto which samples were spotted. The sample spots then passed under a 'vaporisation cell' where the sample was ablated by the laser. The vaporisation cell floated above the tape and entrained the ablated sample plume by means of the annular gas flow. This flow was angled inwards to encourage the gas to flow towards the point of ablation and then towards the outlet. The whole setup of reels and vaporisation cell sat inside an outer box, pressurized with argon, to provide an inert atmosphere.

In 1988, Arrowsmith and Hughes⁶ adapted this design to incorporate a motorised stage capable of supporting large (10×10 cm) samples. The XYZ translation stage, the stepper motors and the sampling cell were all enclosed in a large outer box, pressurised with argon. The inlet gas flow rate (controlled by a mass flow controller) was $5 - 10 \text{ l min}^{-1}$, whilst the outlet gas flow rate of $1 - 2 \text{ l min}^{-1}$, and the pressure in the cell, were controlled by valves. It was found that the optimum conditions for sample transport, ablation efficiency and ICP-MS signal occurred when the inlet gas flow was fixed at a very high flow of 10 l min^{-1} and the outlet gas flow was at approximately 1.5 l min^{-1} . The inlet gas flow was set at this high level because it had to both purge the large outer box, to exclude atmospheric gases, and to entrain the sample.

In 2000, Boué-Bigne⁷, working in this group, adapted the design further in an attempt to reduce the gas consumption. The gas flows for this cell were optimised to an inlet flow of 1 l min^{-1} and an outlet flow of 0.4 l min^{-1} using an ammonium chloride vapour generator to visualise the flow geometry. At these gas flows, the vapour was seen to rise vertically in a thin stream in the centre of the cell and then bend sharply towards the exit channel. However, the cell used o-ring seals to contact a sample holder allowing the gas flow to be reduced whilst still effectively excluding atmospheric gases. No outer containment box was required with this design.

3 Principle of operation of the open, non-contact cell

The cell described in this paper was designed to meet the following criteria:

1. no contact with the sample surface
2. full exclusion of atmospheric gases
3. the capability to accept large samples of indeterminate size and number
4. low gas consumption
5. rapid wash-out
6. good reproducibility and sensitivity

Fig. 1 shows a schematic diagram of the cross-section of the open, non-contact cell. Laser energy passes through an optical window down to the sample surface where ablation takes place. The cell makes use of dual, concentric, annular gas flows. The outer, 'curtain' flow, is used to exclude atmospheric gases from the ablation site, and hence the analyser, and the inner, 'carrier' flow, is used to provide an inert atmosphere and to transport the ablated material to the analyser.

A $100 \mu\text{m}$ thick annular flow restrictor is placed between the two gas flows to provide flow impedance and to vector the curtain gas out towards the surrounding atmosphere and the carrier gas in towards the central channel of the cell.

An array of $18 \mu\text{m}$ holes is placed over the two annular channels to provide stiff micro-jets of gas. A free, turbulent jet entrains gas and virtually doubles its volume for every doubling of length, which implies its axial momentum is gradually partitioned into 3-dimensions as the axial distance increases.^{13, 14} Therefore, these micro-jets maintain stiffness and here we estimate the effective length to be approximately 20 times their diameter (in this case, $360 \mu\text{m}$). This gives the cell a notional sampling distance of up to $260 \mu\text{m}$ between the sample surface and the flow restrictor. In this first iteration of the design, the sampling distance was set manually using a set of feeler gauges.

The micro-jet array provides a quasi-laminar flow towards the sample surface that has low entrainment properties. Its open area is approximately 1% of the total area and, through the stiffness of the micro-jets, it provides effective isolation of the ablation area at a fraction of the flow that would otherwise be required. The low turbulence promotes rapid removal of aerosol from the ablation chamber through the reduction of eddy currents. The micro-jets also improve tolerance to edge effects, compared with open channels, as losing a few jets over the edge of a sample does not distort the total flow.

This array is mounted on a screw-on ring, which means that it is exchangeable and any size of micro-jets can be selected therefore allowing the cell's sampling distance to be tuned for a particular application.

The ablation site is contained within a low volume inner ablation cell with dual output channels, allowing two analysers to be connected simultaneously. More outlets could be provided if necessary. The vertical dimension of the cell from the lower plane of the optical window to the upper plane of the micro-jet array is 16.5 mm. Gas enters the inner ablation cell through a 4 mm diameter opening in the base of the cell. The inner cell has a swept volume of 0.63 cm³ when operating in single output mode, and 0.84 cm³ in dual output mode. Closing one output channel does not affect the gas dynamics for the ablation site or the sample transport through the channel that remains open. Smaller cells could readily be constructed, but here standard 6 mm o.d. tubing and a BNC connector were used with the cell and so connectivity influenced the size of the device.

It was recognised that it would be difficult to achieve full capture of the carrier gas flow and so a micro jet-pump was designed to pump the carrier gas to the analyser. Jet-pumps are quite commonly used in engineering applications, but as far as the authors know, devices on the scale used here have not been previously described, or implemented for laser ablation.

Pisonero¹⁵ *et al.* described a pumping arrangement in their 'HEAD' cell. The pump was configured with a nozzle (size not given) in a cross-flow arrangement with a second nozzle (0.5 mm in diameter). The first nozzle provided a small pressure drop on the downstream side, but, as this was a closed system, this did not influence the flow through the chamber, rather it was demonstrated that the pressure drop enhanced aerosol dispersion. A further benefit of the device was to provide good mixing between the aerosol and the driving make-up gas.

Fig. 2 shows a schematic of a micro jet-pump, consisting of a 160 µm nozzle leading to a 1.5 mm throat (with a diffuser) separated by 0.25 – 2.5 mm, all enclosed within a tee-piece. The third port of the tee-piece was then connected to the open, non-contact cell.

The nozzle of the micro jet-pump provides a free, turbulent jet operated below the critical pressure ratio¹⁶ so that it reaches the sonic velocity at the exit plane of the nozzle and then may expand supersonically beyond that producing a pattern of shock waves. The flow through the nozzle is usually referred to as the motive flow. This jet, through a complex combination of over-expansion (giving a lower than ambient pressure) and strong viscous entrainment in the jet boundary, provides a region of decreased pressure within its housing that enables the carrier gas to be entrained from the ablation site.

The turbulent jet also provides an efficient mixing environment for the ablated material and the motive flow, which would normally be the argon injector flow for an ICP. In ICP-MS, this can reduce fractionation through homogenising the aerosol and provide improved precision and reproducibility by ensuring a constant plasma environment during analysis.

The throat acts as a 'gas diode' in that it isolates the entrained flow and the free jet from conditions downstream from the pump. Further, the diffuser slows the gas and recovers static pressure that can pump the flow to the external analyser. This is important because the cell is open to atmosphere and, without the throat, a change in the impedance of the channel connecting the cell to the ICP could result in the motive flow being directed back into the cell. If required, additional gases or wet aerosols can be added to the flow downstream from the pump without affecting the gas dynamics at the ablation site.

4 Gas dynamics

The cell was tested for transmission of input gases through to one output channel. Helium was used for the carrier flow (as used in most LA experiments), nitrogen for the curtain gas (although argon might also be used) and argon for the motive flow in the jet pump. Using argon as the motive flow, the entrainment of helium (a much lighter gas than argon) is efficient as the micro jet-pump is a momentum exchange device that conserves total momentum in the gas flow.

The cell was mounted to a UP-213 laser ablation system (Electro Scientific Industries, New Wave Research Division, Huntingdon, Cambridgeshire, UK), using the co-axial light source for sample illumination. A plate of clear glass ($20 \times 20 \times 0.4$ cm) was placed under the open, non-contact cell to act as a sample. The distance between the sample surface and the flow restrictor was set at $200 \mu\text{m}$ (using a feeler gauge). Table 1 shows the output flow rate and transmission efficiency (with respect to total input flow) at typical working input flow rates of 1.20 l min^{-1} helium carrier gas and 2.50 l min^{-1} nitrogen curtain gas. The sum of the output flows, when the input channels were enabled independently, was lower than the output when both channels were working simultaneously, which suggests that the curtain flow helped to vector the carrier flow through the cell to the output.

With the micro-jet pump in place, the output of the cell could be tuned up to approximately 1.40 l min^{-1} with a motive flow of 0.40 l min^{-1} argon, which comprised 100% of the helium carrier flow and approximately 5% of the curtain flow. By further tuning the micro jet-pump separation between the nozzle and the throat, the entrainment flow could be reduced to give approximately 0.62 l min^{-1} output, which is in the region of helium flow used for most laser ablation cells.

To test for the exclusion of atmospheric gas, one output of the non-contact cell was connected to a Cirrus quadrupole gas mass spectrometer (MKS Instruments UK Ltd, Altrincham, Cheshire, UK). By looking for atmospheric oxygen and nitrogen in the output, it was found that the output flow contained less than 0.005% atmospheric oxygen and less than 0.04% nitrogen, which could be a combination of atmospheric nitrogen and curtain flow nitrogen, as shown in Fig. 3. The nitrogen content of the output flow was found to be $\sim 0.01\%$ at normal cell operating conditions. The micro jet-pump was not connected for this experiment.

5 LA-ICP-MS performance

The open, non-contact cell was connected to an Agilent 7500 quadrupole ICP-MS instrument (Agilent Technologies, Stockport, Cheshire, UK) and evaluated using NIST-613 CRM glass for wash-in, wash-out, sensitivity, signal-to-background ratio, reproducibility and fractionation effects. When igniting the ICP, a make-up argon flow was used to establish the central sampling channel through the plasma. During cell operation, this make-up argon flow was fine-tuned to optimize plasma conditions.

The cell system was tuned for sensitivity and transient signal response across the mass range from ${}^7\text{Li}$ to ${}^{238}\text{U}$. The LA-ICP-MS settings are shown in Table 2. Fig. 4 shows a short wash-in time of less than 3 seconds and a wash-out time of less than 4 seconds (connected using 1/8" i.d., 1/4" o.d. Tygon® tubing through the standard UP-213 gas valves and manifold), which means the cell has good dynamic response for spatial resolution and mapping experiments. The drop in signal over the first 10 s occurred because the initial pulse illuminated the full 55 μm spot in focus, and subsequently on scanning, the laser spot only illuminated a segment of the sample completely in focus; therefore, the total ablated volume per-pulse decreased.

It must be noted that NIST-613 CRM has an outer diameter of 15 mm, which is smaller than the outer diameter of the curtain channel of the non-contact cell (18 mm). During line scans, the edge of the NIST glass approached closely to the outer edge of the flow restrictor, so that much of the curtain would have been spilling over the edge of the sample. As indicated above, the micro-jet array provided good tolerance to edge effects as the distortion in the gas flows were minimised. However, this still may have caused decreased signal stability and slower wash-out than the cell is capable of producing with larger samples.

Limits of detection (LOD's) were established, along with sensitivity, signal-to-background ratios (SBR's) and relative standard deviations (%RSD's) for line scans. The formation of molecular species was also investigated. The cell was operated using both nitrogen and argon as curtain gases and at three different sampling distances between the sample surface and the flow restrictor. Table 3 and Table 4 summarise the performance of the non-contact cell.

From Table 3, it is shown that comparing nitrogen and argon in the curtain flow, there is a small but significant increase in sensitivity for nitrogen. This probably reflects a small ingress of nitrogen into the carrier flow, which has been demonstrated to be potentially beneficial for many elements.^{17, 18}

The detection limits show an improving trend towards high mass elements, which is characteristic of ICP-MS, and additionally the background interferences tend to be lower in this region of the mass spectrum. There is a trend towards favouring nitrogen in the curtain gas at higher mass-to-charge ratios, which may be indicative of the high mass elements benefitting more from the small nitrogen ingress to the plasma.

The SBR's are comparable for each individual element, but not across the whole element suite because their concentrations vary. The data suggests that SBR improved as the sampling distance between the sample surface and the flow restrictor reduced, but no significant difference was observed between the data for argon and nitrogen curtain flows.

An observation made during these experiments was that the SBR's were higher by a factor 2 for the higher mass elements (Rb onwards) compared with the standard UP-213 cell operating under similar helium flows and plasma conditions. The absolute sensitivities were lower with the non-contact cell, and therefore the improvement in SBR was obtained because the background levels were lower by a factor of between 2- and 10-fold using the non-contact cell. This indicates the cell is a clean system, with minimal memory effects and deposition of ablated material on the inner surfaces of the central cell volume.

There appears to be little correlation between the sampling distance and the sensitivity or LOD. There are differences in sensitivity for the higher mass elements, but these are also influenced by the curtain gas as well as the sampling distance, more experiments are required to assess whether these trends are significant.

The %RSD's, however, show that better precision was obtained when the cell was closer to the sample surface. This is due to the curtain flow having greater stiffness at short range; hence at low sampling distances, the gas dynamics at the ablation site are less affected by local pressure pulses. The %RSD's are higher than expected, but this could be due to a combination of the curtain flow spilling over the edge of the glass as well as reflecting genuine inhomogeneity in the NIST glass itself.

^{85}Rb , ^{232}Th and ^{238}U were chosen to monitor molecular species as these elements have the fewest isobaric interferences at their respective molecular ions derived from the NIST glass. From Table 4, the molecular ion formation was less than 0.17% for all species across the three sampling distances using both curtain gases. Using an open cell, it is impossible to exclude 100% of the atmospheric gases from the ablation site due to diffusion through the gas boundaries. However, the cell described was able to minimise this effect; for example, the ThO^+/Th^+ ratio was between 0.12% and 0.17%. This shows that the curtain gas was effective at shielding the ablation site from the atmosphere, irrespective of sampling distance (within the limits of the micro-jet array used).

Fractionation effects were found to be dependent on the operating parameters and by adjustment of the carrier gas flow, the micro jet-pump motive flow and the make-up argon gas flow these could be reduced to negligible levels. For a given laser it does not seem likely that this tuning would have changed fractionation at the ablation site and therefore the observed changes related to transport and fractionation in the plasma.

Fig. 5 shows the transient signals obtained for various elements from six consecutive line scans on NIST-613 CRM, with the acquired $^{238}\text{U}/^{232}\text{Th}$ ratio superimposed above (a logarithmic scale is used, which has tended to over-emphasise the noise at the end of the washout period). Some spikes occurred in the signal during the washout period, which were probably due to the adventitious entrainment of particles on the sample surface from previous ablations as the sample was moved into position for the next ablation pass. The six traces show that the signal was reproducible from ablation to ablation, and the $^{238}\text{U}/^{232}\text{Th}$ ratio was in good agreement with the theoretical ratio of 1.02, assuming 95% ionisation of ^{232}Th (100% abundant, 37.79 ppm) and 99% ionisation of ^{238}U (99.4 % abundant, 37.38 ppm).

6 Conclusions

This paper describes, for the first time, an open, non-contact cell for LA-ICP-MS. Using this novel technology, it is possible to handle samples of any size or number. In the implementation reported here, the device is optimised for planar or samples having limited curvature. Using this particular micro-jet array, it was demonstrated that the cell worked effectively over sampling distances of 50 to 200 μm (the maximum distance investigated in this study) between the sample surface and the flow restrictor, but this may be extended with other micro-jet array configurations. Though not tested here, this indicates a degree of tolerance to surface roughness or curvature.

Potential applications for the cell, not described above, include: analysis of small samples mounted on a planar platform (with the current design, < 2mm), on-line process monitoring e.g. multiple samples on a conveyor belt, gel-plates and membranes, tissue sections, polished geological specimens and silicon wafers. Additionally, the cell is configured with two sample ports (though more could be included) and therefore might be used in cutting, scribing and laser repair operations where toxic fume removal and/or the connection of process control analysers might be required.

The cell has also been designed for use in molecular mass spectrometry where a charged plume is transported to the analyser, e.g. MALDI and DESI. For these applications, the micro-jet array has the facility to be charged to aid ion extraction.

7 Acknowledgements

The authors would like to thank the EPSRC, the Centre for Analytical Science at Loughborough University, the Centre for Innovative and Collaborative Engineering at Loughborough University and the New Wave Research division of Electro Scientific Industries Inc. for funding, sponsorship and the provision of equipment for this project. The Wolfson School of Mechanical Engineering Workshop at Loughborough University is thanked for initial manufacture of the prototype cell, as is Allbrook Engineering in Loughborough for any subsequent modifications. Glenn Woods and Ed McCurdy of Agilent Technologies are also thanked for use of the Agilent 7500, and colleagues and technical staff at the Department of Chemistry at Loughborough University for technical help and support throughout all stages of the project.

8 References

1. D. Bleiner and A. Bogaerts, *Spectrochimica Acta Part B-Atomic Spectroscopy*, 2007, 62, 155-168.
2. D. Fliegel and D. Günther, *Spectrochimica Acta Part B-Atomic Spectroscopy*, 2006, 61, 841-849.
3. I. Feldmann, C. U. Koehler, P. H. Roos and N. Jakubowski, *J. Anal. At. Spectrom.*, 2006, 21, 1006-1015.
4. M. Guillong, P. Heimgartner, Z. Kopajtic, D. Günther and I. Gunther-Leopold, *J. Anal. At. Spectrom.*, 2007, 22, 399-402.
5. A. Barringer, US Patent, 1980, US4220414.
6. P. Arrowsmith and S. K. Hughes, *Appl. Spectrosc.*, 1988, 42, 1231-1239.
7. F. Boué-Bigne, PhD Thesis, Loughborough University, 2000.
8. W. Devos, Ch. Moor, P. Lienemann, *J. Anal. At. Spectrom.*, 1999, 14, 621-626.
9. W. Müller, M. Shelley, P. Miller and S. Broude, *J. Anal. At. Spectrom.*, 2009, 24, 209-214.
10. R. Hutchinson, E. Ryan, S. Graham, K. Elkin, D. Green, C. O'Connor and M. Colucci, Poster: "Benefits of a New Large Format Cell" - 9th European Workshop on Laser Ablation in Elemental and Isotopic Analysis, Prague, 2008.
11. R. Hutchinson, E. Ryan, S. Graham, K. Elkin, D. Green, C. O'Connor and M. Colucci, "The Large Format Cell (LFC): High Volume Sample Processing", New Wave Research Application Note No. QL200 Rev. 8, 2007.
12. D. Asogan, B. L. Sharp, C. J. P. O' Connor, Patent applied for 2009.
13. B. L. Sharp, *J. Anal. At. Spectrom.*, 1988, 3, 939-963.
14. H. Schlichting, "Boundary Layer Theory", Sixth edition, McGraw-Hill, New York, 1968.
15. J. Pisonero, D. Fliegel and D. Günther, *J. Anal. At. Spectrom.*, 2006, 21, 922-931.
16. B. L. Sharp, *J. Anal. At. Spectrom.*, 1988, 3, 613-652.
17. S. F. Durrant, *Fresenius J. Anal. Chem.*, 1994, 349, 768-771.
18. T. Hirata and R. W. Nesbitt, *Geochim. Cosmochim. Acta*, 1995, 59, 2491-2500.

9 Tables

Table 1. Gas transmission efficiencies through the open, non-contact cell. The cell was tested under three regimes: carrier flow only, curtain flow only and both flows. In this instance, the cell was tested without the micro-jet pump in place.

Carrier Flow Rate (l min ⁻¹)	Curtain Flow Rate (l min ⁻¹)	Total Input Flow Rate (l min ⁻¹)	Output Flow Rate (l min ⁻¹)	Transmission Efficiency Rel. to Total Input (%)
1.20	0.00	1.20	0.179	14.9
0.00	2.50	2.50	0.125	5.0
1.20	2.50	3.70	0.360	9.7 (20)*

*The presence of the curtain flow encourages vectoring of the carrier flow to the output port. This is reflected by the figure in brackets, which represents the transmission efficiency relative to the carrier flow.

Table 2. Operating conditions for LA-ICP-MS experiments. During the plasma lighting sequence, the output of the non-contact cell was vented to atmosphere and make-up gas introduced to achieve punch-through in the plasma. Once lit and stabilised, the make-up flow was gradually reduced and the non-contact cell output introduced.

Agilent 7500 ICP-MS	
RF power	1500 W (1350 W for wash-out)
Sampling Depth	7.0 mm
Coolant gas flow	15.0 l min ⁻¹
Auxiliary gas flow	1.00 l min ⁻¹
Dwell time	100 ms
Interface cones	Nickel
Non-contact cell on UP-213	
Carrier gas flow	1.20 l min ⁻¹ for sensitivity 1.22 l min ⁻¹ for fractionation measurements
Curtain gas flow	2.50 l min ⁻¹
Micro jet-pump motive flow	0.40 l min ⁻¹ for sensitivity measurements 0.68 l min ⁻¹ for fractionation measurements
Make-up gas flow (argon)	1.28 l min ⁻¹ for lighting 0.10 l min ⁻¹ for sensitivity measurements 0.28 l min ⁻¹ for fractionation measurements
Energy density	18.5 J cm ⁻² for wash-in/out on NIST 613 10.2 J cm ⁻² for all other tests on NIST 613
Laser repetition rate	20 Hz
Laser spot size	55 µm for wash-in/out 100 µm for all other tests
Scan speed (XY stage)	10 µm sec ⁻¹
Transport tubing	Tygon® ¼" diameter, ~4m long

Appendix B: An open, non-contact cell for LA-ICP-MS (Paper 2)

Table 3. Sensitivity, LOD's, signal-to-background ratios and %RSD's for NIST-613 CRM using the open, non-contact cell attached to a UP-213 laser ablation system. The cell was tested at three different sampling distances of 50, 100 and 200 μm between the sample surface and the flow restrictor, and using two different curtain gases (nitrogen and argon).

	⁷ Li	¹¹ B	⁵² Cr	⁶³ Cu	⁶⁵ Zn	⁸⁵ Rb	¹⁰⁷ Ag	¹¹⁵ In	¹⁴⁰ Ce	²⁰⁸ Pb	²³² Th	²³⁸ U
<u>Sensitivity (Counts s⁻¹ ppm⁻¹)</u>												
<i>Standard UP Ablation Cell</i>												
	1869	397	3773	1942	493	3730	1885	4247	6057	2289	4246	4578
<i>Nitrogen Curtain Gas</i>												
50 μm	705	144	1541	826	222	1589	987	1982	2260	1294	2085	2207
100 μm	687	143	1511	806	206	1515	959	1889	2122	1193	1930	2015
200 μm	621	129	1393	717	183	1413	847	1727	1964	1038	1725	1797
<i>Argon Curtain Gas</i>												
50 μm	568	125	1301	719	215	1384	845	1744	1866	1151	1732	1912
100 μm	541	116	1255	700	199	1312	804	1666	1769	1070	1621	1791
200 μm	350	80.2	828	460	102	870	524	1075	1201	663	1079	1133
<u>Limits of Detection (ppb)</u>												
<i>Standard UP Ablation Cell</i>												
	85	839	880	673	735	594	466	757	631	600	492	641
<i>Nitrogen Curtain Gas</i>												
50 μm	437	653	264	375	342	78	67	96	187	117	104	83
100 μm	394	410	431	634	565	129	102	140	139	88	137	133
200 μm	188	481	388	789	633	119	71	97	55	113	73	90
<i>Argon Curtain Gas</i>												
50 μm	400	551	351	410	392	158	103	164	303	203	132	229
100 μm	312	770	295	498	201	149	52	68	132	34	48	83
200 μm	321	749	401	424	509	79	75	121	298	177	82	72
<u>Signal-to-Background Ratio</u>												
<i>Standard UP Ablation Cell</i>												
	115	42	34	19	41	277	233	333	441	87	512	398
<i>Nitrogen Curtain Gas</i>												
50 μm	94	31	30	7	78	409	363	733	550	483	627	989
100 μm	73	27	26	6	51	323	336	433	469	318	554	553
200 μm	72	25	23	5	34	271	267	349	812	387	551	495
<i>Argon Curtain Gas</i>												
50 μm	75	22	22	7	104	386	392	583	426	421	758	608
100 μm	77	20	22	7	97	334	450	970	773	551	991	863
200 μm	47	13	14	5	38	302	208	458	365	302	827	883
<u>Relative Standard Deviations (%)</u>												
<i>Standard UP Ablation Cell</i>												
	4.3	4.8	5.1	5.5	11.4	4.3	5.7	5.2	5.8	6.8	7.2	7.3
<i>Nitrogen Curtain Gas</i>												
50 μm	8.6	9.1	10.0	8.2	13.9	8.6	8.8	8.4	8.6	9.0	9.0	9.4
100 μm	15.6	15.5	14.9	12.6	19.9	15.2	15.6	15.6	15.8	15.5	16.2	15.7
200 μm	12.7	14.0	11.9	11.3	17.0	13.2	13.9	13.3	13.3	12.6	13.6	13.3
<i>Argon Curtain Gas</i>												
50 μm	7.3	14.1	8.6	7.7	19.1	7.4	7.5	6.6	6.6	8.3	8.0	8.8
100 μm	11.2	41.8	12.5	9.0	16.4	11.0	11.3	11.5	11.5	11.8	12.1	11.5
200 μm	24.0	107	22.1	19.0	22.6	24.5	25.5	24.4	22.5	25.0	23.0	24.4

Table 4. Molecular ion formation for ^{85}Rb , ^{232}Th and ^{238}U obtained for NIST-613 CRM using the open, non-contact cell attached to a UP-213 laser ablation system. The cell was tested at three different sampling distances of 50, 100 and 200 μm between the sample surface and the flow restrictor, and using two different curtain gases (nitrogen and argon).

	$\frac{\text{RbN}}{\text{Rb}}$	$\frac{\text{RbO}}{\text{Rb}}$	$\frac{\text{ThN}}{\text{Th}}$	$\frac{\text{ThO}}{\text{Th}}$	$\frac{\text{UN}}{\text{U}}$	$\frac{\text{UO}}{\text{U}}$
	(%)	(%)	(%)	(%)	(%)	(%)
Nitrogen Curtain Gas						
50 μm	0.08	0.08	0.05	0.12	0.04	0.10
100 μm	0.10	0.08	0.06	0.13	0.05	0.11
200 μm	0.11	0.10	0.07	0.14	0.06	0.12
Argon Curtain Gas						
50 μm	0.10	0.08	0.05	0.12	0.05	0.10
100 μm	0.09	0.08	0.06	0.13	0.05	0.11
200 μm	0.14	0.13	0.09	0.17	0.08	0.13

10 Figures

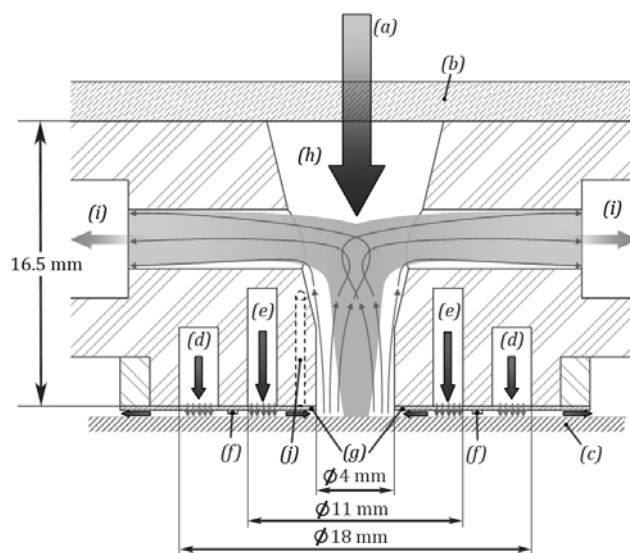


Fig. 1. A schematic diagram showing a cross-section of the open, non-contact cell. Laser energy (a) passes through an optical window (b) down to the sample surface (c) where ablation takes place. The cell has two concentric annular gas flows: a curtain gas (d), which excludes atmospheric gases from the ablation site, and a carrier gas (e), which provides an inert atmosphere for the ablation and transports the sample to the analyser. A flow restrictor (f) is in place between the annular gas channels to vector the gas flows to the correct direction. A micro-jet array (g) provides stiff micro-jets of gas, which lowers both gas consumption and turbulence, providing quasi-laminar flow that has low entrainment properties with respect to atmospheric gases. There is a low volume inner cell (h), which provides quick wash-in and wash-out through the cell, and dual outputs (i) to allow simultaneous coupling to two different analysers. There is also the option for electrically biasing the micro-jet array through an electrical contact channel (j) if the application requires it.

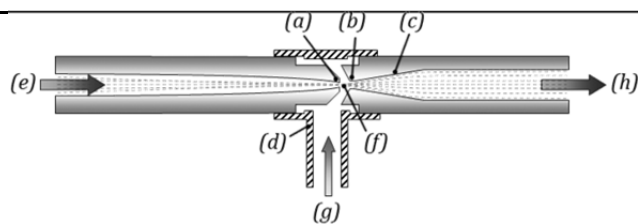


Fig. 2. A schematic diagram of the micro jet-pump. The device consists of a 160 μm nozzle (a), a 1.5 mm throat (b) and a diffuser (c) enclosed within a tee-piece (d). A motive flow (e) produces a supersonic, over-expanded free jet (f), which is very turbulent and has excellent entrainment properties. The throat and the diffuser act as a ‘gas diode’ and minimise self-entrainment of the jet; hence the entrained flow (g) can only enter through the open side-arm of the tee-piece, which is attached to the non-contact cell. The final output flow (h) is then pumped to the analyser.

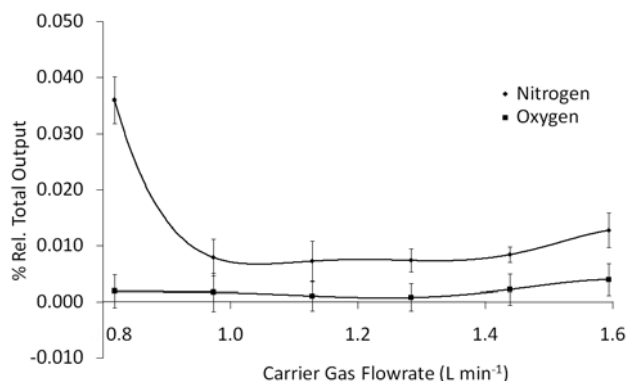


Fig. 3. A graph showing oxygen and nitrogen content in the output flow from the open, non-contact cell. The carrier gas channel was varied from 0.80 to 1.60 l min^{-1} (with no micro jet-pump present), the sampling distance between the sample surface and the flow restrictor was 200 μm , and the curtain gas flow fixed at 2.50 l min^{-1} .

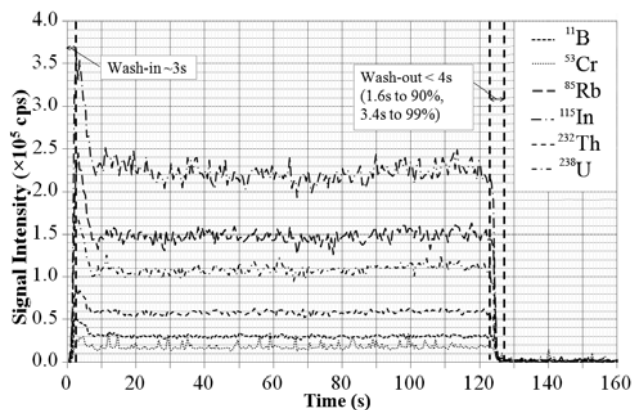


Fig. 4. A graph showing time-resolved signals for NIST 613 glass using the open, non-contact cell. The graph shows the cell has a wash-in time of ~ 3 s and a wash-out of ~ 1.6 sec for 90% wash-out and ~ 3.4 sec for 99% wash-out.

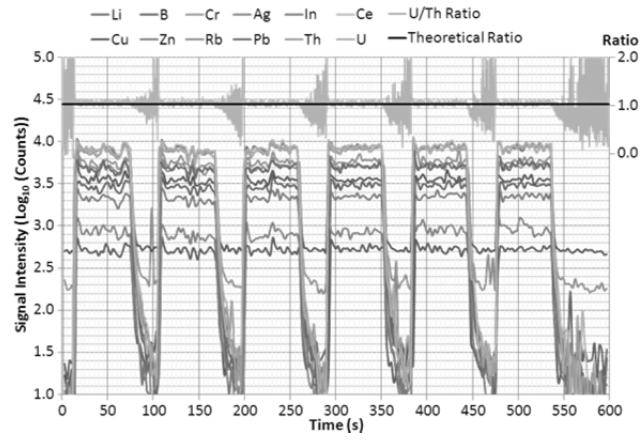


Fig. 5. A graph showing both time-resolved logarithmic signal intensity for NIST 613 glass using the open, non-contact cell, and the $^{238}\text{U}/^{232}\text{Th}$ ratio (i.e. ^{238}U signal intensity divided by ^{232}Th signal intensity) superimposed at the top.

* * * * *

Appendix C Numerical simulations of gas flows through an open, non-contact cell for LA-ICP-MS (Paper 3)

Dhinesh Asogan, ^{a,b} Barry L. Sharp^a, Ciaran J. P. O'Connor^c, Damon A. Green^c and Jay Wilkins^d, 2011, **26**, 631 – 634

^a*Centre for Analytical Science, Department of Chemistry, Loughborough University, Loughborough, Leicestershire, UK LE11 3TU, e-mail: B.L.Sharp@lboro.ac.uk*

^b*Centre for Innovative and Collaborative Engineering, Department of Civil and Building Engineering, Loughborough University, Loughborough, Leicestershire, UK LE11 3TU*

^c*Electro Scientific Industries Europe Ltd., New Wave Research Division, 8 Avro Court, Ermine Business Park, Huntingdon, Cambs, UK PE29 6XS*

^d*Electro Scientific Industries Inc., New Wave Research Division, 685 Old Buffalo Trail, Bozeman, MT 59715 USA*

DOI: 10.1039/CoJA00166J

ABSTRACT

Numerical simulations of gas flows through an open, non-contact cell for laser ablation are presented. The cell consists of dual, annular, concentric micro-jet gas arrays to entrain ablated material (the carrier flow) and exclude atmosphere (the curtain flow). This study shows that the design of the cell affords a very high degree of exclusion of atmospheric gases using a relatively low curtain flow of 2.5 l min⁻¹ (with a carrier flow of 1.2 l min⁻¹ He), and demonstrates the efficacy of the micro-jet arrays in providing an axially symmetric exclusion zone. Minimum particle transit times through the cell were calculated to be of the order of 50 – 100 ms.

Keywords – Laser Ablation, ICP-MS, Large Samples, Silicon Wafers, Numerical Simulation

Paper type – Technical Note (Journal)

1. Introduction

Laser ablation-inductively coupled plasma-mass spectrometry (LA-ICP-MS) is a powerful elemental analysis technique that employs high irradiance lasers for the analysis of solid samples. The ICP itself, however, is unstable when excessive amounts of atmospheric gases, especially oxygen, are entrained into the central plasma channel.¹ Additionally, air has relatively low thermal conductivity, which can lead to larger particles being formed in the ablated aerosol through condensation/agglomeration processes.² This can lead to both inefficient particle processing within the plasma (i.e. lowered sensitivity) and elemental fractionation. Consequently, LA sample chamber design addresses two major factors: rapid, quantitative sample transport and atmosphere exclusion. This is most easily achieved by enclosing the sample in a chamber³⁻⁵, which can be flushed with an appropriate inert gas, or by using an open cell with another form of sealing⁶⁻¹², e.g. a flexible 'wall' offered up to the sample surface, or a gas curtain.¹³

An open, non-contact cell for laser ablation was described by the authors previously.¹³ Briefly, it consists of two concentric, annular gas flows for atmosphere exclusion (the 'curtain' flow) and sample entrainment (the 'carrier' flow), and a central channel that allows ablated material to exit the cell through two output ports which can be connected simultaneously to two separate analysers. The concentric, annular inlet channels are separated by a flow restrictor that is designed to vector the carrier flow inwards, towards the central outlet channel, and the curtain flow outwards to atmosphere.

The carrier flow in LA experiments is usually helium, as it is inert, of low density and has a relatively high thermal conductivity. These properties aid ablation and subsequent ICP analyses as they allow the plume to expand away from the ablation crater and minimise condensation and agglomeration processes. The curtain flow chosen was nitrogen, as it is stable, inert and relatively cheap. Additionally, it can be easily generated *in situ* in many labs. Argon can also be used as a curtain gas; however, the authors found argon provides decreased sensitivity over nitrogen in experiments reported previously.

Numerical simulations of ablation chambers have been shown to offer a good understanding of gas flows around the ablation site, and to estimate particle transport dynamics through the chamber.¹⁴

2. Aims

This technical note shows simulated data obtained from a scoping study aimed at confirming experimental data that indicated effective separation of the carrier flow, the curtain flow and atmosphere. Additional aims were:

1. investigation of any possible entrainment of the curtain flow or atmosphere into the carrier flow
2. demonstration of the effectiveness of a micro-jet array for reducing gas consumption and producing a symmetric flow field
3. estimation of particle transit time through the inner volume of the cell; this equates to the minimum achievable wash-in/wash-out time. (This is, in practice, difficult to achieve as connecting tubing, gas-valves and other flow impedances have to be taken into account.)

3. Fluid model and numerical method

SolidWorks FlowSimulation 2010 was used to compute the flows through the non-contact cell. This is an add-in package embedded into SolidWorks 2010 Computer Aided Design (CAD) software, and as such development of a fluid mesh model is easily accomplished from the original CAD model. Mesh optimisation was performed in accordance to SolidWorks literature.¹⁵

Once the computational mesh had been created, an iterative solver was used to calculate the gas flows. This solves the Navier-Stokes equations, which are equations that describe mass, momentum and energy conservation laws for fluid flows.¹⁵ FlowSimulation was developed to solve engineering problems, and as such it is geared towards turbulent flows. Because of this, the system uses the *Favre-averaged Navier-Stokes equations*, which consider time-averaged effects of flow turbulence such as large scale vorticity. In this case, Reynolds-stresses are taken into account and add terms to the equations. Finally, the turbulent kinetic energy of the fluid system, and its dissipation rate, is also calculated using the *k-ε model*.

The conservation laws for momentum, with respect to Cartesian axes, can be written as:

$$\frac{\partial \rho}{\partial t} + \frac{\partial}{\partial x_i} (\rho u_i) = 0 \quad (1)$$

$$\frac{\partial \rho u_i}{\partial t} + \frac{\partial}{\partial x_i} (\rho u_i u_j) + \frac{\partial p}{\partial x_i} = \frac{\partial}{\partial x_j} (\tau_{ij} + \tau_{ij}^R) + S_i \quad (2)$$

$$\begin{aligned} & \frac{\partial \rho H}{\partial t} + \frac{\partial \rho u_i H}{\partial x_i} \\ & = \frac{\partial}{\partial x_i} (u_j (\tau_{ij} + \tau_{ij}^R) + q_i) + \frac{\partial P}{\partial t} - \tau_{ij}^R \frac{\partial u_i}{\partial x_j} + \rho \varepsilon + S_i u_i + Q_H \end{aligned} \quad (3)$$

$$H = h + \frac{u^2}{2} \quad (4)$$

where ρ is the fluid density, u is the fluid velocity, P is the pressure, τ is the viscous shear stress tensor, τ^R is the Reynolds-stress tensor, S is a mass-distributed external force term (a combination of force exerted by porous media, a buoyancy term and force resulting from

rotation of the coordinate system [rotation was not used in this study]), q is the diffusive heat flux, ε is the turbulent energy, Q_H is a heat source/sink per unit volume and h is the thermal enthalpy. (Note x_i , x_j , and the suffixes i and j refer to two generic axes in the Cartesian coordinate system.)

The initial conditions were set so that the calculation started in a pure air environment. The micro-jet array was modeled as a unidirectional porous medium to free up computer resources and reduce computation time. For geometrically regular, open arrays such as the micro-jet array, this is a recommended approximation.¹⁶ The solver software applies a contribution to S in eqn (3) that is dependent on the array's open volume to total volume ratio (the porosity) and the pressure drop through the array with respect to a calibration viscosity. The calculation stopped once steady-state conditions had been reached.

The pressure drop through the micro-jet array was estimated by simulation because equipment was not readily available to accurately measure it. This was initially calculated using a single repeat unit for the mesh with air as the fluid at 293 K, a mesh consisting of 104,460 cells was used. The repeat unit was a parallelogram with 400 μm sides and a thickness of 100 μm , with four 18 μm holes arranged 200 μm apart (see Fig. 1). From the calculated pressure drop and the dynamic viscosity of air at 293 K (1.983×10^{-5} Pa s), the solver was able to scale the pressure drop to the geometry of the micro-jet array used in the final CAD model. This was found to be in the order of a few hundred Pa at this scale.

The model geometry was such that the non-contact cell was floating 200 μm above a sample surface, which in this case was an 8 cm silicon wafer modeled as an ideal surface with zero surface roughness, a mesh consisting of 683,502 cells was used. After the calculation completes, the software allows particle tracking along streamlines by 'injecting' a certain number of particles from a selected geometric feature. The aerodynamic diameter, the material (density) and the mass flux can be set to predict approximate particle trajectories, i.e. deviations from gas streamlines. However, this prediction does not take into account collisions and only predicts the particle trajectories from momentum and gas streamlines.

Additional initial calculation conditions are summarised in Table 1. Particle injection was performed from a dummy feature placed at the central channel opening on the bottom plane of the cell. 20 injection points were chosen, and the resultant particle trajectories used to estimate the minimum particle transit time. The mass flux and aerodynamic diameter were chosen as estimates for nanosecond ablation of glassy substrates, i.e. approximately 1 μm particle diameter (representing the upper range of particle sizes) and 5 $\mu\text{g min}^{-1}$ material mass flux (calculated approximately assuming 40 μm ablation depth from 10 $\mu\text{m s}^{-1}$ scan speed and 100 μm spot diameter, 20 Hz repetition rate and 11 J cm^{-2} fluence). The ablation depth was found experimentally on NIST 612 glass using a New Wave Research UP-213 Laser Ablation System (ElectroScientific Industries, New Wave Research Div., Huntingdon, UK).

4. Results and discussions

The calculated flow fields, initially without the micro-jet array, showing the volume fraction of air distributed across the sample surface are presented in Fig. 2. The inlet gas flows are off-centre relative to their respective annular gas channels, forming antagonistic concentric helical flows. In the absence of the micro-jet array, no backpressure is present at the exit plane of the channels in the interface region between the sample and the cell. Therefore, the

helical flows continue their structure on the surface of the sample, resulting in asymmetric exclusion of air about the ablation site.

With the micro-jet array in place, there is adequate backpressure to disrupt the helical flow and transform it into quasi-laminar flow perpendicular to the sample surface. From here, the air exclusion zone adopts a symmetric shape with full exclusion across the entire sample.

The volume fraction shows minimal air entrainment without the micro-jet array and minimal curtain channel ingress; however, from a carrier flow input of 1.2 l min^{-1} and a curtain flow input of 2.5 l min^{-1} , the output flow was predicted to be 0.231 l min^{-1} , which corresponds to a transmission efficiency of approximately 19.3 % with respect to the carrier flow. This is accompanied by a minimum particle transit time of $116 \pm 13 \text{ ms}$.

The curtain flow without the micro-jet array, operating at these flow conditions, is not stiff enough to vector the carrier flow inwards towards the central outlet, even with the flow restrictor in place. The carrier flow ends up mixing with the curtain flow and both gases escape to atmosphere. Intuitively, to create enough stiffness the curtain flow would have to be increased; however, this serves to entrain the carrier flow and vector it away from the central outlet channel. Increasing the carrier flow to compensate for this effect, results in faster flow only, and the asymmetric exclusion zone remains on the sample surface (not shown).

When the micro-jet array is included in the simulation, the results show full exclusion of air and approximately 20 % (v/v) ingress of the curtain flow into the output flow, with a total output flow rate of 0.944 l min^{-1} . This comprises of 0.752 l min^{-1} of the carrier flow and 0.192 l min^{-1} of the curtain flow (62.7 % and 7.7 % flow transmission efficiency respectively), and a minimum particle transit time of $49 \pm 12 \text{ ms}$. Thus in summary, the micro-jet array provides a symmetrical air exclusion zone and greatly increases the transport efficiency of the central channel.

In LA experiments, in practice, there is a need for an additional ‘make-up flow’ to be combined with the outlet flow from the cell to provide stability in the central channel of the ICP. The addition of $0.330 - 0.975 \text{ l min}^{-1}$ of argon make-up flow reduces the concentration of nitrogen in the ICP injector flow to 10 – 15%. This level of nitrogen has been shown previously to improve sensitivity in LA-ICP-MS experiments.¹⁷

The curtain flow through the micro-jet array has enough stiffness to help the flow restrictor vector the carrier flow inwards towards the central outlet channel, at a much lower flow rate than previously required. This lowers gas consumption but maintains efficient separation.

When attached to an ICP, the ingress of the curtain flow into the outlet stream will form an Ar-He-N₂ mixed plasma, which will have different characteristics from the Ar-He mixed plasma currently seen in most LA experiments. For this reason, the calculation was repeated with the same flow rates changing the curtain flow from nitrogen to argon.

In this case, air was fully excluded in a symmetric pattern with a curtain flow ingress of approximately 31.4 % (v/v) at an output flow rate of 0.924 l min^{-1} , which equates to 0.634 l min^{-1} of the carrier flow (52.8 % transmission efficiency) and 0.290 l min^{-1} of the curtain flow (11.6 % transmission efficiency).

Argon exiting the plane of the micro-jet array has a higher momentum than nitrogen in an analogous setup; therefore, the argon can 'push' through the helium carrier flow (causing higher ingress). Additionally, it can entrain more helium in the interface between the carrier and curtain flows, through momentum exchange, thus reducing the transmission efficiency of the carrier flow through to the outlet.

The minimum particle transit time in this case was 39.3 ± 10.2 ms, which suggests this outlet gas mix would entrain particles more efficiently than the analogous setup using a nitrogen curtain flow, possibly due to the fact that the calculated Ar-He mix is more dense than the calculated N₂-He mix (0.65 kg m^{-3} vs 0.37 kg m^{-3}).

5. Conclusions

The calculated flow fields presented in this paper show that efficient exclusion of atmosphere can be achieved from an ablation site using an open, non-contact cell. Further, the use of a micro-jet array reduces the required gas flows to achieve this condition, promotes a symmetric exclusion zone around the ablation site and improves transport of the carrier flow to the ICP. Ingress of the curtain flow into the output was calculated to be in the order of 20 %, which reduces to around 10 – 15 % with the addition of a downstream Ar make-up flow.

Minimum transit time was calculated to be in the order of 120 ms without the micro-jet array, and on the order of 50 ms with the micro-jet array in place. As previously stated, this figure will be difficult to achieve in practice due to the tubing needed to transport the ablated aerosol to the ICP.

6. Acknowledgements

The authors would like to thank the EPSRC, the Centre for Analytical Science at Loughborough University, the Centre for Innovative and Collaborative Engineering at Loughborough University and the New Wave Research Division of Electro Scientific Industries Inc. for funding, sponsorship and the provision of software used in this study

7. References

1. R. Kovacs, K. Nishiguchi, K. Utani and D. Günther, *J. Anal. At. Spectrom.*, 2010, **25**, 25, 142–147.
2. I. Horn and D. Günther, *Appl. Surf. Sci.*, 2003, **207**, 144–157
3. D. Fleigel and D. Günther, *Spectrochimica Acta Part B-Atomic Spectroscopy*, 2006, **61m** 841–849
4. I. Feldmann, C. U. Koehler, P. H Roos and N. Jakubowski, *J. Anal. At. Spectrom.*, 2006, **21**, 1006–1015
5. M Guillong, P. Heimgartner, Z. Kopajtic, D. Günther and I. Gunther-Leopold, *J. Anal. At. Spectrom.*, 2007, **22**, 399–402
6. Barringer, *US Pat.*, 4220414, 1980
7. P. Arrowsmith and S. K. Hughes, *Appl. Spectrosc.*, 1988, **42**, 1231–1239
8. F. Boué-Bigne, PhD Thesis, Loughborough University, 2000.

9. W. Devos, Ch. Moor and P. Lienemann, *J. Anal. At. Spectrom.*, 1999, **14**, 621–626
10. W. Müller, M. Shelley, P. Miller and S. Broude, *J. Anal. At. Spectrom.* 2009, **24**, 209–214
11. R. Hutchinson, E. Ryan, S. Graham, K. Elkin, D. Green, C. O’connor and M Colucci, Poster: “Benefits of a New Large Format Cell” – 9th European Workshop on Laser Ablation in Elemental and Isotopic Analysis, Prague, 2008
12. R. Hutchinson, E. Ryan, S. Graham, K. Elkin, D. Green, C. O’Connor and M Colucci, Poster: “The Large Format Cell (LFC): High Volume Sample Processing”, New Wave Research Application Note No. QL200 Rev. 8, 2007
13. D. Asogan, B. L. Sharp, C. J. P. O’Connor, D. A. Green and R. W. Hutchinson, *J. Anal. At. Spectrom.*, 2009, **24**, 917-923.
14. D. Bleiner and A. Bogaerts, *Spectrochimica Acta Part B - Atomic Spectroscopy*, 2007, **62**, 155–168.
15. DSS, SolidWorks Flow Simulation 2010: Technical Reference, Dassault Systemes, 2010.
16. DSS, SolidWorks Flow Simulation 2010: Solving Engineering Problems, Dassault Systemes, 2010.
17. S. F. Durrant, *Fresenius J. Anal. Chem.*, 1994, **349**, 768–771.

8. Tables

Table 1. Initial conditions for numerical simulation

Carrier inlet volumetric flow rate	1.2 l min ⁻¹
Curtain inlet volumetric flow rate	2.5 l min ⁻¹
Micro-jet array porosity	0.745 % (v/v)
Ambient temperature	293.15 K
Ambient pressure	101325 Pa
Outlet pressure	101325 Pa, static
Particle material	Glass ($\rho = 2.32 \text{ g cm}^{-3}$)
Particle aerodynamic diameter	1 μm
Particle mass flux	5 $\mu\text{g min}^{-1}$

Table 2. Results of numerical simulations, highlighting volumetric flow rate at one outlet, composition of the outlet gas and the average minimum particle transit time through the inner volume of the cell

Condition	Carrier Flow Content (%)	Curtain Flow Content (%)	Atmosphere Content (%)	Volumetric Flow Rate (l min ⁻¹)	Minimum Particle Transit Time (ms)
<i>Micro-jet array absent</i>	99.98	0.01	0.01	0.231	116.2 ± 13.3
<i>Micro-jet array present, N₂ curtain flow</i>	79.71	20.29	0.00	0.944	49.2 ± 12.1
<i>Micro-jet array present, Ar curtain flow</i>	68.59	31.41	0.00	0.924	39.3 ± 10.2

9. Figures

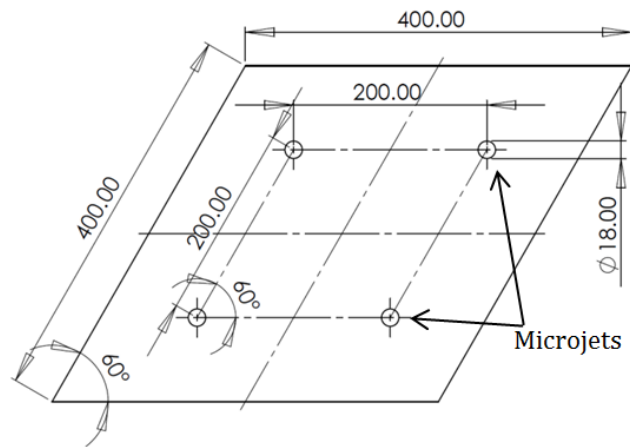


Fig. 1 A single repeat unit of the micro-jet array used for pressure drop calculations. All measurements are in micrometres, with a thickness of 100 μm . The porosity of this system is 0.745% (v/v).

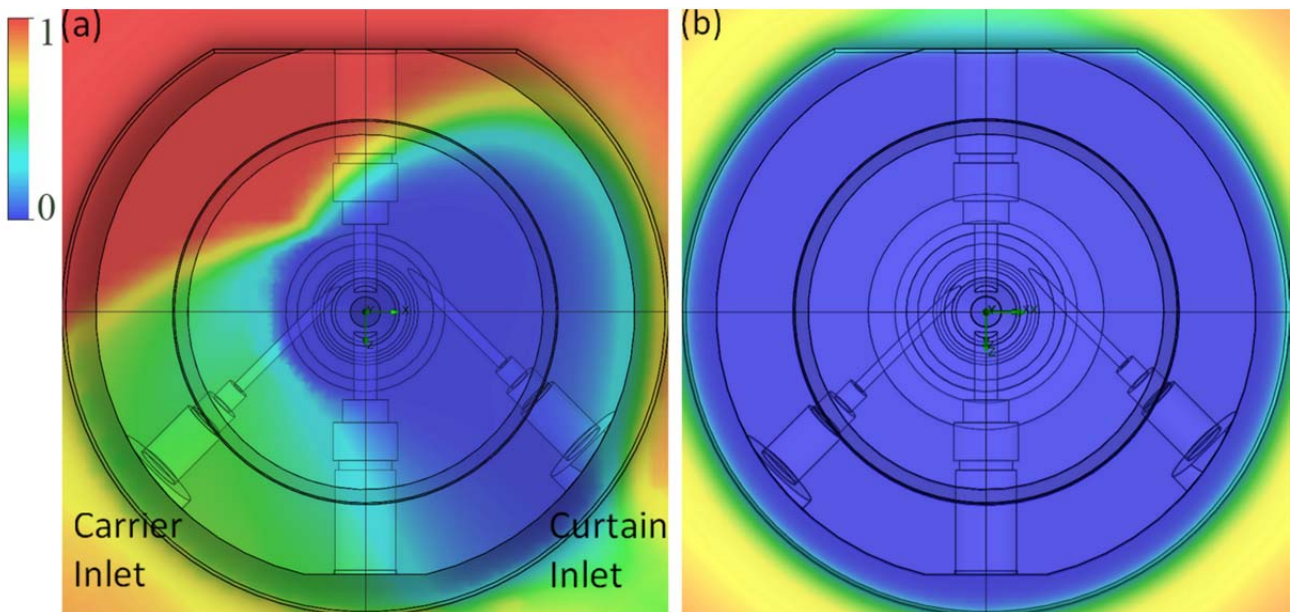


Fig. 2 Calculated distribution of air across the sample surface (a) without a micro-jet array and (b) with a micro-jet array. Since both the inlets are off-centre relative to their respective annular channels, the flows swirl into a helical pattern at the interface region between the cell and the sample that results in asymmetric air exclusion around the ablation site. With the micro-jet array in place, the flow pattern becomes linear and perpendicular to the sample surface, which causes a symmetric exclusion zone to be set up around the ablation site.

* * * * *

Appendix D Technical Drawings

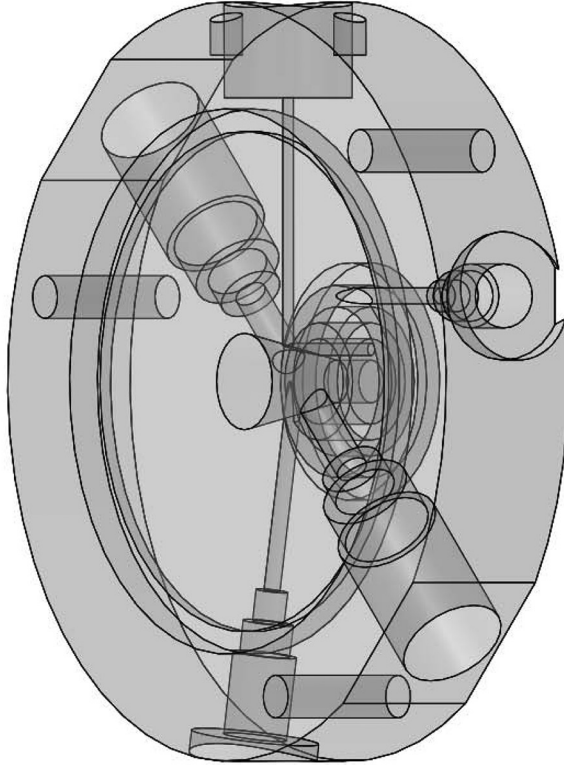
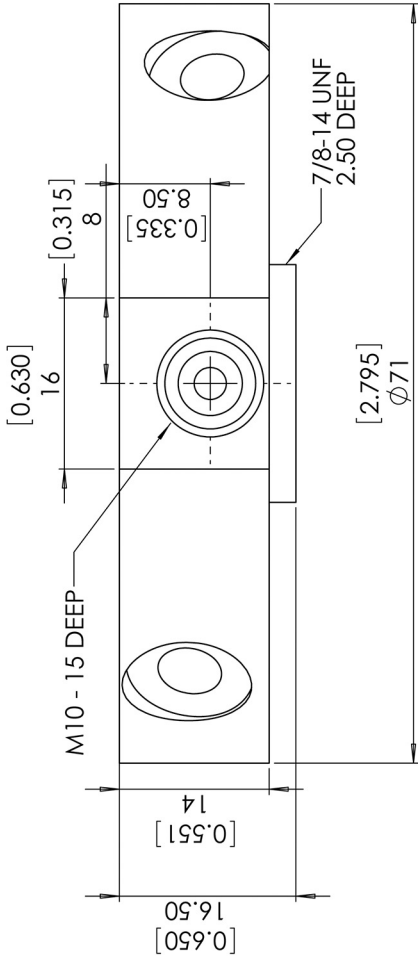
This appendix comprises the technical drawings used for the manufacture of the prototype non-contact cell and associated components.

The components, along with version history, are as follows:

ID	Name	Page	Ver.	Version History	Date
<i>Non-Contact Cell</i>					
NCC-001	Main Body	D-2	A	Original	30 Nov 2005
			B	Removed material from underside to reduce surface area	08 Dec 2005
			C	Removed outer lip	08 Dec 2005
			D	Overall reduction in dimensions	09 Dec 2005
			E	Tapered centre channel, further reductions in dimensions	16 Dec 2005
			F	Added second exit channel and electrical contact mounting	24 Feb 2006
			G	Adjusted dimensions as per machinist recommendations	06 Mar 2006
			H	Modified mesh mounting	12 Feb 2007
NCC-002	Top Plate	D-8	A	Original	11 Jan 2006
			B	Altered height of attachment arm	24 Feb 2006
NCC-003	Mounting Plate	D-10	A	Original	24 Feb 2006
NCC-004	BNC Seal	D-12	A	Original	24 Feb 2006
NCC-005	BNC Mount	D-13	A	Original	10 Mar 2006
NCC-006	Micro-jet Array Mesh	D-14	A	Modified mesh to fit modified mesh mounting on NCC-001	12 Feb 2007
NCC-007	Flow Restrictor	D-15	A	Modified flow restrictor to fit modified NCC-006	12 Feb 2007
NCC-008	Mesh Sealing Screw Ring	D-16	A	Original	12 Feb 2007
NCC-009	Vacuum Seal Ferrule – 6 mm	D-17	A	Original	06 Mar 2006
NCC-010	Vacuum Seal Fitting – 6 mm	D-18	A	Original	06 Mar 2006
<i>Micro Jet-Pump</i>					
JP-001	Jet Pump Nozzle	D-19	A	Original	21 Sept 2007
			B	Added adjustment thread	29 Jul 2008
JP-002	Jet Pump Throat	D-20	A	Original	21 Sept 2007
			B	Added Adjustment Thread	29 Jul 2008
JP-003	Jet Pump Tee-Piece	D-21	A	Original	30 Jul 2008

THE INFORMATION CONTAINED IN THIS DRAWING IS THE SOLE PROPERTY OF NEW WAVE RESEARCH. ANY REPRODUCTION IN PART OR WHOLE WITHOUT THE WRITTEN PERMISSION OF NEW WAVE RESEARCH IS PROHIBITED.

D-2



UNLESS OTHERWISE SPECIFIED DIMENSIONS ARE IN MM	CAD GENERATED DRAWING DO NOT MANUALLY UPDATE		NEW WAVE RESEARCH a division of esi
	APPROVALS	DATE	
FINISH: DECIMALS' ANGLES XX ± 0.00 ± 1/2° XXX ± 0.00 ± 1/2° BREAK SHARP EDGES .005"	DRAWN	CHECKED	NON CONTACT CELL MAIN BODY ISOMETRIC AND FRONT VIEWS
MATERIAL PMMA	RESP ENG	MFG ENG	SIZE B
FINISH OPTICALLY POLISHED	QUAL ENG		DWG. NO. NCC-001
DO NOT SCALE DRAWING			REV H
			SCALE: 2:1 CAD FILE: Main Body.sldprt

D

C

B

A

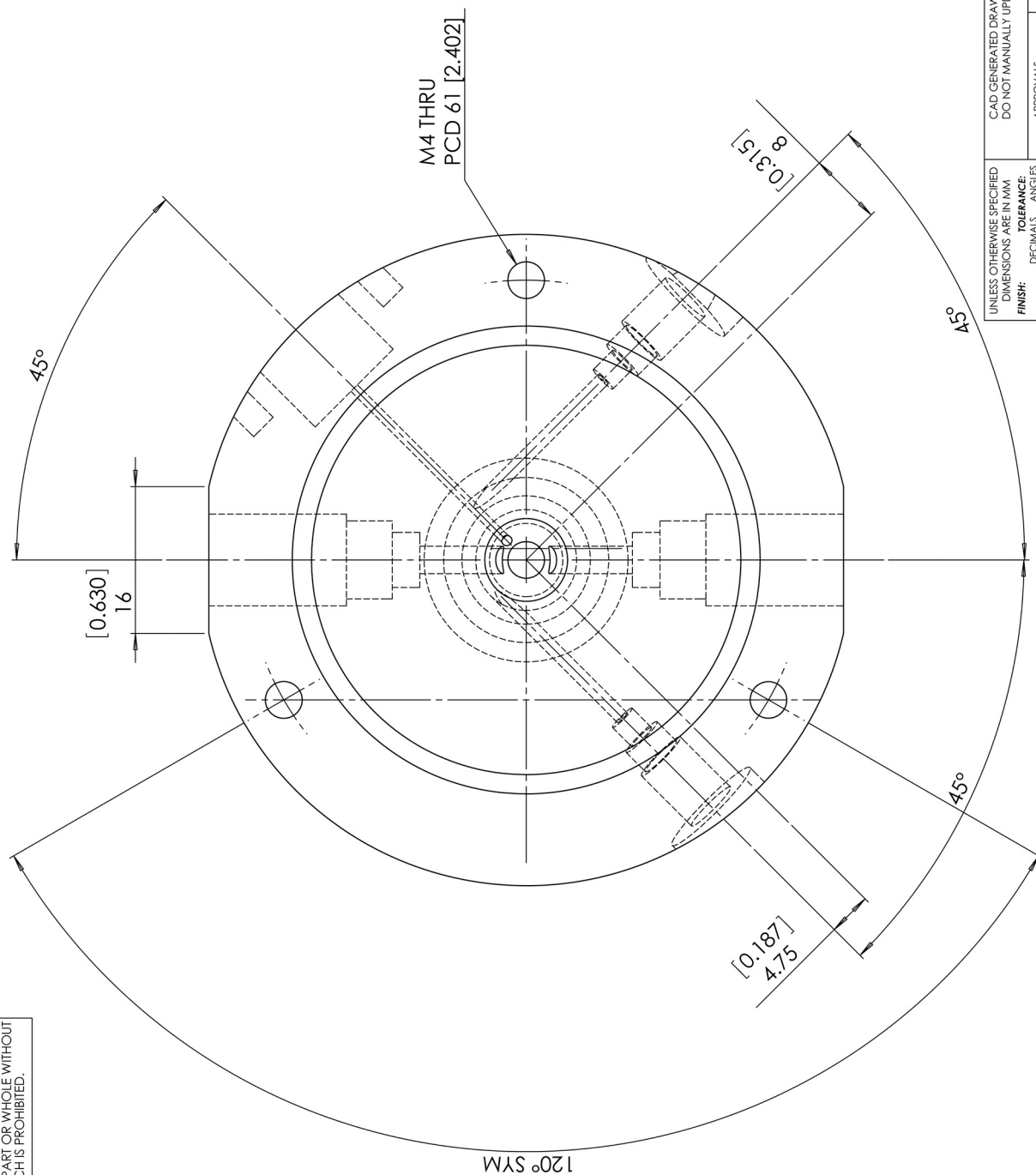
D

C

B

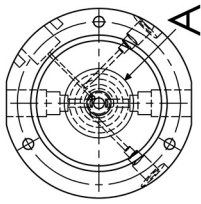
A

THE INFORMATION CONTAINED IN THIS DRAWING IS THE SOLE PROPERTY OF NEW WAVE RESEARCH. ANY REPRODUCTION IN PART OR WHOLE WITHOUT THE WRITTEN PERMISSION OF NEW WAVE RESEARCH IS PROHIBITED.

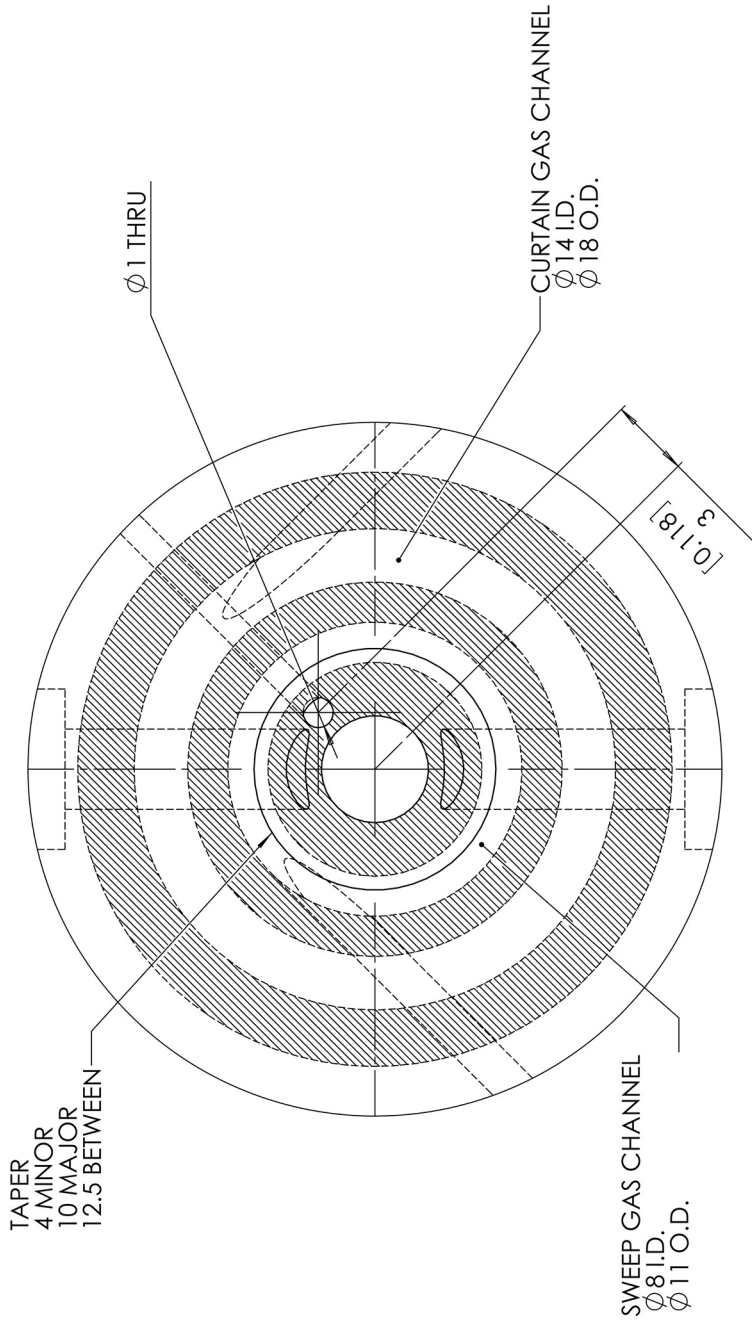


NEW WAVE RESEARCH a division of esi		CAD GENERATED DRAWING DO NOT MANUALLY UPDATE	
NON CONTACT CELL MAIN BODY TOP VIEW		APPROVALS DRAWN CHECKED REVISIONS	DATE
UNLESS OTHERWISE SPECIFIED DIMENSIONS ARE IN MM		FINISH: TOLERANCE: ANGLES: .XX ± 0.10 ± 1/2° .XXX ± .005 ± 1/2° BREAK SHARP EDGES .005"	
MATERIAL: PMMA		FINISH: OPTICALLY POLISHED	
DO NOT SCALE DRAWING		MFG ENG QUAL ENG	
SITE: B	DWG: T10	NCC: 001	REV: H
SCALE: 2:1		CAD FILE: MainBody.stp	

THE INFORMATION CONTAINED IN THIS DRAWING IS THE SOLE PROPERTY OF NEW WAVE RESEARCH. ANY REPRODUCTION IN PART OR WHOLE WITHOUT THE WRITTEN PERMISSION OF NEW WAVE RESEARCH IS PROHIBITED.



D-4



DETAIL A
SCALE 5:1

UNLESS OTHERWISE SPECIFIED
DIMENSIONS ARE IN MM
DO NOT MANUALLY UPDATE

FINISH:
DECIMALS ANGLES
.XX ± 0.0 ± 1/2°
.XXX ± 0.005 ± 1/2°
BREAK SHARP EDGES .005"

MATERIAL
PMMA

FINISH
OPTICALLY POLISHED

DO NOT SCALE DRAWING

CAD GENERATED DRAWING
DO NOT MANUALLY UPDATE

APPROVALS	DATE
DRAWN	
CHECKED	
RESP ENG	
MFG ENG	
QUAL ENG	

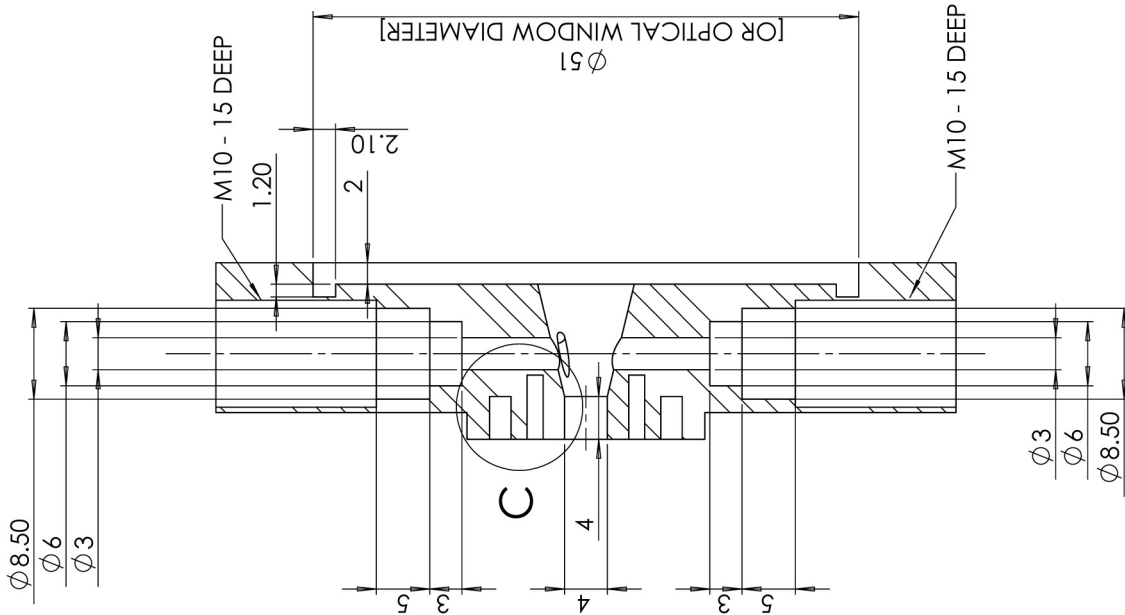
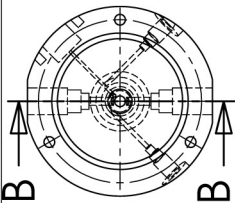
NEW WAVE
RESEARCH
a division of **esi**

NON CONTACT CELL
MAIN BODY
CENTRAL REGION DETAIL

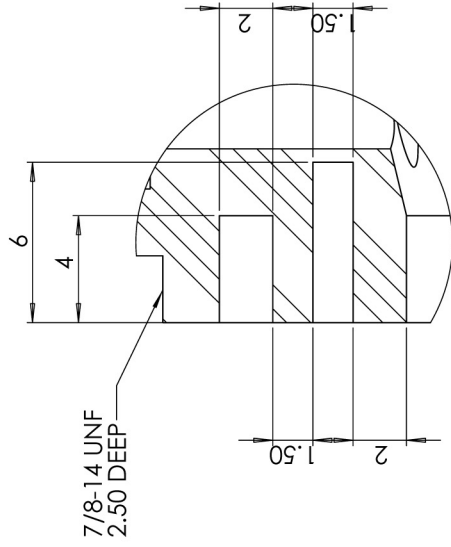
SIZE	DWG. NO.	REV
B	NCC-001	H

SCALE: 1:2 | CAD FILE: Main Body.sldprt | SHEET 3 OF 6

THE INFORMATION CONTAINED IN THIS DRAWING IS THE SOLE PROPERTY OF NEW WAVE RESEARCH. ANY REPRODUCTION IN PART OR WHOLE WITHOUT THE WRITTEN PERMISSION OF NEW WAVE RESEARCH IS PROHIBITED.



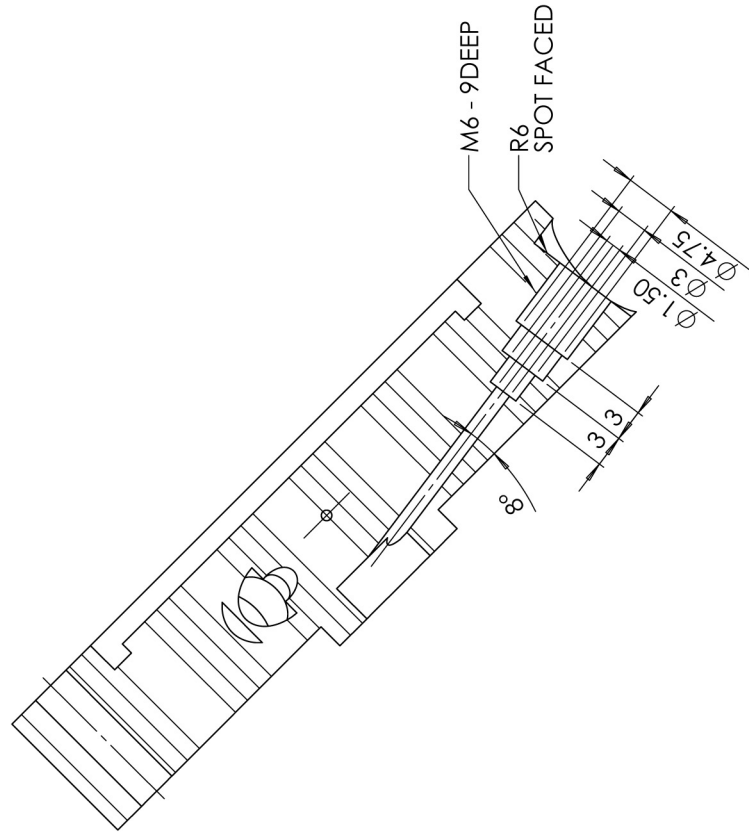
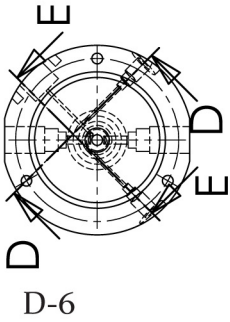
SECTION B-B
SCALE 2:1



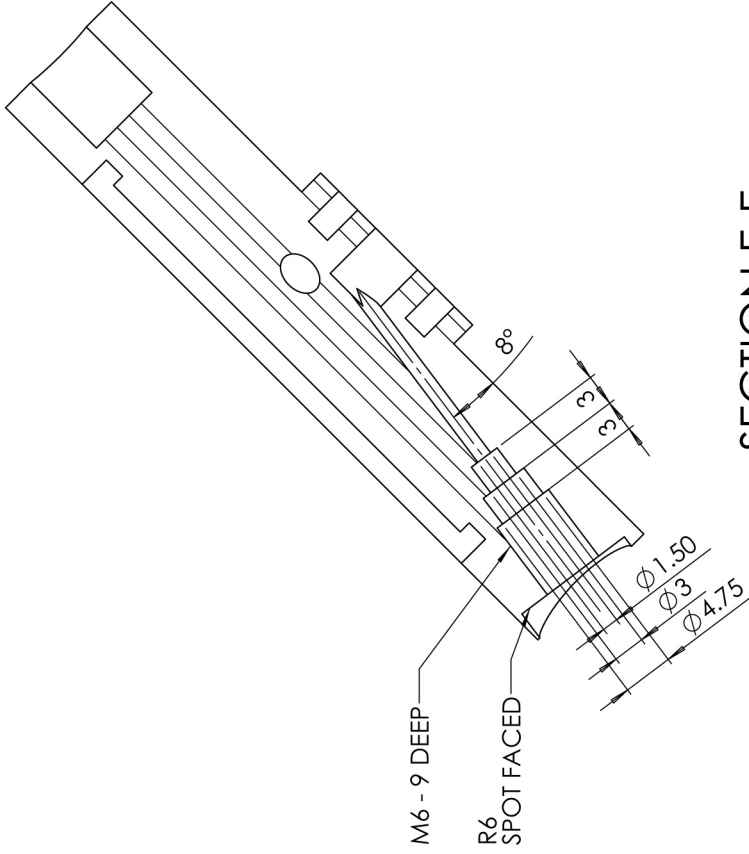
DETAIL C
SCALE 5:1

UNLESS OTHERWISE SPECIFIED DIMENSIONS ARE IN MM	CAD GENERATED DRAWING DO NOT MANUALLY UPDATE	
	APPROVALS	DATE
FINISH: DECIMALS .XX ± 0.10 ANGLES ± 1/2° .XXX ± .005 BREAK SHARP EDGES .005"	DRAWN	CHECKED
MATERIAL PMMA	RESP ENG	MFG ENG
FINISH OPTICALLY POLISHED	QUAL ENG	
DO NOT SCALE DRAWING		
NEW WAVE RESEARCH a division of esi		NON CONTACT CELL MAIN BODY CENTRELINE SECTION VIEW
SIZE B	DWG. NO. NCC-001	REV H
SCALE: 2:1	CAD FILE: Main Body.dppt	SHEET 4 OF 6

THE INFORMATION CONTAINED IN THIS DRAWING IS THE SOLE PROPERTY OF NEW WAVE RESEARCH. ANY REPRODUCTION IN PART OR WHOLE WITHOUT THE WRITTEN PERMISSION OF NEW WAVE RESEARCH IS PROHIBITED.



SECTION D-D
SCALE 2:1

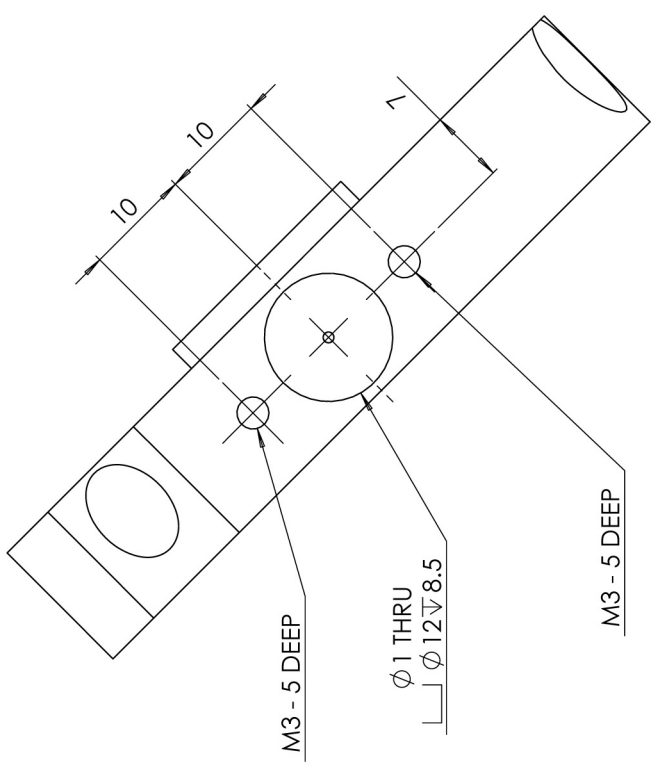
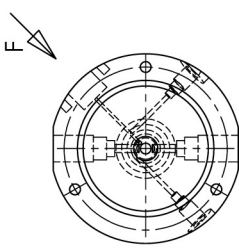


SECTION E-E
SCALE 2:1

UNLESS OTHERWISE SPECIFIED DIMENSIONS ARE IN MM	CAD GENERATED DRAWING DO NOT MANUALLY UPDATE		NEW WAVE RESEARCH a division of esi
	FINISH: TOLERANCE DECIMALS ANGLES XXX ± 0.0 ± 1/2° BREAK SHARP EDGES .005"	APPROVALS DATE	
MATERIAL PMMA	RESF ENG	SIZE B	DWG. NO. NCC-001
FINISH OPTICALLY POLISHED	MFG ENG	REV H	SCALE: 2:1
DO NOT SCALE DRAWING	QUAL ENG	CAD FILE: MainBody.sldprt	

1 2 3 4 5 6 7 8

THE INFORMATION CONTAINED IN THIS DRAWING IS THE SOLE PROPERTY OF NEW WAVE RESEARCH. ANY REPRODUCTION IN PART OR WHOLE WITHOUT THE WRITTEN PERMISSION OF NEW WAVE RESEARCH IS PROHIBITED.



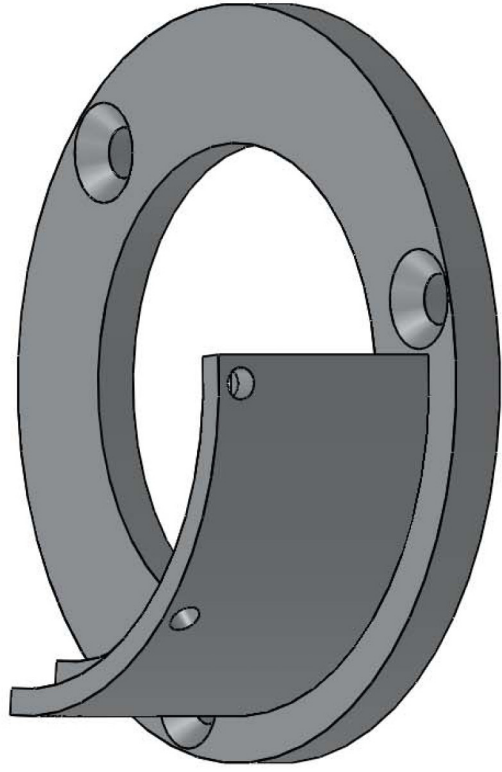
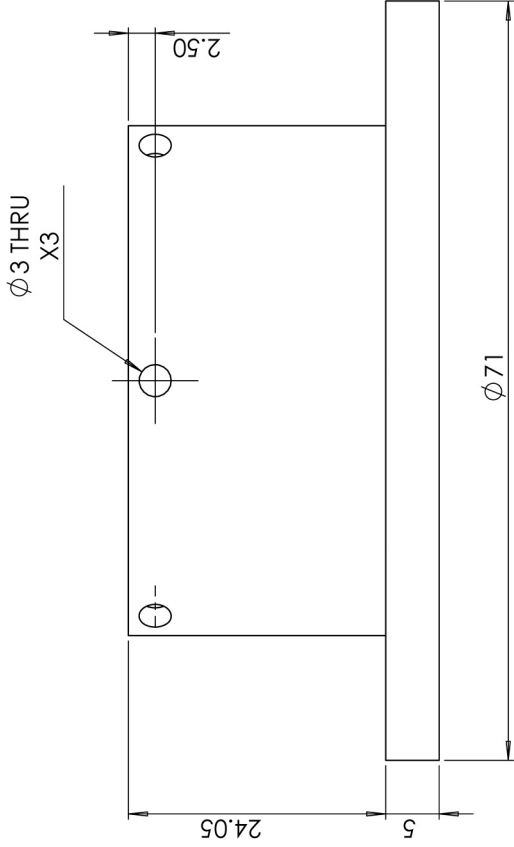
VIEW F
SCALE 2 : 1

UNLESS OTHERWISE SPECIFIED DIMENSIONS ARE IN MM	CAD GENERATED DRAWING DO NOT MANUALLY UPDATE		DATE												
	APPROVALS	DRAWN													
FINISH: DECIMALS: .XX ± 0.10 ANGLES: ±1/2° .XXX ± .005 BREAK SHARP EDGES .005"	CHECKED	RES'P ENG													
MATERIAL: PMMA	MFG ENG	QUAL ENG													
FINISH: OPTICALLY POLISHED	DO NOT SCALE DRAWING														
<table border="1"> <tr> <td colspan="2">NEW WAVE RESEARCH a division of esi</td> <td colspan="2">NON CONTACT CELL MAIN BODY</td> </tr> <tr> <td colspan="2">BNC CONNECTION DETAIL</td> <td>SIZE: B</td> <td>REV: H</td> </tr> <tr> <td colspan="2"></td> <td>DWG. NO: NCC-001</td> <td></td> </tr> </table>				NEW WAVE RESEARCH a division of esi		NON CONTACT CELL MAIN BODY		BNC CONNECTION DETAIL		SIZE: B	REV: H			DWG. NO: NCC-001	
NEW WAVE RESEARCH a division of esi		NON CONTACT CELL MAIN BODY													
BNC CONNECTION DETAIL		SIZE: B	REV: H												
		DWG. NO: NCC-001													
SCALE: 2:1		CAD FILE: Main Body.sldprt													

1 2 3 4 5 6 7 8

THE INFORMATION CONTAINED IN THIS DRAWING IS THE SOLE PROPERTY OF NEW WAVE RESEARCH. ANY REPRODUCTION IN PART OR WHOLE WITHOUT THE WRITTEN PERMISSION OF NEW WAVE RESEARCH IS PROHIBITED.

D-8



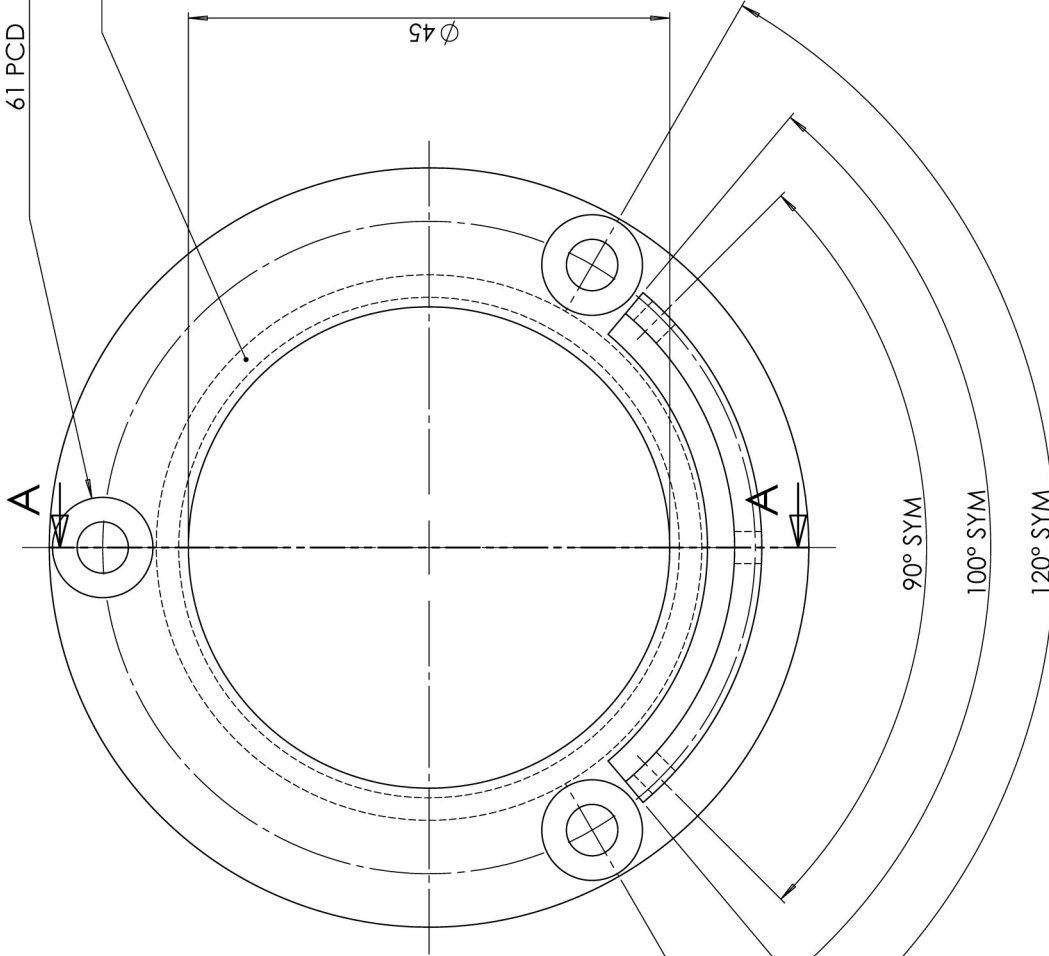
UNLESS OTHERWISE SPECIFIED DIMENSIONS ARE IN MM	CAD GENERATED DRAWING DO NOT MANUALLY UPDATE		NEW WAVE RESEARCH a division of esi
	APPROVALS	DATE	
FINISH: TOLERANCE: DECIMALS ANGLES XXX ± 0.00 ± 1/2° BREAK SHARP EDGES .005"	DRAWN	CHECKED	NON CONTACT CELL TOP PLATE ATTACHMENT ARM ISOMETRIC AND FRONT VIEWS
MATERIAL 6061-T6 AL ALLOY	RESP ENG	MFG ENG	SIZE B
FINISH	QUAL ENG		DWG. NO. NCC-002
DO NOT SCALE DRAWING			REV B
			SCALE: 2:1 CAD FILE: Top Plate.stp

SHEET 1 OF 2

THE INFORMATION CONTAINED IN THIS DRAWING IS THE SOLE PROPERTY OF NEW WAVE RESEARCH. ANY REPRODUCTION IN PART OR WHOLE WITHOUT THE WRITTEN PERMISSION OF NEW WAVE RESEARCH IS PROHIBITED.

3 x ϕ 4.80 THRU ALL
 \sphericalangle ϕ 9.40 X 90°
 61 PCD

O-RING GROOVE
 ϕ 46.80 I.D.

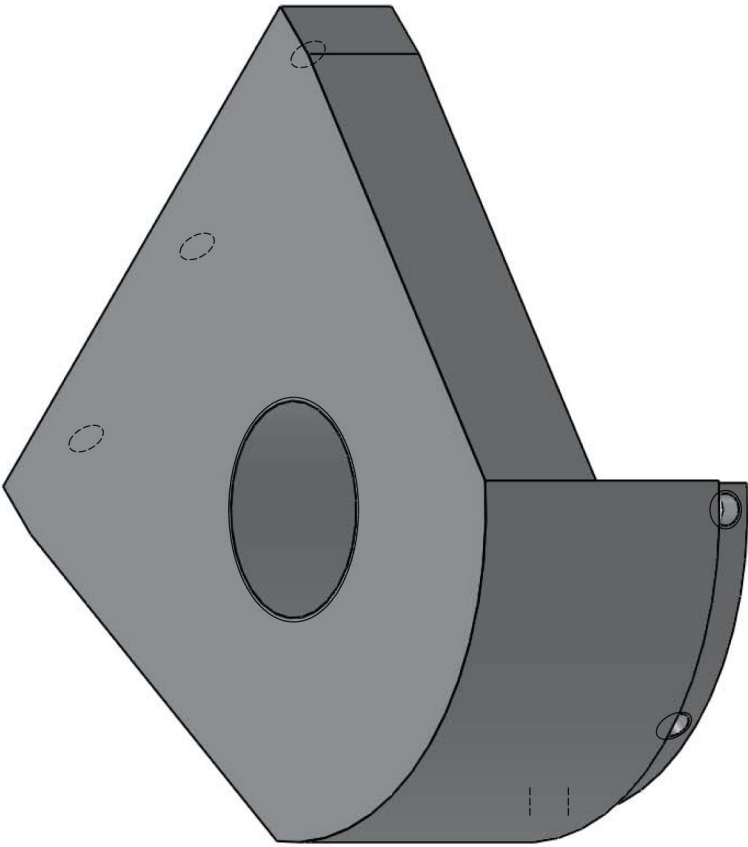
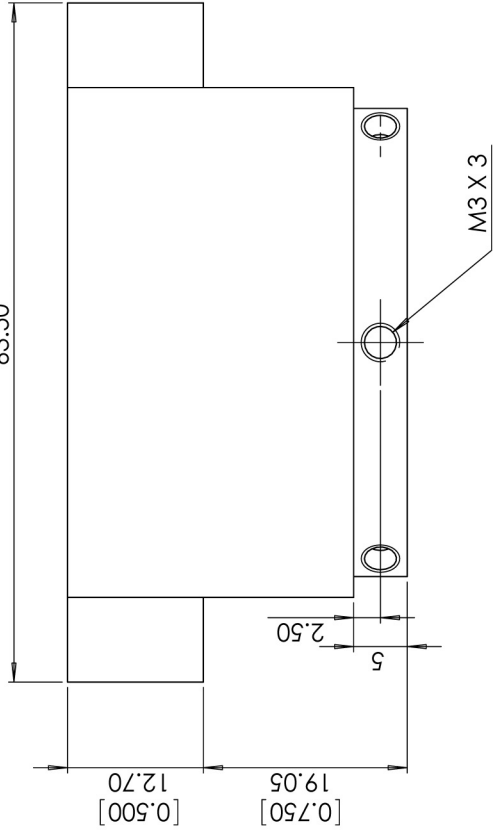


SECTION A-A
 SCALE 2:1

UNLESS OTHERWISE SPECIFIED DIMENSIONS ARE IN MM		CAD GENERATED DRAWING DO NOT MANUALLY UPDATE	
FINISH:	TOLERANCE:	APPROVALS:	DATE:
DECIMALS: .XX ± .010 .XXX ± .005	ANGLES: ± 1/2°	DRAWN:	
BREAK SHARP EDGES .005"		CHECKED:	
MATERIAL: 6061-T6 AL ALLOY		RESP ENG:	
FINISH:		MFG ENG:	
		QUAL ENG:	
DO NOT SCALE DRAWING		SCALE: 2:1	
NEW WAVE RESEARCH a division of esi		NON CONTACT CELL TOP AND CENTRELINE SECTION VIEW	
SIZE: B		UWS: NO	REV: B
NCC-002		CAD FILE: Top Plate.sldprt	
SHEET 2 OF 2		1	

THE INFORMATION CONTAINED IN THIS DRAWING IS THE SOLE PROPERTY OF NEW WAVE RESEARCH. ANY REPRODUCTION IN PART OR WHOLE WITHOUT THE WRITTEN PERMISSION OF NEW WAVE RESEARCH IS PROHIBITED.

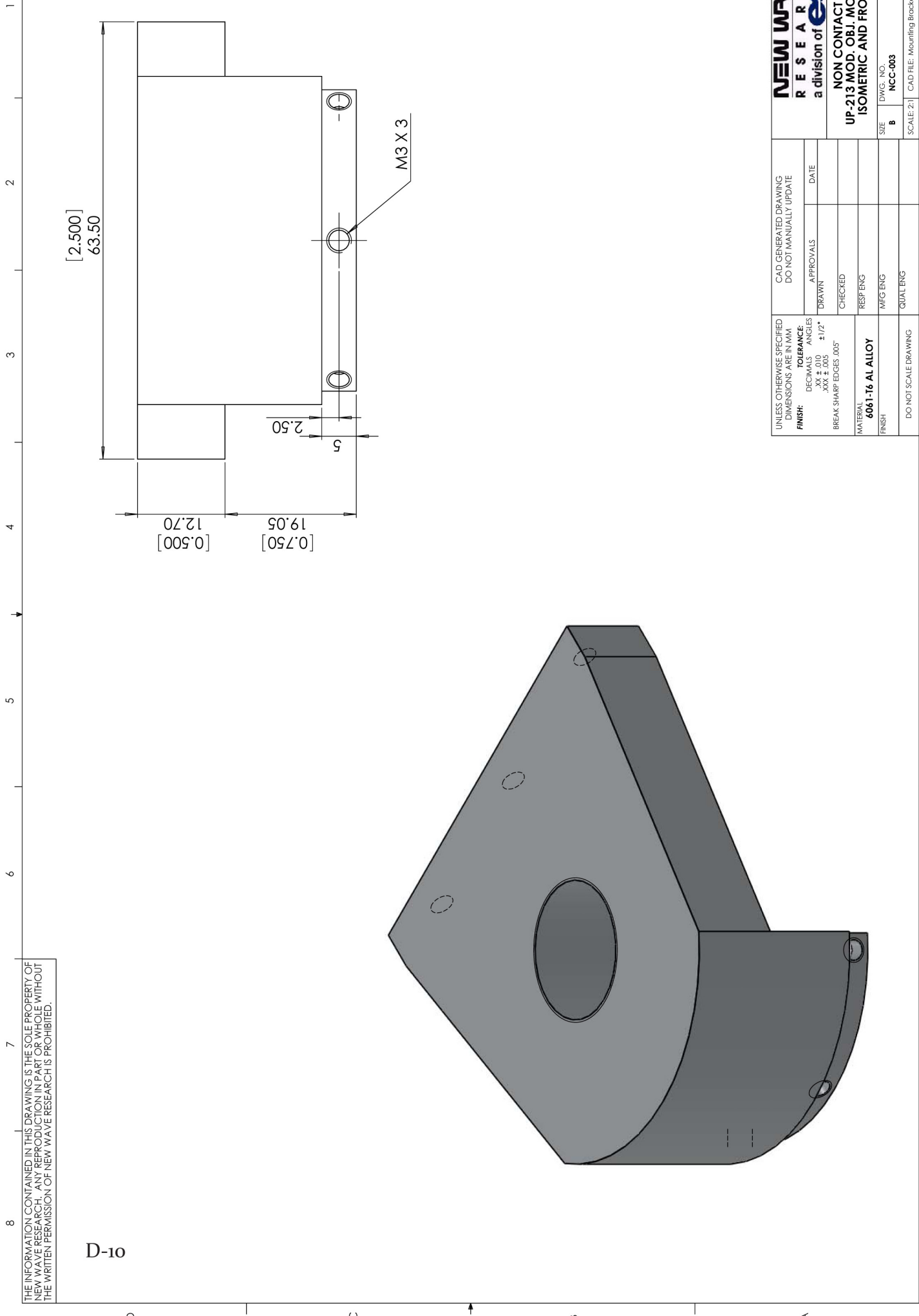
D-10



UNLESS OTHERWISE SPECIFIED DIMENSIONS ARE IN MM		CAD GENERATED DRAWING DO NOT MANUALLY UPDATE	
FINISH: DECIMALS: ANGLES: XXX ± 0.00 ± 1/2° BREAK SHARP EDGES .005"		DRAWN	DATE
TOLERANCE: XXX ± 0.00 ± 1/2°		CHECKED	
MATERIAL: 6061-T6 AL ALLOY		RESP ENG	
FINISH:		MFG ENG	
DO NOT SCALE DRAWING		QUAL ENG	
		SIZE	REV
		B	A
		SCALE: 2:1 CAD FILE: Mounting Bracket.rst.dwg SHEET 1 OF 2	

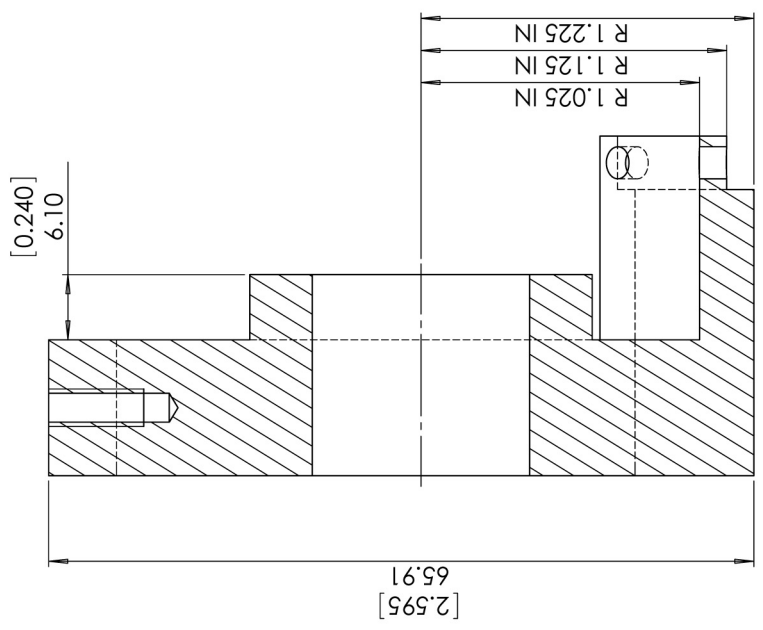
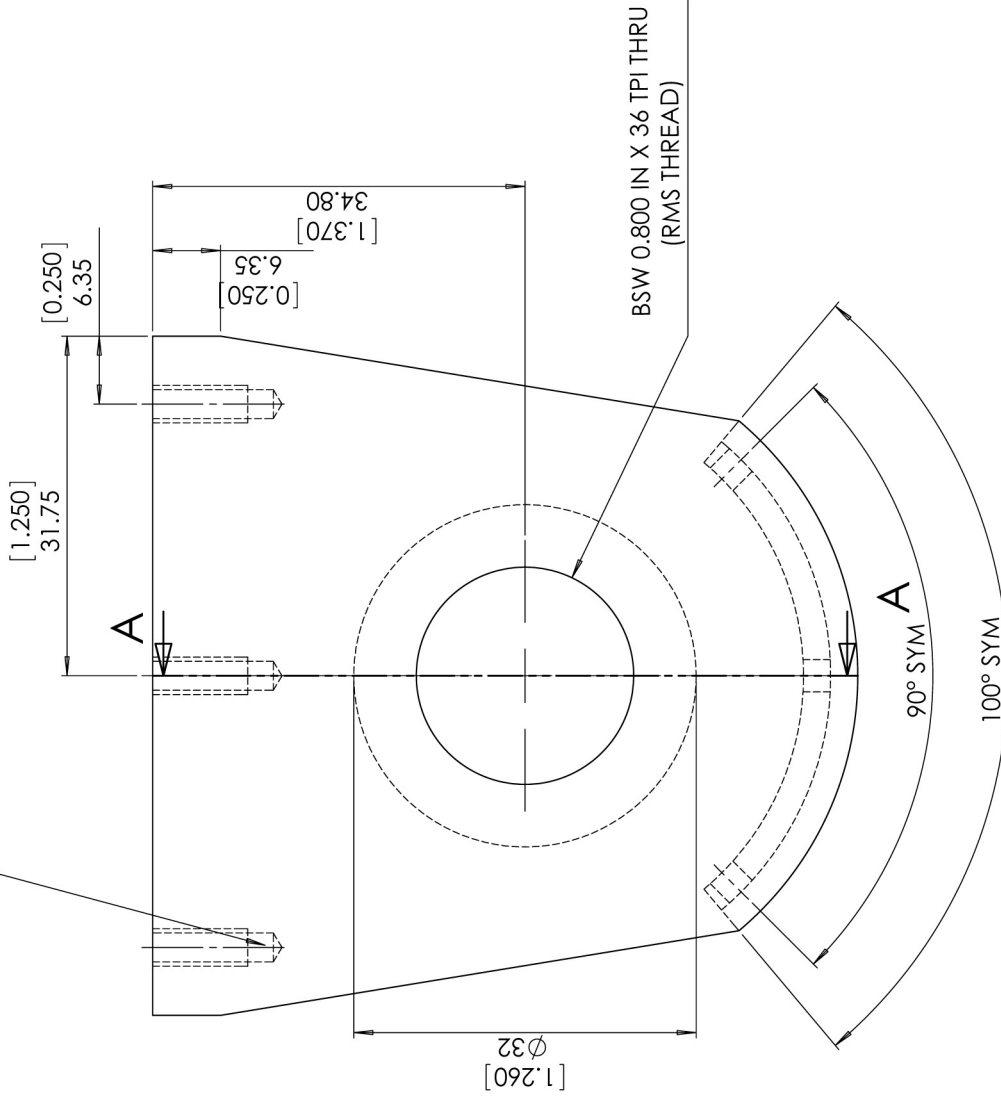
**NEW WAVE
RESEARCH**
a division of **esi**

**NON CONTACT CELL
UP-213 MOD. OBJ. MOUNT. PLATE
ISOMETRIC AND FRONT VIEWS**



THE INFORMATION CONTAINED IN THIS DRAWING IS THE SOLE PROPERTY OF NEW WAVE RESEARCH. ANY REPRODUCTION IN PART OR WHOLE WITHOUT THE WRITTEN PERMISSION OF NEW WAVE RESEARCH IS PROHIBITED.

3 x 6-32 UNC ∇ 0.35

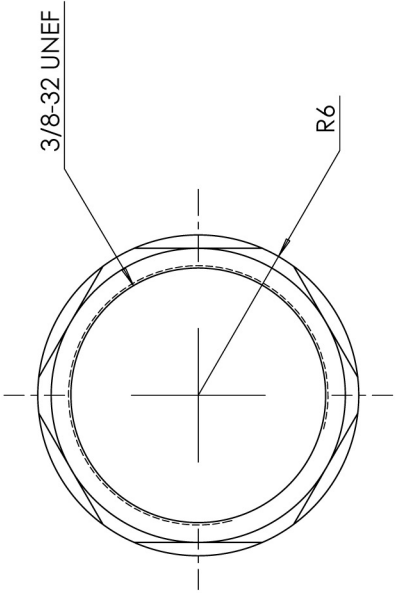


SECTION A-A
SCALE 2:1

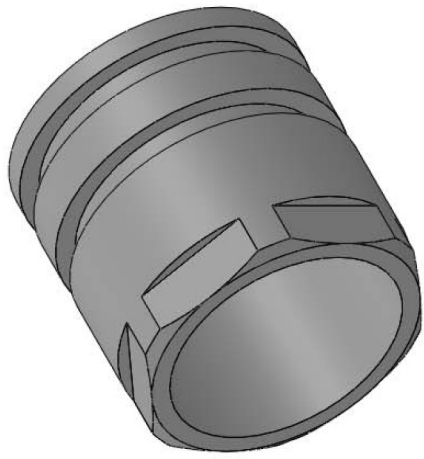
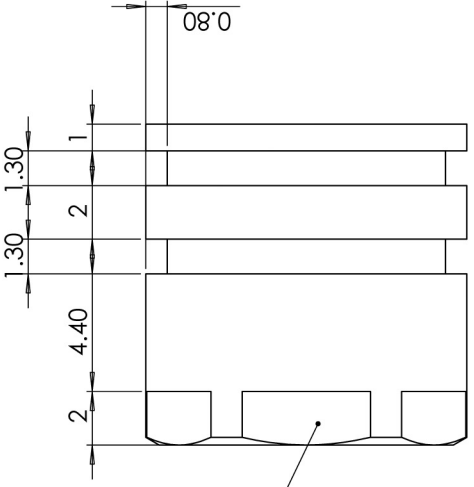
UNLESS OTHERWISE SPECIFIED DIMENSIONS ARE IN MM	CAD GENERATED DRAWING DO NOT MANUALLY UPDATE	
	APPROVALS	DATE
FINISH: DECIMALS: .XX \pm .010 ANGLES: .XXX \pm .005 \pm 1/2° BREAK SHARP EDGES .005"	DRAWN	CHECKED
MATERIAL: 6061-T6 AL ALLOY	RESP ENG	MFG ENG
FINISH: DO NOT SCALE DRAWING	QUAL ENG	
	SIZE: B	DWG. NO.: NCC-003
	REV: A	
NEW WAVE RESEARCH a division of esi		NON CONTACT CELL UP-213 MOD. OBL. MOUNT. PLATE TOP AND CENTRELINE SECTION VIEWS
SCALE: 2:1		CAD FILE: Mounting Bracket.dwg

THE INFORMATION CONTAINED IN THIS DRAWING IS THE SOLE PROPERTY OF NEW WAVE RESEARCH. ANY REPRODUCTION IN PART OR WHOLE WITHOUT THE WRITTEN PERMISSION OF NEW WAVE RESEARCH IS PROHIBITED.

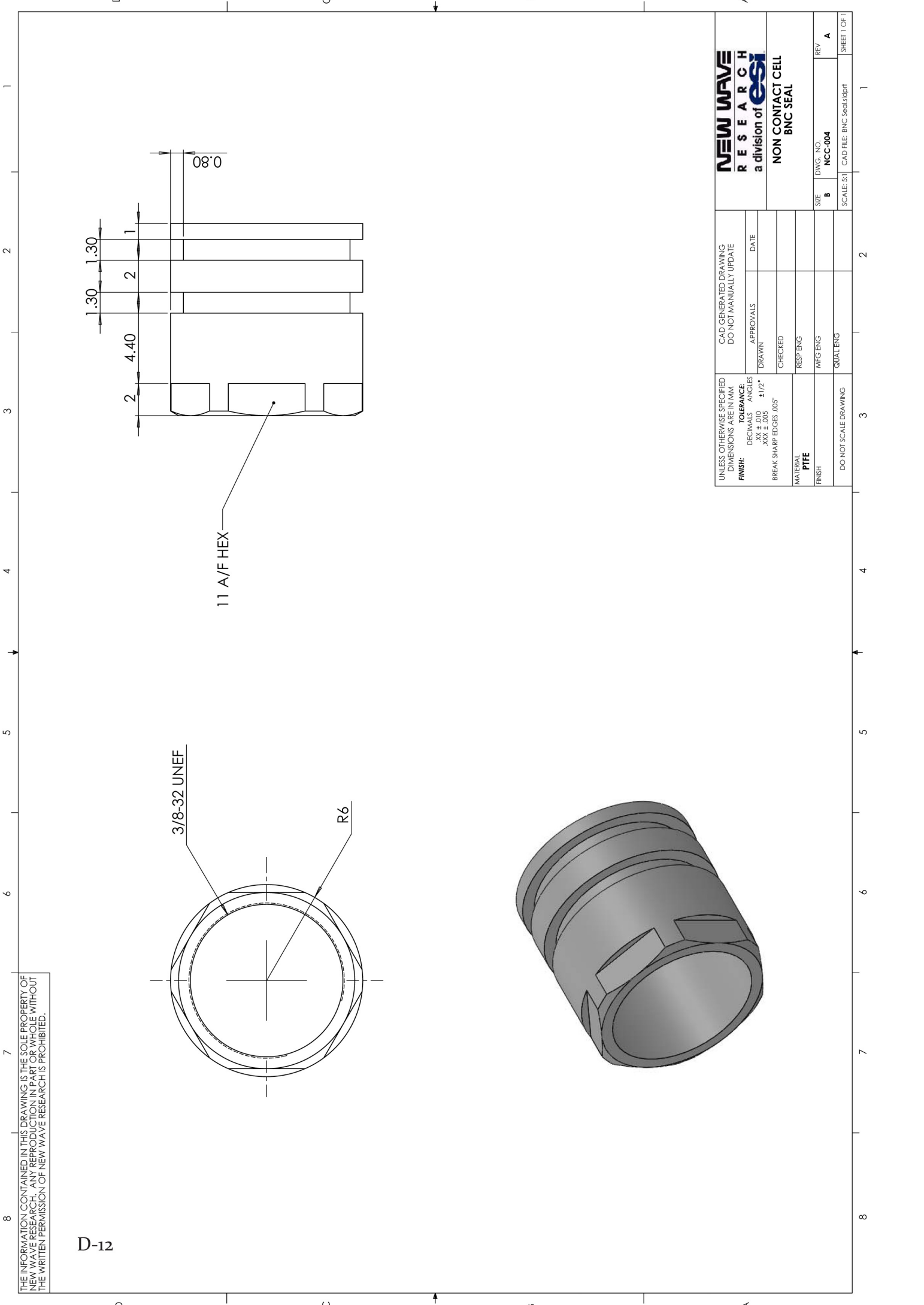
D-12



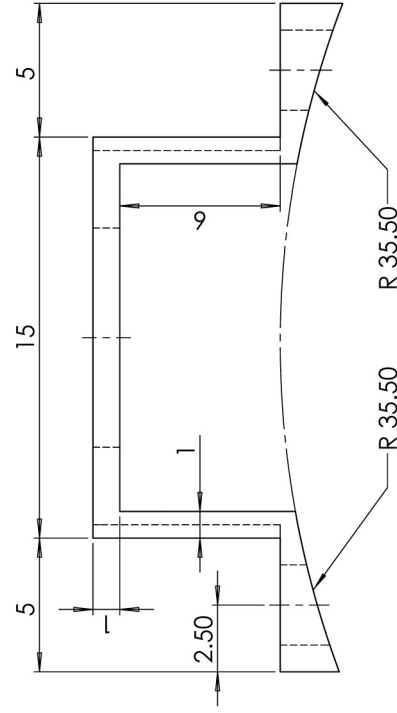
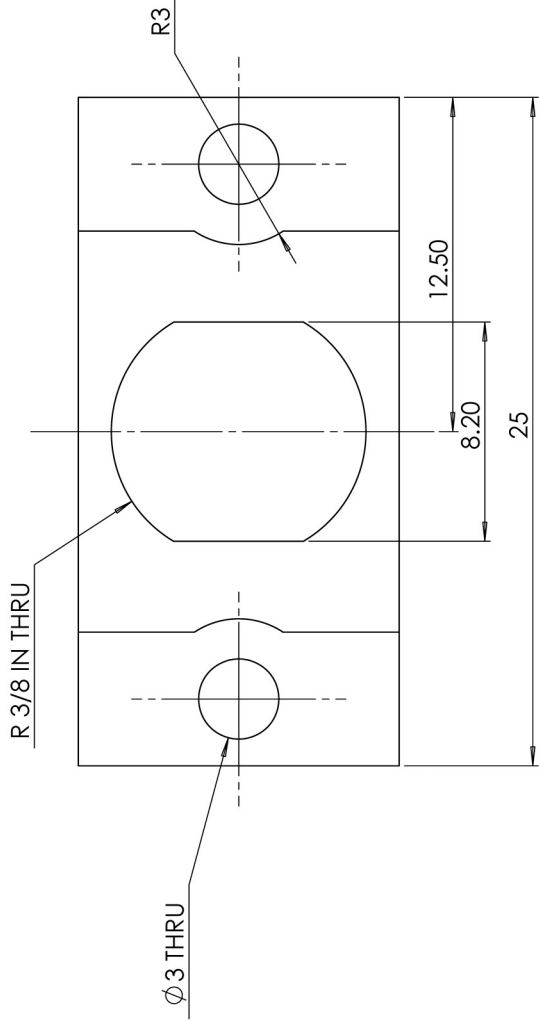
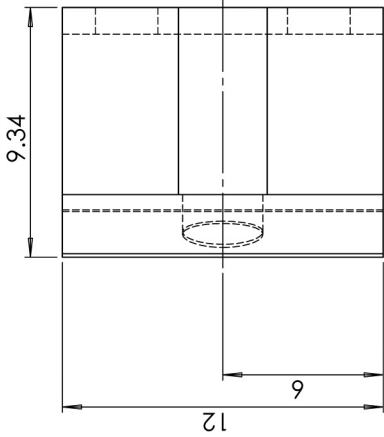
11 A/F HEX



UNLESS OTHERWISE SPECIFIED DIMENSIONS ARE IN MM	CAD GENERATED DRAWING DO NOT MANUALLY UPDATE		NEW WAVE RESEARCH a division of esi NON CONTACT CELL BNC SEAL
	APPROVALS	DATE	
FINISH: DECIMALS: ANGLES XXX ± 0.00 ± 1/2° BREAK SHARP EDGES .005"	DRAWN	CHECKED	
MATERIAL PIPE	RESP ENG	MFG ENG	SIZE B
FINISH	QUAL ENG		DWG. NO. NCC-004
DO NOT SCALE DRAWING			REV A
			SCALE: S:1 CAD FILE: BNC Seal.dwg



THE INFORMATION CONTAINED IN THIS DRAWING IS THE SOLE PROPERTY OF NEW WAVE RESEARCH. ANY REPRODUCTION IN PART OR WHOLE WITHOUT THE WRITTEN PERMISSION OF NEW WAVE RESEARCH IS PROHIBITED.



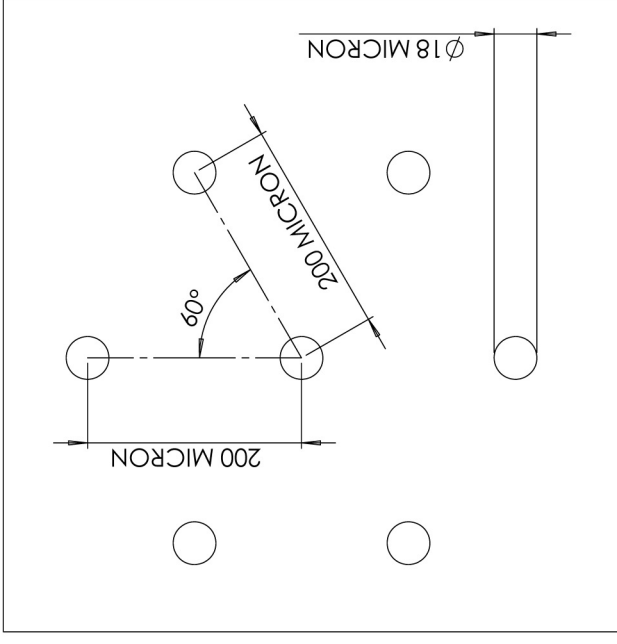
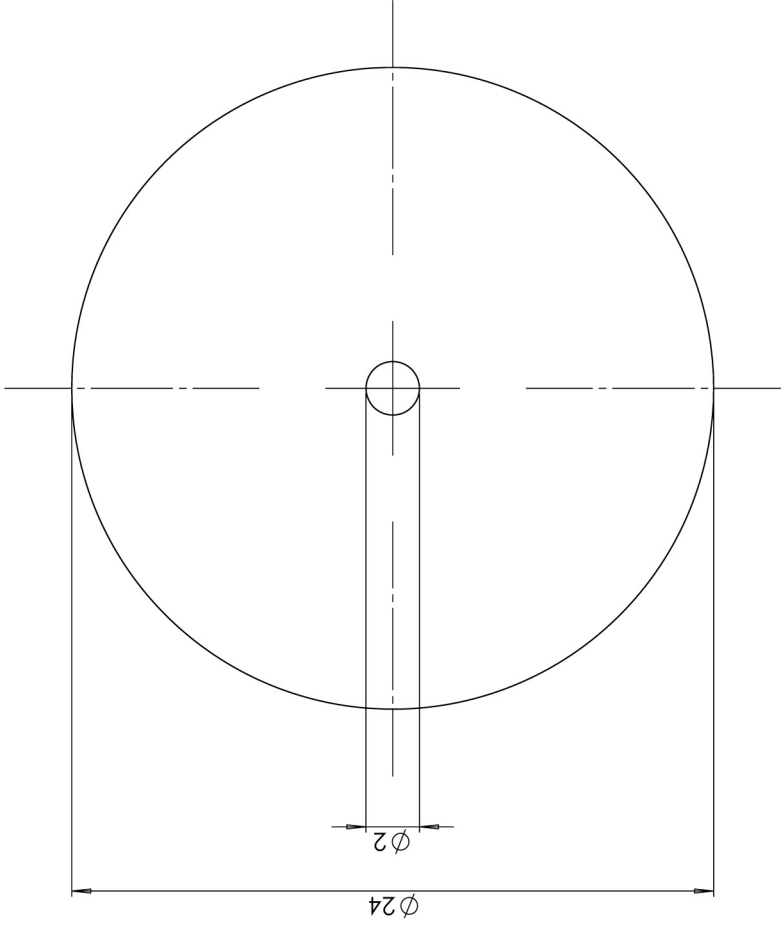
UNLESS OTHERWISE SPECIFIED DIMENSIONS ARE IN MM	FINISH:	DECIMALS	TOLERANCE	ANGLES	CAD GENERATED DRAWING DO NOT MANUALLY UPDATE	APPROVALS	DATE
	XX ± 0.10	± 1/2°	XXX ± .005	BREAK SHARP EDGES .005"			
MATERIAL	STAINLESS STEEL			CHECKED	RESF ENG	MFG ENG	QUAL ENG
FINISH	DO NOT SCALE DRAWING			DO NOT SCALE DRAWING	DO NOT SCALE DRAWING	DO NOT SCALE DRAWING	DO NOT SCALE DRAWING
SIZE	DWG. NO.	NCC-005	REV	A	SCALE: 5:1	CAD FILE: BNC Mount.sdppt	SHEET 1 OF 1

NEW WAVE RESEARCH
a division of **esi**

**NON CONTACT CELL
BNC MOUNTING BRACKET**

THE INFORMATION CONTAINED IN THIS DRAWING IS THE SOLE PROPERTY OF NEW WAVE RESEARCH. ANY REPRODUCTION IN PART OR WHOLE WITHOUT THE WRITTEN PERMISSION OF NEW WAVE RESEARCH IS PROHIBITED.

D-14



HOLE PATTERN DETAIL
NOT TO SCALE

UNLESS OTHERWISE SPECIFIED
DIMENSIONS ARE IN MM

FINISH:
DECIMALS ANGLES
XXX ± 0.00 ± 1/2°
BREAK SHARP EDGES .005"

CAD GENERATED DRAWING
DO NOT MANUALLY UPDATE

DRAWN	APPROVALS	DATE
CHECKED		
RESP ENG		
MFG ENG		
QUAL ENG		

**NEW WAVE
RESEARCH**
a division of **esi**

**NON CONTACT CELL
GAS STIFFENING MESH**

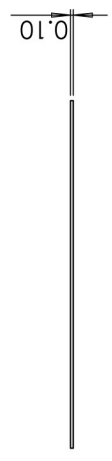
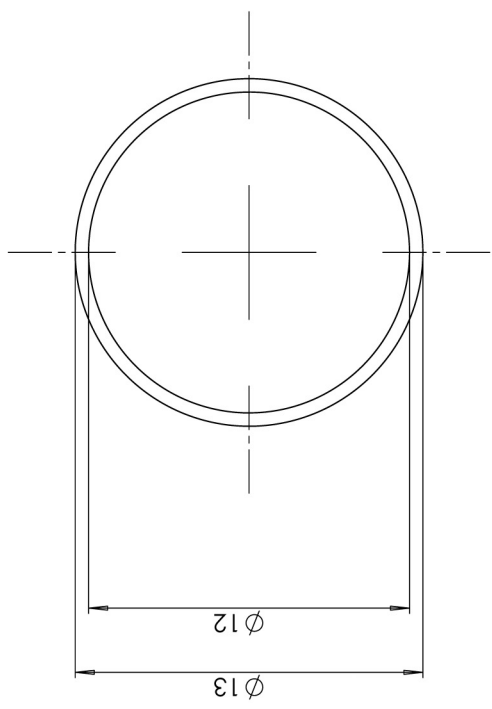
MATERIAL	NICKEL MESH
FINISH	
SIZE	DWG. NO. NCC-006
REV	A
SCALE: S:1	CAD FILE: Mesh.sldprt

SHEET 1 OF 1

1 2 3 4 5 6 7 8

D C B A

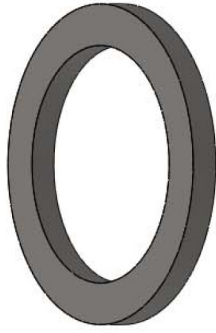
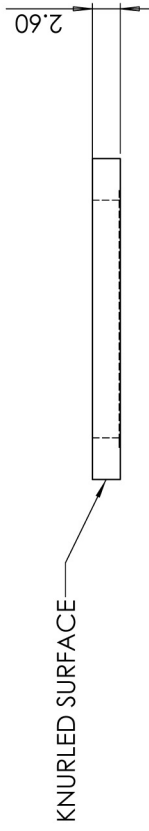
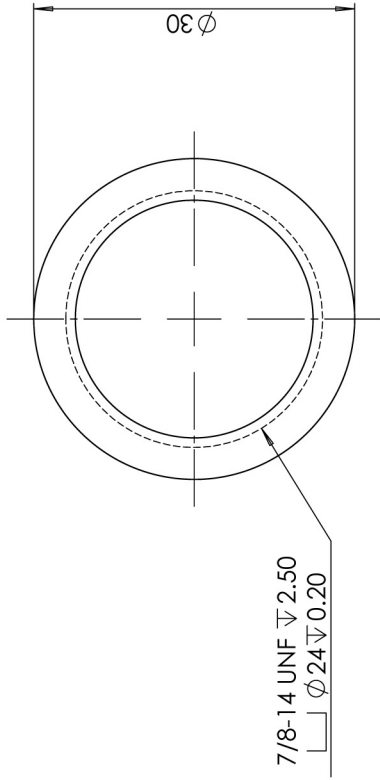
THE INFORMATION CONTAINED IN THIS DRAWING IS THE SOLE PROPERTY OF NEW WAVE RESEARCH. ANY REPRODUCTION IN PART OR WHOLE WITHOUT THE WRITTEN PERMISSION OF NEW WAVE RESEARCH IS PROHIBITED.



UNLESS OTHERWISE SPECIFIED DIMENSIONS ARE IN MM	CAD GENERATED DRAWING DO NOT MANUALLY UPDATE		DATE
	APPROVALS	DRAWN	
FINISH: DECIMALS: .XX ± 0.10 ANGLES: ±1/2° .XXX ± .005 BREAK SHARP EDGES .005"	CHECKED		
MATERIAL: STAINLESS STEEL	RESP ENG		
FINISH: DO NOT SCALE DRAWING	MFG ENG		
	QUAL ENG		
NEW WAVE RESEARCH a division of esi		SIZE: B DWG. NO: NCC-007 REV: A	
NON CONTACT CELL FLOW RESTRICTOR		SCALE: 5:1 CAD FILE: Flow Restrictor.dwg SHEET 1 OF 1	

THE INFORMATION CONTAINED IN THIS DRAWING IS THE SOLE PROPERTY OF NEW WAVE RESEARCH. ANY REPRODUCTION IN PART OR WHOLE WITHOUT THE WRITTEN PERMISSION OF NEW WAVE RESEARCH IS PROHIBITED.

D-16



UNLESS OTHERWISE SPECIFIED DIMENSIONS ARE IN MM FINISH: DECIMALS ANGLES XXX ± 0.00 ± 1/2° BREAK SHARP EDGES .005"	CAD GENERATED DRAWING DO NOT MANUALLY UPDATE		DATE
	DRAWN	APPROVALS	
	CHECKED		
	RESP ENG		
	MFG ENG		
	QUAL ENG		
MATERIAL STAINLESS STEEL			
FINISH			
DO NOT SCALE DRAWING			
	SIZE B	DWG. NO. NCC-008	REV A
SCALE: 2:1	CAD FILE: Screw Ring.sldprt		SHEET 1 OF 1

**NEW WAVE
RESEARCH**
a division of **esi**

**NON CONTACT CELL
NI MESH SEALING SCREW RING**

1 2 3 4 5 6 7 8

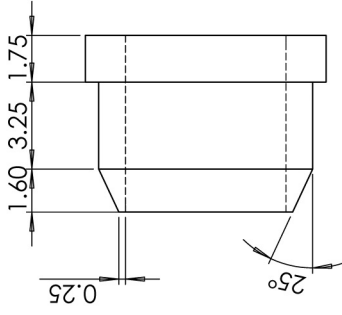
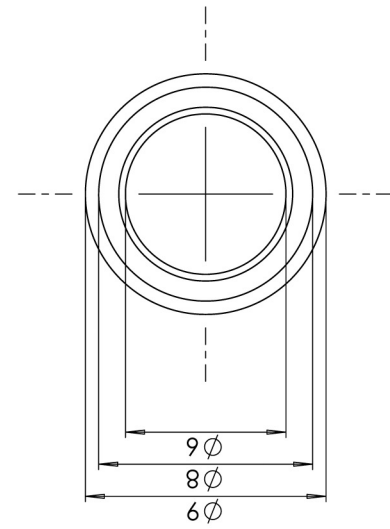
D

C

B

A

THE INFORMATION CONTAINED IN THIS DRAWING IS THE SOLE PROPERTY OF NEW WAVE RESEARCH. ANY REPRODUCTION IN PART OR WHOLE WITHOUT THE WRITTEN PERMISSION OF NEW WAVE RESEARCH IS PROHIBITED.

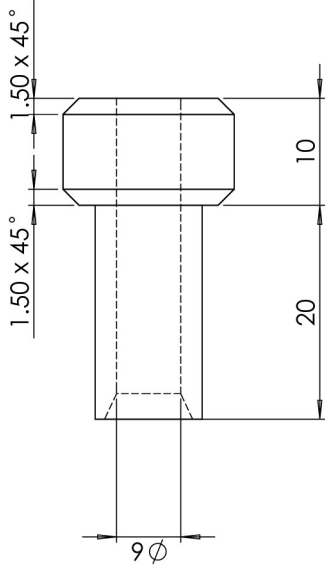
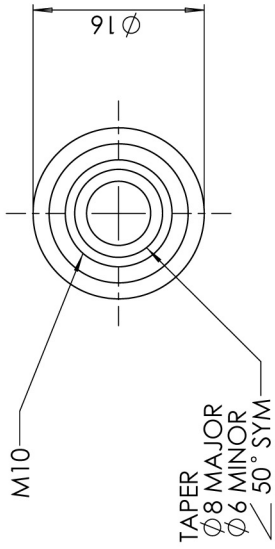


D-17

UNLESS OTHERWISE SPECIFIED DIMENSIONS ARE IN MM	CAD GENERATED DRAWING DO NOT MANUALLY UPDATE	
	APPROVALS	DATE
FINISH: DECIMALS: .XX ± 0.10 ANGLES: ±1/2° .XXX ± .005	DRAWN	
BREAK SHARP EDGES .005"	CHECKED	
MATERIAL PEEK	RESP ENG	
FINISH	MFG ENG	
DO NOT SCALE DRAWING	QUAL ENG	
NEW WAVE RESEARCH a division of esi		SIZE: DWG: NO. NCC-009 REV: A
NON CONTACT CELL VACUUM SEAL FERRULE 6 MM O.D. TUBING		SCALE: 5:1 CAD FILE: Ferrule 6mm.sdppt SHEET 1 OF 1

THE INFORMATION CONTAINED IN THIS DRAWING IS THE SOLE PROPERTY OF NEW WAVE RESEARCH. ANY REPRODUCTION IN PART OR WHOLE WITHOUT THE WRITTEN PERMISSION OF NEW WAVE RESEARCH IS PROHIBITED.

D-18



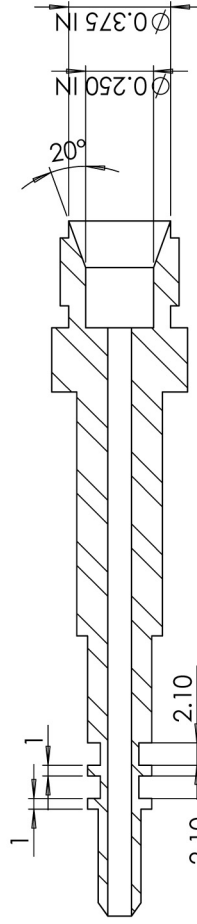
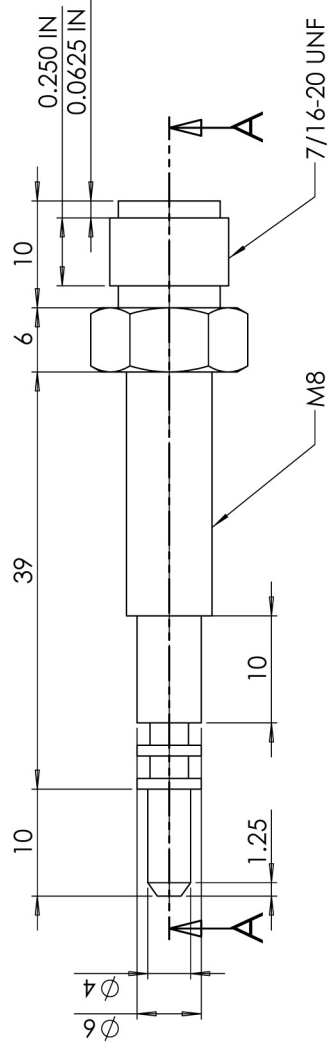
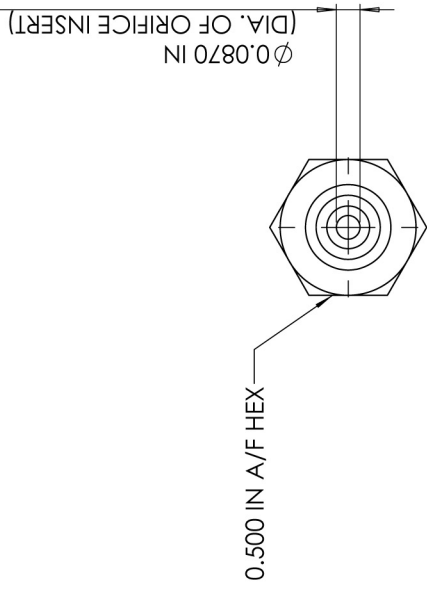
UNLESS OTHERWISE SPECIFIED DIMENSIONS ARE IN MM	CAD GENERATED DRAWING DO NOT MANUALLY UPDATE	
	APPROVALS	DATE
FINISH: TOLERANCE: DECIMALS ANGLES XXX ± .000 ± 1/2° BREAK SHARP EDGES .005"	DRAWN	CHECKED
MATERIAL: PEEK	RESP ENG	MFG ENG
FINISH:	QUAL ENG	
DO NOT SCALE DRAWING	SCALE: S:1	CAD FILE: Fitting 6mm.sdppt
	SIZE B	DWG. NO. NCC-010
	REV A	

**NEW WAVE
RESEARCH**
a division of **esi**

**NON CONTACT CELL
VACUUM SEAL FITTING
6 MM O.D. TUBING**

SHEET 1 OF 1

THE INFORMATION CONTAINED IN THIS DRAWING IS THE SOLE PROPERTY OF NEW WAVE RESEARCH. ANY REPRODUCTION IN PART OR WHOLE WITHOUT THE WRITTEN PERMISSION OF NEW WAVE RESEARCH IS PROHIBITED.



SECTION A-A

UNLESS OTHERWISE SPECIFIED DIMENSIONS ARE IN MM	CAD GENERATED DRAWING DO NOT MANUALLY UPDATE	
	APPROVALS	DATE
FINISH: DECIMALS .XX ± 0.10 ANGLES .XXX ± .005 * ± 1/2° BREAK SHARP EDGES .005"	DRAWN	CHECKED
MATERIAL: STAINLESS STEEL	RESP ENG	
FINISH: DO NOT SCALE DRAWING	MFG ENG	
	QUAL ENG	
	SIZE B	DWG. NO. JP-001
	REV B	

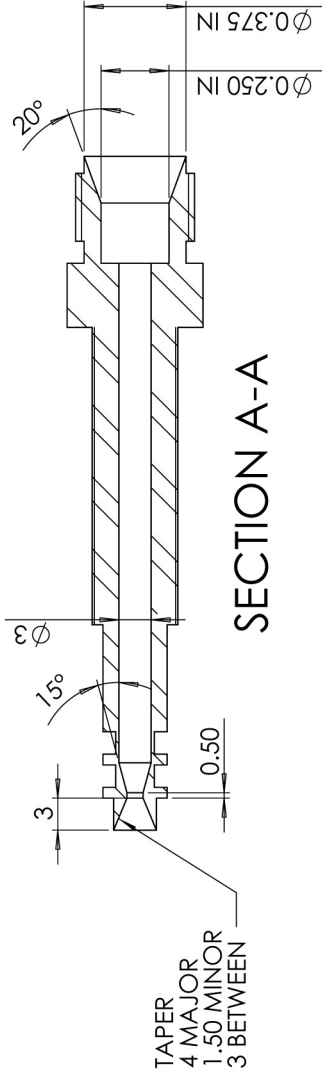
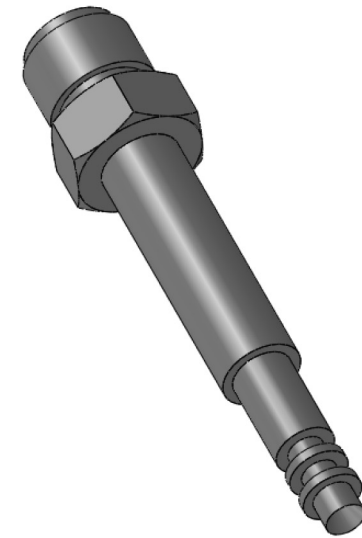
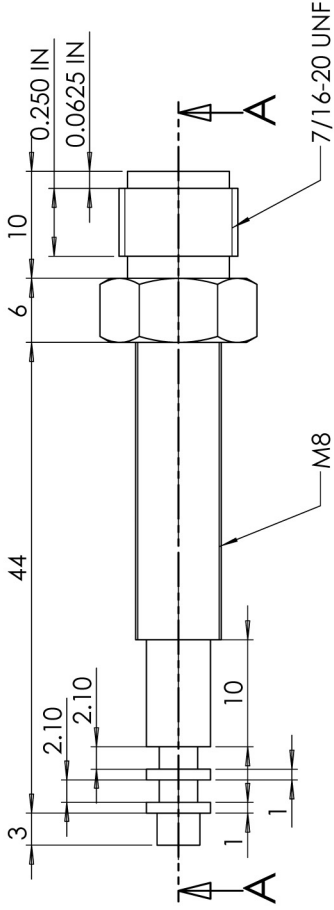
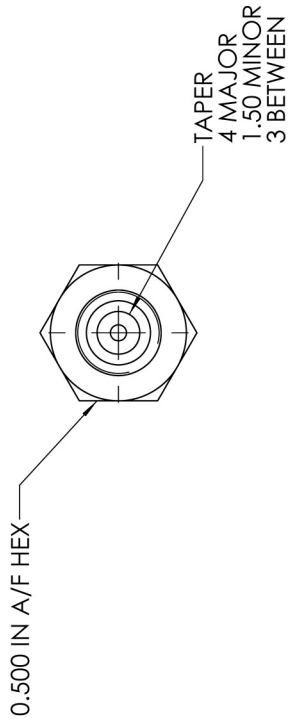
NEW WAVE RESEARCH
a division of **esi**

MICRO JET-PUMP NOZZLE

SCALE: 2:1 | CAD FILE: jet Pump Nozzle.dwg | SHEET 1 OF 1

THE INFORMATION CONTAINED IN THIS DRAWING IS THE SOLE PROPERTY OF NEW WAVE RESEARCH. ANY REPRODUCTION IN PART OR WHOLE WITHOUT THE WRITTEN PERMISSION OF NEW WAVE RESEARCH IS PROHIBITED.

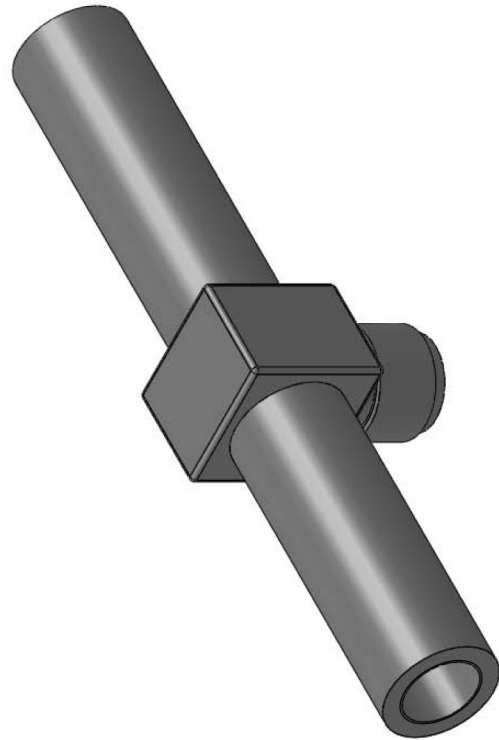
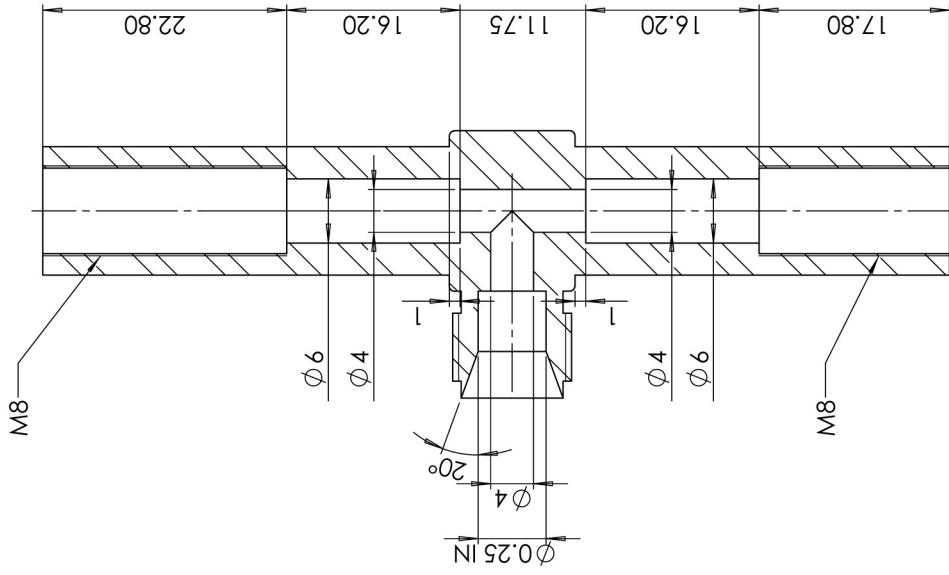
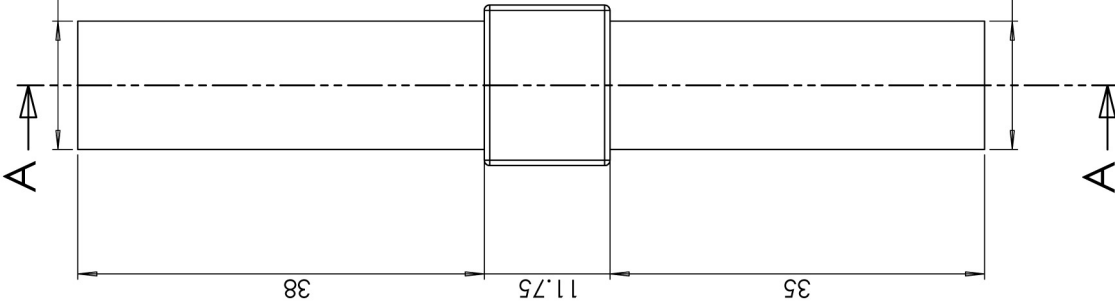
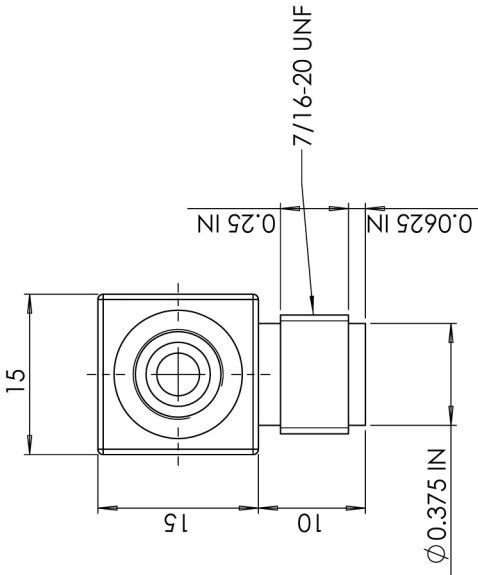
D-20



UNLESS OTHERWISE SPECIFIED DIMENSIONS ARE IN MM	CAD GENERATED DRAWING DO NOT MANUALLY UPDATE	
	APPROVALS	DATE
FINISH: DECIMALS ANGLES XXX ± 0.00 ± 1/2° BREAK SHARP EDGES .005"	DRAWN	
MATERIAL: STAINLESS STEEL	CHECKED	
FINISH:	RESP ENG	
DO NOT SCALE DRAWING	MFG ENG	
	QUAL ENG	
	SIZE	DWG. NO.
	B	JP-002
	REV	B
	SCALE: 2:1 CAD FILE: Jet Pump_Collector.sldprt SHEET 1 OF 1	

NEW WAVE
RESEARCH
a division of **esi**
MICRO JET-PUMP
COLLECTOR

THE INFORMATION CONTAINED IN THIS DRAWING IS THE SOLE PROPERTY OF NEW WAVE RESEARCH. ANY REPRODUCTION IN PART OR WHOLE WITHOUT THE WRITTEN PERMISSION OF NEW WAVE RESEARCH IS PROHIBITED.



SECTION A-A

UNLESS OTHERWISE SPECIFIED DIMENSIONS ARE IN MM		CAD GENERATED DRAWING DO NOT MANUALLY UPDATE	
FINISH: DECIMALS .XX ANGLES ±1/2° TOLERANCE .XX ± 0.10 .XXX ± .005 BREAK SHARP EDGES .005"	APPROVALS	DATE	
	DRAWN	CHECKED	
MATERIAL STAINLESS STEEL	RESP ENG		
FINISH DO NOT SCALE DRAWING	MFG ENG		
	QUAL ENG		
SIZE B	DWG. NO. JP-003	REV B	SHEET 1 OF 1
NEW WAVE RESEARCH a division of esi MICRO JET-PUMP TEE PIECE			
SCALE: 2:1 CAD FILE: jetPump Tee.sldprt			

* * * * *